# HYDRAULIC FRACTURE DRIVEN BY TURBULENT FLOW

by

**Navid Zolfaghari Moheb**

Bachelor of Science, Sharif University of Technology, 2011

Submitted to the Graduate Faculty of
the Swanson School of Engineering in partial fulfillment
of the requirements for the degree of
**Doctor of Philosophy**

University of Pittsburgh
2017

UNIVERSITY OF PITTSBURGH

SWANSON SCHOOL OF ENGINEERING

This dissertation was presented

by

Navid Zolfaghari Moheb

It was defended on

August 18, 2017

and approved by

Andrew P. Bunger, Ph.D., Assistant Professor, Department of Civil
and Environmental Engineering & Department of Chemical and Petroleum Engineering

Amit Acharya, Ph.D., Professor, Department of Civil and Environmental Engineering,
Carnegie Mellon University

Jeen-Shang Lin, Ph.D., Associate Professor, Department of Civil and Environmental Engineering
& Bioengineering Department

Lev Khazanovich, Ph.D., Professor, Department of Civil and Environmental Engineering

Dissertation Director: Andrew P. Bunger, Ph.D., Assistant Professor, Department of Civil
and Environmental Engineering & Department of Chemical and Petroleum Engineering

Copyright © by Navid Zolfaghari Moheb

2017

# HYDRAULIC FRACTURE DRIVEN BY TURBULENT FLOW

Navid Zolfaghari Moheb, PhD

University of Pittsburgh, 2017

High flow rate, water-driven hydraulic fractures are increasingly popular in the oil and gas industry. The high injection rate and low fluid viscosity associated with these treatments leads to high Reynolds numbers. While there is some recent recognition of the growing need to extend the classical hydraulic fracture models beyond the laminar flow regime, there is little understanding of the impact of turbulent flow on hydraulic fracture growth nor are there existing solutions for simplified geometries that can provide benchmarks for numerical simulators and means for rapid estimation of hydraulic fracture dimensions.

Thus motivated, the goal of this research is to quantify the impact of replacing laminar flow with turbulent flow in HF by developing a benchmark solutions for classical HF crack propagation geometries. This study therefore is comprised of 3 main parts, each associated with a particular geometry (plane strain, blade-shaped, and radial). Each geometry brings its own challenges and a need to adopt a solution method suited to these challenges.

The noteworthy contributions of this work begin with providing a complete suite of benchmarks for simplified but practically-relevant geometries that can be used to estimate fracture dimensions and to benchmark more general numerical simulators. Secondly, this study provides a new numerical approach to HF simulation including laminar, turbulent, and laminar-turbulent transition regimes. Thirdly, this investigation demonstrates the evolution of turbulent-laminar regime in a radial HF, which has implications also for the overall behavior and evolution in more general planar fracture growth geometries. Fourthly, this study has identified that the transition range of fluid regime from turbulent-to-laminar fluid flow is relatively small and practically, it will often suffice to approximate the HF growth using the asymptotic solutions obtained from either the laminar or turbulent solution.

## TABLE OF CONTENTS

# LIST OF TABLES

# LIST OF FIGURES

# PREFACE

Mathematics and its beautiful complexity fired me with enthusiasm to follow its lead and recite its poetry. I appreciate the rationality of mathematics while expounding the physics of Nature. In other words, as Albert Einstein said in his appreciation letter for Emmy Noether, “Pure mathematics is, in its way, the poetry of logical ideas”. My long journey to finish this study is ending at this point, even though I am writing these lines at the beginning; I want to demonstrate my gratitude and appreciation to everyone who made this happen.

I would first like to thank Dr. Andrew Bunger, my advisor who trusted me on this path, supported my career goals during this work, and gave me excellent opportunities to conduct my research and pursue my passion toward applied mechanics. Andrew is not only my advisor but also a great mentor who taught me how to think better not only scientifically but also in my life.

Moreover, I would like to thank each of my committee members for their wise counsel, professional guidance, and time that they dedicated to this dissertation. Special thanks go to my colleagues, Pengju Xing, Guanyi Lu, Wei Fu, Qiao Lu, Delal Gunaydin, and Di Wang for their support, passionate intellectual debates, and collaboration. I would also like to thank Charles Hager (Scooter) for his assistance and enormous help in the laboratory. Also, I want to extend my sincere gratitude to all the collaborators in my research, Dr. Colin Meyer and Dr. Egor Dontsov.

I want to reserve a special thanks to the members of my family without whom it would have been impossible for me to pursue this project. I would like to express my gratitude to Akbar and Nahid, my parents and my ultimate role models, whose love and advice are with me in all parts of my life. I would not be at this point without their support. Also, Neda and Vahid, my sister and brother, for their endorsement, endless love, and support. Most importantly, I wish to thank my beautiful, awesome, and smart wife, Alexandra, who was always beside me, unconditionally supportive, and who always encouraged me all along this period.

This work would not have been possible without the support of the University of Pittsburgh Swanson School of Engineering and Center for Energy, and the University of Pittsburgh Center for Research Computing.

# I. INTRODUCTION

## A. BACKGROUND

Fluid pressure-driven cracks are widely observed and utilized in different fields of science and engineering and have thus attracted wide ranging contributions. A notable example of fluid-driven fracture in nature is magma intruding into rocks by driving dyke and sill formation (see e.g. the review of Rivalta et al., 2015). Another example is rapid sub-glacial drainage of the melted water in ice sheets via fluid-driven fractures (Tsai and Rice, 2010). Fluid pressure-driven fractures are not only limited to natural events, but also carried out in industry. A classic example of fluid-driven crack propagation is hydraulic fracturing (HF) to increase the productivity of oil and gas wells. Here, the fluid is used to break the rock to create high permeability pathway for hydrocarbon transport back to the well (King, 2010). Moreover, increasing hydraulic conductivity of enhanced geothermal systems (e.g. Matsunaga and Yamaguchi, 1992; Gérard et al., 2006), preconditioning rock masses for effective block cave mining (e.g. Van As and Jeffrey, 2000), and measuring underground in-situ stresses (e.g. Cornet and Valette, 1984; Zoback et al., 1982) are all examples of hydraulic fracture applications. For additional discussion see the review of Adams and Rowe (2013).

Of these, the major application of HF is in well stimulation to increase oil and gas production. In the global oil and gas industry, hydraulic fracture (HF) has played a vital role, particularly in "unconventional" gas reservoirs. And the changes experienced by this industry over the past two decades are indeed astounding. As estimated by Montgomery and Smith (2010), more than 60% of wells are stimulated through hydraulic fracturing, and essentially all wells completed in shale formations are stimulated using HF. With the growth of water, as opposed to higher viscosity gels, as the main driving fluid for HF in the petroleum industry in 1990s-2000s, fluid-driven induced fracture has become less expensive, more effective in certain formations, and hence even more widespread. What is important to also realize is that the governing physics of the problem has changed due to this transition to higher rate pumping of lower viscosity fluids. Most notably, the fluid flow regime is much more often turbulent or in the laminar-turbulent transition. Failure to recognizing this shift and continuing to inappropriately use an assumption of laminar flow can lead to predictions that underestimate fluid pressure and hence propensity for failure growth that penetrates neighbouring layers. Laminar simulations also overestimate HF length and underestimate HF aperture ("opening" or "width", see Ames and Bunger (2015)).

Early examples of research into HF including the turbulent flow regime back to the seminal work of Perkins and Kern (1961), who provide a model for both vertically confined HF growth (blade-shaped geometry), and horizontal HF growth (radial geometry). For a vertically confined HF, they obtained a solution for both the laminar and turbulent regimes. For turbulent fluid flow, Perkins and Kern (1961) considered a constant Fanning friction factor of $0.0125$ for the fracture that corresponds to a relative roughness (ratio of roughness scale to characteristic HF width) of $0.02$. They then solved the problem to find the crack opening, again, limiting consideration to a vertical HF.

Moreover, a series of research conducted by Nilson (1981, 1988) considered plane strain (and extended to radial flow), gas-driven hydraulic fractures under a constant pressure inlet boundary condition. Nilson (1981) modeled an isothermal ideal gas flow in a plane strain geometry and identified three self-similar solutions associating with laminar, turbulent, and inviscid regimes. Hence, Nilson (1981) explained that by having these three solutions, we can grasp an overall behavior of the fluid flow. Following from this work, Nilson (1988) provides an extension to a more general form of multi-phase flow, again for the plane strain geometry.

Other important works that consider turbulent flow include Emerman et al. (1986), who obtain similarity solutions for a plane-strain HF with constant inlet flow. Anthonyrajah et al. (2013) follow the turbulent model from Emerman et al. (1986) to solve for blade-shape HF with generalized inlet boundary conditions, and demonstrate a numerical solution method for general injection boundary conditions. Additionally, Newman (2016) extends the model presented by Anthonyrajah et al. (2013) for the PKN problem with general boundary condition using Prandtl's mixing length model.

More recently, Zia and Lecampion (2016, 2017) develop a semi-analytical model and numerical simulation to model a height contained HF. Specifically, Zia and Lecampion (2017) solve the problem numerically using the drag reduction approach from Yang and Dou (2010) to estimate the friction factor. Also, they find an asymptotic solution by considering that the crack is fully turbulent and under a rough-walled condition, and/or the crack is fully turbulent and under a smooth-walled condition (the latter case conforms to the Blasius approximation Blasius (1913)).

Furthermore, Dontsov (2016) studies the crack tip transition of the fluid regime, from turbulent to laminar flow in plane-strain geometry. Dontsov (2016) used the Churchill approximation Churchill (1977) to estimate the friction factor in the HF. He also derives an asymptotic solution to fully turbulent HF and, at the end, Dontsov (2016) studies the transition regime at the crack tip. Also, Kano et al. (2015) solved the fully turbulent rough-walled HF for large leakoff using Gauckler-Manning-Strickler (GMS) approach Manning (1891); Strickler (1923, 1981).

However, in spite of these past contributions and the growing importance of the turbulent and laminar-turbulent flow regimes in HF modeling, there is at least two major gaps in the literature that will be addressed by this research. The first is that there are no benchmark solutions that demonstrate the behavior in the limit of fully-rough-walled turbulent flow for the classical simplified geometries (plane strain, radial, and blade-shaped). As a result, the growing body of simulators that incorporate turbulent flow cannot be appropriately validated. The second issue is that the importance of the transition regime and the conditions for applicability of the fully turbulent solution(s) are unknown. Hence, it is not understood the range of nominal Reynold's numbers for which each model should be used.

## B. PROJECT GOAL AND SCOPE

The goal of this research is to quantify the impact of replacing laminar flow with turbulent flow in HF by developing benchmark solutions for classical HF crack propagation geometries. This research is divided into the following sections:

- **Modeling the effect of turbulent fluid flow on the blade-shaped (PKN) geometry**:
  This component of the research is described in Chapter 2 and consists of:

    I. Introducing a mathematical model to predict the opening, length, and fluid pressure of the HF by considering turbulent flow for blade-shaped (PKN) geometry.
    II. Solving the resulting system of equations to provide a closed form semi-analytical benchmark solution.
    III. Comparing the results from the classical laminar flow model with the new turbulent model.
    IV. Developing a rigorous method to define the transition criteria from laminar to turbulent flow within HFs.

- **Solving the plane strain (KGD) model with turbulent fluid flow**:

  This component of the research is described in Chapter 3 and consists of:

    I. Introducing a mathematical model to predict the opening, length, and fluid pressure of the HF by considering turbulent flow for plane-strain geometry.
    II. Solving the resulting system of equations to provide a closed form semi-analytical benchmark solution.
    III. Comparing the results from the classical laminar flow model with the new turbulent model.
    IV. Discern the useful range of the fully turbulent solution through collaboration allowing comparison to simulations that account for the laminar-turbulent transition.

- **Modeling radial HF with fully turbulent rough-walled approximation**:

  This component of the research is described in Chapter 4 and consists of:

    I. Introducing a mathematical model to predict the opening, length, and fluid pressure of the HF by considering turbulent flow for penny-shaped (radial) geometry.
    II. Solving the resulting system of equations to provide a closed form semi-analytical benchmark solution.
    III. Comparing the results from the classical laminar flow model with the new turbulent model.
    IV. Discern the useful range of the fully turbulent solution by comparison to results obtained from a numerical simulation developed as a part of this research.

- **Solving the radial model accounting for simultaneous presence of turbulent and laminar regions**:

  This component of the research is described in Chapter 5 and consists of:

    I. Develop a numerical solution for radial crack growth, including finding the turbulent, laminar, and transition sections along a growing HF.

II. Demonstrate the evolution of flow regime within the HF as it grows.

III. Compare the results from laminar and turbulent limiting solutions with the new model., and distinguishing the differences and clarifying the conditions of validity for the limiting solutions.

This study is therefore comprised of 3 main parts, each associated with a particular geometry (plane strain, PKN, radial). Each geometry brings its own challenges and the need to adopt a solution method suited to these challenges. Since this research examines the emerging role of turbulent flow in the context of fluid-driven crack propagation; therefore, for each geometry the work is divided into three themed subsections. 1) developing the solution.2) defining the laminar to turbulent transition, and 3) demonstrating conditions under which the turbulent regime is appropriate and consequences of inappropriate use of models that assume laminar flow.

## C. IMPACT OF THE RESULTS

Importing classical models aimed at laminar flow of gelled fluids in order to model high rate water driven HF treatments without examining the consequences of the accompanying higher range of Reynolds number has resulted in a preponderance of issues, recognized by industry but not typically seen as tied to the physics of fluid flow. These issues include underestimation of fluid pressure and width, and overestimation of length. All of these have important impacts on practice. One of the most important aspects of successful HF design is aimed at ensuring the HF grows in the desired layers. Underestimation of pressure will lead to incorrect modeling of height growth across subsurface strata. This can lead to designs resulting in growth into unwanted zones. Typically the main problem with unwanted height growth is stimulation of water inflow, creating a costly issue of disposal and exacerbating the potential for environmental impacts due to accidental surface release of produced water, ineffective treatment of flow-back waters that are highly saline and which often contain substantial levels of naturally occurring radioactive materials, and induced seismicity associated with subsurface injection of waste water. In shallow reservoirs, especially shallow conventional gas/oil as well as coal seam methane reservoirs, unwanted height growth can lead to direct contamination of nearby underground drinking and irrigation water sources. Hence, one outcome of this project is to inspire wider inclusion of turbulent and transition fluid in models used to predict HF height growth. By not only inspiring these advances but also providing necessary benchmarks to ensure the simulators accurately compute the correct behavior in simple geometries and limiting regimes, this work can lead to better fracture height prediction and decreased environmental risk.

Secondly, miscalculation of the crack opening will lead to a wrong choice of proppant size and/ or scheduling such errors can in turn cause other problems, like reducing the conductivity of the reservoir and/or increasing the risk of premature screen-out. Both of these issues lead to failure or otherwise ineffective treatments. Also, overestimation of length can lead to inappropriate well spacing and inefficient development of the resource.

Multiplied across $10^4$ new wells per year, inefficiencies costing on the order of $10^5$ dollars per well (a few percent of the total cost of developing a typical unconventional oil/gas well) would be expected to have billions of dollars of economic impact. Reducing these substantial inefficiencies through improved design enabled by more appropriate HF models can therefore contribute significantly to enabling economically-feasible production even at depressed oil/gas prices.

And finally, because of this emergence of the importance of the turbulent flow regime, it is anticipated that the future will bring an increasing number of numerical simulators accounting for the turbulent regime. The research presented in this thesis is aimed at impacting these advances by providing a basic understanding of the fluid flow regimes present in an ever-evolving HF. The solutions developed here also enable benchmarking this new generation of HF simulators to analytical or semi-analytical solutions as a part of their development.

## D. BACKGROUND KNOWLEDGE

Throughout this dissertation, some assumptions and terminologies are relied upon from the HF literature. While some of these are well-established, the justification can be technically involved. Those with the most relevance to this thesis are presented here.

### 1. Incompressible Fluid

The first assumption is the use of an incompressible fluid. The fluid compressibility appears in the continuity equation in the form of $wc_f \partial p/\partial t$, where $w$ and $p$ are the crack opening and fluid pressure respectively and $c_f$ is the fluid compressibility. Lecampion et al. (2017) explained in detail that this compressibility term is almost always negligible compared to the other terms in the continuity equation. While there are in some cases nuances to this assumption, for the purpose of this study it suffices to limit consideration to incompressible fluids.

### 2. Fluid Flow Equation

In this thesis, the fluid flow equation is defined through Darcy-Weisbach equation as

$$q = \left( -\frac{4w^3}{\rho f} \frac{\partial \overline{p}}{\partial x} \right)^{1/2} \tag{I.1}$$

where $q$ is the fluid flow inside the crack, $w$ is the crack opening, $p$ is the fluid pressure inside the crack, $\rho$ is the fluid density, and $f_p$ is the Darcy-Weisbach friction factor. It is important to note that the linear momentum law for the fluid is satisfied implicitly by using Equation I.1. Therefore, there is no need to explicitly satisfy the linear momentum for the fluid flow. This equation is basically defined through dimensional analysis and is explained in section III.D. To supplement this dimensional analysis, here the derivation of this equation through Navier-Stokes equations is provided in order to show its compatibility with linear momentum balance.

First we start by considering the fluid flow between two parallel plates as in Figure I.1. Therefore, the linear momentum balance in the $x$-direction for a fluid element gives

$$-\frac{\partial p}{\partial x} wbdx - 2\tau_w bdx = \rho bwdx \frac{Dv_x}{Dt}$$

where $\rho$ is fluid density, $\tau_w$ is the shear stress at the wall, and the operator $D/Dt$ refers to the material derivative and is defined as

$$\frac{D}{Dt} = \frac{\partial}{\partial t} + \boldsymbol{v} \cdot \nabla = \frac{\partial}{\partial t} + v_x \frac{d}{dx} + v_y \frac{d}{dy} + v_z \frac{d}{dz}$$

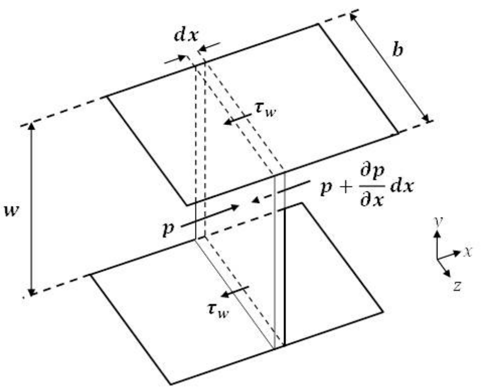

Figure I.1: A free body diagram of an infinitesimal fluid element.

Note that $v_x$ is the velocity of the element in $x$-direction. After simplifying we can obtain

$$-\frac{\partial p}{\partial x} - 2\frac{\tau_w}{w} = \rho\left(\frac{dv_x}{dt} + v_x\frac{dv_x}{dx}\right) \tag{I.2}$$

Now, we develop the time average of Equation I.2. In order to do that, we can find the term by term time-average of Equation I.2, whereby for the first term

$$\frac{1}{2\Delta t}\int_{t-\Delta t}^{t+\Delta t} \frac{\partial p}{\partial x} dt' = \frac{\partial}{\partial x}\frac{1}{2\Delta t}\int_{t-\Delta t}^{t+\Delta t} p dt' = \frac{\partial \overline{p}}{\partial x}$$

For the second term on the left hand side of Equation I.2

$$\frac{1}{2\Delta t}\int_{t-\Delta t}^{t+\Delta t} \tau_w dt' = \overline{\tau_w}$$

And for the right hand side, we find

$$\frac{1}{2\Delta t}\int_{t-\Delta t}^{t+\Delta t} \frac{dv_x}{dt} dt' = \frac{d\overline{v_x}}{dt}$$

and

$$\frac{1}{2\Delta t}\int_{t-\Delta t}^{t+\Delta t} v_x\frac{dv_x}{dx} dt' = \frac{1}{2\Delta t}\int_{t-\Delta t}^{t+\Delta t} (\overline{v_x} + v_x')\frac{d(\overline{v_x} + v_x')}{dx} dt' = \overline{v_x}\frac{d\overline{v_x}}{dx} + \overline{v_x'\frac{dv_x'}{dx}}$$

where $v_x'$ is the fluctuation part and $\overline{v_x}$ is the time averaged part of $v_x$. For more details about derivation of the time average parameters, refer to Whitaker (1968). Also, it can be obtain that (see again Whitaker, 1968)

$$\overline{v_x'\frac{dv_x'}{dx}} = \frac{d\overline{v_x'^2}}{dx}$$

Combining all the time averaged equations, the resulting equation will simplify as

$$-\frac{\partial \overline{p}}{\partial x} - 2\frac{\overline{\tau_w}}{w} = \rho\left(\frac{d\overline{v_x}}{dt} + \overline{v_x}\frac{d\overline{v_x}}{dx} + \frac{d\overline{v_x'^2}}{dx}\right) \tag{I.3}$$

Then, by considering that the time-averaged acceleration is steady state, or

$$\frac{D\overline{v}}{Dt} = 0 \rightarrow \frac{d\overline{v_x}}{dt} + \overline{v_x}\frac{d\overline{v_x}}{dx} + \frac{d\overline{v_x'^2}}{dx} = 0$$

Thus, Equation I.3 will change to

$$2\frac{\overline{\tau_w}}{w} = -\frac{\partial \overline{p}}{\partial x} \tag{I.4}$$

On the other hand, we can define the friction factor as (Whitaker, 1968)

$$f = \frac{F_D}{AKE}$$

where $A$ is the characteristic area, $KE$ is the characteristic kinetic energy per unit volume, and $F_D$ is the drag force applied by the fluid on the solid. After simplification we can obtain (again following Whitaker, 1968)

$$f = \frac{8\overline{\tau_w}}{\rho\overline{v_x}^2} \tag{I.5}$$

Hence, putting Equation I.5 into I.4 yields

$$\overline{v_x} = \left(-\frac{4w}{\rho f}\frac{\partial \overline{p}}{\partial x}\right)^{1/2} \tag{I.6}$$

Then, considering that $q = \overline{v_x}w$, we find

$$q = \left(-\frac{4w^3}{\rho f}\frac{\partial \overline{p}}{\partial x}\right)^{1/2} \tag{I.7}$$

It is apparent that Equation I.7 is the Darcy-Weisbach equation, obtained here through the combination of a friction factor, defined semi-empirically based on experiments and dimensional analysis, with a Navier-Stokes equations for time-averaged 1D flow. Hence we see that by using Darcy-Weisbach equation, we have already satisfied the linear momentum law in fluid flow and there is no need for explicit consideration of Navier-Stokes equations in the subsequent model.

## 3. Zero-Toughness

All asymptotic solutions provided in this thesis are derived for the zero-toughness asymptotic limit. In this limit, the propagation velocity is determined from the coupled fluid flow and elasticity equations, and is independent of the fracture toughness. While this concept of a zero-toughness crack can be conceptually challenging, it is very well established through asymptotic analysis Desroches et al. (1994); Garagash and Detournay (2000), laboratory experiments Bunger and Detournay (2008); Xing et al. (2017), and numerical simulations (e.g. Lecampion et al., 2013). The unfamiliar reader is encouraged to examine these prior works. Here a brief overview is provided.

Based on conservation of energy in HF problems, the external energy provided to the system should be equivalent to the energy stored internally in the system plus the energy used in system due to work done by the system. In HF, the external energy is supplied to the system by fluid injection, it stored in the system by opening the crack, and it is predominantly dissipated through three different mechanisms: 1) fracturing the rock and making new surfaces (toughness dissipation), 2) lost through friction in the fluid (viscous dissipation), 3) fluid loss to the surrounding domain. The fracture propagation is mainly determined through the governing energy dissipation process. In this thesis, the fluid leakoff is considered to be zero. Therefore, the energy dissipation is controlled by toughness dissipation and viscosity dissipation. If the energy dissipation through toughness is much bigger than viscosity dissipation, the HF problem is categorized as small-viscosity (large-toughness) problem, and if the toughness dissipation is negligible in compare with viscosity dissipation, the HF problem is considered as small-toughness (large-viscosity) problem. Thus, small-toughness problem does not necessarily means that the fracture toughness of the rock is small, but it infers that most of the energy is dissipated through viscosity rather than crack propagation and the group of parameter that contains toughness is small. Zero-toughness is a limiting case of small-toughness HF that let us develop semi-analytical solution that captures some behavior of small-toughness problem. The case of HF growth between two plates with no bounding is an example of zero-toughness problem.

In zero-toughness problem the tip singularity is weaker than the LEFM singularity (Carbonell, 1996; Desroches et al., 1994). In order to have zero-toughness problem, the fracture intensity factor should be equal to zero. The zero-toughness criterion is explained in terms of stress intensity factor as (slightly different for various geometries)

$$\int_0^{\ell} \frac{p(r,t)}{\sqrt{\ell^2 - x^2}} dx = 0 \quad \text{(KGD)}, \qquad \text{or} \qquad \int_0^{R} \frac{rp(r,t)}{\sqrt{R^2 - r^2}} dr = 0 \quad \text{(Radial)} \tag{I.8}$$

Mathematically speaking, in both cases in Equation I.8, the weight function is always positive, so the pressure profile along the crack should change sign to be able to maintain zero integral which means that at some region inside the crack the net pressure is negative.

In this investigation the fluid leakoff is zero, so according to conservation of mass, the amount of fluid pumped in is equal to the amount of fluid fill the entire volume of the crack (no fluid lag at crack tip). Therefore, the crack cannot excessively grow since it needs to have sufficient amount of the fluid inside it. Also in zero-toughness HF, the crack tip singularity is dominated by the fluid pressure singularity rather than the singularity in the solid domain (LEFM). And therefore the crack tip opening is in the form that follows fluid pressure singularity which implies that the crack can grow only if the crack tip follows a proper profile. The crack tip shape is a function of the crack velocity which is function of fluid pumping. So the crack cannot grow unstably under predefined fluid pumping.

# II. BLADE-SHAPED (PKN) HYDRAULIC FRACTURE DRIVEN BY A TURBULENT FLUID IN AN IMPERMEABLE ROCK

## A. PREAMBLE

This chapter constitutes a preprint of Zolfaghari et al. (2017). Its main focus is derivation of a semi-analytical asymptotic solution for the blade-like HF (PKN) geometry for rough-walled fully turbulent fluid regime. The result is contrasted with laminar fluid regime solution provided by Nordgren (1972). The tip asymptotic solution is also developed as a part of the solution and a method to obtain the solution for the laminar-turbulent transition regime is suggested.

## B. ABSTRACT

High flow rate, water-driven hydraulic fractures are more common now than ever in the oil and gas industry. Although the fractures are small, the high injection rate and low viscosity of the water, lead to high Reynolds numbers and potentially turbulence in the fracture. Here we present a semi-analytical solution for a blade-shaped (PKN) geometry hydraulic fracture driven by a turbulent fluid in the limit of zero fluid leak-off to the formation. We model the turbulence in the PKN fracture using the Gaukler-Manning-Strickler parametrization, which relates the the flow rate of the water to the pressure gradient along the fracture. We consider the fully tubulent limit with no transition region any where at any time, and we do not consider the effect of the fracture toughness on the crack propagation. The key parameter in this relation is the Darcy-Weisbach friction factor for the roughness of the crack wall. Coupling this turbulence parametrization with conservation of mass allows us to write a nonlinear pde for the crack width as a function of space and time. By

way of a similarity ansatz, we obtain a semi-analytical solution using an orthogonal polynomial series. Embedding the asymptotic behavior near the fracture tip into the polynomial series, we find very rapid convergence: a suitably accurate solution is obtained with two terms of the series. This closed-form solution facilitates clear comparisons between the results and parameters for laminar and turbulent hydraulic fractures. In particular, it resolves one of the well known problems whereby calibration of models to data has difficulty simultaneously matching the hydraulic fracture length and wellbore pressure.

## C. INTRODUCTION

Hydraulic fracturing is a method of stimulating relatively impermeable subsurface reservoir rocks to extract oil and gas. In the past two decades, there has been a transition from using high viscosity gels to the use of water in hydraulic fracturing (King, 2010). Associated with this change is a 2 to 3 orders of magnitude increase in the characteristic Reynolds number $Re^*$, which we define as

$$Re^* = \frac{\rho q_{in}}{H\mu}, \tag{II.1}$$

where $\rho$ is the fluid density, $q_{in}$ is the volumetric injection rate, $H$ is the hydraulic fracture height $H$, and $\mu$ is the fluid viscosity (Tsai and Rice, 2010). Table II.1 shows that a shift from typical gel-based fluids to water leads to an increase from $Re^* \approx 0.01 - 10$ to $Re^* \approx 10^2 - 10^4$, respectively. While a local Reynolds number will vary along the fracture and decrease rapidly near the tip, the Reynolds number defined in Equation (II.1) is a constant set by external parameters. In this paper, we describe parameter regimes where $Re$ is large enough for turbulence to exist throughout the hydraulic fracture save the very tip.

The emerging importance of the turbulent flow regimes will likely increase the number of hydraulic fracture numerical simulations that incorporate turbulence. In order to benchmark these numerical simulations, analytical or semi-analytical solutions are required. One example of analytical solution is the large leakoff limit for a PKN hydraulic fracture with rough-walled turbulent flow (Kano et al., 2015). Otherwise, the analytical/semi-analytical solutions, necessary for benchmarking numerical simulations do not yet exist for turbulent flow. This is in contrast to a large

Table II.1: Typical Reynolds numbers for water and gel working fluids with flow rate $q_{in} = 0.05 - 0.2$ m$^3$ s$^{-1}$ and fracture height $H = 50 - 200$ m.

| Fluid | Density $\rho$ (kg m$^{-3}$) | Viscosity $\mu$ (Pa·s) | Reynolds Number $Re^*$ |
|---|---|---|---|
| Water | 1000 | $10^{-3}$ | $10^2$-$10^4$ |
| Gel | 1200 | 0.5-1 | 0.01-10 |

body of benchmark solutions for the laminar regime (e.g. Geertsma and De Klerk (1969); Nordgren (1972); Savitski and Detournay (2002)).

The tractability of the problem for analytical and semi-analytical solutions requires simple geometries such as plane strain (Geertsma and De Klerk, 1969), radial (e.g. Savitski and Detournay (2002)), and blade-shaped (after Perkins and Kern (1961), and Nordgren (1972)). While all have usefulness as approximations under particular conditions, the blade-shaped geometry is of practical importance. The minimum stress in most reservoirs is horizontally-directed, so it is easier for the crack to open in the horizontal direction which leads to vertically-oriented hydraulic fractures. Furthermore, reservoir layers are often bounded by layers that serve to block upward and downward growth of hydraulic fracture, meaning that the horizontal propagation velocity far exceeds the vertical propagation velocity. A large body of field data indicates the resulting blade-like geometry occurs in a wide-range of reservoirs, probably comprising the idealization of the most common fracture geometry (e.g. De Pater (2015)). The limiting end-member of zero vertical (e.g. height) growth corresponds to the geometry of Perkins and Kern (1961) which was revisited by Nordgren (1972), and this so-called "PKN" geometry is used in the present study (see Figure II.1).

The need to consider the turbulent regime for water-driven hydraulic fractures was recognized by Perkins and Kern (1961). A small number of papers have since considered the turbulent regime of hydraulic fracturing, and some hydraulic fracturing design models (e.g. Meyer 1989) incorporate ability to simulate flow under turbulent conditions. Nilson (1981, 1988) considered plane strain, gas-driven hydraulic fractures under a constant pressure inlet boundary condition. Nilson showed the system evolving among laminar, turbulent, and inviscid regimes and solved the self-similar problems associated with each of these limits of the system. Similarly Emerman et al. (1986) examined the problem of a plane strain fluid-driven crack, but instead assuming a constant influx boundary condition. These authors presented an approximate solution, arguing for its practical suitability for modeling magmatic intrusions and natural hydrothermal injections. Turbulent flow is also considered in other geosciences-inspired models. These include the model of drainage of glacial lakes via subglacial fluid-driven cracks developed by Tsai and Rice (2010), as well as the model of dyke ascent and propagation developed by Lister (1990) and Lister and Kerr (1991). Tsai and Rice (2010) used Gaukler-Manning-Strickler (GMS) (Gauckler, 1867; Manning, 1891; Strickler, 1923) approximation in order to model turbulent flow for glacial and sub-surface HF. Also Tsai and Rice (2012) used GMS approach to model near surface hydraulic fracture, motivated by the phenomenon of rapid subglacial drainage. Expanding to account for time-dependent deformation of ice, Rice et al. (2015) used creep flow with GMS to model the rapid glacial lake drainage. These contributions provide a useful background for the fluid flow model, but the boundary conditions and elasticity formulation are specific to their problem and not applicable to industrial HFs.

More recently Anthonyrajah et al. (2013) considered turbulent flow for hydraulic fractures with blade-shaped geometry with a generalized inlet condition. These authors present analytical solutions for the particular (arguably non-physically motivated) cases of constant fracture speed and volume, and demonstrate a numerical solution method for general injection boundary conditions. The specific case of constant injection rate for a blade-shaped hydraulic fracture was subsequently considered by Zia and Lecampion (2016), who point out that many practical cases will consist of flow in the transition between laminar and turbulent flow. For rough-walled fractures, this work numerically demonstrates departure from the laminar solution of about 10-20% for $Re = 2500$ and 30-50% for $Re = 10^5$, as well as complete convergence to a fully turbulent asymptotic solution for $Re = 10000$ (though the details of the asymptotic solution are not presented). Dontsov (2016), then, points out the necessity in many practical cases to consider that flow can be in the laminar regime near the tip of the hydraulic fracture and turbulent regime away from the tip. This work is mainly motivated by development of numerical simulations for generalized geometries wherein the behavior near the fracture tip must be properly treated. The solution presented is therefore specified to the moving tip region, allowing the length of the laminar region to be determined and appropriate tip conditions to be imposed in simulations.

In this paper, we present a solution for a PKN-geometry hydraulic fracture driven by a turbulent fluid through an impermeable rock. Although turbulent flows in general remain difficult to describe mathematically, many parameterizations have been developed to describe turbulence through channels and narrow slits. Here we use the solution begins with a generalized expression of the Darcy-Weisbach friction factor, after Gaukler-Manning-Strickler (GMS) (Gauckler, 1867; Manning, 1891; Strickler, 1923) approximation for rough-walled turbulence in channel flow. While our solution remains general enough to capture future advances in modeling turbulent flow within hydraulic fractures, provided these can be captured by a power-law relationship between the friction factor and the scale of the fracture roughness.

The solution presented here is semi-analytical, derived using a Jacobi polynomial series. It follows in the spirit of previous semi-analytical solutions that obtain very rapid series convergence by constructing the family of polynomials so as to embed the appropriate asymptotic behavior near the leading edge (Adachi and Detournay, 2002; Savitski and Detournay, 2002; Bunger and Detournay, 2007). For this reason, our solution method begins with derivation of the near-tip behavior, after which the form of the Jacobi polynomial series is specified. Coefficients of the series are then selected to minimize an objective function that embodies the error of the solution. A convergence study shows that a practically-useful solution is by first two terms of the series. This rapid convergence of the solution justifies the approach, allowing the solution to be written down once for all cases rather than requiring computation for each individual combination of parameters, as is the case for numerical simulations. Finally, the paper concludes with an exploration of the sensitivity to the particulars of the expression for the Darcy-Weisbach friction factor (Weisbach, 1855; Darcy, 1857) and with a comparison between solutions resulting from models that impose laminar versus turbulent flow.

## D. MATHEMATICAL MODEL

This study considers the propagation of a rough-walled crack driven by fully turbulent fluid flow. The fluid regime is modeled as turbulent along the entirety of the crack and we do not model the potential relaminarization of the flow near the tip (see Dontsov (2016) and Dontsov and Peirce

(2016)). The conclusions about the validity of the transition to laminar flow close to the tip (see discussion around Figs. II.8 and II.9) have to be seen in this context as because we impose that the model can not autonomously transition to laminar flow near the tip. For the case of low viscosity, and high flowrate (i.e. supercritical $CO_2$) the Reynolds number is very large and this relaminarization region will be quite small. Yet when the Reynolds number is closer to the value for transition to turbulence, our conclusions about the flow near the tip will not be correct and a model that incorporates relaminarization would be required.

We also consider the local elasticity approximation associated with the PKN model. The vanishing tip boundary condition used for the PKN model (as is used here) precludes the incorporation of the effect of fracture toughness into the model. Thus conclusions about the behavior of the solution within a distance of $\sim H$ of the tip where $H$ is the fracture height, are likely to be inaccurate. We note that assuming turbulent flow throughout the fracture, as is done in our model, likely over estimates the effective viscosity of the fluid near the tip. Therefore transition to laminar flow close to the tip may bring toughness in to play, which is not accounted for in this model. Although a way forward could be provided by a recently published toughness correction to the PKN model (Dontsov and Peirce (2016))

As a final caveat related to the assumption that the fluid is fully turbulent everywhere, we note that, the fracture width and the fluid velocity both decrease as one approaches the two containment interfaces at the stress barriers (Figure II.1). In these regions the flow will certainly transition to the laminar regime. This transition is not accounted for in our model.

Having clarified these limitations, let us now outline the model. We consider a reservoir layer of uniform thickness $H$ contained at the top and bottom by two, higher stress layers assumed to be effective barriers to upward and/or downward hydraulic fracture (HF) growth (Perkins and Kern, 1961). A sketch of this geometry is given by Figure II.1. Provided the HF length is several times greater than the thickness $H$, we assume a uniformly-pressurized HF cross section and slowly-varying HF width (opening) with respect to coordinate $x$ (Perkins and Kern, 1961; Adachi and Peirce, 2008). These assumptions allow us to derive an expression for the opening $W$ of an elliptical crack in an elastic rock (Nordgren, 1972), which is given by

$$W(x,z,t) = \frac{1-\nu}{G}(H^2 - 4z^2)^{1/2}(p(x,t) - \sigma), \tag{II.2}$$

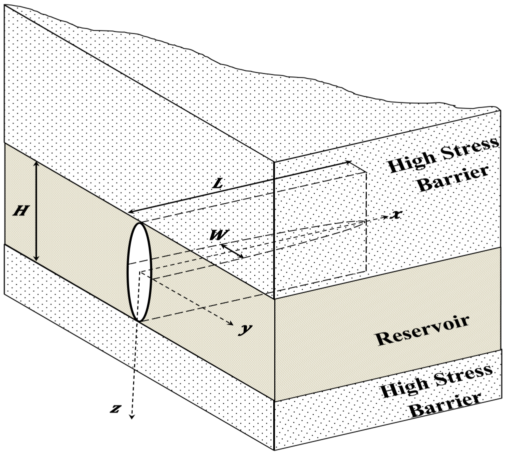

Figure II.1: PKN fracture geometry

where $G$ is the shear modulus of elasticity, $\nu$ is the Poisson's ratio, $H$ is the height of the HF. The fluid pressure $p(x,t)$ is taken as uniform in each vertical cross section, and $\sigma$ is the uniform in-situ stress in the reservoir opposing the HF opening.

Mass conservation for the incompressible fluid flow in the crack is

$$\frac{\partial A}{\partial t} + \frac{\partial q}{\partial x} = 0, \tag{II.3}$$

where $A = \pi\omega(x,t)H/4$ is the area of the elliptical crack and $\omega(x,t)$ is the maximum opening in the cross section $\omega(x,t) = W(x,0,t)$. Instead of using the Poiseuille equation for laminar flow (Nordgren, 1972), we model the turbulent flow in the crack using the Gaukler-Manning-Strickler (Gauckler, 1867; Manning, 1891; Strickler, 1923) parametrization

$$q_{2D} = \left(-\frac{4W^3}{\rho f_p}\frac{\partial p}{\partial x}\right)^{1/2}, \tag{II.4}$$

where $f_p$ is the Darcy-Weisbach friction factor which can be expressed as

$$f_p = m\left(\frac{k}{W}\right)^{\alpha}, \tag{II.5}$$

where $k$ is surface roughness, and $\alpha$ and $m$ are constants with typical values $\alpha = 1/3$ and $m = 0.143$ gioia2006,tsai2010model and we explore the effect of varying these parameters later in the paper. The subscript "2D" in Equation II.4 indicates that the flux is through two-dimensional, horizontal slices at every height $z$. The total flux $q$ is given by the integral over the height of the crack as

$$q = \int_{-H/2}^{H/2} q_{2D} dz, \tag{II.6}$$

where the details of this integration are given in the Appendix A.A. The result for the total flux is

$$\begin{aligned} q &= \Lambda \Upsilon \omega^{2\varphi} \left( -\frac{\partial \omega}{\partial x} \right)^{1/2}, \\ \Lambda &= \left( \frac{4}{m} \right)^{1/2} B \left( \frac{1}{2}, \varphi + 1 \right), \\ \Upsilon &= \sqrt{\frac{GH}{4\rho k^{\alpha} (1-\nu)}}, \\ \varphi &= \frac{3+\alpha}{4}, \end{aligned} \tag{II.7}$$

where $B$ is the Beta function (see Equation A.8, or Abramowitz and Stegun (1972)), and $\Lambda$ and $\Upsilon$ are parameters of geometry and material properties, respectively. We note that $\Upsilon$ depends on rock properties and reservoir geometry while $\Lambda$ depends only on the parameters of the friction factor $\alpha$ and $m$, which gives a typical value of $\Lambda = 7.406$.

We now substitute the total flux, Equation II.7, into the continuity Equation II.3 and define

$$\Xi = \frac{4\Lambda\Upsilon}{\pi H}. \tag{II.8}$$

Thus, we find the non-linear partial differential equation governing the maximum opening $\omega(x,t)$, which is given by

$$\frac{\partial \omega}{\partial t} = -\Xi \frac{\partial}{\partial x} \left[ \omega^{2\varphi} \left( -\frac{\partial \omega}{\partial x} \right)^{\frac{1}{2}} \right]. \tag{II.9}$$

In Equation II.9, the gradient of opening follows by negative sign ($-\partial w/\partial x$) that comes through fluid flow equation (II.7). In Equation II.9, the gradient of opening should be a negative value, otherwise the square root will produce a complex number. This can be explained by the fact that, the fluid always flow from high pressure to lower pressure and not the other way. Therefore, the gradient of pressure, which in this case is directly proportional to gradient of width with positive coefficient, is always negative. Hence,

$$\frac{\partial w}{\partial x} < 0$$

We then specify three boundary conditions and an initial condition. The third boundary condition is necessary as the total length of the crack $\ell(t)$ is unknown *a priori* and must be determined as part of the analysis. We apply a zero opening initial condition at $t = 0$ and by the following boundary conditions:

I. No opening at the crack tip:

$$x = \ell \quad \Rightarrow \quad \omega(\ell, t) = 0.$$

II. No fluid loss through the crack tip:

$$x = \ell \quad \Rightarrow \quad q(\ell, t) = 0.$$

III. Constant volume rate of flow at the inlet:

$$x = 0 \quad \Rightarrow \quad q(0, t) = q_{in}.$$

where $q_{in}$ is half of the total fluid injection in the case of symmetric (bi-wing) growth. Alternatively, $q_{in}$ can be the entire injection rate if HF propagation is biased in one direction so as to form a single-wing geometry as observed in analysis of some field data such as Cotton Valley (Rutledge and Phillips, 2003), west Texas (Fischer et al., 2008), east Texas (Mayerhofer et al., 2000), Mound site in Oklahoma (Warpinski et al., 1999), the Lost hill field (Emanuele et al., 1998), and in Barnett shale (Maxwell et al., 2002) and also discussed in (Wright et al., 1999; Murdoch and Slack, 2002).

## E. SCALING

We now look for a similarity solution to Equation II.9. An alternative method of scaling, in the spirit of Savitski and Detournay (2002), is detailed in the Appendix A.E. This nonlinear pde resembles the equations for viscous gravity currents (Huppert, 1982) and bouyant hydraulic fractures (Lister, 1990) and, therefore, we look for a similarity solution of the first kind (Barenblatt, 1996). We start by writing the inlet flux as

$$q_{in} = \Lambda\Upsilon \left[ w^{2\varphi} \left( -\frac{\partial w}{\partial x} \right)^{1/2} \right]_{x=0} . \tag{II.10}$$

Thus, we can scale the pde, Equation (II.9), and inlet flux conditions as

$$\begin{aligned} \frac{w}{t} &\sim \Xi \frac{w^{2\varphi+1/2}}{x^{3/2}}, \\ \frac{q_{in}}{\Lambda\Upsilon} \equiv Q &\sim \frac{w^{2\varphi+1/2}}{x^{1/2}}, \end{aligned} \tag{II.11}$$

where we define the scaled flux $Q$ as the ratio of the flux in $q_{in}$ divided by $\Lambda\Upsilon$. Combining these two scalings allows us to define the similarity variables

$$\xi = \frac{x}{Q^{-2}\left(Q^3 \Xi t\right)^{(4\varphi+1)/(4\varphi+2)} \lambda}, \tag{II.12}$$

and

$$w = \left(Q^3 \Xi t\right)^{1/(4\varphi+2)} \Omega(\xi), \tag{II.13}$$

We define the length of the crack $\ell(t)$ such that $\xi = 1$ coincides with the fracture tip, therefore, we have that

$$\ell(t) = \left[ Q^{-2} \left(Q^3 \Xi t\right)^{(4\varphi+1)/(4\varphi+2)} \right] \lambda, \tag{II.14}$$

where $\lambda$ is dimensionless length (for more detail about the scaling see Appendix A.E). We can insert the similarity formulation into the governing pde and find

$$\Omega - (4\varphi+1)\xi\Omega' = -(4\varphi+2) \left[ \Omega^{2\varphi} \left(-\Omega'\right)^{1/2} \right]', \tag{II.15}$$

The boundary conditions to Equation (II.15) are

$$\begin{aligned} \Omega(\xi = 1) &= 0, \\ \left[\Omega^{2\varphi}\left(-\Omega'\right)^{1/2}\right]_{\xi=1} &= 0, \\ \left[\Omega^{2\varphi}\left(-\Omega'\right)^{1/2}\right]_{\xi=0} &= 1. \end{aligned} \tag{II.16}$$

This ode can be integrated once by replacing $\xi\Omega'$ by $(\xi\Omega)' - \Omega$, which gives

$$\int_{\xi}^{1} \Omega d\zeta - \frac{4\varphi+1}{4\varphi+2}\left[\zeta\Omega\right]_{\xi}^{1} = -\left[\Omega^{2\varphi}\left(-\Omega'\right)^{1/2}\right]_{\xi}^{1}. \tag{II.17}$$

Using the tip boundary conditions, we find

$$\int_{\xi}^{1} \Omega \, d\zeta + \frac{4\varphi+1}{4\varphi+2}\xi\Omega = \Omega^{2\varphi}\left(-\Omega'\right)^{1/2}. \tag{II.18}$$

To solve this equation, we will use an orthogonal polynomial series method to obtain a semi-analytical solution to Equation II.18. The opening width changes most rapidly near the tip and, therefore, by embedding the asymptotic solution near the tip, we can derive a rapidly-converging series (Savitski and Detournay, 2002). Near the fracture tip, we expect the fracture width $\Omega$ to be small but changing rapidly. Thus, we expect a dominant balance between the second two terms in Equation (II.15), which is equivalent to saying that the integral over the fracture width in the integrated ode, Equation (II.18), is very small. Thus, to leading order, the near tip behavior is characterized by the ODE

$$\frac{4\varphi+1}{4\varphi+2}\Omega = \Omega^{2\varphi}\left(-\Omega'\right)^{1/2}. \tag{II.19}$$

Simplifying and separating, we find

$$-\int_{\xi}^{1} \Omega^{4\varphi-2} \, d\Omega = \left(\frac{4\varphi+1}{4\varphi+2}\right)^{2}(1-\xi). \tag{II.20}$$

Thus, the solution for the width near the tip is

$$\Omega = \left[\sqrt{4\varphi-1}\left(\frac{4\varphi+1}{4\varphi+2}\right)\right]^{2/(4\varphi-1)}(1-\xi)^{1/(4\varphi-1)}. \tag{II.21}$$

We analyze the tip region later in the paper and show that, although, there is relaminarization in a small boundary layer near the tip it is a sufficiently small region that the turbulent expression derived in Equation II.21 still holds.

Embedding this asymptotic solution into the polynomial series allows us to approximate the series using only a few terms which clearly shows the dependence upon the parameters and can be readily adopted for benchmarking purposes. Numerical solutions, although certainly feasible with existing methods, would not provide the insights or usability of a semi-analytical solution.

## F. SOLUTION

### 1. Overview of the Method

To solve Equation II.18, we construct an orthogonal polynomial series (Savitski and Detournay, 2002). Orthogonal polynomials are sets of functions that follow

$$\int_a^b R(x) B_m(x) B_n(x) dx = 0, \tag{II.22}$$

for all $m \neq n$ (where $R(x)$ is the weight function) and

$$\int_a^b R(x) B_n(x)^2 dx = h_n, \tag{II.23}$$

if $m = n$ (Abramowitz and Stegun, 1972). The proposed solution is thus in the form of infinite series using basis functions $\hat{\Omega}_k$

$$\Omega = \sum_{i=0}^{\infty} \mathcal{A}_i \hat{\Omega}_i, \tag{II.24}$$

where $\mathcal{A}_i$ are coefficients selected so that the solution satisfies the governing equations. The base functions $\hat{\Omega}_i$ must be orthogonal, therefore

$$\int_0^1 \hat{\Omega}_i \hat{\Omega}_j dx = \delta_{ij}, \tag{II.25}$$

where $\delta_{ij}$ is the Kronecker delta function.

Rapid convergence of the series is promoted by selecting the base functions so as to embed the near-tip behavior (Savitski and Detournay, 2002), which we found to be of the form $\Omega \sim \mathcal{X}(1-\xi)^{\mathcal{B}}$ where $\mathcal{X}$ and $\mathcal{B}$ are

$$\mathcal{X} = \left[\sqrt{4\varphi - 1}\left(\frac{4\varphi + 1}{4\varphi + 2}\right)\right]^{2/(4\varphi-1)} \quad \text{and} \quad \mathcal{B} = \frac{1}{4\varphi - 1}. \tag{II.26}$$

The base functions will then be constructed so that

$$\hat{\Omega}_i = \mathfrak{D}_i \mathfrak{f}_i(\xi) \mathcal{X} (1-\xi)^{\mathcal{B}}, \tag{II.27}$$

where $\mathfrak{D}_i$ are constants chosen so as to satisfy the orthogonality relationship, Equation II.25. Upon substitution

$$\int_0^1 (\mathfrak{D}_i \mathfrak{D}_j) \mathcal{X}^2 (1-\xi)^{2\mathcal{B}} \mathfrak{f}_i(\xi) \mathfrak{f}_j(\xi) d\xi = \delta_{ij}. \tag{II.28}$$

A convenient choice for the functions $\mathfrak{f}_i$ are the Jacobi polynomials, which have the following orthogonality relationship (Abramowitz and Stegun, 1972)

$$\int_0^1 (1-\xi)^{c-e} \xi^{e-1} G_i(c,e,\xi) G_j(c,e,\xi) d\xi = h_i(c,e) \delta_{ij}, \tag{II.29}$$

where $G_i(c,e,\xi)$ is the $i^{th}$ order Jacobi polynomial, expressible as

$$G_i(c,e,\xi) = \frac{\Gamma(e+i)}{\Gamma(c+2i)} \sum_{j=0}^{i} (-1)^j \binom{i}{j} \frac{\Gamma(c+2i-j)}{\Gamma(e+i-j)} \xi^{i-j}, \tag{II.30}$$

where $\Gamma(i)$ is the Gamma function (Abramowitz and Stegun, 1972) and $h_i(c,e)$ is the norm of $G_i(c,e,\xi)$ and given by

$$h_i(c,e) = \frac{i! \Gamma(i+e) \Gamma(i+c) \Gamma(i+c-e+1)}{(2i+c) \Gamma^2(2i+c)}. \tag{II.31}$$

Setting $e = 1$, $c = 2\mathcal{B} + 1$ and rearranging Equation II.29 we have

$$\int_0^1 \left( \frac{1}{h_i\left(2\mathcal{B}+1,1\right)} \right) (1-\xi)^{2\mathcal{B}} G_i\left(2\mathcal{B}+1,1,\xi\right) G_j\left(2\mathcal{B}+1,1,\xi\right) d\xi = \delta_{ij}. \tag{II.32}$$

Now comparing Equation II.32 with Equation II.28 leads to the conditions

$$\begin{gathered} \mathcal{D}_i = \frac{1}{\mathcal{X} h_i^{1/2}\left(2\mathcal{B}+1,1\right)}, \\ \mathfrak{f}_i(\xi) = G_i\left(2\mathcal{B}+1,1,\xi\right). \end{gathered} \tag{II.33}$$

As a result, the base functions are given by

$$\hat{\Omega}_i = \frac{(1-\xi)^{\mathcal{B}}}{h_i^{1/2}\left(2\mathcal{B}+1,1\right)} G_i\left(2\mathcal{B}+1,1,\xi\right). \tag{II.34}$$

Using the asymptotic near-tip solution, the form of the orthogonal base functions is therefore given by

$$\hat{\Omega}_i = \frac{(1-\xi)^{1/(4\varphi-1)}}{\sqrt{h_i\left(\frac{4\varphi+1}{4\varphi-1},1\right)}} G_i\left(\frac{4\varphi+1}{4\varphi-1},1,\xi\right), \tag{II.35}$$

where $h_i$ is the norm of the basis.

### 2. Calculating Coefficients of the Series

Given the basis functions in Equation II.35, we can now calculate the coefficients $\mathcal{A}_i$ of the series in Equation II.24. The approach is to designate equally spaced control points on $0 < \xi < 1$ (we typically used 10 control points) and retain the first $n$ terms of the polynomial series.

Now, it is possible to construct a residual function in terms of $\mathcal{A}_i$ and minimize that function. The chosen residual function embodies the sum of the squares of the mismatch between the left and right hand sides Equation II.18 at each control point (Savitski and Detournay, 2002). Its formal expression is given by

$$\Delta(\mathcal{A}_1, \cdots, \mathcal{A}_n) = \sum_{i=1}^{Q} \left( \frac{\Delta^L(\xi_i, \mathcal{A}_1, \cdots, \mathcal{A}_n)}{\Delta^R(\xi_i, \mathcal{A}_1, \cdots, \mathcal{A}_n)} - 1 \right)^2, \tag{II.36}$$

where $\Delta^L(\xi_i, \ \mathcal{A}_1, \ \cdots, \ \mathcal{A}_n)$ is the left side of Equation II.18 for specific value of $\xi_i$, and $\Delta^R(\xi_i, \ \mathcal{A}_1, \ \cdots, \ \mathcal{A}_n)$ is similarly the right side of Equation II.18 with the solution parametric in the flow law parameter $\varphi$. By minimizing $\Delta(\mathcal{A}_1, \cdots, \mathcal{A}_n)$, we can find the value of each unknown variable $\mathcal{A}_i$.

### 3. Length

Now we express evolution of the crack length with respect to time. Recalling Equation II.14,

$$\ell(t) = Q^{-2} \left( Q^3 \Xi t \right)^{(4\varphi+1)/(4\varphi+2)} \lambda.$$

the crack length evolves with time with power of $(4\varphi + 1)/(4\varphi + 2)$. For illustration, if we consider values $\alpha = 1/3$ and $m = 0.143$ for the Darcy-Weisbach friction factor (Tsai and Rice, 2010), from Equation II.7 the value of $\varphi$ will be $5/6$. Therefore, the value of the power in Equation II.14 for turbulent flow is

$$\frac{4\varphi + 1}{4\varphi + 2} = \frac{13}{16}, \tag{II.37}$$

while for laminar flow this value is $4/5$ (see Equation II.45, recall from Nordgren (1972) solution for no-leakoff case). By comparing the value of the power of the time in length formula for laminar and turbulent flow, we can see that the power in laminar flow is within $1\%$ of turbulent flow and they are very close to each other.

### 4. Pressure

In order to find the distribution of pressure along the HF, we invoke elasticity (Equation A.2). The net pressure inside the crack is therefore expressed in terms of the maximum opening at each cross section, the height of the crack $H$, and material properties of the rock according to

$$p(x,t) - \sigma \equiv p_{net}(x,t) = \frac{G}{1-\nu}\frac{w(x,t)}{H}. \tag{II.38}$$

Thus, by replacing the opening from Equation II.13 into Equation II.38

$$p_{net}(x,t) = \frac{G}{1-\nu}\frac{1}{H}\left(Q^3 \Xi t\right)^{1/(4\varphi+2)} \Omega(\xi). \tag{II.39}$$

Now by combining Equation II.39 and Equation II.24

$$p_{net}(x,t) = \frac{G}{1-\nu}\frac{1}{H}\left(Q^3 \Xi t\right)^{1/(4\varphi+2)} \sum_{i=0}^{\infty} \mathcal{A}_i \hat{\Omega}_i(\xi(x,t)). \tag{II.40}$$

Hence, given the solution for the series coefficients $\mathcal{A}_i$, Equation II.35, and the equation for length scale parameter $\xi = x/\ell(t)$, the pressure is readily computed.

And finally, in order to ensure that the solution solves the original problem, we can substitute the results back to Equation II.9, bringing everything to one side, and comparing the result with zero. Figure II.2 indicates that the solution obtained accurately solves the original governing equations.

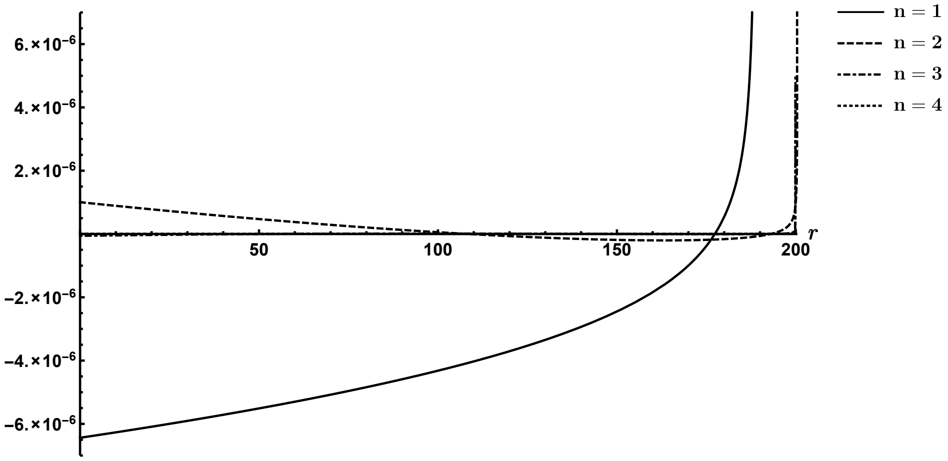

Figure II.2: Substituting back the solution and confirming it solves the problem. The time is 100 sec and other material properties are given in Table II.3

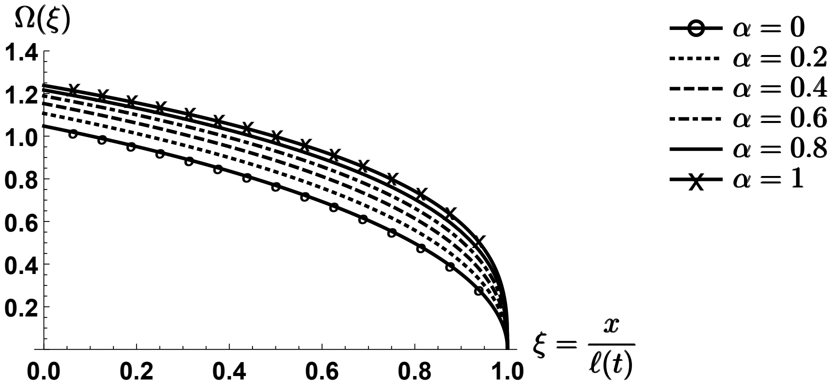

Figure II.3: Variation of scaled opening with respect to change of dimensionless length $\xi$ for different value of $\alpha$.

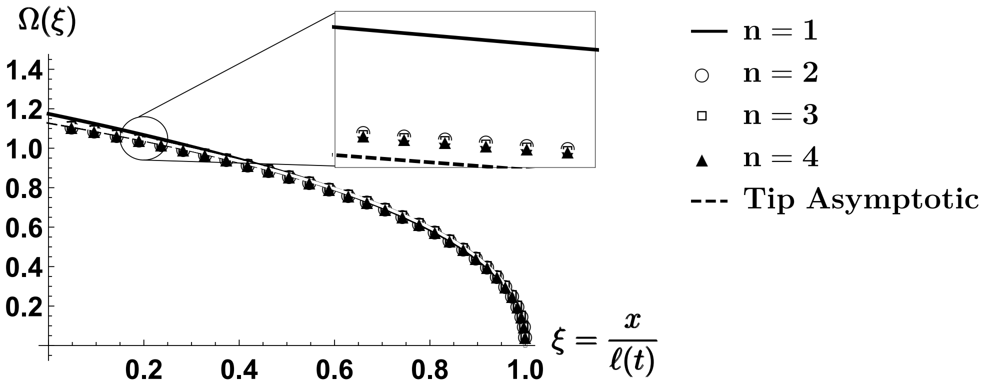

Figure II.4: Scaled opening along the hydraulic fracturing. Noting that using just one term is a very good approximation and $n \geq 2$ gives solutions that are indistinguishable. Dashed line correspond to tip asymptotic solution (look Appendix A.D).

## G. RESULTS

The dimensionless opening depends only on the exponent $\alpha$ from the Darcy-Weisbach friction factor through $\varphi$ (refer to Equation II.7). Figure II.3 shows the sensitivity of the dimensionless opening $\Omega$ with respect to $\alpha$. It is clear from these results the sensitivity of the dimensionless opening, $\Omega$, to $\alpha$ is relatively small. However, the actual opening and length will be strongly affected via the dependence of the scaling quantities on $\alpha$ (see Equation II.13 and II.14).

Here we consider the particular values $\alpha = 1/3$ and $m = 0.143$ for the parameters of the Darcy-Weisbach friction factor. We truncate the Jacobi polynomial series at four terms and the coefficients are given in Table II.2. From Figure II.4, we can firstly confirm that there is an excellent match between the tip asymptotic solution and the complete solution over the whole fracture length. This is because in the PKN problem the average fluid velocity in the fracture is approximately uniform (Economides and Nolte (2000), see also Kovalyshen and Detournay (2010)). Moreover, it can be seen that after the second term ($n = 2$) the solution is indistinguishable with additional terms. This shows the very rapid convergence enabled by embedding the tip asymptotic behavior in the form of the base functions. The truncated solution for $n = 2$ terms for opening is given as

Table II.2: Coefficients for Jacobi polynomial series for $n = 1, 2, 3, 4$ with $\alpha = 1/3$.

| **n** | **1** | **2** | **3** | **4** |
|---|---|---|---|---|
| $\mathcal{A}_1$ | $8.616 \times 10^{-1}$ | $8.517 \times 10^{-1}$ | $8.515 \times 10^{-1}$ | $8.515 \times 10^{-1}$ |
| $\mathcal{A}_2$ | - | $1.115 \times 10^{-2}$ | $1.124 \times 10^{-2}$ | $1.124 \times 10^{-2}$ |
| $\mathcal{A}_3$ | - | - | $2.904 \times 10^{-4}$ | $2.954 \times 10^{-4}$ |
| $\mathcal{A}_4$ | - | - | - | $6.156 \times 10^{-6}$ |

$$\begin{aligned} \Omega &= (1-\xi)^{\frac{3}{7}}(1.1387 + 0.0626\xi), \\ \lambda &= 1.0874. \end{aligned} \tag{II.41}$$

The truncated solution in dimensional variables can be obtained from similarity scaling, Equation II.41, which gives

$$\begin{aligned} w(x,t) &= 0.8122 \, \left( \frac{k^{1/3} q_{in}^3 \rho}{H^2} \frac{1-\nu}{G} \right)^{\frac{3}{16}} t^{\frac{3}{16}} \left(1 - \frac{x}{\ell(t)}\right)^{\frac{3}{7}} \left(1 + 0.05497 \, \frac{x}{\ell(t)}\right), \\ \ell(t) &= 2.1619 \, \frac{q_{in}}{H} \left( \frac{H^2}{k^{1/3} q_{in}^3 \rho} \frac{G}{1-\nu} \right)^{\frac{3}{16}} t^{\frac{13}{16}}, \\ p_{net}(x,t) &= 0.8122 \, \left( \frac{k q_{in}^9 \rho^3}{H^{22}} \left( \frac{G}{1-\nu} \right)^{13} \right)^{\frac{1}{16}} t^{\frac{3}{16}} \left(1 - \frac{x}{\ell(t)}\right)^{\frac{3}{7}} \left(1 + 0.05497 \, \frac{x}{\ell(t)}\right), \\ q &= q_{in} \left(1 - \frac{x}{\ell(t)}\right)^{\frac{3}{7}} \left(1 + 0.05497 \, \frac{x}{\ell(t)}\right)^{\frac{5}{3}} \left(1 + 0.21005 \, \frac{x}{\ell(t)}\right)^{\frac{1}{2}}. \end{aligned} \tag{II.42}$$

We can also write this truncated solution for general form of $\Omega$ as

$$\Omega = (1-\xi)^{\frac{1}{2+\alpha}} \left[ \mathcal{C}_1(\alpha) + \mathcal{C}_2(\alpha)\xi \right], \tag{II.43}$$

where $\mathcal{C}_1(\alpha)$ and $\mathcal{C}_2(\alpha)$ are constants that vary with the value of $\alpha$ as shown in Figure II.5.

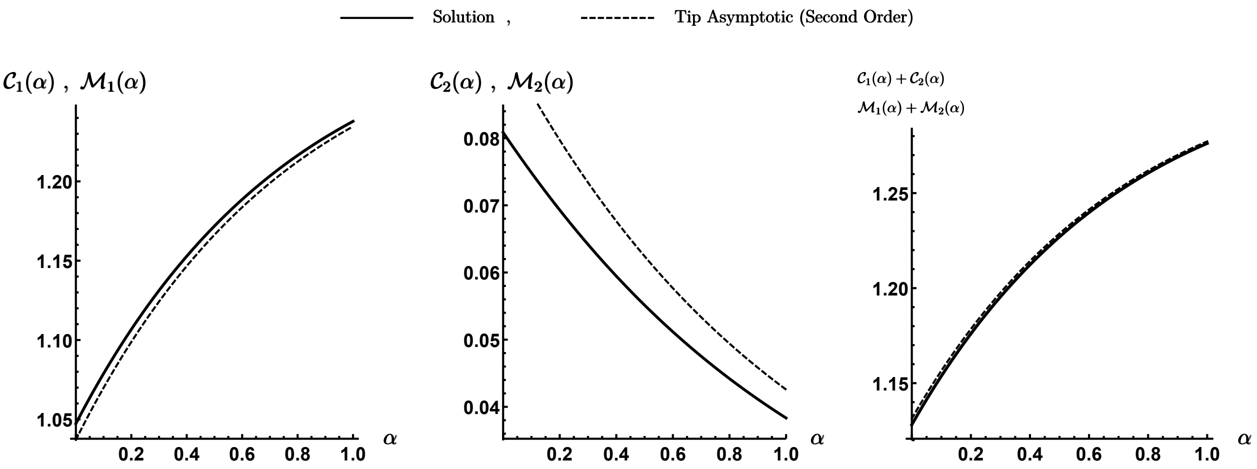

Figure II.5: Constants $C_i$ and $M_i$ in Equations. II.43 and II.44 as functions of $\alpha$.

The rapid convergence of the polynomial series motivates us to derive a second order asymptotic solution near the tip (see Appendix A.D for derivation of this solution). The asymptotic solution has the same structure as the truncated solution and is given by

$$\begin{aligned}
\Omega_{tip} &= (1-\xi)^{\frac{1}{2+\alpha}}\left[\mathcal{M}_1(\alpha)+\mathcal{M}_2(\alpha)\xi\right], \\
\mathcal{M}_1(\alpha) &= (\alpha+2)^{-\frac{\alpha+1}{\alpha+2}}\left(\frac{\alpha+4}{\alpha+5}\right)^{2/(\alpha+2)}\left(1+\alpha+\frac{(\alpha+2)(\alpha+5)}{(\alpha+3)(\alpha+4)}\right), \\
\mathcal{M}_2(\alpha) &= (\alpha+2)^{-\frac{\alpha+1}{\alpha+2}}\left(\frac{\alpha+4}{\alpha+5}\right)^{2/(\alpha+2)}\left(1-\frac{(\alpha+2)(\alpha+5)}{(\alpha+3)(\alpha+4)}\right).
\end{aligned} \tag{II.44}$$

A comparison between the coefficients of the asymptotic solution and the truncated solution is given in Figure II.5

## 1. Applications

We now present a few examples illustrating the practical relevance of the newly-derived solution. The purpose is:

I. To provide a comparison between laminar and turbulent flow solutions for an example high-rate water-driven HF to show that the difference is significant and therefore use of the laminar model in instances where Reynolds number is large can lead to substantial errors.

II. To compare the expected Reynolds numbers for different fluid families (refer to the Appendix A.C.1) in order to clarify conditions under which the turbulent and laminar models are expected to be relevant.

III. To show the size of the near-tip laminar zone relative to the fracture as a whole, thereby clarifying conditions under which the majority of the HF is in turbulent regime.

Here we compare the turbulent solution with the laminar solution of Nordgren (1972), where the opening, net pressure, and length are given by

$$\begin{aligned} w_N(0,t) &= 2.5\left[\frac{\mu q_{in}^2}{H}\frac{(1-\nu)}{G}\right]^{\frac{1}{5}} t^{\frac{1}{5}}, \\ \ell_N(t) &= 0.68\left[\frac{q_{in}^3}{\mu H^4}\frac{G}{(1-\nu)}\right]^{\frac{1}{5}} t^{\frac{4}{5}}, \\ p_{net_N}(0,t) &= 2.5\left[\frac{\mu q_{in}^2}{H^6}\frac{G^4}{(1-\nu)^4}\right]^{\frac{1}{5}} t^{\frac{1}{5}}. \end{aligned} \tag{II.45}$$

The parameter values used in the example case are given in Table II.3 and the characteristic Reynolds number is $Re^* = 10^4$. At this Reynolds number, the flow is turbulent for all values of roughness and, therefore, the Nordgren (1972) solution does not apply. Hence, this comparison illustrates the magnitude of the error associated with inappropriately choosing the laminar model instead.

Figure II.6 shows that the crack opening profile for the turbulent solution is similar to the Nordgren (1972) solution for laminar flow when the opening is normalized by the opening at the wellbore. However, the magnitude of the opening, shown in Figure II.7a, is over 50% greater for the turbulent model. This greater opening is caused by a larger fluid net pressure in the turbulent case (Figure II.7b). Finally, because the total volume is the same in both cases, the laminar model overpredicts the length by over 40% (Figure II.7c). Hence, the turbulent model shows that high Reynolds number treatments will result in higher pressure, greater widths, and shorter lengths than predicted by incorrectly-applied laminar models. This result is also consistent with comparisons for the large leak-off PKN-type solution presented by Kano et al. (2015) and discussed based on scaling arguments by Ames and Bunger (2015).

Table II.3: Material properties and physical constants for illustration.

| Parameter | Value |
|---|---|
| $q_{in}$ | 0.2 m$^3$ s$^{-1}$ |
| $\nu$ | $0.25$ |
| $\mu$ | $0.001$ Pa·s |
| $\rho$ | 1000 kg m$^{-3}$ |
| $k$ | 0.3 mm |
| $m$ | $0.143$ |
| $H$ | 20 m |
| $G$ | 30 GPa |
| $\alpha$ | $1/3$ |

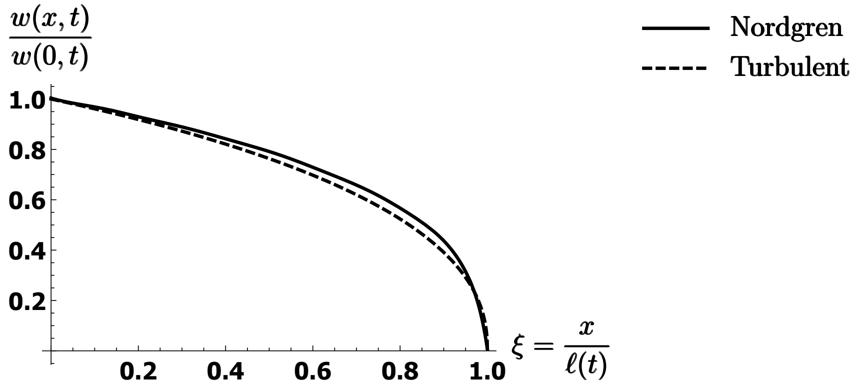

Figure II.6: Normalized variation of maximum fracture width in different cross sections for laminar and turbulent flow.

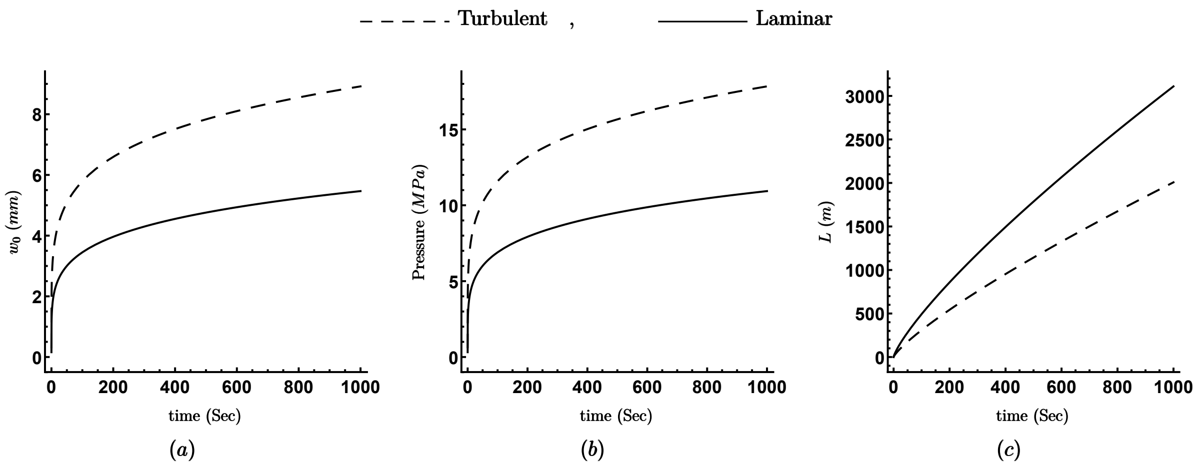

Figure II.7: Comparison between laminar and turbulent solutions for the parameters given in Table II.3. (a) Maximum fracture width at $x = 0$, (b) Predicted fluid net pressure at the wellbore, (c) Fracture length.

It is therefore shown that substantial errors in predictions can arise due to misuse of the laminar or turbulent models. Instead, the choice should be made based on a calculated value of Reynolds number characterizing the regime for a given case.

To address the second objective of this section, comparing the expected Reynolds numbers for different fluid families, we examine four fluids. To see the effect of changing the fluid on the value of the characteristic Reynolds number, we assume the flux $q_{in}$ and height $H$ are constant and use the values given in Table II.3. Referring to Table II.4, the value of $\mu/\rho$ for different fluids is given. The biggest number in the table corresponds to cross-linked gel and is equal to $41.67 \times 10^{-5}$ m$^2$ s$^{-1}$. The smallest value is associated with CO$_2$ ($8.34 \times 10^{-8}$ m$^2$ s$^{-1}$). Hence, the ratio of characteristic Reynolds number for those two cases is equivalent to the ratio of density over viscosity for those two fluids, namely around 5000. This contrast of Reynolds number can be large enough to change the flow regime from laminar to turbulent. We now examine the role of geometry and pumping rate. Typical heights of HFs fall in the range 20 m $< H <$ 200 m (Fisher and Warpinski, 2012). We will take the range of injection rates from $0.01$ m$^3$ s$^{-1}$ $< q_{in} <$ 0.2 m$^3$ s$^{-1}$. Hence the ratio is $5 \times 10^{-5}$ m$^2$ s$^{-1}$ $< q_{in}/H <$ 0.01 m$^2$ s$^{-1}$. Typical Reynolds numbers for the 4 fluids and their densities and viscosities are listed in Table II.4. Based on open channel

Table II.4: Different fracturing fluids and their rheology.

| Fluid | Density<br>$\rho$ (kg m$^{-3}$) | Viscosity<br>$\mu$ (Pa·s) | Kinematic Viscosity<br>$\frac{\mu}{\rho}$ (m$^2$ s$^{-1}$) |
|---|---|---|---|
| Water | 1000 | 0.001 | $10^{-6}$ |
| X-linked Gel | 1200 | 0.5 | $41.67 \times 10^{-5}$ |
| $CO_2$ (Supercritical $CO_2$) | 600 | $5 \times 10^{-5}$ | $8.34 \times 10^{-8}$ |
| Linear Gel | 1200 | 0.05 | $41.67 \times 10^{-6}$ |

problems (Henderson, 1966; Munson et al., 2002), the corresponding range Reynolds number for the laminar regime $Re < 500$, while $Re > 12500$ is considered as turbulent regime. The values in between are thus considered to occupy a transition from laminar to turbulent flow. Accordingly, fracturing with $CO_2$ will be mostly turbulent flow. The flow regime of the water in most cases is in transition between laminar and turbulent and in the most field relevant cases is closer to, and therefore better approximated by, the turbulent regime. The other two fluids lead to laminar flow (for more details, refer to to the Appendix A.C.1).

The suggested Reynolds numbers are experimentally determined and may change based on geometric details for open channel problems. For most of the practical cases, Reynolds number less than 500 is laminar. However, there is no definitive upper limit defining the transition to turbulent flow (Te Chow, 1959; Munson et al., 2002; Gioia and Chakraborty, 2006). In open channel problems an upper limit for the transition depends on other parameters like the channel geometry. Therefore, we discuss two alternative methods for estimating an appropriate $Re$ to define transition to turbulent flow in order to select an appropriate fluid flow law. First, we compare the characteristic fluid pressure associated with laminar flow $P_{laminar}$ to the characteristic pressure associated with turbulent flow $P_{turb}$. In this approach we define $P_{laminar} > P_{turb}$ as the laminar regime and $P_{laminar} < P_{turb}$ as the turbulent regime. Although the transition $Re$ depends on the fluid properties (see the Appendix A.C.2 for details), a typical transition value is around $Re = 500$.

With this definition and the proposed ranges for different parameters, $CO_2$ is always turbulent and water is turbulent for nearly all relevant cases (see Appendix A.C.2 for more details).

Returning (briefly) to the definition of GMS, to develop the friction factor, the hydraulic radius is used. Hydraulic radius ($R_h$) is a characteristic length that helps to calculate the effect of different cross sections. Originally, this parameter is introduced so that the pipe flow equations can be expanded to other non-circular conduits. Mathematically, the hydraulic radius is the ratio of cross section of the fluid flow over the wetted perimeter ($R_h = A/\mathfrak{P}$). For elliptical cracks, the area is $A = \pi\omega H/4$, and if the eccentricity of the ellipse defined as $e = \sqrt{1-(\omega/H)^2} \approx 1$ its perimeter is defined as

$$\mathfrak{P} = \pi H \left[1 - \sum_{i=1}^{\infty} \frac{(2i)!^2}{(2^i.i!)^4} \frac{e^{2i}}{2i-1}\right] \approx 2H, \tag{II.46}$$

so the value of hydraulic radius is $\pi\omega/8$. In the PKN model, the cross section is ellipse, so the average value of the opening in one cross section is (Zia and Lecampion, 2016)

$$\overline{\omega} = \frac{1}{H}\int_{-H/2}^{H/2} W(x,z,t)dz = \frac{\pi}{4}\omega, \tag{II.47}$$

thus, hydraulic radius is half the average value of the opening of the crack at a specific cross section ($R_h = \overline{\omega}/2$).

The Moody diagram can be used to determine the transition $Re$ for the purpose of selecting a fluid flow model (see the Appendix A.B for more details). The premise of this argument is that for most cases in HF the scaled value of the fracture roughness is in order of 0.05 or higher ($k/w > 0.05$). According to the Moody diagram (Appendix A.B), for such a roughness, the fully turbulent regime occurrs at $Re > 10^4$ and the transition from the laminar regime starts around $Re > 2000$. We further note that the friction factor in this transition regime is for the most part closely enough approximated by the turbulent GMS model that it is a viable selection from a practical perspective.

Finally, the Reynolds number discussed so far is determined by the fluid flow only in the neighborhood of the injection point. This Reynolds number, however, may not represent the flow near the fracture tip, where there is a switch from a Reynolds number dominated by the fracture depth $H$ to a local Reynolds number where the small width of the fracture dominates. As a result, there is a transition along the crack where the flow regime switches from turbulent flow to laminar flow. Thus, we would like to know the ratio of the length of the turbulent regime over the laminar region. Due to the fact that $q$ is independent of $H$ and only depends on time through $x/\ell(t)$, the quantity $HRe$ is a unique function of $x/\ell(t)$ for a given fluid. This relationship is shown in Figure II.8. Comparing the values presented in Figure II.8 shows that the value of Reynolds number near the crack tip where the value of $x/\ell(t)$ approaches to 1 is close to zero and the behavior of the fluid in that region is thus laminar. Moreover, Figure II.8 indicates that there is a similarity between all the graphs; indeed the only thing that changes from one plot to the other is the value of the kinematic viscosity $\mu/\rho$. Combining, then, Equation II.42 and the definition of Reynolds numbers gives

$$\begin{aligned} Re &= Re^{*}\mathcal{F}(\xi), \\ Re^{*} &= \frac{\rho q_{in}}{\mu H}, \\ \mathcal{F}(\xi) &= (1-\xi)^{\frac{3}{7}}\left(1+0.05497\xi\right)^{\frac{5}{3}}\left(1+0.21005\xi\right)^{\frac{1}{2}}. \end{aligned} \tag{II.48}$$

The change of $\mathcal{F}(\xi)$, which determines the variation of $Re$ for different values of $\xi$ is presented in Figure II.9. In order to change the order of magnitude of $Re$ compared to $Re^{*}$, the value of $\mathcal{F}(\xi)$ should drop at least one order of magnitude which occurs for $\xi > 0.9970$. Similarly, a two order of magnitude drop corresponds to $\xi > 0.999986$.

With the variation of $Re$ along the fracture in mind, consider the example of water as an injecting fluid ($\mu = 0.001$ Pa·s and $\rho = 1000$ kg m$^{-3}$). The characteristic Reynolds number is $Re^{*} = 10^{6}q_{in}/H$. If the height is 20 m and the injecting fluid flow is $0.2$ m$^{3}$ s$^{-1}$, then $Re^{*}$ is $10^{4}$. Thus the fluid flow regime based on the characteristic Reynolds number is turbulent. However, as discussed, $Re$ decreases along the fracture, reaching a transition value of $Re \approx 2000$ at around $x/\ell(t) > 0.98$. This indicates that about 98% of the HF length is either in transition or turbulent regime. Thus, the GMS approximation is accurate enough for practical purposes in the transition regime. Due to the fact that HFs have a relatively large roughness scale compared to the fracture opening, in this case a valid global approximate solution can be obtained neglecting the laminar region near the tip. In other words, this example would correspond to a valid application of the present model. In contrast, if fluid flow is $0.2$ m$^{3}$ s$^{-1}$ and the height of the crack is 70 m, then $Re^{*} \approx 2900$, which is in transition to turbulent regime. In this case, Reynolds number drops to less than 2000 at about $x/\ell(t) > 0.68$. In this case, then, 68% of the HF is either in transition or is

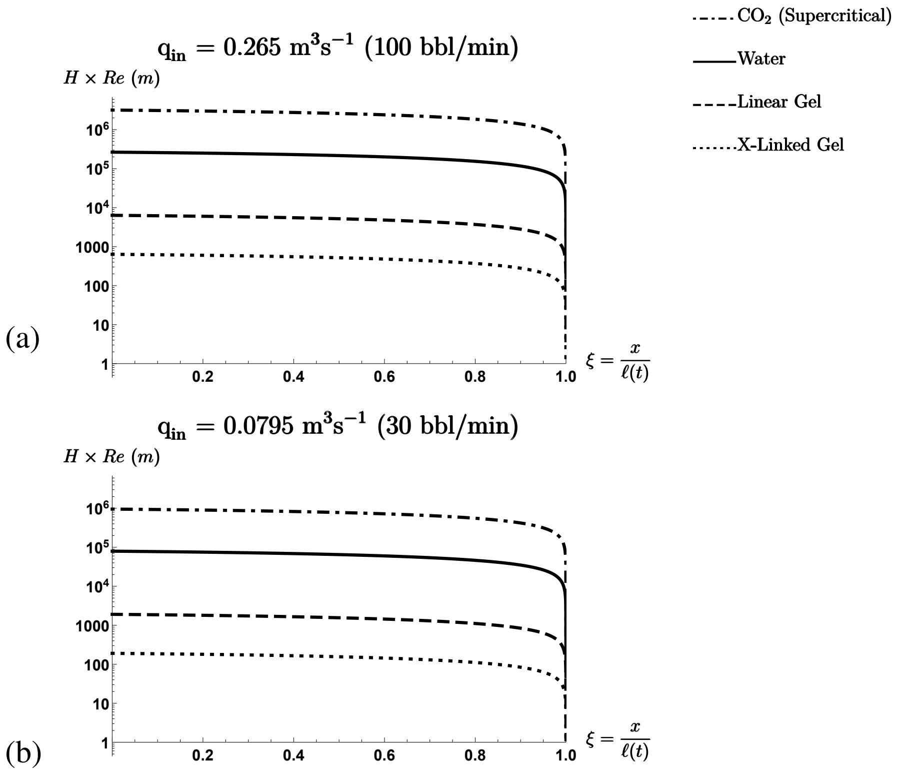

Figure II.8: Reynolds number variation along the crack. By knowing the height of the barrier $H$, it is possible to find the Reynolds number at any points inside the crack. The time dependence is embedded in length of the crack which can be seen in $x/\ell(t)$. Note that this graph still depends on pumping rate $q_{in}$.

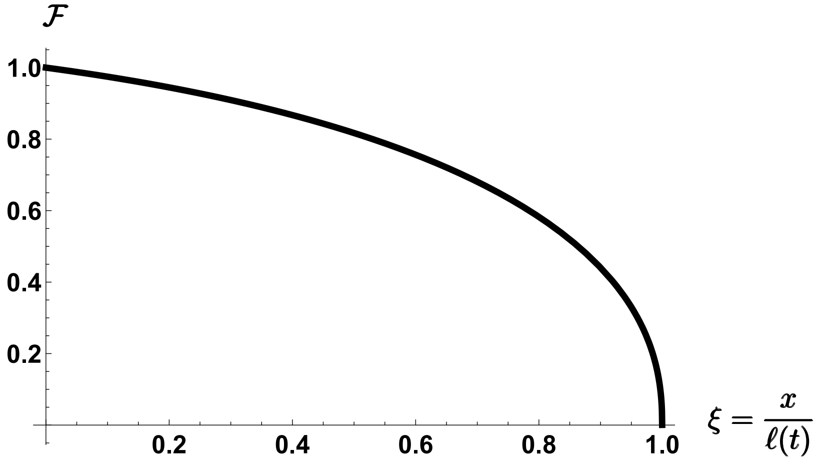

Figure II.9: Change of $\mathcal{F}(\xi)$ versus $\xi$.

in turbulent regime which shows that around 1/3 of the crack is still in the laminar regime. In this latter example an approach considering the presence of both a turbulent and laminar region within the HF would be required.

## H. CONCLUSIONS

The flow regime for some HF treatments is turbulent over the vast majority of the HF length. In particular, high-rate, water-driven HFs, as well as $CO_2$ driven fractures, tend to this regime. This is in contrast to the lower-rate, gel-driven fractures which comprised the main interest during the development of many HF solutions based on laminar flow models. With these limitations in mind the scope of this study was limited to consider fully turbulent flow throughout the fracture, ignoring the effect of the transition of the fluid regime from turbulent to laminar flow at crack tip or in the boundary at top and bottom of the reservoir. Also, considering this limiting regime, the solution ignores the effect of fracture toughness.

Here we have presented a model for a blade-shaped (PKN) geometry HF growing in an impermeable rock and driven by a turbulent fluid. We derive a semi-analytical solution which: (a) embeds all rock, fluid, and geometric parameters in a scaling so that the resulting ode can be solved once for all cases, and (b) provides an accurate solution keeping only 2 terms of a polynomial series solution. The rapid convergence is enabled by embedding the near-tip behavior, also solved here in the course of the solution method, in the form of orthogonal polynomials. Failure to recognize the appropriate flow regime will lead to erroneous application of models based on laminar flow. Incorrect models are estimated to over predict the fracture length and under predict the fracture width and pressure by 40-50%. As such, this model not only provides a benchmark solution for numerical simulation and a means for rapid estimation of fracture dimensions. It also provides impetus for ongoing research including experimental studies to find the most appropriate values of parameters $m$ and $\alpha$ for turbulent flow within a rough-walled deformable slot such as is encountered in HF applications.

Here we show that using laminar flow instead of turbulent flow under conditions where most of the HF has $Re > 2500$ can lead to enormous errors in calculating the fracture opening (i.e. more than 100% at 1000 seconds of injection). And also a sizable error (>50% as shown in Figure II.7) is induced on the crack length and fluid pressure estimation. Ongoing efforts are aimed at expanding the ability of the model to consider the turbulent regime when it is appropriate to use a different form other than the generalized GMS equation. It is expected this will be particularly necessary under conditions where proppant transport and the use of rheological-modifying additives are considered.

# III. SOLUTION FOR A PLANE STRAIN ROUGH-WALLED HYDRAULIC FRACTURE DRIVEN BY TURBULENT FLUID THROUGH IMPERMEABLE ROCK

## A. PREAMBLE

The content of this chapter comprises a preprint of Zolfaghari et al. (2017). It presents the asymptotic semi-analytical solution for plane strain HF driven by fluid with flow in the rough-walled fully turbulent regime. The solution is generated using a method inspired by Adachi (2001a) for the laminar regime. The tip asymptotic solution is developed for a crack filled with fully-turbulent fluid. The solution is compared with the numerical model provided by collaborator, Dr. Egor Dontsov. The comparisons between the numerical simulations and the semi-analytical solutions indicates a good agreement, and further it shows that the laminar-turbulent transition region is relatively small. This means that an accurate solution can typically be obtained by either the laminar or turbulent solution, without need for numerical simulation, choosing the solution corresponding to the larger pressure, larger opening, and shorter length.

## B. ABSTRACT

The impact of turbulent flow on plane-strain fluid-driven crack propagation is an important, but still poorly understood consideration in hydraulic fracture modeling. The changes that hydraulic fracturing has experienced over the past decade, especially in the area of fracturing fluids, have played a major role in the transition of the typical fluid regime from laminar to turbulent flow. Motivated by the increasing preponderance of high rate, water-driven hydraulic fractures with high Reynolds number, we present a semi-analytical solution for the propagation of a plane-strain hydraulic fracture driven by a turbulent fluid in an impermeable formation. The formulation uses a power law relationship between the Darcy-Weisbach friction factor and the scale of the fracture roughness, where one specific manifestation of this generalized friction factor is the classical Gaukler-Manning-Strickler approximation for turbulent flow in a rough walled channel. Conservation of mass, elasticity, and crack propagation are also solved simultaneously. We obtain a semi-analytical solution using an orthogonal polynomial series. An approximate closed form solution is enabled by a choice of orthogonal polynomials embedding the near-tip asymptotic behavior and thus giving very rapid convergence; a precise solution is obtained with two terms of the series. By comparison to numerical simulations we show that the transition region between the laminar and turbulent regime can be relatively small so that full solutions can often be well-approximated by either a fully laminar or fully turbulent solution.

## C. INTRODUCTION

Hydraulic Fracturing is one of the major tools used to stimulate extraction of oil and gas from subsurface reservoir rocks. In this method fluid is used to drive crack propagation. The research to date has tended to use laminar flow models to describe fluid movement within hydraulic fractures Khristianovic and Zheltov (1955); Geertsma and De Klerk (1969); Nordgren (1972); Adachi and Detournay (2002); Garagash and Detournay (2000); Garagash (2006). Apart from high flow rate and relatively small crack opening, the recently increasing tendency to use water as a fracturing fluid instead of highly viscous gels King (2010) can significantly increase the Reynolds number. Therefore, the flow regime for hydraulic fracturing applications that have emerged over the past two decades is not strictly laminar, but instead can be in transition and even fully turbulent flow regimes. As an illustration, in a typical hydraulic fracture (HF), the injection flow rate is usually $0.05-0.2\ (m^3/s)$, and the reservoir thickness is $50-200\ (m)$. A typical way to illustrate Reynolds number Reynolds (1883) is through $\rho\langle v\rangle D_h/\mu$, where $\langle v\rangle$ is the average fluid velocity and $D_h$ is the hydraulic diameter of the flow distribution. Here the hydraulic diameter is defined as $D_h = 4A/P$ where $A$ is the cross section of the fluid flow and $P$ is the perimeter of the wet region and for plane-strain geometry is $D_h \simeq 2w$. For a plane-strain HF, the parameter $Q_0$ is defined as the ratio of total volumetric injection rate over the heigth of the reservoir. It can thus be expressed as the average fluid velocity ($\langle v \rangle$) over the crack width multiply the crack width ($Q_0/2 = \langle v \rangle w$), both taken at the inlet. We can then express a characteristic value of the classical Reynolds number as

$$Re^* = \rho Q_0/\mu,$$

where $\rho$ and $\mu$ are the fluid density and viscosity, respectively, and $Q_0$ is the fluid flow rate per unit length that has a dimension of $(m^2/s)$. If water is used as a fracturing fluid, the density and viscosity will be $1000\ (kg/m^3)$ and $0.001\ (Pa.s)$, respectively. If gel is being used, the density and viscosity will be $1200\ (kg/m^3)$ and $0.5 - 1\ (Pa.s)$. Thus, for water $Re^* = 10^2 - 10^4$ and for gel $Re^* = 0.01 - 10$. This indicates that by changing the fracturing fluid from gel to water, we expect 2 to 3 orders of magnitude increase of Reynolds number.

Note that here, and throughout this paper, we use water and slickwater as a fluids for comparison purposes. Many “water” hydraulic fractures have friction reducing additives, leading to the name “slickwater”. Here we do not address important rheological differences between water and slickwater except to use $\mu = 0.001\ Pa.s$ for water and $\mu = 0.003\ Pa.s$ for slickwater. Also note that it is a common practice to express Reynolds number for non-circular cross-sections using hydraulic diameter. However, it has been proven experimentally that keeping Reynolds number constant with hydraulic diameter and changing the aspect ratio, the friction factor will change. Therefore, there is an ongoing discussion that the definition of Reynolds number through hydraulic diameter is not accurate Jones (1976). According to Jones (1976) the modified Reynolds number for plane strain geometry is 2/3 of characteristic value of the classical Reynolds number (as $Re = \frac{2}{3}\frac{\rho \langle v \rangle D_h}{\mu}$). Thus the characteristic Reynolds number is reduced with constant factor of $2/3$ ($Re = 2\rho \langle v \rangle D_h/3\mu = 2\rho Q_0/3\mu = 2/3 Re^*$). In this manuscript, for the sake of comparison everything is defined in terms of characteristic Reynolds number. However, in order to do numerical modeling, one should use the modified Reynolds number.

Hydraulic fracture models, by and large, account for four physical couplings: 1) solid deformation due to fluid pressure, 2) fluid flow inside the crack, 3) crack propagation, and 4) leak-off of the fluid into the rock matrix. Each of these coupled processes is accompanied by its own characteristic time and length scales. Consideration of turbulent flow introduces transition time and length scales from laminar to turbulent regime. This transition is unique to fluid-driven crack propagation because of the coupling with elastic deformation and crack propagation. From an industrial point of view, consideration of turbulent flow will change the calculation of crack geometry, fluid pressure, and rate of crack propagation. Miscalculation of these quantities can lead to problems like wrong choice of proppant size and scheduling and unwanted crack growth into non-productive zones. Hence, furthering the understanding the impact of turbulent flow is both challenging and important.

In order to obtain semianalytical solutions, which are desireable for rapid estimation of fracture dimensions and for benchmarking numerical simulations, simple geometries are required. One of the classical models to describe a two dimensional HF is the plane-strain geometry Geertsma and De Klerk (1969). Its origins are tied to the fact that, in most of the HF treatments, the horizontal confining stresses are smaller than the vertical overburden stress which will cause the crack growth to orient in vertical direction. Also the reservoirs in most cases are bounded by barrier layers, usually with higher stresses, that limit the vertical growth of HFs. At early time, when the length of the crack is much smaller than the height of the barrier (less than three times the height), yet much longer than wellbore diameter, the plane-strain estimation is a useful estimate model (Figure III.1a).

Awareness of the turbulent regime in hydraulic fracturing is not recent, having been recognized in the seminal work of Perkins and Kern (1961). The subsequent literature has emphasized the importance of considering turbulent flow (e.g. Ames and Bunger (2015)) especially if the fluid is a gas Settari et al. (2002); Wei and Economides (2005); Martin and Economides (2010).

For HF, Nilson (1981, 1988) considered unidirectional flow for gas-driven HFs in a high inertia regime for constant pressure inlet boundary condition. In a similar way, Emerman et al. (1986) investigated the plane-strain problem for gas-driven fractures with constant inlet flow boundary condition. In another study Siriwardane and Layne (1991) modeled the plane-strain growth of multiple HFs. In this model there is a constant inlet flux boundary condition and the fluid flow equations are obtained from analogy to agitated pipe flow. Among the other models that incorporate turbulent flow, Hayashi and Taniguchi (1999) used the Manning-Strickler channel flow equation with logarithmic friction factor to model radial HF growth, but without expressing the opening and length of the crack, and hence the answer provides only an estimation for the pressure. In addition, some numerical models to simulate HF that considered the turbulent regime have been developed Nilson and Griffiths (1983); Nilson (1986); Li et al. (2012, 2013). And, indeed there are design models which incorporate turbulent regime capability (e.g. Meyer (1989)).

The study of the effect of turbulent flow in fluid driven crack growth is not just limited to industrial hydraulic fracturing. A few investigations consider either constant pressure injection or buoyancy-driven propagation, appropriate to the geosciences Perkins and Kern (1961); Huang et al. (1990); Lister (1990); Lister and Kerr (1991); Tsai and Rice (2010); Anthonyrajah et al. (2013). Tsai and Rice (2010) modeled a very fast drainage of a glacial lake through a sub-glacial fluid driven crack. They used the Gauckler-Manning-Strickler (GMS) Manning (1891); Strickler (1923, 1981) to model the fluid flow in the rough-walled turbulent regime. This contribution provides a useful background for the fluid flow model, but the boundary conditions and elasticity formulation are specific to their problem and not applicable to industrial HFs. Also,Lister (1990) and Lister and Kerr (1991) solved the problem of dyke propagation by considering turbulent flow.

In recent years, there has been a slowly increasing amount of literature on turbulent flow in hydraulic fracturing. Kano et al. (2015) published a solution for the large leakoff limit for a blade-shapped (PKN) HF with rough-walled turbulent flow. Zolfaghari et al. (2017) developed a PKN HF soultion considering turbulent flow in an impermeable rock, using a general form of the GMS model to develop their semi-analytical solution. Dontsov (2016) derived a solution for the near-tip region of a plane-strain HF driven by a turbulent fluid that captures transition from laminar near the tip to turbulent away from the tip. And, most recently, Zia and Lecampion (2016, 2017) considered the PKN model with constant injection inlet flux boundary condition for the transition from laminar to turbulent flow.

The goal of this research is to develop benchmark solutions that can be used to estimate fracture dimensions and fluid pressure for a plain strain HF driven by a turbulent fluid through impermeable rock. Because of the open question of the best turbulent flow model for HF, we employ the general form of Gaukler-Manning-Strickler, thereby capturing a range of behaviors that can be tested in future experimentation. In order to derive the solution, we use a Gegenbauer series which follows by the spirit of Adachi and Detournay (2002), and Garagash (2006). This solution provides rapid convergence due to embedding of the crack tip singularity in the polynomials. This approach is similar to the more classical case of Chebyshev polynomial series to solve crack problems Erdogan et al. (1973). At the end, we provide a discusion of the transition from laminar to turbulent flow, clarifying the Reynolds number associated with this transition by comparison to numerical simulations and showing, by way of these comparisons, that the transition region is relatively small. In other words, the numerical simulations show that a full solution to the problem can often be usefully approximated by either a fully laminar or fully turbulent asymptotic solution, with the appropriate choice of solution depending upon the Reynold's number and the fracture roughness.

## D. METHOD

The plane-strain HF refers to the geometry wherein the height of the crack, $H$, is very large with respect to the crack half length, $\ell(t)$ (see Figure III.1). It was originally considered by Khristianovic and Zheltov (1955) and Geertsma and De Klerk (1969), hence it is often called the KGD HF geometry. The length of the crack, $\ell(t)$ is also considerably larger than the well diameter such that the mechanical influence of the wellbore is ignored and the fluid is considered to be injected from a point source at $x = 0$. The plane strain fluid injection from the wellbore is considered to be $Q_0 = Q_{in}/H$ where H is the height of the reservoir and $Q_{in}$ is the volumetric injection rate. The width of the crack, the fluid flux, and the pressure at any time and location is given by $w(x,t)$, $q(x,t)$, and $p(x,t)$, respectively (see Figure III.1b). Note $q = \langle v \rangle w$, where $\langle v \rangle$ is the mean velocity across the fracture width. The conservation of momentum for incompressible fluid flow in the crack for Newtonian fluid in the plane strain geometry is

$$-\frac{\partial p}{\partial x} - \frac{2\tau_w}{w} = \rho\left(\frac{\partial \bar{u}}{\partial t} + \bar{u}\frac{\partial \bar{u}}{\partial x}\right) \tag{III.1}$$

where $\tau_w$ is the shear stress on the wall due to fluid flow, $\bar{u}$ is the time averaged fluid velocity in the direction of the crack propagation. The shear stress in the turbulent regime is

$$\tau = \mu\frac{d\bar{u}}{dy} - \rho\overline{u'v'}$$

which consists of two parts, the laminar shear stress and the turbulent shear stress (see Streeter (1961a); Munson et al. (2002)). In this model, the fluid velocity has two components, $u$ is the velocity in the direction of the crack propagation ($x$ direction), and $v$ the other component of the fluid velocity is perpendicular to crack walls ($y$ direction). Therefore, each components of the velocity consists of a time averaged part ($\bar{u}$ and $\bar{v}$), and fluctuation with respect to time ($u'$ and $v'$). Thus, the shear stress is a quantity that is time averaged, which means it can be treated as a steady-state value. Therefore, the inertia part of the Equation III.1 is negligible (see Zia and Lecampion (2016, 2017)) and the pressure drop in the crack is

$$\Delta p = f(v, w, \Delta x, k, \mu, \rho).$$

After dimensional analysis (using $\Pi$-theorem Barenblatt (1996)), the scaled pressure drop is (see Munson et al. (2002) for more detail)

$$\frac{\Delta p}{1/2\rho v^2} = \frac{\Delta x}{w} f\left(\frac{\rho v w}{\mu}, \frac{k}{w}\right).$$

Consistent with this dimensional analysis and classical experimental results, fluid flow is modeled via the Gaukler-Manning-Strickler Gauckler (1867); Manning (1891); Strickler (1923) relationship

$$q = \left(-\frac{4w^3}{\rho f_p}\frac{\partial p}{\partial x}\right)^{1/2}, \tag{III.2}$$

where $f_p$ is the Darcy-Weisbach friction factor and can be calculated as

$$f_p = m\left(\frac{k}{w}\right)^{\alpha}. \tag{III.3}$$

Here $k$ is the crack surface roughness, and $\alpha$ and $m$ are constants. For the sake of generality, they are kept variable. Typically in hydraulic fracturing the values for $\alpha$ and $m$ are taken as $\alpha = 1/3$ and $m = 0.143$ Gioia and Chakraborty (2006); Tsai and Rice (2010).

For the plane-strain problem in an impermeable rock, conservation of mass is defined as

$$\frac{\partial w}{\partial t} + \frac{\partial q}{\partial x} = 0, \tag{III.4}$$

where $q$ is the fluid flux and defined through Equation III.2. We can then replace the turbulent flow (Equations III.2 and III.3) in the continuity equation (Equation III.4) to eliminate $q$ from the equations. Also by letting

$$\beta' = \frac{2}{\sqrt{\rho m k^{\alpha}}}, \qquad E' = \frac{E}{1-\nu^2}, \qquad K' = \frac{8}{\sqrt{2\pi}}K_{IC}$$

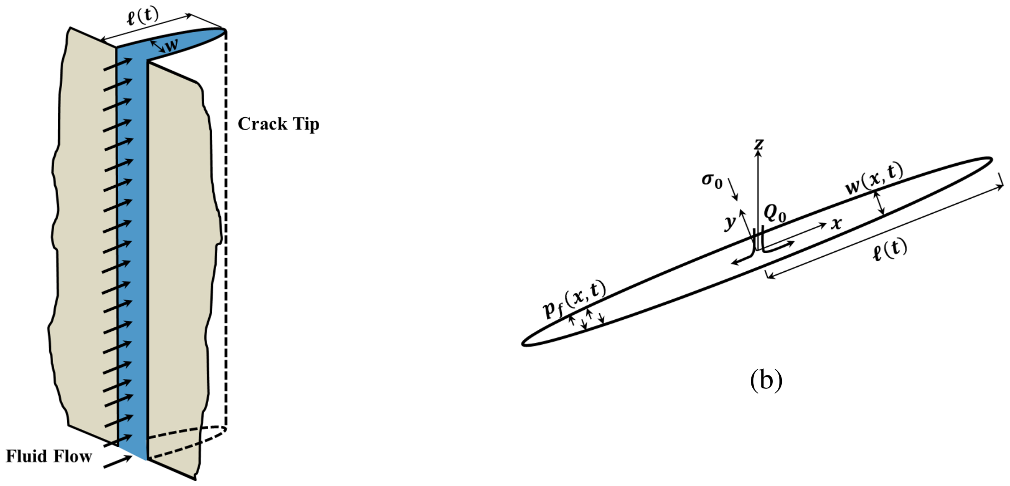

(a)

(b)

Figure III.1: Plane strain geometry.**(a)** Three dimensional. **(b)** Two dimensional view.

the continuity equation will be given by

$$\frac{\partial w}{\partial t} = -\beta' \frac{\partial}{\partial x}\left[\left(-\frac{\partial p}{\partial x}\right)^{1/2} w^{\frac{3+\alpha}{2}}\right] \tag{III.5}$$

In addition to fluid flow, the width, pressure, and length are related by an elasticity equation (based on dislocation theory Hills et al. (1996)), given by

$$p(x,t) = p_f(x,t) - \sigma_0 = -\frac{E'}{4\pi}\int_{-\ell}^{\ell} \frac{\partial w}{\partial s}\frac{ds}{s-x} \tag{III.6}$$

where $p$ is a net pressure, given by the difference between the fluid pressure and a uniform far field stress $\sigma_0$. Also, from linear elastic fracture mechanics, crack propagation proceeds when the stress intensity factor $K_I$ equals a material strength parameter, the fracture toughness $(K_{IC})$. For the plane strain case Irwin (1957)

$$\begin{aligned} K_I &= 2\sqrt{\frac{\ell}{\pi}}\int_0^l \frac{p(x,t)}{\sqrt{\ell^2 - x^2}}dx \\ K_I &= K_{IC} \end{aligned} \tag{III.7}$$

Finally, the boundary conditions and initial condition are Detournay and Peirce (2014)

$$
\begin{gathered}
x = \pm\ell \Rightarrow w = 0, \quad q = 0 \\
q(0^+, t) = \frac{Q_0}{2}, \quad q(0^-, t) = -\frac{Q_0}{2} \\
t = 0 \Rightarrow w = 0, \quad \ell = 0, \quad p = 0
\end{gathered}
\tag{III.8}
$$

These embody conditions of: 1) zero opening at the fracture tip, 2) zero flux at the fracture tip, which ensures the fluid and fracture advance together, 3) fluid flux at the inlet balance the influx from the wellbore, and 4) the fracture has zero initial width, length, and net pressure.

## E. SCALING

We define the dimensionless opening $\Omega$, pressure $\Pi$, fluid flow rate $\Psi$, and crack length $\gamma$ as a function of time and coordinate $\xi$ as (after Detournay (2004))

$$
w = \varepsilon L \Omega(\xi, t), \quad p = \varepsilon E' \Pi(\xi, t), \quad \ell = L\gamma(t), \quad q = Q_0 \Psi(\xi, t), \quad \xi = \frac{x}{l} \tag{III.9}
$$

Here $\varepsilon(t)$ and $L(t)$ are scaling factors yet to be determined. By considering the total mass balance (integral of Equation III.4 over the crack), we obtain:

$$
\frac{Q_0 t}{\varepsilon L^2} = 2\gamma \int_0^1 \Omega(\zeta, t) d\zeta \tag{III.10}
$$

Since we want to preserve the conservation of the mass throughout the analysis, we can choose $\varepsilon(t)$ in a way that simplify our calculations, so

$$
\frac{Q_0 t}{\varepsilon L^2} = 1 \Rightarrow \varepsilon = \frac{Q_0 t}{L^2} \tag{III.11}
$$

Now by inserting the scaling parameters from Equation III.9 and Equation III.11 into the continuity equation (III.4), elasticity equation (III.6), fluid flux (III.2), and crack propagation (III.7), we can obtain:

$$\begin{aligned} &\left(1-\frac{\dot{L}t}{L}\right)\Omega+\dot{\Omega}t-\xi\left(\frac{\dot{\gamma}t}{\gamma}+\frac{\dot{L}t}{L}\right)\frac{\partial\Omega}{\partial\xi}= \\ &\qquad -\frac{\beta' E'^{1/2}Q_0^{1+\alpha/2}t^{2+\alpha/2}}{L^{3+\alpha/2}\gamma^{3/2}}\frac{\partial}{\partial\xi}\left[\Omega^{\frac{3+\alpha}{2}}\left(-\frac{\partial\Pi}{\partial\xi}\right)^{\frac{1}{2}}\right] \end{aligned} \tag{III.12a}$$

$$\Pi=-\frac{1}{4\pi\gamma}\int_{-1}^{1}\frac{\partial\Omega}{\partial\zeta}\frac{d\zeta}{\zeta-\xi} \tag{III.12b}$$

$$\Psi=\frac{\beta' E'^{\frac{1}{2}}Q_0^{1+\frac{\alpha}{2}}t^{2+\frac{\alpha}{2}}}{L^{3+\frac{\alpha}{2}}\gamma^{1/2}}\left(-\frac{\partial\Pi}{\partial\xi}\right)^{1/2}\Omega^{\frac{3+\alpha}{2}} \tag{III.12c}$$

$$\frac{K' L^{3/2}}{Q_0 t E'}=\frac{2^{7/2}\sqrt{\gamma}}{\pi}\int_0^1\frac{\Pi}{\sqrt{1-\zeta^2}}d\zeta \tag{III.12d}$$

where two dimensionless groups can be defined

$$\mathcal{G}_T=\frac{L^{3+\alpha/2}}{\beta' E'^{1/2}Q_0^{1+\alpha/2}t^{2+\alpha/2}} \quad , \qquad \mathcal{G}_k=\frac{K' L^{3/2}}{Q_0 t E'} \tag{III.13}$$

The accompanying boundary and initial conditions are

$$\Omega(\pm 1,t)=0 \quad , \quad \Omega^{(3+\alpha)/2}\left(-\frac{\partial\Pi}{\partial\xi}\right)^{\frac{1}{2}}\Bigg|_{\xi=\pm 1}=0 \tag{III.14a}$$

$$\Psi(0^+,t)=\frac{1}{2} \quad , \quad \Psi(0^-,t)=-\frac{1}{2} \tag{III.14b}$$

$$\gamma(0)=0 \quad , \quad \Omega(\xi,0)=0 \quad , \quad \Pi(\xi,0)=0 \tag{III.14c}$$

After scaling the problem, the system of partial differential equations can be solved analytically/ semi-analytically for two limiting cases. One limit is when the fracture toughness is vanishingly small ($\mathcal{G}_k \to 0$) and the other case is for when the fluid friction is vanishingly small ($\mathcal{G}_T \to 0$).

The fluid friction scaling factor $\mathcal{G}_T$ is defined in a way that it multiplies the left hand side of Equation III.12a. Hence, for the case of zero fluid friction ($\mathcal{G}_T \to 0$), the left side of Equation III.12a will become insignificant and the problem reduces to the case of crack growth with uniform internal pressure. This zero-fluid friction (similar to zero-viscosity in laminar flow) limit for HFs has already been solved Adachi (2001b). However, for zero toughness the problem remains to be solved. Thus for the case of negligible toughness, choosing the characteristic scales $L$ so that $\mathcal{G}_T = 1$ leads to (for $\varepsilon$ see Equation III.11)

$$\begin{aligned} \varepsilon &= \left(\beta'^2 E' Q_0^{(\alpha-2)/2}\right)^{-\frac{2}{\alpha+6}} t^{-\frac{\alpha+2}{\alpha+6}} \\ L &= \left(\beta' E'^{1/2} Q_0^{(\alpha+2)/2}\right)^{\frac{2}{\alpha+6}} t^{\frac{\alpha+4}{\alpha+6}} \end{aligned} \tag{III.15}$$

Prior to commencing the solution, we should replace this scaling into Equation III.12. After substitution, we simplify the equations with following changes of variables

$$\gamma^{4/(2+\alpha)}\bar{\Omega} = \Omega, \qquad \gamma^{(2-\alpha)/(2+\alpha)}\bar{\Pi} = \Pi, \qquad \gamma^{(6+\alpha)/(2+\alpha)}\bar{\Psi} = \Psi. \tag{III.16}$$

Once the equation is simplified it becomes independent from the dimensionless parameter $\gamma$. Hence, we can take the integral of both sides of Equation III.12a from $\zeta$ to 1, making use also of the boundary conditions. The governing equations and boundary conditions for $\bar{\Omega}$, $\bar{\Pi}$, and $\bar{\Psi}$ are then given by

$$\int_\xi^1 \bar{\Omega} d\zeta = -\frac{\alpha+4}{\alpha+6}\xi\bar{\Omega} + \bar{\Omega}^{\frac{3+\alpha}{2}}\left(-\frac{d\bar{\Pi}}{d\xi}\right)^{1/2} \tag{III.17a}$$

$$\bar{\Pi} = -\frac{1}{4\pi}\int_{-1}^1 \frac{d\bar{\Omega}}{d\zeta}\frac{d\zeta}{\zeta-\xi} \tag{III.17b}$$

$$\int_0^1 \frac{\bar{\Pi}}{\sqrt{1-\zeta^2}} d\zeta = 0 \tag{III.17c}$$

$$\bar{\Psi} = \left(-\frac{\partial\bar{\Pi}}{\partial\xi}\right)^{1/2}\bar{\Omega}^{\frac{3+\alpha}{2}} \tag{III.17d}$$

$$\bar{\Omega}(\pm 1) = 0 \tag{III.17e}$$

$$\bar{\Omega}^{\frac{3+\alpha}{2}}\left(-\frac{d\bar{\Pi}}{d\xi}\right)^{1/2}\Bigg|_{\xi=\pm 1} = 0 \tag{III.17f}$$

$$2\gamma^{\frac{\alpha+6}{\alpha+2}}\int_0^1 \bar{\Omega} d\zeta = 1 \tag{III.17g}$$

From the scaled equations, we can see that the coupled integro-differential equations (IDE) for $\bar{\Omega}$ and $\bar{\Pi}$ are described with homogeneous boundary conditions (these are given by the equations, III.17a, III.17b, III.17c, III.17e, and III.17f). Hence, the IDE has been decoupled from $\gamma$, and is only a function of the coordinate $\xi$ and the constant $\alpha$. Once this system of IDEs solved, we can come back to Equation III.17g and solve for the scaled length $\gamma$. Moreover, when we define the fluid flow law, the value of the $\alpha$ will be assigned, i.e. for GMS, $\alpha = 1/3$. Thus, by assigning a value for $\alpha$, the problem will only be function of spatial coordinate $\xi$.

We will solve this problem using an orthogonal polynomial series. In order to promote rapid convergence, we construct the polynomial series embedding the near-tip behavior. The near-tip behavior for crack propagation in plane strain conditions in an impermeable rock is obtained from semi-infinite crack propagation with constant velocity. The near-tip solution was prepared according to the procedure used by Adachi (2001b) (see also Desroches et al. (1994), Garagash and Detournay (2000)). Therefore, the solution for crack tip is given as follows.

$$\bar{\Omega}_{tip} = \Xi(1-\xi^2)^{\varphi} \tag{III.18a}$$

$$\bar{\Pi}_{tip} = \chi(1-\xi^2)^{\varphi-1} \tag{III.18b}$$

where

$$\Xi = \left[\left(\frac{2+\alpha}{2}\right)\left(\frac{\alpha+4}{\alpha+6}\right)\sqrt{\frac{2}{\alpha}\tan(\frac{\alpha\pi}{2+\alpha})}\right]^{\frac{2}{2+\alpha}} \tag{III.18c}$$

$$\chi = \frac{cot(\frac{2\pi}{2+\alpha})}{4+2\alpha}\left[\left(\frac{2+\alpha}{2}\right)\left(\frac{\alpha+4}{\alpha+6}\right)\sqrt{\frac{2}{\alpha}\tan(\frac{\alpha\pi}{2+\alpha})}\right]^{\frac{2}{2+\alpha}} \tag{III.18d}$$

$$\varphi = \frac{2}{2+\alpha} \tag{III.18e}$$

The details of this solution are provided in Appendix B.B.

## F. SOLUTION

Inspired by the approach of Adachi (2001b) and Savitski and Detournay (2002), the scaled crack opening $\bar{\Omega}$, scaled fluid net pressure $\bar{\Pi}$, and scaled fluid flow $\bar{\Psi}$ are presented as linear superpositions of general and particular solutions. That is

$$\bar{\Omega} = \bar{\Omega}^{*} + \mathcal{B}\bar{\Omega}^{**} \tag{III.19a}$$

$$\bar{\Pi} = \bar{\Pi}^{*} + \mathcal{B}\bar{\Pi}^{**} \tag{III.19b}$$

$$\bar{\Psi} = \bar{\Psi}^{*} + \mathcal{B}\bar{\Psi}^{**} \tag{III.19c}$$

where $\bar{\Omega}^*$, $\bar{\Pi}^*$, and $\bar{\Psi}^*$ are general solutions that satisfy the field equations including the pressure singularity at the crack tip, and $\bar{\Omega}^{**}$, $\bar{\Pi}^{**}$, and $\bar{\Psi}^{**}$ are particular solutions that satisfy the inlet boundary conditions. We will construct the general solution, and after that we can find the particular solution.

### 1. General Solution

We will start by introducing the polynomial series built with the base function $\widehat{\Omega}^*$ as

$$\bar{\Omega}^* = \sum_{i=0}^{\infty} \mathcal{A}_i \widehat{\Omega}_i \tag{III.20}$$

where $\mathcal{A}_i$ are the unknown coefficients that need to be determined. Since we want to promote the rapid convergence of the series (with only a few terms), the near-tip solution should be embeded in the base function. Following Adachi (2001b), the base functions will then be constructed as $\widehat{\Omega}_i^* = \mathcal{X}(1-\zeta)^{\varphi}\mathfrak{f}_i(\zeta)$, where $\mathcal{X}(1-\zeta)^{\varphi}$ embeds Equation III.18a.

Now the attention turns to finding the proper set of functions, $\mathfrak{f}_i$. A convenient choice is the Ultraspherical polynomials (Gegenbauer) similar to Adachi (2001b), which have the following orthogonality relationship (see Abramowitz and Stegun (1972))

$$\int_{-1}^{1} (1-r^2)^{a-1/2} C_i^{(a)}(r) C_j^{(a)}(r) dr = h_i^{(a)} \delta_{ij} \tag{III.21}$$

where $C_i^{(a)}(r)$ is the $i^{th}$ order Gegenbauer polynomial, expressible as

$$C_i^{(a)}(r) = \frac{\Gamma(a+\frac{1}{2})\Gamma(2a+i)}{\Gamma(2a)\Gamma(a+i+\frac{1}{2})} P_i^{a-\frac{1}{2},a-\frac{1}{2}}(r), \qquad (a \neq 0,\ a > -1/2) \tag{III.22}$$

Here $\Gamma(i)$ is the Gamma function, $P_i^{(m,n)}(r)$ is the Jacobi polynomial (see Abramowitz and Stegun (1972)), and $h_i^{(a)}$ is the norm of $C_i^{(a)}(r)$ given by

$$h_i^{(a)} = \frac{\pi 2^{1-2a}\Gamma(i+2a)}{2!(i+a)\Gamma^2(a)} \tag{III.23}$$

As a result, the base functions are given by (see in Appendix B.E for details)

$$\begin{aligned} \widehat{\Omega}_0 &= (1-\xi^2)^{\varphi} \\ \widehat{\Omega}_j &= (1-\xi^2)^{\varphi+1} C_{2j-2}^{\varphi+\frac{1}{2}}(\xi) \ , \quad j > 0 \end{aligned} \tag{III.24}$$

Note that $\mathcal{A}_0$ is thus given through Equation III.18. Similarly, for the pressure, we can construct the polynomials as

$$\begin{aligned}
\widehat{\Pi}_0 &= \frac{\varphi}{2\pi}\beta(\frac{1}{2},\varphi)\,{}_2F_1\left(\frac{1}{2}-\varphi,1;\frac{1}{2};\xi^2\right)\\
\widehat{\Pi}_1 &= \frac{\varphi(\varphi+1)}{(2\varphi+1)\pi}\beta(\frac{1}{2},\varphi)\,{}_2F_1\left(-\frac{1}{2}-\varphi,1;\frac{1}{2};\xi^2\right)\\
\widehat{\Pi}_j &= \frac{2j-1}{2\pi}\beta(\varphi+j,\frac{1}{2}-j)\left[\xi^2(\varphi+1)\,{}_2F_1\left(\frac{3}{2}-j-\varphi,j;\frac{3}{2};\xi^2\right)\right.\\
&\qquad\left.-\frac{1}{2}\,{}_2F_1\left(\frac{1}{2}-j-\varphi,j-1;\frac{1}{2};\xi^2\right)\right] \quad , \qquad j \geq 2
\end{aligned} \tag{III.25}$$

where ${}_2F_1(a,b;c;d)$ is Gauss' hypergeometric function. As detailed in Appendix B.E, these polynomials are constructed such that the elasticity Equation III.17b is satisfied for any solution with the form

$$\bar{\Omega} = \sum_{i=0}^{\infty}\mathcal{A}_i\widehat{\Omega}_i^* + \mathcal{B}\bar{\Omega}^{**} \quad , \qquad \bar{\Pi} = \sum_{i=0}^{\infty}\mathcal{A}_i\widehat{\Pi}_i^* + \mathcal{B}\bar{\Pi}^{**},$$

that is, with $\mathcal{A}_i$ and $\mathcal{B}$ coefficient, in both series solutions for $\bar{\Omega}$ and $\bar{\Pi}$.

## 2. Particular Solution

We also must find the particular solution that satisfies the inlet boundary conditions. These are given by (for details see Appendix B.C)

$$\bar{\Omega}^{**} = 4\sqrt{1-\xi^2} + 2\xi^2 ln\left|\frac{1-\sqrt{1-\xi^2}}{1+\sqrt{1-\xi^2}}\right| \tag{III.26}$$

$$\bar{\Pi}^{**} = 2 - \pi|\xi| \tag{III.27}$$

### 3. Complete Solution

Upon superposition of the general and particular solution,

$$
\begin{aligned}
\bar{\Omega} &= \mathcal{A}_0 \Xi (1-\xi^2)^{\varphi} + \sum_{j=1}^{\infty} \mathcal{A}_j (1-\xi^2)^{\varphi+1} C_{2j-2}^{(\varphi+\frac{1}{2})}(\xi) \\
&\quad + \mathcal{B}\left[4\sqrt{1-\xi^2} + 2\xi^2 ln\left|\frac{1-\sqrt{1-\xi^2}}{1+\sqrt{1-\xi^2}}\right|\right] \\
\bar{\Pi} &= \mathcal{A}_0 \Xi \frac{\varphi}{2\pi}\beta(\frac{1}{2},\varphi)_2F_1\left(\frac{1}{2}-\varphi,1;\frac{1}{2};\xi^2\right) \\
&\quad + \mathcal{A}_1 \frac{\varphi(\varphi+1)}{(2\varphi+1)\pi}\beta(\frac{1}{2},\varphi)_2F_1\left(-\frac{1}{2}-\varphi,1;\frac{1}{2};\xi^2\right) \\
&\quad + \sum_{j=2}^{\infty} \mathcal{A}_j \frac{(2j-1)}{2\pi}\beta(\varphi+j,\frac{1}{2}-j)\left[\xi^2(\varphi+1)_2F_1\left(\frac{3}{2}-j-\varphi,j;\frac{3}{2};\xi^2\right)\right. \\
&\quad \left. -\frac{1}{2}{}_2F_1\left(\frac{1}{2}-j-\varphi,j-1;\frac{1}{2};\xi^2\right)\right]
\end{aligned}
\tag{III.28}
$$

In the above equations, $\beta$ is the beta function Abramowitz and Stegun (1972). The only unknowns here are the value of the constants $\mathcal{A}_i, \mathcal{B}$ that need to be evaluated, noting again that the coefficients$\mathcal{A}_i$ are the same for both the series for $\bar{\Omega}$ and $\bar{\Pi}$ because Equation III.25 is constructed so as to automatically satisfy elasticity as long as the two series use the same coefficients.

### 4. Calculating Coefficients of the Series

After designating an appropriate orthonormal set of base functions, we can find the value of the coefficients $\mathcal{A}_i$ and $\mathcal{B}$. We will set $\mathcal{Q}$ equally spaced control points on $-1 < \zeta < 1$ – accurate results were possible with $\mathcal{Q} = 20$ control points – and a truncation order whereby the first $n$ terms of the polynomial series are retained. Now, it is possible to construct a residual function in terms of $\mathcal{A}_i$ and $\mathcal{B}$, minimizing that function over the coefficient values. The chosen residual function embodies the sum of the squares of the mismatch between the fluid flow calculated directly from the scaled form of Equation III.2, and by integration of the scaled continuity Equation III.4 at each control point. Its formal expression is given by

$$
\Delta(\mathcal{B},\mathcal{A}_1,\cdots,\mathcal{A}_n) = \sum_{i=1}^{\mathcal{Q}}\left(\frac{\left.\left(-\frac{d\bar{\Pi}}{d\xi}\right)^{\frac{1}{2}}\bar{\Omega}^{\frac{1}{\varphi}+\frac{1}{2}}\right|_{\xi=\xi_i}}{\bar{\Psi}(\xi_i)} - 1\right)^2 \tag{III.29}
$$

where $\bar{\Psi}$ is

$$\bar{\Psi} = \Psi\gamma^{-\frac{6+\alpha}{2+\alpha}}.$$

Thus from the definition of the continuity Equations III.3 and III.4, and using the scaling parameter and the relation that is given above between $\bar{\Psi}$ and $\Psi$ (see Equation III.16) is

$$\bar{\Psi} = \left(-\frac{d\bar{\Pi}}{d\xi}\right)^{\frac{1}{2}} \bar{\Omega}^{\frac{1}{\varphi}+\frac{1}{2}}, \tag{III.30}$$

So, from Equation III.17a

$$\bar{\Psi} = \int_{\xi}^{1} \bar{\Omega} d\zeta + \frac{\alpha+4}{\alpha+6}\xi\bar{\Omega} \tag{III.31}$$

The value of $\int_{\xi}^{1} \bar{\Omega} d\zeta$ for the opening given in Equation III.28 is thus (see Appendix B.D for details)

$$\begin{aligned}
\int_{\xi}^{1} \bar{\Omega} d\eta = {} & \mathcal{A}_0 \Xi \left[\frac{\beta(1+\varphi, \frac{1}{2})}{2} - \xi \;\, {}_2F_1\left(\frac{1}{2}, -\varphi; \frac{3}{2}; \xi^2\right)\right] \\
& + \mathcal{A}_1 \left[\frac{\beta(2+\varphi, \frac{1}{2})}{2} - \xi \;\, {}_2F_1\left(\frac{1}{2}, -1-\varphi; \frac{3}{2}; \xi^2\right)\right] \\
& + \mathcal{A}_2 \left(\frac{1+2\varphi}{4}\right) \left[-2\beta(2+\varphi, \frac{3}{2}) + \frac{2(3+2\varphi)}{(5+2\varphi)}\xi(1-\xi^2)^{2+\varphi}\right. \\
& \qquad \left. + \frac{4}{5+2\varphi}\xi \;\, {}_2F_1\left(\frac{1}{2}, -1-\varphi; \frac{3}{2}; \xi^2\right)\right] \\
& + \frac{(2\varphi+1)(2\varphi+3)}{2}\left(1-\xi^2\right)^{\varphi+2} \sum_{j=3}^{\infty} \frac{\mathcal{A}_j}{(4j+2\varphi-3)} \times \\
& \qquad \left[\frac{C_{2j-3}^{\varphi+\frac{5}{2}}(\xi)}{(j-1)(2j+2\varphi+1)} - \frac{C_{2j-5}^{\varphi+\frac{5}{2}}(\xi)}{(j-2)(2j+2\varphi-1)}\right] \\
& + \frac{2\mathcal{B}}{3}\left[-\xi^3 ln\left|\frac{1-\sqrt{1-\xi^2}}{1+\sqrt{1-\xi^2}}\right| + 2\left[\arccos(\xi) - 2\xi\sqrt{1-\xi^2}\right]\right]
\end{aligned} \tag{III.32}$$

As a result, the scaled flux is

$$
\begin{aligned}
\bar{\Psi} = {} & \mathcal{A}_0 \Xi \left[ \frac{\beta(1+\varphi, \frac{1}{2})}{2} - \xi \;\, {}_2F_1\left(\frac{1}{2}, -\varphi; \frac{3}{2}; \xi^2\right) + \frac{1+\varphi}{1+2\varphi} \xi \left(1-\xi^2\right)^{\varphi} \right] \\
& + \mathcal{A}_1 \left[ \frac{\beta(2+\varphi, \frac{1}{2})}{2} - \xi \;\, {}_2F_1\left(\frac{1}{2}, -1-\varphi; \frac{3}{2}; \xi^2\right) + \frac{1+\varphi}{1+2\varphi} \xi \left(1-\xi^2\right)^{\varphi+1} \right] \\
& + \mathcal{A}_2 \left(\frac{1+2\varphi}{4}\right) \Bigg[ -2\beta(2+\varphi, \frac{3}{2}) + \frac{2(3+2\varphi)}{(5+2\varphi)} \xi (1-\xi^2)^{2+\varphi} \\
& \qquad\qquad + \frac{4\xi}{5+2\varphi} {}_2F_1\left(\frac{1}{2}, -1-\varphi; \frac{3}{2}; \xi^2\right) \\
& \qquad\qquad - \frac{2(1+\varphi)}{1+2\varphi} \xi \left[1-(3+2\varphi)\xi^2\right] \left(1-\xi^2\right)^{1+\varphi} \Bigg] \\
& + \frac{(2\varphi+1)(2\varphi+3)}{2} \left(1-\xi^2\right)^{\varphi+2} \sum_{j=3}^{\infty} \frac{\mathcal{A}_j}{(4j+2\varphi-3)} \times \\
& \qquad \left[ \frac{C_{2j-3}^{\varphi+\frac{5}{2}}(\xi)}{(j-1)(2j+2\varphi+1)} - \frac{C_{2j-5}^{\varphi+\frac{5}{2}}(\xi)}{(j-2)(2j+2\varphi-1)} \right] \\
& + \frac{2\mathcal{B}}{3(1+2\varphi)} \Bigg[ 2(1-\varphi)\xi\sqrt{1-\xi^2} + (2+\varphi)\xi^3 ln \left| \frac{1-\sqrt{1-\xi^2}}{1+\sqrt{1-\xi^2}} \right| \\
& +2(1+2\varphi)\arccos(\xi) \Bigg] + \frac{1+\varphi}{1+2\varphi} \xi (1-\xi^2)^{\varphi+1} \sum_{j=3}^{\infty} \mathcal{A}_j C_{2j}^{(\varphi+\frac{1}{2})}(\xi)
\end{aligned}
\tag{III.33}
$$

Minimizing $\Delta(\mathcal{B}, \mathcal{A}_1, \cdots, \mathcal{A}_n)$ leads to a solution for the value of each unknown variable $\mathcal{A}_i$ and $\mathcal{B}$. These are given, for the various truncation orders, in Table III.1, which shows that even after $n = 0$, the error value (residual function $\Delta$, see Equation III.29) is small and we obtain excellent accuracy with just $n = 1$.

The result for the unknown quantities in table III.1 is valid for the GMS model with any value of material properties. For different values of $\alpha$ and $m$ from these used in the GMS model we can use the constants developed in next section (III.G.1).

And finally, in order to ensure that the solution solves the original problem, we can substitute the results back to Equation III.5 and bring everything into one side, comparing the result to zero. Figure III.2 indicates that the error is very small and hence the solution obtained is accurate.

Table III.1: Numerical coefficient and the cost function with 20 control points for series given in Equation III.33 for $\alpha = 1/3$.

| | **n = 0** | **n = 1** | **n = 2** | **n = 3** | **n = 4** | **n = 5** | **n = 6** |
|---|---|---|---|---|---|---|---|
| $\mathcal{A}_0 \cdot 10^{-1}$ | 8.0713 | 9.0139 | 9.1858 | 9.4415 | 9.4515 | 9.5869 | 9.5439 |
| $\mathcal{A}_1 \cdot 10^{-1}$ | — | $-2.2352$ | $-2.3760$ | $-2.9232$ | $-2.9353$ | $-3.1958$ | $-3.1323$ |
| $\mathcal{A}_2 \cdot 10^{-3}$ | — | — | $-4.3260$ | $-14.2971$ | $-14.7491$ | $-21.5904$ | $-19.3527$ |
| $\mathcal{A}_3 \cdot 10^{-3}$ | — | — | — | $-2.6314$ | $-2.7701$ | $-5.4676$ | $-4.5752$ |
| $\mathcal{A}_4 \cdot 10^{-5}$ | — | — | — | — | $-3.6924$ | $-92.6891$ | $-56.0962$ |
| $\mathcal{A}_5 \cdot 10^{-4}$ | — | — | — | — | — | $-2.2782$ | $-1.0473$ |
| $\mathcal{A}_6 \cdot 10^{-5}$ | — | — | — | — | — | — | $-3.0192$ |
| $\mathcal{B} \cdot 10^{-2}$ | 6.2160 | 9.4108 | 9.6593 | 9.5281 | 9.5176 | 9.6158 | 9.6370 |
| $\Delta$ | $1.09 \cdot 10^{-1}$ | $2.40 \cdot 10^{-3}$ | $1.49 \cdot 10^{-3}$ | $7.98 \cdot 10^{-5}$ | $7.90 \cdot 10^{-5}$ | $1.10 \cdot 10^{-5}$ | $8.73 \cdot 10^{-6}$ |
| $\gamma \cdot 10^{-1}$ | 8.1926 | 8.0910 | 8.0810 | 8.0691 | 8.0687 | 8.0636 | 8.0651 |

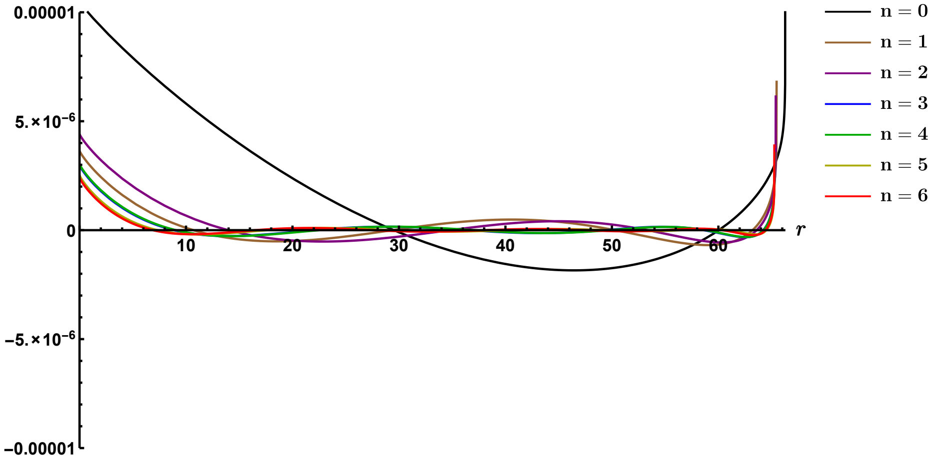

Figure III.2: Substituting back the solution and confirming it solves the problem. The figure is for $t = 100\ sec$ and the rest of the material properties are given in Table III.3 .

## G. RESULTS

### 1. Behavior of the Solution

The truncated solutions for two terms $(n = 1)$ for the dimensionless opening and pressure are given as

$$\begin{aligned}
\bar{\Omega} &= \mathcal{A}_0\Xi(1-\xi^2)^{\varphi} + \mathcal{A}_1(1-\xi^2)^{\varphi+1} + 4\mathcal{B}\sqrt{1-\xi^2} \\
&\quad + 2\mathcal{B}\xi^2 \ln\left|\frac{1-\sqrt{1-\xi^2}}{1+\sqrt{1-\xi^2}}\right|, \\
\bar{\Pi} &= \mathcal{A}_0\Xi\frac{\varphi}{2\pi}\beta\left(\frac{1}{2},\varphi\right)\ {}_2F_1\left(\frac{1}{2}-\varphi,1;\frac{1}{2};\xi^2\right) \\
&\quad + \mathcal{A}_1\frac{\varphi(\varphi+1)}{(2\varphi+1)\pi}\beta\left(\frac{1}{2},\varphi\right)\ {}_2F_1\left(-\frac{1}{2}-\varphi,1;\frac{1}{2};\xi^2\right) + \mathcal{B}(2-\pi\left|\xi\right|). \\
\varphi &= \frac{2}{2+\alpha}
\end{aligned} \tag{III.34}$$

Equation III.34 thus shows the general form of the dimensionless opening and pressure for different values of $\alpha$. The corresponding values for $\mathcal{A}_0$, $\mathcal{A}_1$, and $\mathcal{B}$ for different values of $\alpha$ are obtained by the solution method and presented in Figure III.5.

One important observation from Equation III.28 is that the dimensionless opening and pressure are dependent on the exponent $\varphi$, which in turn depends on $\alpha$ from the Darcy-Weisbach friction factor. We wish first to explore if this exponent has a substantial impact on the scaled solution, or if its main influence is accounted for by the scaling factors (Equation III.15). Figure III.3 shows the change of the dimensionless opening $\bar{\Omega}$, and pressure $\bar{\Pi}$ versus scaled coordinate $\xi$ by changing the variable $\alpha$. It is clear from these results the sensitivity of the dimensionless opening, $\bar{\Omega}$, and pressure $\bar{\Pi}$, to $\alpha$ is sufficient only to generate variation of about 30% over the entire possible range of $\alpha$. While this is not necessarily "small", it does demonstrate that the main variation is still captured via the scaling (Equation III.15).

Next we will examine the convergence of the solution in terms of number of terms $(n)$ retained in the series solution. To find the values for the constants for this comparison, we used the values $\alpha = 1/3$ and $m = 0.143$, corresponding to the parameters of the GMS. The coefficients are given in Table III.1 for up to six terms of the Gegenbauer Polynomial series. Figure III.4 indicates that

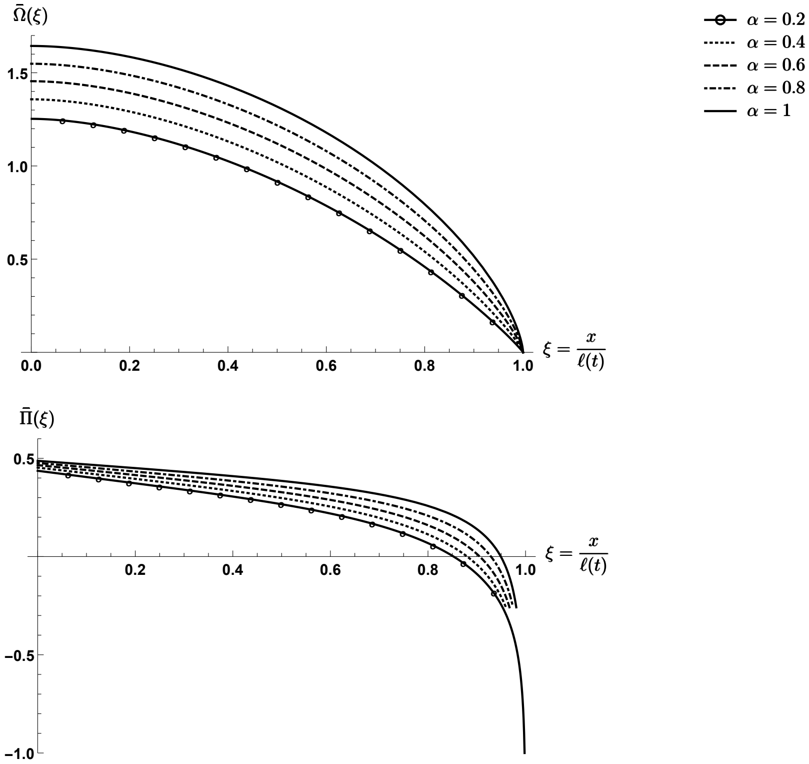

Figure III.3: Variation of scaled opening with change of dimensionless length $\xi$ for different value of $\alpha$.

Table III.2: Relative values of the solution for increasing numbers of terms in the series.

| | **i = 1** | **i = 2** | **i = 3** | **i = 4** | **i = 5** | **i = 6** |
|---|---|---|---|---|---|---|
| $\frac{\gamma\big\|_{n=i-1}}{\gamma\big\|_{n=i}}$ | 1.01256 | 1.00123 | 1.00148 | 1.00005 | 1.00063 | 0.999813 |
| $\frac{\overline{\mathbf{\Omega}}(0)\big\|_{n=i-1}}{\overline{\mathbf{\Omega}}(0)\big\|_{n=i}}$ | 0.979822 | 0.9977 | 0.997308 | 0.999907 | 0.998812 | 1.00035 |
| $\frac{\overline{\mathbf{\Pi}}(0)\big\|_{n=i-1}}{\overline{\mathbf{\Pi}}(0)\big\|_{n=i}}$ | 0.980313 | 0.999533 | 0.997991 | 0.999974 | 0.999286 | 1.00013 |
| $\frac{\overline{\mathbf{\Psi}}(0.5)\big\|_{n=i-1}}{\overline{\mathbf{\Psi}}(0.5)\big\|_{n=i}}$ | 0.955812 | 0.996164 | 0.99522 | 0.999839 | 0.997991 | 1.0006 |

essentially after $n = 1$ the solution is unchanged by inclusion of more terms. It is also possible to see this rapid convergence of the series by comparing the value of scaled length, fluid flux at middle of the crack, as well as the opening and pressure at the borehole for different values of $n$. In doing so, it is clear that the $n = 1$ solution represents about a $2\%$ change in the predicted length, width, and pressure compared with the $n = 0$ solution. Additional terms ($n \geq 2$) impact the solution by only a fraction of a percent (see Table III.2). This proves the very rapid convergence of the polynomial series due to embedding the tip asymptotic solution in the base functions. Note that special care should be taken about how the pressure solution compares with the tip asymptotic solution. From the opening shown in Figure III.4 we can see that at the crack tip the asymptotic solution and the polynomial series are starting from one point with same shape. As we go further, the asymptotic solution deviates from the polynomial solution, as expected. However, for the pressure in Figure III.4, we do not see the same trend. The reason is because at the crack tip the pressure is going to infinity, which indicates the singularity of the fluid pressure at the crack tip. We can see that the behavior of the pressure at crack tip and the asymptotic are both going to infinity with the same trend. The difference is a constant shift that accurs because we needed to satisfy the inlet condition. This shifting parameter can be found in Appendix B.E (Equation B.76).

### 2. Dimensional Expressions

Solutions for $w$, $p$, and $\ell$ are obtained by inverting the scaling procedure explained in the previous sections. The crack width $(w)$ considering two terms of the series as $(n = 1)$ is

$$\begin{aligned} w(x,t) = {} & \left(\frac{Q_0^2}{\beta' E'^{1/2}}\right)^{\frac{2}{\alpha+6}} \left[\mathcal{A}_0 \Xi \beta\left(\frac{1}{2}, \frac{4+\alpha}{2+\alpha}\right) + \mathcal{A}_1 \beta\left(\frac{1}{2}, \frac{6+2\alpha}{2+\alpha}\right)\right. \\ & \left. + \frac{4\pi\mathcal{B}}{3}\right]^{\frac{-4}{6+\alpha}} \left[\mathcal{A}_0 \Xi \left(1-\xi^2\right)^{\frac{2}{2+\alpha}} + \mathcal{A}_1 \left(1-\xi^2\right)^{\frac{4+\alpha}{2+\alpha}} + 4\mathcal{B}\sqrt{1-\xi^2}\right. \\ & \left. + 2\mathcal{B}\xi^2 \ln\left|\frac{1-\sqrt{1-\xi^2}}{1+\sqrt{1-\xi^2}}\right|\right] t^{\frac{2}{\alpha+6}} \end{aligned} \tag{III.35}$$

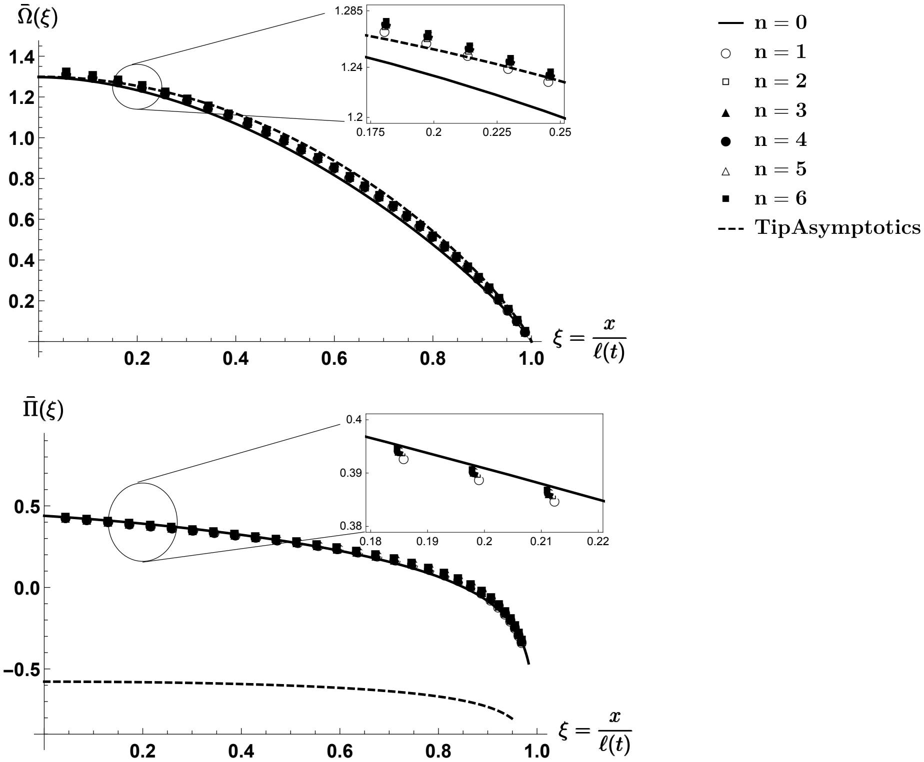

Figure III.4: Scaled opening along the hydraulic fracturing. Noting that using just one term is a very good approximation and $n \geq 2$ gives solutions that are indistinguishable. Dashed line correspond to tip asymptotic solution. Refer to Table III.1 for the values of error function (Equation III.29) that associate with different $n$

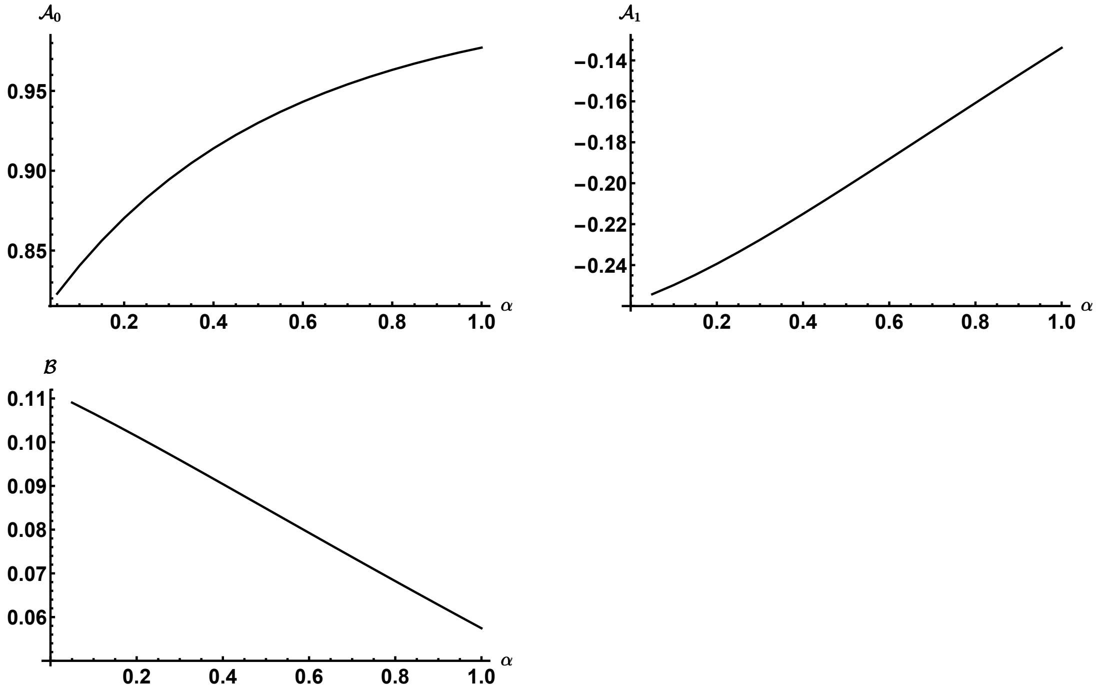

Figure III.5: Constants $\mathcal{A}_i$ and $\mathcal{B}$ in Equation III.34 for different values of $\alpha$.

where from Table III.1, $\mathcal{A}_0 = 0.90139$, $\mathcal{A}_1 = -0.22352$, and $\mathcal{B} = 0.094108$. Similarly, the two term $(n = 1)$ solution for the pressure is given by

$$\begin{aligned} p(x,t) = {} & \frac{\beta\left(\frac{1}{2},\frac{2}{2+\alpha}\right)}{(2+\alpha)\pi} E' \left(E'\beta'^2 Q_0^{\frac{\alpha-2}{2}}\right)^{\frac{-2}{\alpha+6}} \left[\mathcal{A}_0 \Xi \beta\left(\frac{1}{2},\frac{4+\alpha}{2+\alpha}\right) + \frac{4\pi\mathcal{B}}{3}\right. \\ & \left. + \mathcal{A}_1 \beta\left(\frac{1}{2},\frac{6+2\alpha}{2+\alpha}\right)\right]^{-\frac{2-\alpha}{6+\alpha}} \left[\mathcal{A}_0 \Xi \ {}_2F_1\left(\frac{\alpha-2}{2(2+\alpha)},1;\frac{1}{2};\xi^2\right)\right. \\ & \left. + 2\mathcal{A}_1 \left(\frac{4+\alpha}{6+\alpha}\right) \ {}_2F_1\left(-\frac{\alpha+6}{2(2+\alpha)},1;\frac{1}{2};\xi^2\right) + \frac{\mathcal{B}(2+\alpha)\pi}{\beta\left(\frac{1}{2},\frac{2}{2+\alpha}\right)}(2-\pi|\xi|)\right] t^{-\frac{\alpha+2}{\alpha+6}} \end{aligned} \tag{III.36}$$

Finally, evolution of the crack length is found firstly by recalling Equation (III.17g), then using Equation III.32 we arrive to

$$\gamma = \left[\mathcal{A}_0 \Xi \beta\left(\frac{1}{2}, 1+\varphi\right) + \mathcal{A}_1 \beta\left(\frac{1}{2}, 2+\varphi\right) - \mathcal{A}_2 (2\varphi+1) \beta\left(\frac{3}{2}, 2+\varphi\right) + \frac{4\pi\mathcal{B}}{3}\right]^{-\frac{\alpha+2}{\alpha+6}}.$$

Therefore, by combining Equations III.15 and III.9 with the scaled length

$$
\begin{aligned}
&\ell = \left(\beta' E'^{1/2} Q_0^{(\alpha+2)/2}\right)^{\frac{2}{\alpha+6}} t^{\frac{\alpha+4}{\alpha+6}} \times \\
&\left[\mathcal{A}_0 \Xi \beta\left(\frac{1}{2}, 1+\varphi\right) + \mathcal{A}_1 \beta\left(\frac{1}{2}, 2+\varphi\right) - \mathcal{A}_2(2\varphi+1)\beta(\frac{3}{2}, 2+\varphi) + \frac{4\pi\mathcal{B}}{3}\right]^{-\frac{\alpha+2}{\alpha+6}}
\end{aligned}
\tag{III.37}
$$

The crack length thus evolves with time with power of $(\varphi+1)/(2\varphi+1)$. For illustration, if we consider values $\alpha = 1/3$ and $m = 0.143$ for the Darcy-Weisbach friction factor Tsai and Rice (2010), from Equation III.18 the value of $\varphi$ will be $6/7$. Therefore, the value of the power in Equation III.37 for turbulent flow is $13/19$ ($\approx 0.68$).

Now we can go back the same path that we took to derive the equations and solve for different parameters. The truncated solution in dimensional variables for the specific case of GMS with $\alpha = 1/3$ can be obtained from similarity scaling, Equation III.34, which gives

$$
\begin{aligned}
w(x,t) =& 0.6955\left(\frac{Q_0^2}{\beta'\sqrt{E'}}\right)^{\frac{6}{19}} t^{\frac{6}{19}} \left[1.1709\left(1-\frac{x^2}{\ell^2}\right)^{\frac{6}{7}} + 0.3764\sqrt{1-\frac{x^2}{\ell^2}}\right. \\
&\left. -0.2235\left(1-\frac{x^2}{\ell^2}\right)^{\frac{13}{7}} + 0.1882\frac{x^2}{\ell^2}\ln\left|\frac{1-\sqrt{1-\left(\frac{x}{\ell}\right)^2}}{1+\sqrt{1-\left(\frac{x}{\ell}\right)^2}}\right|\right] \\
\ell(t) =& 0.8091\left(\beta'\sqrt{E'}Q_0^{\frac{7}{6}}\right)^{\frac{6}{19}} t^{\frac{13}{19}}, \\
p(x,t) =& 0.2581E'\left(E'\beta'^2 Q_0^{\frac{\alpha-2}{2}}\right)^{\frac{-6}{19}} \left[1.1709\ {}_2F_1\left(\frac{-5}{14}, 1; \frac{1}{2}; \frac{x^2}{\ell^2}\right)\right. \\
&\left. -0.3059\ {}_2F_1\left(-\frac{19}{14}, 1; \frac{1}{2}; \frac{x^2}{\ell^2}\right) + 0.31342\left(2-\pi\left|\frac{x}{\ell}\right|\right)\right] t^{-\frac{7}{19}} \\
q(x,t) =& \frac{Q_0}{2} + 1.036\ Q_0\left(\frac{x}{\ell}\right)\left[0.8011\ \left(1-\frac{x^2}{\ell^2}\right)^{\frac{6}{7}} - 0.1529\ \left(1-\frac{x^2}{\ell^2}\right)^{\frac{13}{7}}\right. \\
& -1.1709\ {}_2F_1\left(\frac{1}{2}, -\frac{6}{7}; \frac{3}{2}; \frac{x^2}{\ell^2}\right) + 0.2235\ {}_2F_1\left(\frac{1}{2}, -\frac{13}{7}; \frac{3}{2}; \frac{x^2}{\ell^2}\right) \\
& +0.0066\sqrt{1-\frac{x^2}{\ell^2}} - 0.1255\ \frac{\ell}{x} sin^{-1}\left(\frac{x}{\ell}\right) \\
& \left. +0.066\left(\frac{x}{\ell}\right)^2 \ln\left|\frac{1-\sqrt{1-\left(\frac{x}{\ell}\right)^2}}{1+\sqrt{1-\left(\frac{x}{\ell}\right)^2}}\right|\right].
\end{aligned}
\tag{III.38}
$$

Table III.3: Material properties and physical constants for illustration, corresponding to supercritical $CO_2$ as the fracturing fluid and Barnett Shale as the rock.

| **Parameter** | **Value** |
|---|---|
| $Q_0$ | 0.001 $\mathrm{m}^2\ \mathrm{s}^{-1}$ |
| $\nu$ | 0.2 |
| $\mu$ | $5 \times 10^{-5}$ Pa·s |
| $\rho$ | 600 kg $\mathrm{m}^{-3}$ |
| $k$ | 0.1 mm |
| $m$ | 0.143 |
| $E$ | 25 GPa |
| $\alpha$ | $1/3$ |

### 3. Comparison Between Turbulent and Laminar Solution

Here we compare the solution for turbulent flow to the laminar flow solution Adachi (2001b) (see also Appendix B.A). For comparison we use parameters intended to be relevant to field-scale treatments (Table III.3, which correspond to a characteristic Reynolds number of 12000). It is also important to note that the compressibility of gas has more effect on the crack propagation at early stage. However, for intermediate/long time, the compressibility has negligible impact on the solution (see Lecampion et al. (2017)).

The first comparison between laminar and turbulent flow is for the normalized opening. Figure III.6 illustrates the difference between normalized opening along the crack is relatively subtle; the scaled turbulent crack width is just slightly narrower. However, this similarity is due to the normalization. The greater difference is for the opening, pressure, and fluid flow along the crack for specified time (in this case $t = 1000\ sec$). As we can see in Figure III.7 , there is a more substantial difference between the solutions in their dimensional forms, around 10% - 30% for this example.

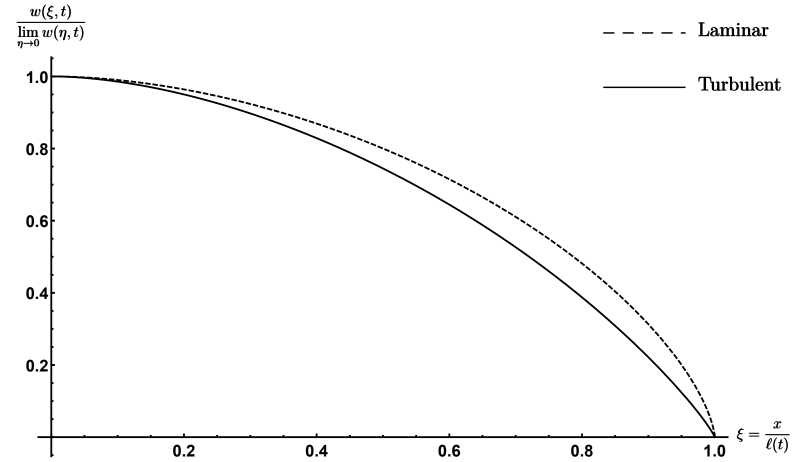

Figure III.6: Scaled opening profiles.

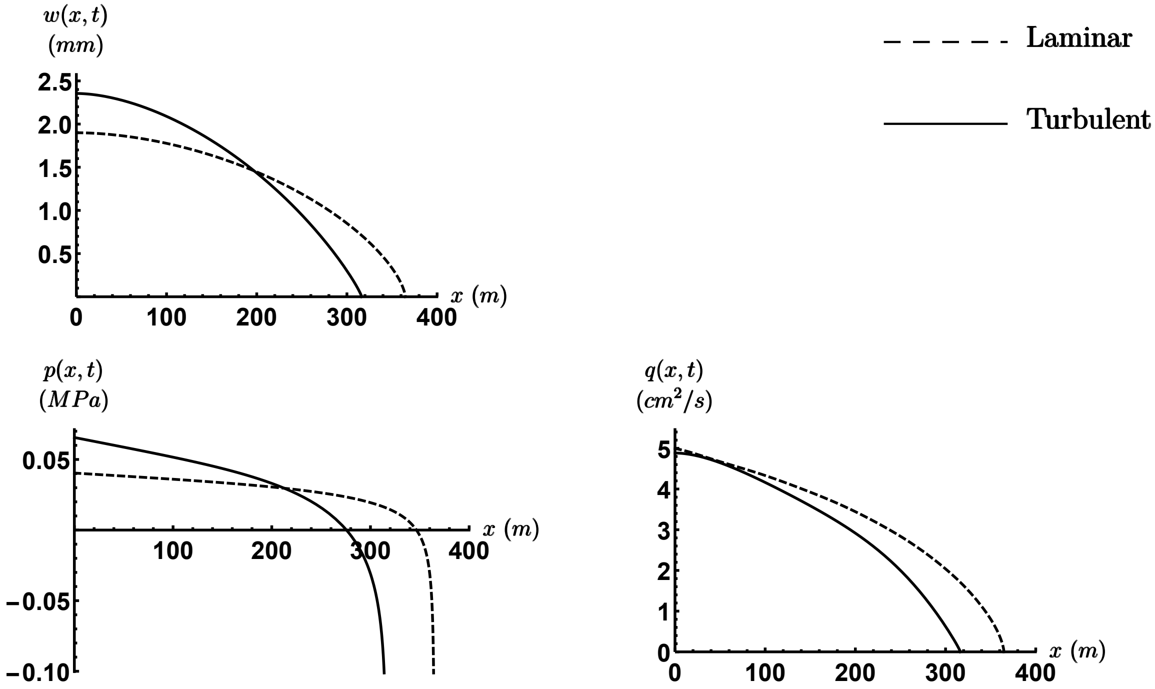

Figure III.7: Opening, pressure, and fluid flow changes along the crack for two cases of laminar flow and turbulent flow at $t = 1000\ sec$ and characteristic Reynolds number of 12000.

The last comparison is the evolution of crack opening, pressure and length, shown in Figure III.8. This comparison shows again a difference of $10\%$ - $30\%$ . For example, at $t = 600\ sec$ the crack opening for the laminar solution is $25\%$ greater than the turbulent regime solution.

To generalize these observations, consider the ratios of the turbulent solution compared to the laminar solution (Equations III.38 and B.1). The ratios of $w_{turb}/w_{lam}$, $\ell_{turb}/\ell_{lam}$, and $p_{turb}/p_{lam}$ are thus given by

$$\begin{aligned}
\frac{w_{turb}(0,t)}{w_{lam}(0,t)} &= 0.4832\left(\frac{t^*}{t}\right)^{\frac{1}{57}} \\
\frac{\ell_{turb}(t)}{\ell_{lam}(t)} &= 2.2253\left(\frac{t}{t^*}\right)^{\frac{1}{57}} \\
\frac{p_{turb}(0,t)}{p_{lam}(0,t)} &= 0.2467\left(\frac{t^*}{t}\right)^{\frac{2}{57}} \\
t^* = \frac{Q_0^{\frac{15}{2}}\rho^9 k^3 E'^{\frac{1}{2}}}{\mu'^{\frac{19}{2}}} &= Re^{19/2}\times\left(\frac{k^3E'^{1/2}}{12^{19/2}Q_0^2\rho^{1/2}}\right)
\end{aligned} \tag{III.39}$$

where $Re$ is the characteristic Reynolds number. If we consider the cases that are physically feasible (check Table III.4), the extended range of the parameters for the different fracturing fluids is shown in Table III.5. These ratios indicate several properties of the turbulent and laminar solutions. Firstly, their ratio is determined not only by the Reynold's number, but also by the roughness scale, $k$, which enters via the GMS equation (Equation III.3). Secondly, the power of time is very small; $-1/57$, $1/57$, and $-2/57$ for the ratio of width, length, and pressure, respectively. This means that the ratios will be relatively constant with time. Finally, the range of these ratios is determined by the range of $t^*$. In its extreme value for cross-linked gel – a fully laminar case (Table III.4), $t^* = 2.95 \times 10^{-18}$ and the ratios evolve, with very weak dependence upon time, as shown in Figure III.9. This comparison essentially shows that inappropriate choice of the turbulent solution for a case which is actually laminar can result in underestimation of the width by a factor of 10, underestimation of the wellbore pressure by a factor of nearly 70, and overestimation of the length by a factor of 9. However, in the other extreme, corresponding to supercritical $CO_2$, $t^* = 1.04 \times 10^{38}$. In this extreme, the ratios shown in Figure III.9 indicate inappropriate use of the laminar solution instead of the turbulent solution will result in underestimation of the width by a factor of about 3.6, underestimation of the wellbore pressure by a factor of nearly 14, and overestimation of the length by a factor of about 3.

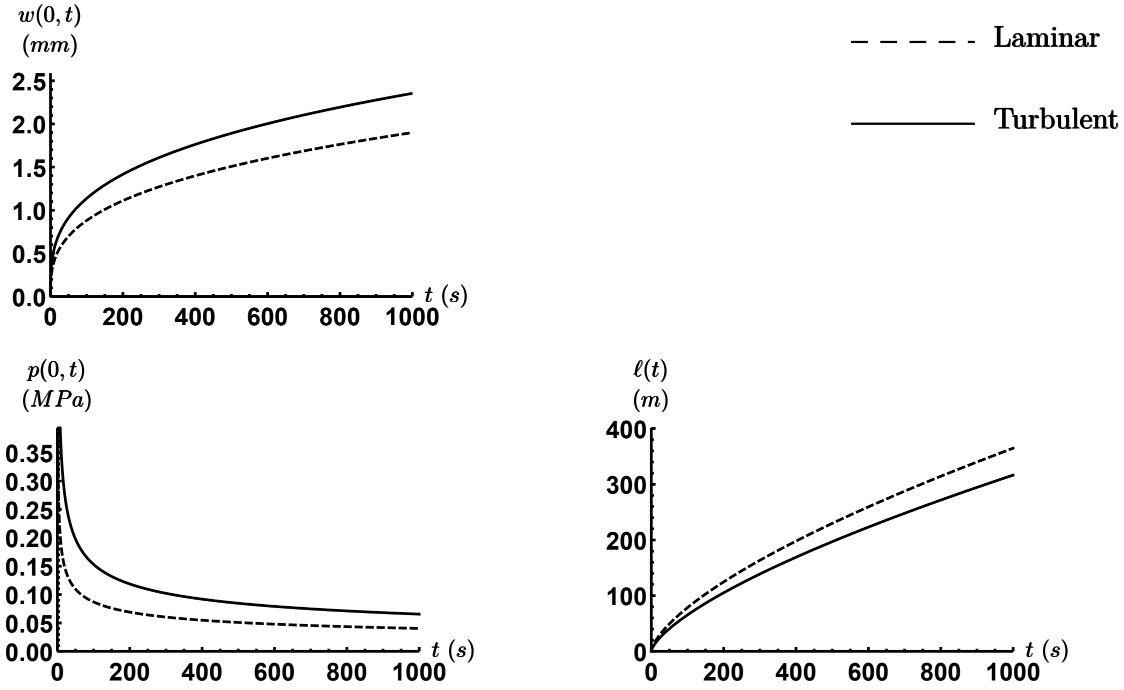

Figure III.8: Opening, pressure, and length of the crack changes by changing the time. For opening and pressure are the opening and pressure at wellbore when $x = 0$ and characteristic Reynolds number of 12000

Table III.4: Range of parameters used in Equation III.39. The maximum value for fluid flow is overestimated from real field data to capture wider range of parameters.

| Parameter | Minimum | Maximum |
|---|---|---|
| $Q_0$ | $2.5 \times 10^{-4}\ m^2/s$ | $0.01\ m^2/s$ |
| $k$ | 0.01 mm | 2 mm |
| $\nu$ | 0.15 | 0.35 |
| $E$ | 5 GPa | 100 GPa |

Table III.5: Different fracturing fluids and their physical properties.

| Fluid | Density | Viscosity | Kinematic Viscosity | Reynolds ($Re^*$) | |
|---|---|---|---|---|---|
| | $\rho$ (kg m$^{-3}$) | $\mu$ (Pa·s) | $\frac{\mu}{\rho}$ (m$^2$ s$^{-1}$) | Min | Max |
| CO$_2$ (Supercritical CO$_2$) | $600$ | $5 \times 10^{-5}$ | $8.34 \times 10^{-8}$ | 2997.6 | 119904 |
| Slick-water | $1000$ | $0.003$ | $3 \times 10^{-6}$ | 83.34 | 3333.34 |
| Linear Gel | $1000$ | $0.05$ | $5 \times 10^{-5}$ | 5 | 200 |
| X-linked Gel | $1000$ | $0.5$ | $5 \times 10^{-4}$ | 0.5 | 20 |

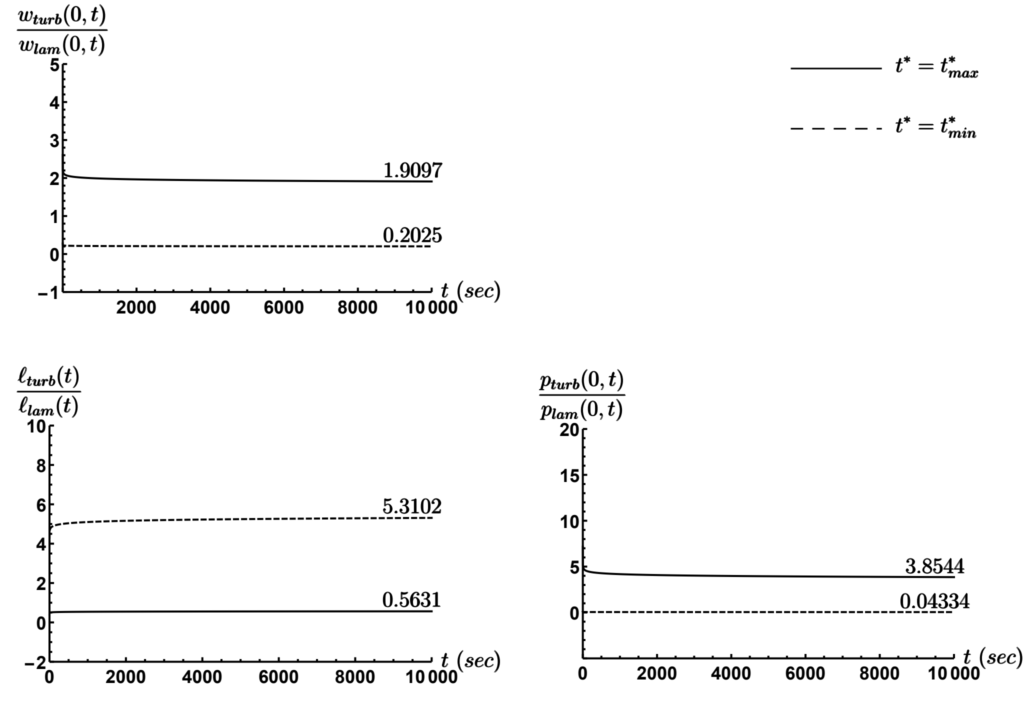

Figure III.9: The ratio of opening, pressure, and length of the crack for the at inlet by changing the time for turbulent over laminar. In each plot, we compare the value if, $t^*$ is minimum or maximum.

## 4. Laminar-to-Turbulent Transition of the Solution

The main conclusion from the previous section is that selection of the appropriate solution, laminar or turbulent, is critically important. It is also clear that arguably the most practically-relevant cases for water/slickwater are near the transition between laminar and turbulent regimes. Hence, it is important to clarify the Reynolds number at which the transition occurs and the error associated with both the laminar and turbulent solutions when the regime is actually in transition. To address this issue, we present comparison with a numerical solution for a plane strain hydraulic fracture. The numerical scheme is similar to that used in Dontsov Dontsov (2017), but utilizes a friction factor that captures the effect of turbulent flow. Two versions of the friction factor are used: Churchill's friction factor Churchill (1977) and "virtual Nikuradse" Yang and Joseph (2009), where the latter is an approximation fitted to Nikuradse's pipe data Nikuradse (1954). Both friction factors are originally derived for circular pipes. In order to adapt them to hydraulic fractures, the concept of hydraulic diameter is used within the fully turbulent zone and the value of the friction factor in the laminar zone is adjusted to precisely capture the laminar solution between two parallel plates; see e.g. Dontsov (2016) for such a modification for Churchill's friction factor.

Figure III.10 shows the variation of the Churchill's friction factor, virtual Nikuradse approximation, Gauckler-Manning-Strickler (GMS) friction factor [III.3], and Nikuradse's pipe data Nikuradse (1954) versus Reynolds number for different values of roughness. Firstly, one can observe that the GMS friction factor coincides with the predictions of the Churchill's formula and virtual Nikuradse only for large values of Reynolds number and for rough fractures. In addition, there is a noticeable discrepancy between the virtual Nikuradse and the Churchill's equation. This is due to the fact that Churchill developed an approximation to the Moody diagram Moody (1944), while "virtual Nikuradse" is an approximation that is fitted to the Nikuradse's data Nikuradse (1954). The Moody diagram is constructed based on the experiments in naturally rough pipes (see e.g. a recent study Wang et al. (2014) where the observed friction factor is accurately captured by the results from Moody diagram), while Nikuradse used pipes with artificially fabricated roughness. As a result, the observed difference may be related to the details of the roughness profile. Indeed, structured roughness may preclude early development of turbulence since the latter is a chaotic phenomenon that requires an instability trigger. Regarding hydraulic fractures in rocks, it is not

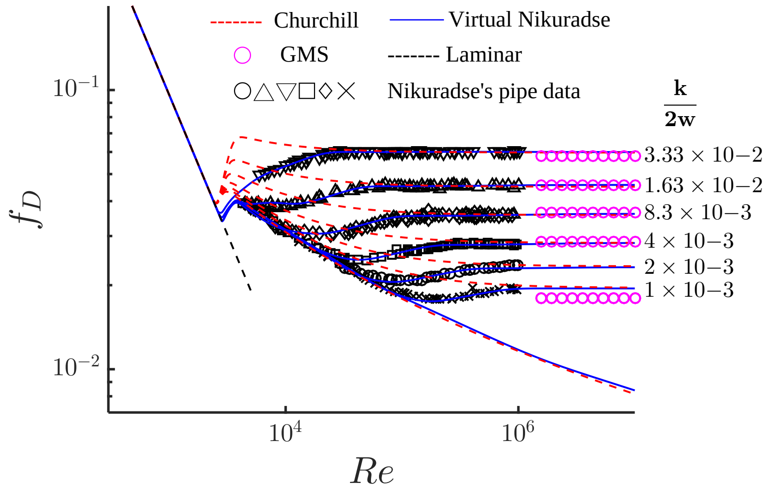

Figure III.10: Variation of the friction factor versus Reynolds number; including Nikuradse's pipe data Nikuradse (1954), the Gauckler-Manning-Strickler (GMS) friction factor (Equation III.3), and approximations of Churchill Churchill (1977) and Yang and Joseph's virtual Nikuradse approximation Yang and Joseph (2009).

exactly clear whether the friction factors measured for circular pipes can be directly applied, especially if there is a manufactured distribution of roughness.

It should also be noted that both friction factors are fitted for the relative roughness not exceeding a few percent. As a result, care must be taken when using them for very rough fractures, for which extrapolation of the results is necessary. Note, for example, that the virtual Nikuradse formula for relative roughness of 0.06, predicts the laminar to turbulent transition at $Re \approx 10^4$, which is clearly an unphysical behavior. The Churchill's friction factor, on the other hand, provides a visually more realistic estimate. To ensure that the friction factors are not used beyond their applicability regions, the relative roughness is bounded by 0.033 for the virtual Nikuradse and by 0.1 for Churchill. Results for both Churchill and virtual Nikuradse friction factors are presented for completeness.

Figure III.11 presents the fracture length, wellbore width, and wellbore pressure versus Re number that is calculated using the numerical solution with Churchill's friction factor, the laminar approximation (Equation B.1), and the developed turbulent solution. All the results are normalized

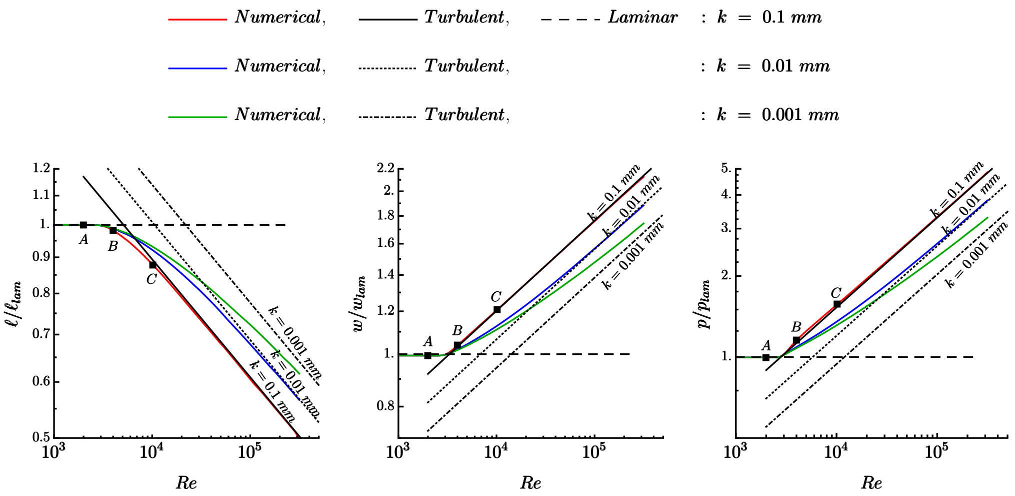

Figure III.11: Variation of the fracture length (left), wellbore width (middle), and wellbore pressure (right) versus Reynolds number. Points A, B, and C are referenced by Figure III.13.

by the laminar solution, and the numerical solution is calculated using the parameters summarized in Table III.3. The results are compared at $t = 1000\ s$. The fluid viscosity was adjusted in order to achieve the desired variation in Reynolds number. The numerical simulations show a transition of the solution from the laminar asymptote to the turbulent asymptote. For this sample the transition occurs at $Re \approx 2000$ for the width and pressure, while the transition $Re$ value is slightly higher for the fracture length $(Re \approx 5000)$. It should be noted here that these results depend on roughness. Figure III.12 shows similar results, but the numerical solution is calculated using virtual Nikuradse friction factor.

From the data in Figure III.11, it is apparent that as the roughness increases, the solution remains close to the laminar and turbulent assymptotics. In hydraulic fracturing, since the roughness of the rock is usually on the order of at least $0.1\ mm$, it is often reasonable to assume that the transition region is small and propagation can be approximated with the turbulent asymptotic solution for Reynolds number of around $2000 \sim 3000$. This shows that for rougher fractures the error associated with approximating the transition regime using either the laminar or turbulent solutions is smaller than for smoother fractures. This observation is consistent with the Moody diagram, (Figure III.10) which shows that for decreasing roughness of the rock, the fully rough turbulent region

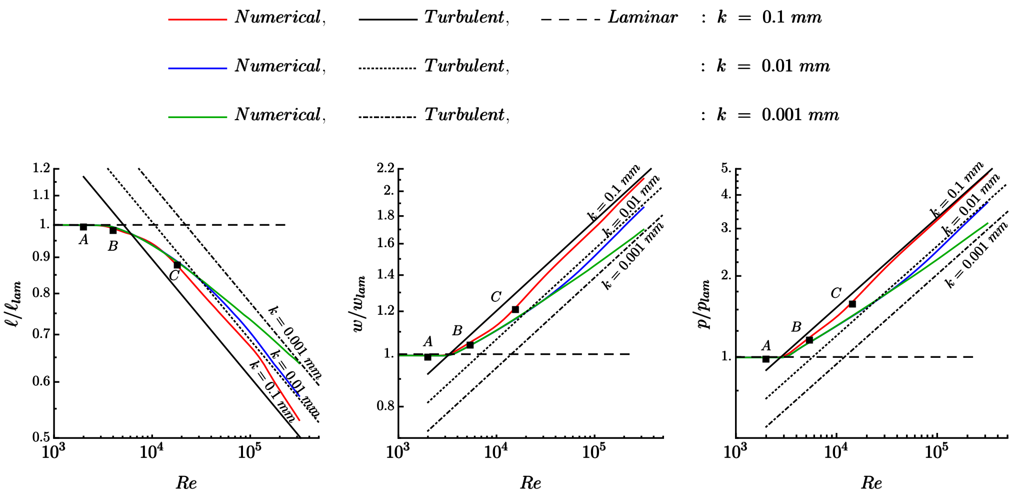

Figure III.12: Variation of the fracture length (left), wellbore width (middle), and wellbore pressure (right) versus Reynolds number that are generated based on virtual Nikuradse approximation Yang and Joseph (2009).

happens at higher Reynolds number and the transition region is larger. Results in Figures III.11 and III.12 demonstrate that the choice of the friction factor may influence the result, in its details especially for rough fractures, while the results for less rough fractures are essentially unchanged. In all cases the qualitative behavior is unchanged by the choice of friction factor, the fully turbulent solution is thus able to define the location of the transition region and to capture the global trend of the solution even for both Churchill and virtual Nikuradse friction factors. Note, however, that the relative roughness is bounded in the numerical solution due to the limits of the original pipe flow experiments, and so, the value of the friction factor may be underestimated for the large roughness cases. This effectively reduces the fluid friction in the numerical solution, which in turn makes the fracture longer in the numerical solution and contributes to a discrepancy with the limiting solution.

To further examine the applicability of turbulent solution, Figure III.13 compares the fracture widths and pressures for $Re = \{2000; 4000; 10000\}$ when $k = 0.1\ mm$; the latter points are indicated by the points A, B, and C in Figure III.11. These three points correspond to the laminar, transition, and turbulent regimes respectively. Figure III.13 shows that, as expected, the numerical solution coincides with the laminar solution for the first case, does not coincide with either laminar or turbulent solutions for the second case, and coincides with the turbulent solution for the third case.

It is also interesting to observe the transition from laminar to turbulent fluid flow within the fracture in Figure III.13, which is characterized by a noticeable change in the pressure behavior. In particular, for the $Re = 10^4$ case, such a transition occurs near the tip and effectively does not affect the global solution, where the latter coincides with the fully turbulent solution. On the other hand, the laminar-to-turbulent transition occurs in the middle of the fracture for the $Re = 4000$ case. Here pressure solution follows the turbulent solution from the wellbore to the middle of the fracture and then abruptly switches to the laminar solution from the middle of the fracture to the tip. Consequently, the "zones" of the laminar and turbulent solutions are comparable and therefore neither of the limiting solutions apply.

Taken together, this comparison between the asymptotic and numerical solutions leads to a striking conclusion that the error associated with the asymptotic solutions can be relatively small even when the regime is, in transition, especially when there is large roughness. Hence, for practical purposes, it will very often suffice to compute both the laminar and turbulent solutions, and then choose the approximation that corresponds to the larger width, larger pressure, and shorter length.

## H. CONCLUSIONS

The use of low viscosity fracturing fluids at high flow rates has become increasingly important in HF applications over the past two decades. This trend drives an increasing tendency for the relevant flow regime to be turbulent. The goal of this study is to implement the general form of the Gaukler-Manning-Strickler (GMS) friction factor into a plane strain HF benchmark solution. A semi-analytical solution is thus derived, embedding the relevant near-tip HF behavior into a Gegenbauer polynomials used to construct the series solution. This approach leads to rapid convergence, with accurate results using just two terms of the polynomial series.

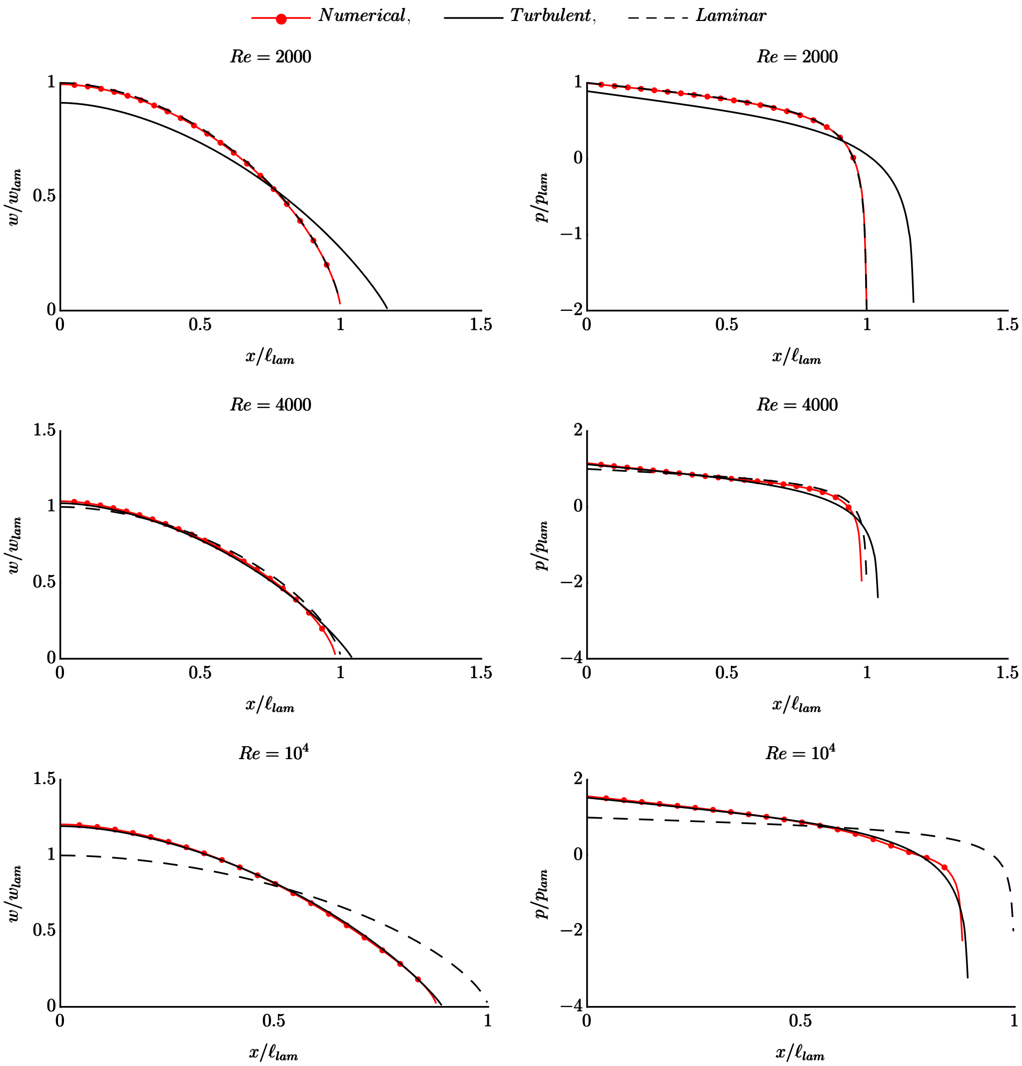

Figure III.13: Spatial variation of the fracture width (left) and the fluid pressure (right) for three different values of $Re = \{2000; 4000; 10000\}$ (from top to bottom) and $k = 0.1\ mm$. These correspond to points A, B, and C in figure III.11. The red solid lines show the numerical solution (with Churchill's friction factor), the dashed black lines show the laminar solutions, and the solid black lines indicate the turbulent solutions.

The main use of this solution is as a benchmark, necessary as simulators are increasingly developed to hand non-laminar flow in more complicated geometries. The present solution enables the important task of benchmarking the limit where flow is fully rough-walled turbulent, the geometry is a straight plane strain crack, and the rock is impermeable. Of course this benchmark, like any simulator that relies upon the GMS equation, bears the limitation that experimental data is not yet available relevant to the geometry of a narrow, rough, flexible walled, closed channel as encounted in an HF.

While the limitations of regime and uncertainties with regards to the fluid friction factor are important caveats, comparison with numerical solutions considering the full laminar to turbulent transition reveal a somewhat surprising utility of the asymptotic solutions. Namely, the transition between the range of Reynolds number where the solution is well-approximated by the laminar solution to the range of Reynolds number where the solution is well-approximated by the turbulent solution is so abrupt that for most plane-strain (2D) cases, estimation of the length, width, and pressure can be obtained within a few percent by simply computing both the laminar and turbulent solutions and selecting the solution that corresponds to the largest wellbore pressure, largest opening, and shorted hydraulic fracture length.

# IV. SEMI-ANALYTICAL SOLUTION FOR A PENNY-SHAPED ROUGH-WALLED HYDRAULIC FRACTURE DRIVEN BY TURBULENT FLUID IN AN IMPERMEABLE ROCK

## A. PREAMBLE

The content of this chapter comprises a preprint of Zolfaghari and Bunger (Submitted A). It shows the asymptotic semi-analytical solution for radial geometry with rough-walled fully turbulent fluid regime HF. The solution is developed using Jacobi orthogonal polynomial series and the result is contrasted with the solution for laminar HF (Savitski and Detournay, 2002). The tip asymptotic solution is developed and a proper inlet solution that satisfies the boundary conditions is suggested as a part of the solution. The solution is compared with the numerical model that has been developed in Chapter V. The results from numerical simulation and semi-analytical solutions indicates a good agreement for larger Reynolds number, and the numerical simulations provide practical bounds on the range over which the asymptotic solution is sufficiently accurate.

## B. ABSTRACT

The popularity of high injection rate hydraulic fracturing treatments using low viscosity fluids is driving a need to consider the turbulent and laminar-turbulent transition regimes of fluid flow in hydraulic fracture simulators. The radial model is one of the most important geometries both for benchmarking and as a starter solution for 3D and Planar 3D models. Here we provide a semi-analytical, orthogonal polynomial series solution for a rough-walled radial (penny-shaped) hydraulic fracture driven by a fully turbulent fluid. Embedding the appropriate pressure singular-

ities in a family of orthogonal polynomials used for derivation of the solution leads to very rapid convergence of the series, requiring just two terms for an accurate result. We conclude with an investigation of the occurrence of this limiting regime by comparison with numerical simulations, illustrating that the fully turbulent regime is typically not encountered for the radial geometry, although the present solution remains necessary as a starter solution and benchmark for the numerical simulators that are required to capture the laminar-turbulent transition. By comparison with numerical simulations that consider the laminar-turbulent transition, we find that such an estimate is expected to be sufficient for practical purposes when the inlet opening predicted by the turbulent solution exceeds the inlet opening predicted by the laminar solution.

## C. INTRODUCTION

Growing popularity of high rate fluid injection accompanied with using low viscosity fluids such as water is one of the key characteristics of modern hydraulic fracturing (HF) King (2010). As a result, there are an increasing number of practically-relevant cases where the laminar flow assumption used in many HF models is not satisfied, at least over some non-negligible portion of the fracture. While most HF models continue to embed a laminar flow assumption (see the review of Adachi et al. (2007)), which is indeed sometimes valid, the need to consider the turbulent regime dates back at least as far as the seminal early work of Perkins and Kern (1961), who developed a laminar and turbulent flow equations for vertically oriented HF and only the laminar flow equation for radial flow. Later contributions include Nilson (1981, 1988), which investigate the influence of turbulent flow on plane strain and radial HF with constant pressure inlet boundary condition. Also, Emerman et al. (1986) and Siriwardane and Layne (1991) have studied the plane-strain HF with constant inlet fluid flow for laminar and turbulent regime.

More recently there is a growing recognition of the relevance of turbulent flow for HF growth. For example, Ames and Bunger (2015) demonstrate the potential for incorrect assumption of laminar flow to lead to poor predictions of HF length and pressure. There has also been a deepening appreciation for not only the importance, but also for the subtleties and complexities of the mathematical problem and physical phenomena associated with turbulent and/or laminar-turbulent transition fluid flow in HF propagation. The complicated multi-scale structure of a turbulent HF is explored by Dontsov (2016), who analyzed the near-tip transition of HF from turbulent to laminar flow using the Churchill approximation to find the friction factor and the Darcy-Weisbach equation to find an asymptotic solution for a fully turbulent HF. Moreover, Zia and Lecampion (2016, 2017) investigate the effect of turbulent flow on height contained HF. They develop a semi-analytical solution for fully rough and smooth flow in a contained (fixed-height) HF. Furthermore, they applied a drag reduction method from Yang and Dou (2010) to numerically model the transition from laminar to turbulent regimes, again for a contained HF. We note that one of the benefits of using the drag reduction method is the ability of it to get extend to model the effect of proppant and drag reducers in the HF, which Zia and Lecampion (2017) also considered.

Along with these recent studies focusing on a more general modeling framework for HF growth in turbulent and transition regimes, several contributions comprise an expanding family of semi-analytical solutions for benchmarking numerical simulators and rapidly computing fracture dimensions in certain simple geometries. These include:

- Kano et al. (2015) develop an analytical solution for large leak-off PKN model using Gauckler-Manning-Strickler (GMS) solution for rough walled open channel.
- Zolfaghari et al. (2017) provides a semi-analytical solution for the blade-shaped (PKN) geometry in an impermeable rock (no leak-off) using a general form of GMS model. This work uses a truncated polynomial series to derive a solution for fully turbulent HF, showing also the crack tip behavior and providing an alternative method to describe the transition from laminar to turbulent flow.
- Zolfaghari et al. (2017) derive a semi-analytical solution for the plane-strain geometry with no leak-off, providing an asymptotic solution for a zero-toughness plane-strain HF in the rough-walled fully turbulent regime. They also compared their result with a numerical solution that uses the Churchill approximation.

In this study, we present a semi-analytical solution for a rough-walled, fully turbulent, radial HF. We use a general form of GMS to model fluid flow within the HF. Then following the approach taken by Savitski and Detournay (2002), we use a Jacobi polynomial series to solve the problem. The tip solution is embedded in the polynomial series to enable rapid convergence. This extension of the approaches of Savitski and Detournay (2002) and Zolfaghari et al. (2017) is non-trivial because the nature of the radial solution leads to some unique challenges. Most notably, the pressure singularity at the inlet is much stronger in the turbulent regime than in the laminar regime, with the consequence of the need to mitigate unbounded values of the crack opening at the center of the HF in the turbulent regime, whereas the opening is always finite in the laminar regime. Also the form of the pressure and opening singularity at the leading edge of the HF is also different from the laminar regime; in order to obtain rapid convergence our solution must account for this unique near-tip behavior. Finally, because the fluid flux for radial flow decays as one moves away from the inlet – in contrast to linear flow encountered in the plane strain and PKN models – the flow regime is much more prone to transitioning flow regime at a scale that cannot be assumed small relative to the total size of the fracture. To this latter point, we present here comparison to numerical results from our companion paper, Zolfaghari and Bunger (Submitted B), in which we develop a numerical solution to analyze the transition of turbulent flow to laminar flow in a radial HF.

The results in this paper indicate that for a radial, rough-walled HF driven by a fully turbulent fluid described by the GMS model, the width, pressure, and radius are given by

$$
\begin{aligned}
w = {} & \left[\left(0.694 + 0.6148\frac{r}{R}\right)\left(1 - \frac{r}{R}\right)^{\frac{6}{7}} - 0.275\sqrt{1 - \left(\frac{r}{R}\right)^2}\right. \\
& \left. -0.6798\left(\frac{r}{R}\right)^{0.31} + 0.8873\,{}_2F_1\left(\frac{1}{2}, -0.155; 0.845; \left(\frac{r}{R}\right)^2\right)\right]\left(\frac{Q_0}{\beta'\sqrt{E'}}\right)^{\frac{6}{13}} \\
p = {} & \left[1.0452 - \frac{0.7683}{(1 - r/R)^{\frac{1}{7}}} + 0.0967\left(\frac{r}{R}\right)^{-0.69}\right]\left(\frac{E'^{17}Q_0^5}{\beta'^{18}}\right)^{\frac{1}{26}} t^{-\frac{1}{2}} \\
R = {} & 0.854\left(\beta' E'^{\frac{1}{2}} Q_0^{\frac{7}{6}}\right)^{\frac{3}{13}} t^{\frac{1}{2}}
\end{aligned}
\tag{IV.1}
$$

where $Q_0$ is the fluid flow, $t$ is time, $r$ is the coordinate (see Figure IV.1), and $\beta'$ and $E'$ are given in Equation IV.5. This solution comprises the first two terms of the orthogonal polynomial series, which we demonstrate to be sufficiently accurate for most benchmarking and estimation purposes. In what follows, we will describe the mathematical model, solution method, and range of validity of this semi-analytical solution.

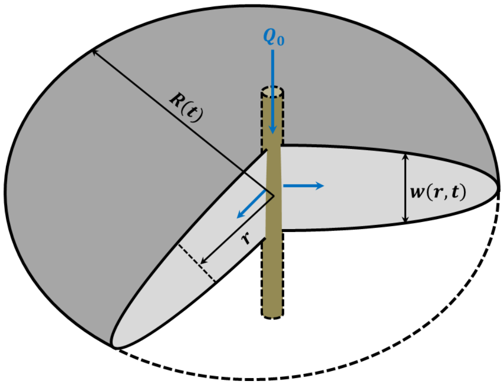

Figure IV.1: Radial hydraulic fracture geometry.

## D. METHOD

The purpose of this paper is to model the effect of turbulent flow on penny shaped (radial) hydraulic fracture, where the radius of the crack is defined as $R(t)$ (see Figure IV.1). In this model the radius of the wellbore is negligible with respect to crack radius, and hence the fluid is taken to be supplied from a point source at the center of the HF (Figure IV.1) with constant flow rate, $Q_0$. In this model the width, pressure, and fluid flux at any time and at any location, $r$, is given by $w(r,t)$, $p(r,t)$, and $q(r,t)$, respectively. Considering the GMS model Gauckler (1867); Manning (1891); Strickler (1981), the fluid flux is given by

$$q = \left(-\frac{4w^3}{\rho f_p}\frac{\partial p}{\partial r}\right)^{\frac{1}{2}} \tag{IV.2}$$

where $\rho$ is the fluid density and $f_p$ is the Darcy-Weisbach friction factor and can be expressed as a general form of

$$f_p = m\left(\frac{k}{w}\right)^{\alpha} \tag{IV.3}$$

where $k$ is the crack surface roughness, and $m$ and $\alpha$ are constants. In this study, $m$ and $\alpha$ are kept variable to maintain the generality of the problem. In the particular case of the GMS model, $m = 0.143$ and $\alpha = 1/3$ Tsai and Rice (2010); Gioia and Chakraborty (2006). Note that we have defined the flux as $q = \langle v \rangle w$, where $\langle v \rangle$ is the mean velocity taken across the fracture opening, perpendicular to the flow direction. With this definition, for radial flow the fluid mass balance equation is

$$\frac{\partial w}{\partial t} + \frac{1}{r}\frac{\partial}{\partial r}(rq) = 0 \tag{IV.4}$$

By letting

$$\beta' = \frac{2}{\sqrt{\rho m k^{\alpha}}} \quad , \qquad E' = \frac{E}{1-\nu^2} \quad , \qquad K' = \frac{8}{\sqrt{2\pi}} K_{IC} \tag{IV.5}$$

it is possible to express the Reynolds equation as the combination of Equations IV.2, IV.3, and IV.4,

$$\frac{\partial w}{\partial t} + \frac{\beta'}{r}\frac{\partial}{\partial r}\left( r w^{\frac{3+\alpha}{2}} \left( -\frac{\partial p}{\partial r} \right)^{\frac{1}{2}} \right) = 0 \tag{IV.6}$$

We then take the HF opening to be described by elasticity equation in radial geometry

$$w = \frac{8R}{\pi E'} \int_0^1 G(\xi, \eta) p(\eta R, t) \eta d\eta \tag{IV.7}$$

where the kernel of the integral is

$$G(\xi, \eta) = \begin{cases} \frac{1}{\xi} \mathcal{F}\left( \arcsin\sqrt{\frac{1-\xi^2}{1-\eta^2}}, \frac{\eta^2}{\xi^2} \right), & \xi > \eta \\ \frac{1}{\eta} \mathcal{F}\left( \arcsin\sqrt{\frac{1-\eta^2}{1-\xi^2}}, \frac{\xi^2}{\eta^2} \right), & \xi < \eta \end{cases} \tag{IV.8}$$

Following linear elastic fracture mechanics (LEFM), the crack will propagate if the stress intensity factor ($K_I$) becomes equal to fracture toughness ($K_{IC}$). In the penny-shaped geometry the fracture intensity factor is Rice (1968)

$$K_I = \frac{2}{\sqrt{\pi R}} \int_0^R \frac{pr}{\sqrt{R^2 - r^2}} dr \tag{IV.9}$$

The system of equations is completed by the boundary and initial conditions. At the crack tip, the fluid flow is zero and the opening is zero. There is no lag between the fluid and crack tip. In the radial geometry the fluid is pumped into the crack through the wellbore (see Figure IV.1), thus the boundary conditions effective on the radial problem are

$$\begin{aligned} & 2\pi \lim_{r \to 0} rq = Q_0 \\ & w(R,t) = 0 \ , \ \ q(R,t) = 0 \\ & w(r,0) = 0 \ , \ \ q(r,0) = 0 \end{aligned} \tag{IV.10}$$

## E. SCALING

The following scaling is introduced

$$\begin{aligned} &w = \varepsilon(t)L(t)\Omega(\xi,t) \ \ , \quad p = \varepsilon(t)E'\Pi(\xi,t) \ \ , \quad R = L(t)\gamma(t) \\ &q = Q_0\Psi(\xi,t) \ \ , \qquad \xi = \frac{r}{R} \end{aligned} \tag{IV.11}$$

where $\varepsilon(t)$, and $L(t)$ are scaling factors and need to be appropriately chosen. Also, we can simplify the equations by using the following change of variables:

$$\Omega = \gamma^{\frac{4}{2+\alpha}}\bar{\Omega} \quad , \qquad \Pi = \gamma^{\frac{2-\alpha}{2+\alpha}}\bar{\Pi} \quad , \qquad \Psi = \gamma^{\frac{6+\alpha}{2+\alpha}}\bar{\Psi} \tag{IV.12}$$

Following the global continuity, using scaling parameters from Equation IV.11, and the fact that the total mass is conserved, we can choose $\varepsilon(t)$ such a way that

$$\gamma^{\frac{2(\alpha+4)}{\alpha+2}}\int_0^1 \bar{\Omega}(s,t)sds = \frac{Q_0 t}{2\pi\varepsilon L^3} \Rightarrow \varepsilon = \frac{Q_0 t}{2\pi L^3} \tag{IV.13}$$

After introducing the scaling parameters and using the change of variables from Equation IV.12, we can obtain the mass balance (IV.6), elasticity (IV.7), fluid flow (IV.2 and IV.3), and crack propagation (IV.9) as

$$\begin{aligned} \dot{\bar{\Omega}}t + \bar{\Omega}\left(1 - 2\frac{\dot{L}t}{L} + \frac{4}{2+\alpha}\frac{\dot{\gamma}t}{\gamma}\right) - \xi\left(\frac{\dot{L}t}{L} + \frac{\dot{\gamma}t}{\gamma}\right)\frac{d\bar{\Omega}}{d\xi} &= -\frac{1}{\mathcal{G}_T}\frac{1}{\xi}\frac{\partial}{\partial\xi}\left(\xi\bar{\Omega}^{\frac{3+\alpha}{2}}\left(-\frac{\partial\bar{\Pi}}{\partial\xi}\right)^{\frac{1}{2}}\right) \\ \bar{\Omega} &= \frac{8}{\pi}\int_0^1 G(\xi,\eta)\bar{\Pi}(\eta,t)\eta d\eta \\ \bar{\Psi} &= \frac{1}{\mathcal{G}_T}\frac{1}{L}\bar{\Omega}^{\frac{3+\alpha}{2}}\left(-\frac{\partial\bar{\Pi}}{\partial\xi}\right)^{\frac{1}{2}} \\ \mathcal{G}_k &= \frac{2^{7/2}}{\pi}\gamma^{\frac{6-\alpha}{2(2+\alpha)}}\int_0^1 \frac{\bar{\Pi}s}{\sqrt{1-s^2}}ds \end{aligned} \tag{IV.14}$$

where the scaling groups are defined as

$$\mathcal{G}_T = \frac{L^{1-\alpha/2}}{\beta t E'^{1/2}\varepsilon^{1+\alpha/2}} \quad , \qquad \mathcal{G}_k = \frac{K'}{\varepsilon E' L^{1/2}} \tag{IV.15}$$

Scaled boundary conditions and initial conditions are then given by

$$\begin{aligned}
&\lim_{\xi\to 0}\xi\bar{\Omega}^{\frac{3+\alpha}{2}}\left(-\frac{\partial\bar{\Pi}}{\partial\xi}\right)^{\frac{1}{2}}=\frac{\mathcal{G}_T}{2\pi\gamma^{\frac{8+2\alpha}{2+\alpha}}}\\
&\bar{\Omega}(1,t)=0\ \ ,\ \ \bar{\Psi}(1,t)=0\\
&\bar{\Omega}(\xi,0)=0\ \ ,\ \ \bar{\Psi}(\xi,0)=0
\end{aligned}\tag{IV.16}$$

Hence, the resulting system of equations is a function of two parameter groups, $\mathcal{G}_T$ and $\mathcal{G}_K$. We can solve the problem for limiting cases in terms of the extreme values of these groups. On the one hand, letting $\mathcal{G}_T \to 0$ results in the governing equations for a crack with constant fluid pressure. On the other hands $\mathcal{G}_K \to 0$ corresponds to the case of zero-toughness. The first limit ($\mathcal{G}_T \to 0$) has already been solved Tada et al. (2000). Therefore, the focus of this paper is on the solution for zero-toughness ($\mathcal{G}_K \to 0$). We then define the characteristic scale $L$ in a way that lets $\mathcal{G}_T = 1$ and subsequently find $\varepsilon$ based on Equation IV.13, hence

$$\begin{aligned}
\varepsilon&=\left(\beta E'^{\frac{1}{2}}\right)^{\frac{-3}{4+\alpha}}Q_0^{\frac{2-\alpha}{2\alpha+8}}t^{-\frac{1}{2}}\\
L&=\left(\beta E'^{\frac{1}{2}}Q_0^{1+\frac{\alpha}{2}}\right)^{\frac{1}{4+\alpha}}t^{\frac{1}{2}}
\end{aligned}\tag{IV.17}$$

It is interesting to note that time appears in $L$ and $\varepsilon$ with opposite powers of equal magnitude and opposite sign. As a result the crack opening, which scales like the product of these factors (see Equation IV.11), is independent of time and in this limit of a fully turbulent, rough crack.

The partial differential equations that define the scaling relationships can then be solved for vanishing fracture toughness ($\mathcal{G}_K \to 0$). Moreover, by considering that the shear stress defined for the turbulent regime is time averaged will enable treating the problem as quasi-steady-state and hence ignoring the inertia (see Zia and Lecampion (2016, 2017); Zolfaghari et al. (2017)). Now, replacing back Equation IV.17 into Equation IV.13, IV.14, and IV.16 gives

$$\frac{\xi^2}{2}\frac{d\bar{\Omega}}{d\xi} = \frac{d}{d\xi}\left(\xi\bar{\Omega}^{\frac{3+\alpha}{2}}\left(-\frac{d\bar{\Pi}}{d\xi}\right)^{\frac{1}{2}}\right) \tag{IV.18a}$$

$$\bar{\Omega} = \frac{8}{\pi}\int_0^1 G(\xi,\eta)\bar{\Pi}(\eta,t)\eta d\eta \tag{IV.18b}$$

$$\int_0^1 \frac{\bar{\Pi}s}{\sqrt{1-s^2}}ds = 0 \tag{IV.18c}$$

$$\bar{\Psi} = \left(\beta E'^{\frac{1}{2}}Q_0^{1+\frac{\alpha}{2}}\right)^{\frac{-1}{4+\alpha}} t^{\frac{-1}{2}}\bar{\Omega}^{\frac{3+\alpha}{2}}\left(-\frac{d\bar{\Pi}}{d\xi}\right)^{\frac{1}{2}} \tag{IV.18d}$$

$$\lim_{\xi\to 0}\xi\bar{\Omega}^{\frac{3+\alpha}{2}}\left(-\frac{d\bar{\Pi}}{d\xi}\right)^{\frac{1}{2}} = \frac{1}{2\pi\gamma^{\frac{8+2\alpha}{2+\alpha}}} \tag{IV.18e}$$

$$\bar{\Omega}(1) = 0 \ \ , \ \ \bar{\Omega}^{\frac{3+\alpha}{2}}\left(-\frac{d\bar{\Pi}}{d\xi}\right)^{\frac{1}{2}}\Bigg|_{\xi=\pm 1} = 0 \tag{IV.18f}$$

Equations IV.18a, IV.18b, IV.18c, and IV.18f define a complete system of non-linear ordinary differential equations (ODE). It will also be useful to integrate Equation IV.18a subject to boundary conditions (IV.18f) to obtain the global volume balance expression

$$\gamma^{\frac{2(\alpha+4)}{\alpha+2}}\int_0^1 \bar{\Omega}(s,t)sds = \frac{1}{2\pi} \tag{IV.19}$$

One of the interesting properties of this set of equations is that the change of variables defined by Equation IV.12 decoupled Equations IV.18a-IV.18d from the normalized crack length, $\gamma$. So, after solving the system of ODEs given by Equations IV.18a-IV.18d for $\overline{\Omega}$ and $\overline{\Pi}$, we can use Equation IV.18e to solve for $\gamma$.

An orthogonal polynomial series is used to solve the problem. Prior to constructing the orthogonal series, the problem is solved for near-tip asymptotic in order to use this result in the form of the polynomials, thus promoting rapid convergence of the series solution. The near-tip behavior is obtained through perturbation analysis and the solution that is given by Desroches et al. (1994) (see Appendix C.A)

$$\begin{aligned} \bar{\Omega}_{\text{tip}} &= a_0(1-\xi)^{\varphi} \\ \bar{\Pi}_{\text{tip}} &= b_0(1-\xi)^{\varphi-1} \end{aligned} \tag{IV.20}$$

where

$$\begin{aligned}
\varphi &= \frac{2}{2+\alpha} \\
a_0 &= \left[\left(\frac{\alpha+2}{2}\right)\sqrt{\frac{2}{\alpha}\tan\frac{\alpha\pi}{\alpha+2}}\right]^{\frac{2}{2+\alpha}} \\
b_0 &= \frac{\cot\frac{2\pi}{\alpha+2}}{2\alpha+4}\left[\left(\frac{\alpha+2}{2}\right)\sqrt{\frac{2}{\alpha}\tan\frac{\alpha\pi}{\alpha+2}}\right]^{\frac{2}{2+\alpha}}
\end{aligned} \tag{IV.21}$$

## F. SOLUTION

Following the same approach that has been taken by Savitski and Detournay (2002), we can define the scaled opening and pressure as the superposition of: 1) the orthogonal polynomials that define the general solution and constructed based on tip solution, and 2) a particular solution that incorporates the strong singularity at the crack opening. That is

$$\begin{aligned}
\bar{\Omega} &= \sum_{i=1}^{\infty} \mathcal{A}_i \widehat{\Omega}_i + \mathcal{B}\bar{\Omega}^* \\
\bar{\Pi} &= \sum_{i=1}^{\infty} \mathcal{C}_i \widehat{\Pi}_i + \mathcal{B}\bar{\Pi}^*
\end{aligned} \tag{IV.22}$$

where $\widehat{\Omega}$ and $\widehat{\Pi}$ are the general solutions that contains the tip behavior, $\bar{\Omega}^*$ and $\bar{\Pi}^*$ are the particular solution, and $\mathcal{A}_i$, $\mathcal{C}_i$, and $\mathcal{B}$ are the constants that need to be calculated. In order to solve the problem we: 1) derive the general solution, 2) solve for the particular solution, 3) define a relation between constants, and 4) solve for the constants.

### 1. General Solution

We define the general solution of the problem in the form of superposition of orthogonal polynomial series. To promote rapid convergence of the solution, we embed the tip asymptotic in the general solution. Hence, following Adachi (2001b) and Savitski and Detournay (2002), the base functions are defined in the form of $\widehat{\Omega}_i = a_0(1-\xi)^{\varphi}\mathfrak{f}_i(\xi)$ and $\widetilde{\Pi}_i = b_0(1-\xi)^{\varphi-1}\mathfrak{g}_i(\xi)$, where $\mathfrak{f}_i(\xi)$ and $\mathfrak{g}_i(\xi)$ are the functions that need to be chosen. Bear in mind that $\widehat{\Pi}_i(\xi) = \omega_i - \widetilde{\Pi}_i(\xi)$, where $\omega_i$ is the adjustment parameter that ensures the pressure satisfies the propagation criteria (Equation IV.18c) and will be calculated later. So, we can define the orthogonality of the functions comprising the solution as

$$\begin{aligned}
\int_0^1 \widehat{\Omega}_i(\eta)\widehat{\Omega}_j(\eta)\eta d\eta = \delta_{ij} &\Rightarrow \int_0^1 a_0^2(1-\eta)^{2\varphi}\mathfrak{f}_i(\eta)\mathfrak{f}_j(\eta)\eta d\eta = \delta_{ij}, \\
\int_0^1 \widetilde{\Pi}_i(\eta)\widetilde{\Pi}_j(\eta)\eta d\eta = \delta_{ij} &\Rightarrow \int_0^1 b_0^2(1-\eta)^{2\varphi-2}\mathfrak{g}_i(\eta)\mathfrak{g}_j(\eta)\eta d\eta = \delta_{ij},
\end{aligned} \tag{IV.23}$$

Note that the orthogonality is defined between $\widehat{\Omega}_i(\eta)$, $\widehat{\Omega}_j(\eta)$, and $\eta$; the $\widehat{\Omega}_i(\eta)$ functions alone are not orthogonal, and the reason is to help the construction of the elasticity function which in the radial solution has the form $\eta\widehat{\Omega}_i(\eta)$. The functions for $\mathfrak{f}_i(\xi)$ and $\mathfrak{g}_i(\xi)$ that satisfy the above orthogonality equation are the Jacobi polynomials ($G_i(a,b,\xi)$, similar to the function used by Savitski and Detournay (2002) for laminar flow), which have a norm of $h_i(a,b)$ and can be obtained as

$$\begin{aligned}
&\int_0^1 (1-\eta)^{a-b}\eta^{b-1}G_i(a,b,\eta)G_j(a,b,\eta)d\eta = h_i(a,b)\delta_{ij}, \\
&G_i(a,b,\xi) = \frac{\Gamma(b+i)}{\Gamma(a+2i)}\sum_{j=0}^{i}(-1)^j\binom{i}{j}\frac{\Gamma(a+2i-j)}{\Gamma(b+i-j)}\xi^{i-j}, \\
&h_i(a,b) = \frac{i!\Gamma(i+b)\Gamma(i+a)\Gamma(i+a-b+1)}{(2i+a)\Gamma^2(2i+a)}.
\end{aligned} \tag{IV.24}$$

Thus, the general solution for scaled fracture opening and fluid pressure are

$$\begin{aligned}
\widehat{\Omega}_i(\xi) &= \frac{(1-\xi)^{\varphi}}{h_{i-1}^{\frac{1}{2}}(2\varphi+2,2)}G_{i-1}(2\varphi+2,2,\xi), \\
\widetilde{\Pi}_i(\xi) &= \frac{(1-\xi)^{\varphi-1}}{h_{i-1}^{\frac{1}{2}}(2\varphi,2)}G_{i-1}(2\varphi,2,\xi)
\end{aligned} \tag{IV.25}$$

The adjustment parameter $\omega_i$ is then defined in a way that $\widehat{\Pi}_i(\xi)$ satisfies the propagation condition (zero toughness), therefore

$$\omega_i = \frac{1}{h^{\frac{1}{2}}_{i-1}(2\varphi,2)} \frac{\Gamma(i+1)\Gamma(\varphi-\frac{1}{2})}{\Gamma(2\varphi+2i-2)} \sum_{j=0}^{i-1}(-1)^j \binom{i-1}{j} \frac{\Gamma(2\varphi+2i-j-2)}{\Gamma(\varphi+i-j+\frac{1}{2})} \times \\ {}_2F_1(\frac{1}{2}, i-j+1; \varphi+i-j+\frac{1}{2}; -1) \tag{IV.26}$$

where ${}_2F_1(a,b;c;d)$ is Gauss' hypergeometric function.

### 2. Particular Solution

The next step is to find a particular solution that satisfies the inlet boundary condition. According to fluid flow equation (Equation IV.18e) near the inlet source,

$$\bar{\Omega}^{\frac{3+\alpha}{2}} \left(-\frac{d\bar{\Pi}}{d\xi}\right)^{\frac{1}{2}} \propto \frac{1}{\xi}.$$

Also, because we do not want to have a singularity in the fracture opening, the fluid pressure will be strongly singular close to inlet, $\bar{\Pi} \propto \frac{1}{\xi}$. On the other hand, as soon as fluid pressure becomes singular in the form of $\frac{1}{\xi}$, the opening will also become singular through the elasticity equation ($\bar{\Omega} \propto \ln 1/\xi$). Hence, the total singularity of the fluid flow will change from $1/\xi$ to $1/\xi \ln(1/\xi)$. To capture the most appropriate singularity for the crack opening, we choose $\bar{\Pi} \propto \frac{1}{\xi^\kappa}$, and we then find the optimal value for $\kappa$ that gives the best solution in terms of minimizing a cost function embodying the mismatch between terms which must be equated according to the governing equations. It is important to interpret cautiously because choosing the singularity in the form of $\bar{\Pi} \propto \frac{1}{\xi^\kappa}$ is not an exact solution to the problem. It is only a proposed method to satisfy the governing equations, although it is likely that the exact solution behaves similarly.

Building on this proposed form of the particular solution, to also satisfy the crack propagation condition (Equation IV.18c), the appropriate exact form of scaled pressure is

$$\bar{\Pi}^*(\xi) = \frac{1}{\xi^\kappa} - \frac{1}{2}\left(\frac{\sqrt{\pi}\Gamma(1-\kappa/2)}{\Gamma(3/2-\kappa/2)}\right) \tag{IV.27}$$

Also, from the elasticity equation, the exact form of the crack opening is

$$\bar{\Omega}^*(\xi) = \begin{cases} \frac{4\beta(\frac{1}{2},1-\frac{\kappa}{2})}{\pi} \left[ \frac{\Gamma\left(\frac{\kappa-1}{2}\right)}{2} \left( \frac{\sqrt{\pi}\xi^{1-\kappa}}{\Gamma\left(\frac{\kappa}{2}\right)} - \frac{{}_2F_1(\frac{1}{2},\frac{\kappa-1}{2};\frac{\kappa+1}{2};\xi^2)}{\Gamma\left(\frac{1+\kappa}{2}\right)} \right) - \sqrt{1-\xi^2} \right], & \kappa \neq 1 \\ 4\ln\left(\frac{1+\sqrt{1-\xi^2}}{\xi}\right) - 4\sqrt{1-\xi^2}. & \kappa = 1 \end{cases} \tag{IV.28}$$

where $\beta(a, b)$, and $\Gamma(x)$ are the Beta-function, and Gamma-function respectively Abramowitz and Stegun (1972). To find the proper value of $\kappa$, we will solve the rest of the problem and will choose $\kappa$ so as to obtain the most accurate solution.

### 3. Calculating Coefficients of the Series

Before finding the values of the constants, we need to obtain the relation between $\mathcal{A}_i$ and $\mathcal{C}_i$ that satisfies the elasticity equation. If we consider a finite number of terms in the series, we can find that

$$\mathcal{A}_i = \sum_{j=1}^{n_\Pi} \mathcal{C}_j L_{ij} \tag{IV.29}$$

where $n_\Pi$ is the number of terms in the polynomial expansion that defines the pressure. Similarly, we have $n_\Omega$ that defines the number of terms for the opening of the crack. Based on substitution of

Equation IV.29 into Equation IV.18b we obtain (see Appendix C.B)

$$
\begin{aligned}
L_{ij} =& \frac{8}{\pi}\frac{\omega_i\mathcal{N}_i + \mathcal{P}_{i,j}}{h^{\frac{1}{2}}_{i-1}(2\varphi+2,2)} \\
\mathcal{N}_i =& \int_0^1 \eta(1-\eta)^{\varphi} G_{i-1}(2\varphi+2,2,\eta)\left(1+\frac{\rho}{2}\ln\left(\frac{4(1-\eta)}{1+\eta}\right)\right)d\eta \\
&+\int_0^1 \mathcal{H}(\eta)\eta(1-\eta)^{\varphi}G_{i-1}(2\varphi+2,2,\eta)d\eta \\
\mathcal{P}_{i,j} =& \int_0^1 \mathcal{M}_j(\eta)\eta(1-\eta)^{\varphi}G_{i-1}(2\varphi+2,2,\eta)d\eta \\
&-\frac{1}{h^{\frac{1}{2}}_{j-1}(2\varphi,2)}\int_0^1 \eta(1-\eta)^{2\varphi-1}G_{i-1}(2\varphi+2,2,\eta)\times \\
&G_{j-1}(2\varphi,2,\eta)\left(1+\frac{\rho}{2}\ln\left(\frac{4(1-\eta)}{1+\eta}\right)\right)d\eta \\
\mathcal{H}(\xi) =& \int_0^{\xi}\left[\frac{\eta}{\xi}\mathcal{F}\left(\arcsin\sqrt{\frac{1-\xi^2}{1-\eta^2}},\frac{\eta^2}{\xi^2}\right)-\frac{1}{2}\ln\left(\frac{1-\xi}{1+\xi}\frac{16\xi^2}{\xi^2-\eta^2}\right)\right]d\eta \\
\mathcal{M}_j(\xi) =& \int_{\xi}^1\left(\frac{(1-\xi)^{\varphi-1}G_{j-1}(2\varphi,2,\xi)-(1-\eta)^{\varphi-1}G_{j-1}(2\varphi,2,\eta)}{h^{\frac{1}{2}}_{j-1}(2\varphi,2)}\right)\times \\
&\mathcal{F}\left(\arcsin\sqrt{\frac{1-\eta^2}{1-\xi^2}},\frac{\xi^2}{\eta^2}\right)d\eta-\frac{1}{h^{\frac{1}{2}}_{j-1}(2\varphi,2)}\times \\
&\int_0^{\xi}\left[\frac{\eta(1-\eta)^{\varphi-1}G_{j-1}(2\varphi,2,\eta)}{\xi}\mathcal{F}\left(\arcsin\sqrt{\frac{1-\xi^2}{1-\eta^2}},\frac{\eta^2}{\xi^2}\right)\right. \\
&\left.-\frac{(1-\xi)^{\varphi-1}G_{j-1}(2\varphi,2,\xi)}{2}\ln\left(\frac{1-\xi}{1+\xi}\frac{16\xi^2}{\xi^2-\eta^2}\right)\right]d\eta
\end{aligned}
\tag{IV.30}
$$

where $\mathcal{F}(\Lambda,k)$ is the incomplete elliptical integral of first kind Abramowitz and Stegun (1972).

So far this section focuses on finding a connection between $\mathcal{A}_i$ and $\mathcal{C}_i$ that ensures the elasticity equations is satisfied. In the following, we will discuss how to find values for the $\mathcal{A}_i$, $\mathcal{B}$, and $\mathcal{C}_i$ constants. Taking the integral of both sides of Equation IV.18a leads to

$$
\frac{\xi^2\bar{\Omega}(\xi)}{2}+\int_{\xi}^1\eta\bar{\Omega}(\eta)d\eta=\xi\bar{\Omega}(\xi)^{\frac{3+\alpha}{2}}\left(-\frac{d\bar{\Pi}(\xi)}{d\xi}\right)^{\frac{1}{2}}
\tag{IV.31}
$$

Once we substitute the polynomial series, the problem will be dependent on the value of $\kappa$ and the coefficients $(\mathcal{A}_i,\mathcal{B},\mathcal{C}_i)$ that construct the polynomial series. In order to find the unknown constants, we use a numerical method to minimize the error between the right hand side and left hand side of the integrated Reynolds equation (Equation IV.31). Therefore, choosing $\mathcal{Q}$ equally spaced control points on $0 < \xi < 1$, we can construct the residual function $\Delta$, which is a function of the constants $(\mathcal{A}_i, \mathcal{B}, \mathcal{C}_i)$ and the parameter $\kappa$ that define the inlet singularity. In this method, the polynomial series are truncated with $n$ number of terms.

$$\Delta(\kappa; \mathcal{B}, \mathcal{C}_1, \cdots, \mathcal{C}_n) = \sum_{i=1}^{\mathcal{Q}} \left( \frac{\Delta^{Left}(\kappa; \mathcal{B}, \mathcal{C}_1, \cdots, \mathcal{C}_n)}{\Delta^{Right}(\kappa; \mathcal{B}, \mathcal{C}_1, \cdots, \mathcal{C}_n)} - 1 \right)^2 \tag{IV.32}$$

Knowing the value of $\kappa$ is enough to solve the problem and find the residual function. Thus, we can find the residual function for different value of $\kappa$, as shown in Figure IV.2a, and for different numbers of terms retained in the polynomial series. Thus, from the results provided in Figure IV.2a, we can generate Figure IV.2b that provides the value of $\kappa$ associated with the minimum value of residual function for different numbers of terms and different values of the fluid parameter $\alpha$.

Figure IV.2a shows that by increasing the number of terms in polynomial, it is possible to get increasingly accurate results. However most importantly, we see that choosing an optimal value of $\kappa$ gives us nearly the same accuracy even with one term.

Now that we have obtained the optimal value of $\kappa$, we can minimize $\Delta(\mathcal{B}, \mathcal{C}_1, \cdots, \mathcal{C}_n)$ to find the constants. The value of constants $\mathcal{B}$, $\mathcal{A}_i$, and $\mathcal{C}_i$ are given in Table IV.1 with the residual value related to them. We can confirm that an acceptable level of accuracy is obtained from just two terms of the series (for more detail see also Table IV.2).

Turning now to the convergence of solution for opening and fluid pressure, the number of terms involved in polynomial series also may have an impact on the final solution.

Figure IV.3 is plotted for GMS parameter ($m = 0.143$ and $\alpha = 1/3$) and it again shows that the solution is accurate to the third digit or so even with just $1 - 2$ terms in the series. Table IV.2 also shows the convergence of the solution by using just two terms in series. Recall this rapid convergence is enabled by embedding the tip asymptotic solution in the polynomial terms.

A note of caution is due here since there is a strong singularity in the pressure, and it can thus be proven that the only value for $\kappa$ that strictly satisfies the inlet boundary condition is $\kappa = 1$, that is, when pressure has the form of $1/\xi$ near the wellbore. For $\kappa < 1$ the opening is not singular and for $\kappa = 1$ the opening will also become singular, as previously discussed , and thus in either case the inlet boundary will not be strongly satisfied. However, for the optimal value of $\kappa$ the left

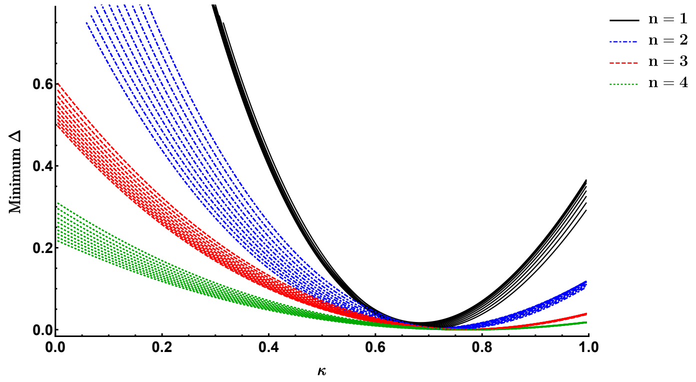

(a)

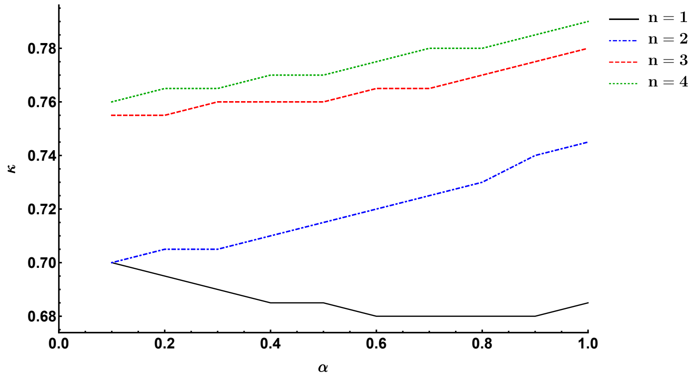

(b)

Figure IV.2: (a) Comparison of the residual function for different values of $\kappa$ and different number of polynomial terms. (b) Optimum value of $\kappa$ for different $\alpha$ and number of terms in polynomial.

Table IV.1: Numerical coefficients, length scale, inlet fluid pressure singularity power, and error function for 50 control points for the series given in Equation IV.32 for the GMS case ($\alpha = 1/3$)

| | **n = 1** | **n = 2** | **n = 3** | **n = 4** |
|---|---|---|---|---|
| $\kappa$ | $0.69$ | $0.71$ | $0.76$ | $0.765$ |
| $\mathcal{A}_1$ | $3.9414 \cdot 10^{-1}$ | $3.9485 \cdot 10^{-1}$ | $3.9998 \cdot 10^{-1}$ | $4.0049 \cdot 10^{-1}$ |
| $\mathcal{A}_2$ | $5.2468 \cdot 10^{-2}$ | $4.8370 \cdot 10^{-2}$ | $4.6615 \cdot 10^{-2}$ | $4.5774 \cdot 10^{-2}$ |
| $\mathcal{A}_3$ | — | $1.9387 \cdot 10^{-3}$ | $1.8216 \cdot 10^{-3}$ | $1.6676 \cdot 10^{-3}$ |
| $\mathcal{A}_4$ | — | — | $1.5714 \cdot 10^{-3}$ | $1.4031 \cdot 10^{-3}$ |
| $\mathcal{A}_5$ | — | — | — | $2.9025 \cdot 10^{-4}$ |
| $\mathcal{B}$ | $1.0818 \cdot 10^{-1}$ | $9.4882 \cdot 10^{-2}$ | $7.7027 \cdot 10^{-2}$ | $7.4377 \cdot 10^{-2}$ |
| $\mathcal{C}_1$ | $7.7713 \cdot 10^{-1}$ | $7.3044 \cdot 10^{-1}$ | $7.3246 \cdot 10^{-1}$ | $7.1507 \cdot 10^{-1}$ |
| $\mathcal{C}_2$ | — | $1.1543 \cdot 10^{-2}$ | $1.4329 \cdot 10^{-2}$ | $1.8262 \cdot 10^{-2}$ |
| $\mathcal{C}_3$ | — | — | $-2.1549 \cdot 10^{-3}$ | $-1.5130 \cdot 10^{-3}$ |
| $\mathcal{C}_4$ | — | — | — | $8.0187 \cdot 10^{-4}$ |
| $\Delta$ | $4.39 \cdot 10^{-3}$ | $2.39 \cdot 10^{-3}$ | $2.34 \cdot 10^{-4}$ | $1.16 \cdot 10^{-4}$ |
| $\gamma$ | $8.5397 \cdot 10^{-1}$ | $8.5660 \cdot 10^{-1}$ | $8.5673 \cdot 10^{-1}$ | $8.5725 \cdot 10^{-1}$ |

Table IV.2: Convergence of the solution with change of the number of terms in the polynomial series.

| | **i = 2** | **i = 3** | **i = 4** |
|---|---|---|---|
| $\dfrac{\gamma\Big\|_{n=i-1}}{\gamma\Big\|_{n=i}}$ | 0.99692 | 0.99986 | 0.99939 |
| $\dfrac{\overline{\mathbf{\Omega}}(0)\Big\|_{n=i-1}}{\overline{\mathbf{\Omega}}(0)\Big\|_{n=i}}$ | 0.98348 | 0.96452 | 0.99459 |
| $\dfrac{\overline{\mathbf{\Pi}}(0.5)\Big\|_{n=i-1}}{\overline{\mathbf{\Pi}}(0.5)\Big\|_{n=i}}$ | 1.00468 | 1.00186 | 1.00149 |
| $\dfrac{\overline{\mathbf{\Psi}}(0.5)\Big\|_{n=i-1}}{\overline{\mathbf{\Psi}}(0.5)\Big\|_{n=i}}$ | 1.00616 | 0.99863 | 1.00388 |

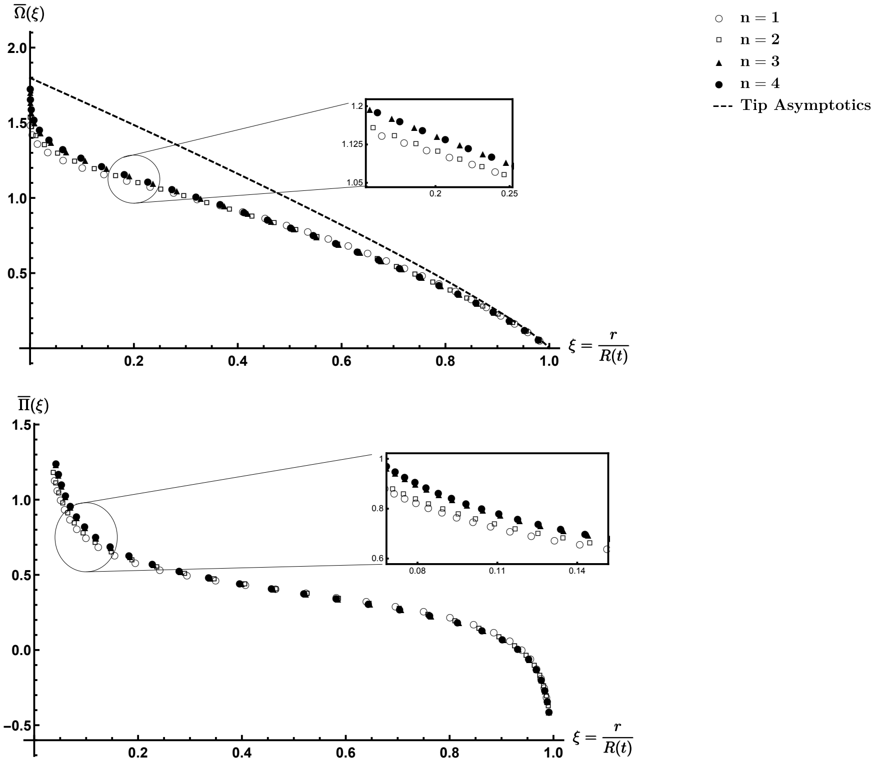

Figure IV.3: Comparison of scaled opening and pressure with the crack tip estimation with different number of terms in the polynomial series.

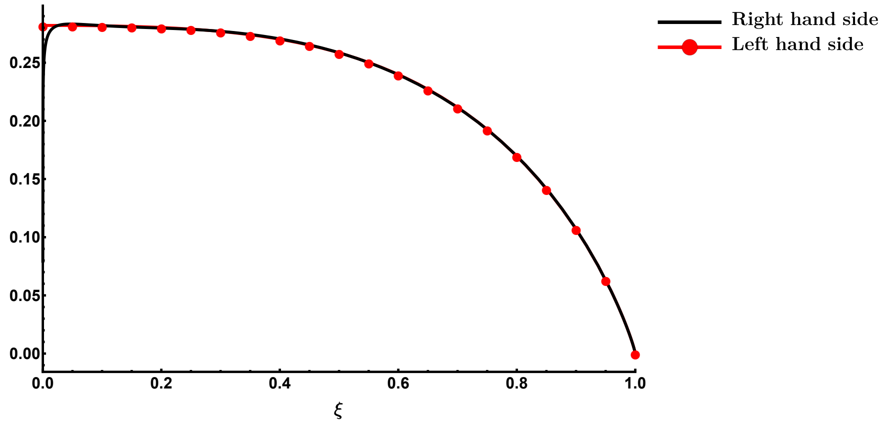

Figure IV.4: Comparison of the left and right hand side of the continuity Equation IV.31 for four terms of the polynomial series.

and right hand side of the Equation (IV.32) are in a very good agreement. Figure IV.4 illustrates this agreement with the only appreciable error occurring near the inlet. Accuracy will be further demonstrated in this paper as we compare the semi-analytical solution with a numerical solution.

And finally, in order to ensure that the solution solves the problem, we can substitute the results back to Equation IV.6 and check if the value of it is negligible. Figure IV.5 indicates that the solution obtained is accurate.

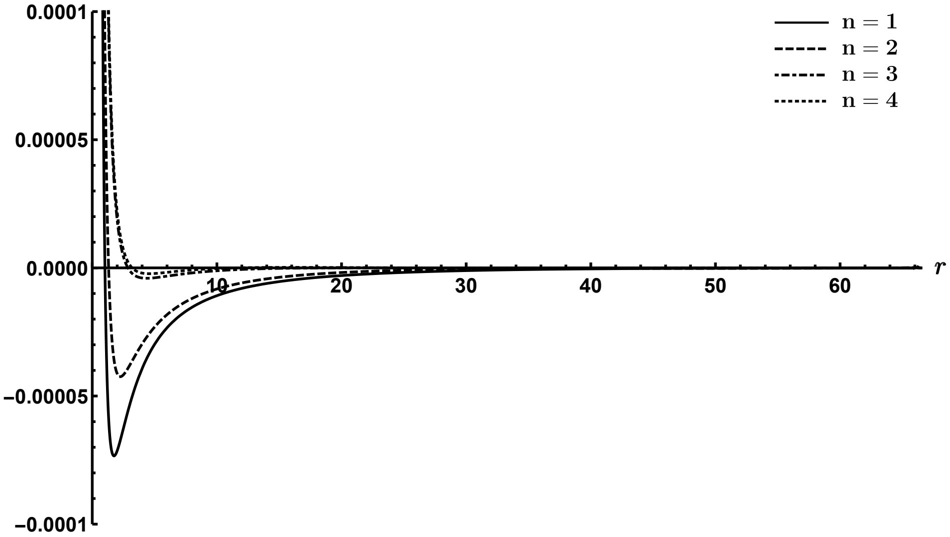

Figure IV.5: Substituting back the solution and confirming it solves the problem. The figure is for $t = 100\ sec$ and the rest of the material properties are given in Table IV.3.

## G. RESULTS

### 1. General Solution

Gathering all the calculations together, we can present the opening and pressure for the radial crack with two terms of the polynomial series as

$$\begin{aligned}\bar{\Omega} &= \mathcal{A}_1 \frac{(1-\xi)^{\varphi}}{h_0^{\frac{1}{2}}(2\varphi+2,2)} G_0(2\varphi+2,2,\xi) + \mathcal{A}_2 \frac{(1-\xi)^{\varphi}}{h_1^{\frac{1}{2}}(2\varphi+2,2)} G_1(2\varphi+2,2,\xi) \\ &\quad + \mathcal{B} \frac{4\beta(\frac{1}{2}, 1-\frac{\kappa}{2})}{\pi} \left[ \frac{\Gamma\left(\frac{\kappa-1}{2}\right)}{2} \left( \frac{\sqrt{\pi}\xi^{1-\kappa}}{\Gamma\left(\frac{\kappa}{2}\right)} - \frac{{}_2F_1(\frac{1}{2}, \frac{\kappa-1}{2}; \frac{\kappa+1}{2}; \xi^2)}{\Gamma\left(\frac{1+\kappa}{2}\right)} \right) - \sqrt{1-\xi^2} \right] \\ \bar{\Pi} &= \mathcal{C}_1 \left[ \omega_1 - \frac{(1-\xi)^{\varphi-1}}{h_0^{\frac{1}{2}}(2\varphi,2)} G_0(2\varphi,2,\xi) \right] + \mathcal{B} \left[ \frac{1}{\xi^{\kappa}} - \frac{1}{2} \left( \frac{\sqrt{\pi}\Gamma(1-\kappa/2)}{\Gamma(3/2-\kappa/2)} \right) \right]\end{aligned} \tag{IV.33}$$

Moreover, it is straightforward to show that that the following holds for the Jacobi polynomials

$$\int_0^1 s(1-s)^{\varphi} G_{i-1}(2\varphi+2,2,s)ds = \frac{\Gamma(i+1)\Gamma(\varphi+1)}{\Gamma(2i+2\varphi)} \sum_{j=0}^{i-1} (-1)^j \binom{i-1}{j} \frac{\Gamma(2i+2\varphi-j)}{\Gamma(i+\varphi-j+2)}$$

and using this identity and Equation IV.19 combined with Equation IV.33 leads to an expression of the crack radius as

$$\gamma = \Bigg[\sum_{i=1}^{\infty} \frac{\mathcal{A}_i}{h_{i-1}^{\frac{1}{2}}(2\varphi+2,2)} \left(\frac{\Gamma(i+1)\Gamma(\varphi+1)}{\Gamma(2i+2\varphi)} \sum_{j=0}^{i-1}(-1)^j \binom{i-1}{j} \frac{\Gamma(2i+2\varphi-j)}{\Gamma(i+\varphi-j+2)}\right) \\ +\mathcal{B}\frac{4\kappa}{3\pi(3-\kappa)}\beta(\frac{1}{2},1-\frac{\kappa}{2})\Bigg]^{\frac{\alpha+2}{-2(\alpha+4)}} \tag{IV.34}$$

For the GMS parameters, this reduces to

$$\gamma = \Bigg[\sum_{i=1}^{\infty} \frac{\mathcal{A}_i}{h_{i-1}^{\frac{1}{2}}(\frac{26}{7},2)} \left(\frac{\Gamma(i+1)\Gamma(\frac{13}{7})}{\Gamma(2i+\frac{12}{7})} \sum_{j=0}^{i-1}(-1)^j \binom{i-1}{j} \frac{\Gamma(2i-j+\frac{12}{7})}{\Gamma(i-j+\frac{20}{7})}\right) \\ +\mathcal{B}\frac{4\kappa}{3\pi(3-\kappa)}\beta(\frac{1}{2},1-\frac{\kappa}{2})\Bigg]^{\frac{-7}{26}}$$

where $\mathcal{A}_1(\alpha)$, $\mathcal{A}_2(\alpha)$, $\mathcal{A}_3(\alpha)$, $\mathcal{B}(\alpha)$, $\mathcal{C}_1(\alpha)$, and $\mathcal{C}_2(\alpha)$ are the general form of the constants that depends on the value of $\alpha$ and are given via Figure IV.6.

As Equation IV.33 shows, in the case of rough-walled fully turbulent fluid flow, the crack opening and fluid pressure are not only functions of the coordinate parameter ($\xi$), but also functions of $\varphi$ which in turn directly depends on Darcy-Weisbach friction factor. Therefore, the nest step is to study the sensitivity of the scaled solution to $\alpha$ (or $\varphi$). Figure IV.7 shows the impact of parameter $\alpha$ on the opening and pressure. This comparison indicates that the opening can differ by 30% when changing the value of $\alpha$ from 0 to 1. So we see that variation of $\alpha$ has an effect on the opening and pressure but this effect is relatively small.

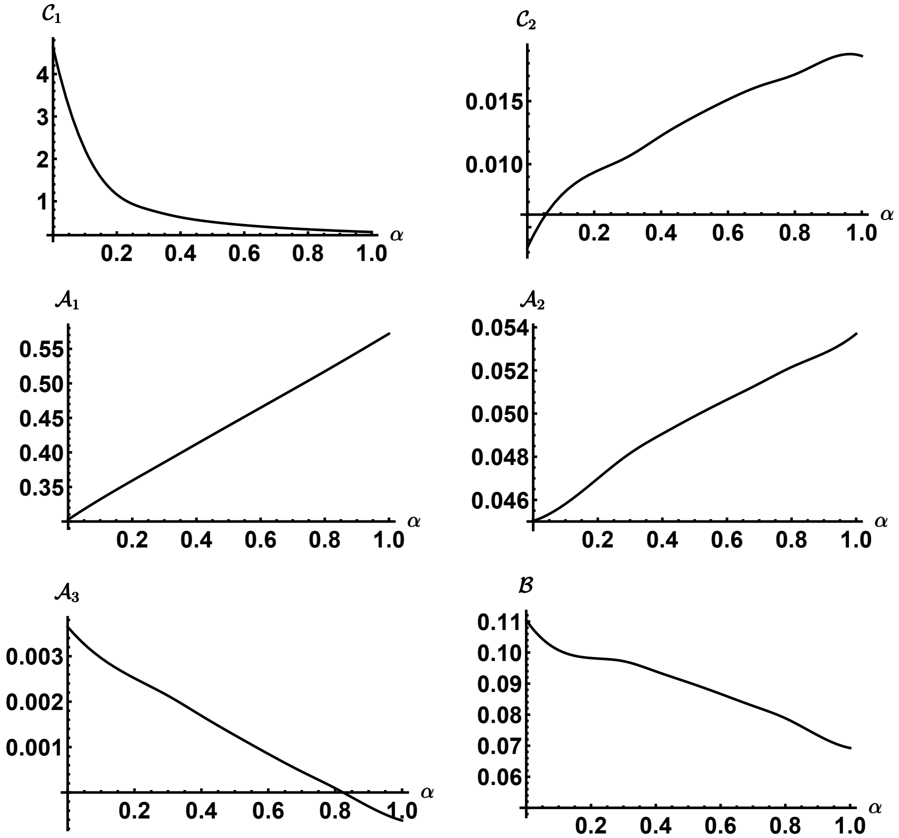

Figure IV.6: The values of the constants in Equation IV.33–IV.34 as function of Darcy-Weisbach friction factor parameter $\alpha$.

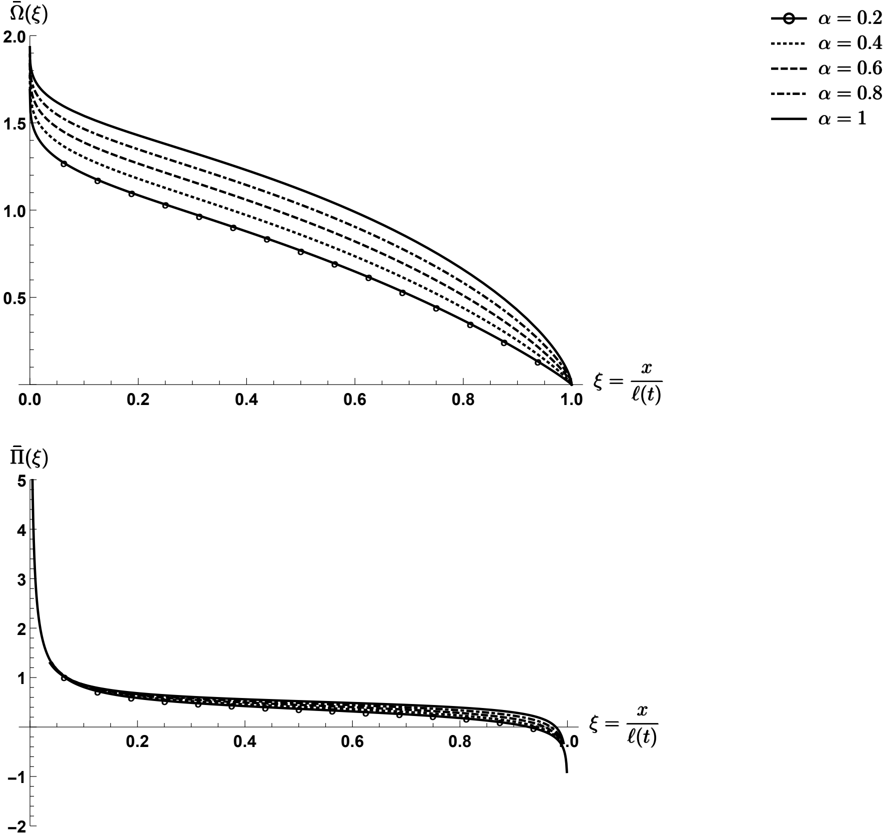

Figure IV.7: Effect of Darcy-Weisbach friction factor parameter ($\alpha$) on the solution.

### 2. Dimensional Solution

Using Equations IV.11, IV.12, IV.17, and IV.33, we can obtain the crack opening and fluid pressure in dimensional form as

$$\begin{aligned} w =& \left(\frac{Q_0}{\beta\sqrt{E'}}\right)^{\frac{2}{4+\alpha}} \gamma^{\frac{4}{2+\alpha}} \times \\ & \Bigg\{\left[\mathcal{A}_1(3+2\varphi)\sqrt{2+\varphi}+\mathcal{A}_2\sqrt{1+2\varphi}\left(\frac{r}{R}-\frac{2}{2\varphi+3}\right)\right]\frac{(1-r/R)^{\varphi}}{\sqrt{2(\varphi+1)}} \\ & + \mathcal{B}\frac{4\beta(\frac{1}{2},1-\frac{\kappa}{2})}{\pi}\left[\frac{\Gamma\left(\frac{\kappa-1}{2}\right)}{2}\left(\frac{\sqrt{\pi}}{\Gamma\left(\frac{\kappa}{2}\right)}\left(\frac{r}{R}\right)^{1-\kappa}\right.\right. \\ & \left.\left. -\frac{{}_2F_1(\frac{1}{2},\frac{\kappa-1}{2};\frac{\kappa+1}{2};\left(\frac{r}{R}\right)^2)}{\Gamma\left(\frac{1+\kappa}{2}\right)}\right)-\sqrt{1-\left(\frac{r}{R}\right)^2}\right]\Bigg\} \\ p =& E'\left(\beta E'^{\frac{1}{2}}\right)^{\frac{-3}{4+\alpha}} Q_0^{\frac{2-\alpha}{2\alpha+8}} t^{\frac{-1}{2}} \gamma^{\frac{2-\alpha}{2+\alpha}} \times \\ & \left[\mathcal{C}_1\left(\omega_1-\sqrt{2\varphi(2\varphi-1)}(1-r/R)^{\varphi-1}\right)\right. \\ & \left. +\mathcal{B}\left(\left(\frac{r}{R}\right)^{-\kappa}-\frac{1}{2}\left(\frac{\sqrt{\pi}\Gamma(1-\kappa/2)}{\Gamma(3/2-\kappa/2)}\right)\right)\right] \end{aligned} \tag{IV.35}$$

Moreover, using Equations IV.11, IV.17, and IV.34 will provide the crack radius as

$$\begin{aligned} R = \left(\beta E'^{\frac{1}{2}} Q_0^{1+\frac{\alpha}{2}}\right)^{\frac{1}{4+\alpha}} t^{\frac{1}{2}} & \left[\sum_{i=1}^{\infty}\frac{\mathcal{A}_i}{h_{i-1}^{\frac{1}{2}}(2\varphi+2,2)}\left(\frac{\Gamma(i+1)\Gamma(\varphi+1)}{\Gamma(2i+2\varphi)}\times\right.\right. \\ & \left.\sum_{j=0}^{i-1}(-1)^j\binom{i-1}{j}\frac{\Gamma(2i+2\varphi-j)}{\Gamma(i+\varphi-j+2)}\right) \\ & \left. +\mathcal{B}\frac{4\kappa}{3\pi(3-\kappa)}\beta(\frac{1}{2},1-\frac{\kappa}{2})\right]^{\frac{\alpha+2}{-2(\alpha+4)}} \end{aligned} \tag{IV.36}$$

And finally, combining Equations IV.11, IV.12, and IV.18d will lead to the fluid flux as

$$q = Q_0\gamma^{\frac{6+\alpha}{2+\alpha}}\left(\beta E'^{\frac{1}{2}} Q_0^{1+\frac{\alpha}{2}}\right)^{\frac{-1}{4+\alpha}} t^{\frac{-1}{2}} \bar{\Omega}^{\frac{3+\alpha}{2}}\left(-\frac{d\bar{\Pi}}{d\xi}\right)^{\frac{1}{2}} \tag{IV.37}$$

Substituting $m = 0.143$ and $\alpha = 1/3$ (GMS parameters), we obtain the solution present in Equation IV.1.

Table IV.3: Material properties and physical constants that are used in this paper for comparison with laminar solution and numerical models.

| **Figures** | **Parameters** | | | | | | | |
|---|---|---|---|---|---|---|---|---|
| | $\boldsymbol{Q_0}$ ($\mathrm{m}^3\ \mathrm{s}^{-1}$) | $\boldsymbol{\nu}$ | $\boldsymbol{\mu}$ (cP) | $\boldsymbol{\rho}$ ($\mathrm{kg\ m}^{-3}$) | $\boldsymbol{k}$ (mm) | $\boldsymbol{m}$ | $\boldsymbol{E}$ (GPa) | $\boldsymbol{\alpha}$ |
| Figure IV.14 | 0.05 | 0.2 | — | 600 | — | 0.143 | 25 | 1/3 |
| Figure IV.15a | 0.05 | 0.2 | 0.126 | | 0.01 | | | |
| Figure IV.15b | 0.05 | 0.2 | 0.032 | | 0.01 | | | |
| Figures IV.5, IV.15c | 0.05 | 0.2 | 0.01 | | 0.01 | | | |
| Figures IV.8-IV.12 | 0.1 | 0.2 | 0.01 | | 0.1 | | | |

### 3. Laminar Versus Rough-Walled Fully Turbulent Solutions

Here we compare the solution obtained from the rough-walled fully turbulent model with the zero-toughness solution for laminar fluid flow provided by Savitski and Detournay (2002). In order to make the comparison, we use the GMS model parameters and the physical parameters that are defined in Table IV.3.

The first comparison is related to normalized opening, which is defined as the ratio of the crack opening at some location inside the crack divided by the crack opening at the inlet (see Figure IV.8). This comparison shows a stronger gradient of the opening near the inlet for the turbulent solution, as expected due to the stronger singularity in the near-inlet fluid pressure.

In the next step, we compare the crack opening, the fluid pressure, and fluid flow along the crack between laminar and turbulent flow, as shown in Figure IV.9. Also, in Figure IV.10, we show the change of crack opening and fluid pressure at wellbore and crack length versus change of time. This comparison shows that the turbulent regime leads to prediction of larger pressure, larger opening, and shorter length hydraulic fractures when compared to the laminar regime.

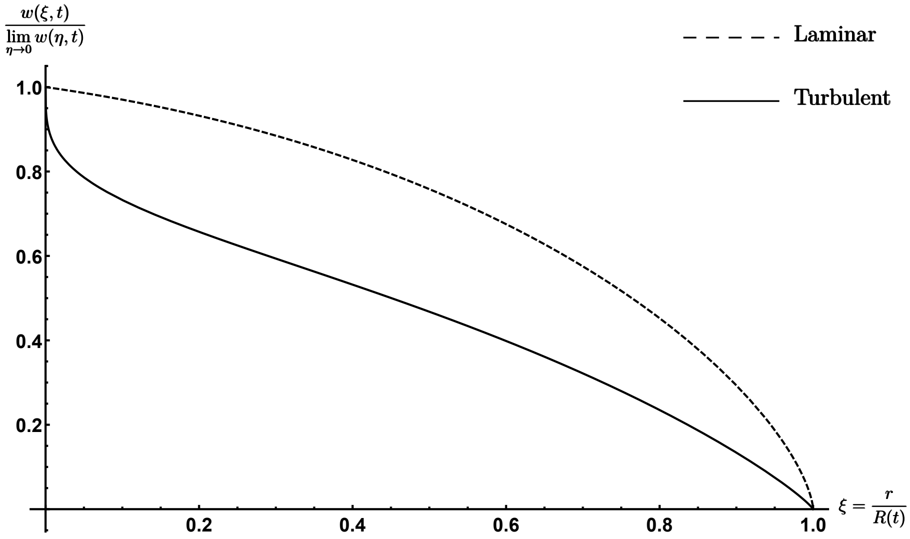

Figure IV.8: Comparison of normalized opening for laminar and turbulent flow at $t = 1000$ sec.

It is also useful to examine the evolution of the solution comparison, which is aided by first defining

$$\begin{aligned} \frac{R_{turb}(t)}{R_{lam}(t)} &= 1.8089 \left(\frac{t}{t^*}\right)^{\frac{1}{18}} \\ t^* &= \frac{Q_0^{\frac{15}{13}} \rho^{27/13} k^{9/13}}{E'^{\frac{1}{13}} \mu'^2} \end{aligned} \tag{IV.38}$$

Since opening and pressure are not only function of time but also of position, we can make a similar comparison graphically via Figure IV.11. Here we give a plot for all values of time by multiplying the ratio of the turbulent to laminar solution by an appropriate power of $t/t^*$. Namely, we obtain from the scaling that $w_{turb}(\xi,t)/w_{lam}(\xi,t) \propto (t^*/t)^{1/9}$, and $p_{turb}(\xi,t)/p_{lam}(\xi,t) \propto (t^*/t)^{1/6}$. Also, from Figure IV.11, we can see that at crack tip, the ratio of the opening from turbulent over laminar is zero. This is to be expected because Equation IV.20 shows that at crack tip for the turbulent case $w \sim \xi^{6/7}$ while for laminar flow $w \sim \xi^{2/3}$. Since, the power of the turbulent flow is larger, when we get closer to the crack tip, the crack opening for turbulent flow can goes to zero faster and make the ratio tend to zero.

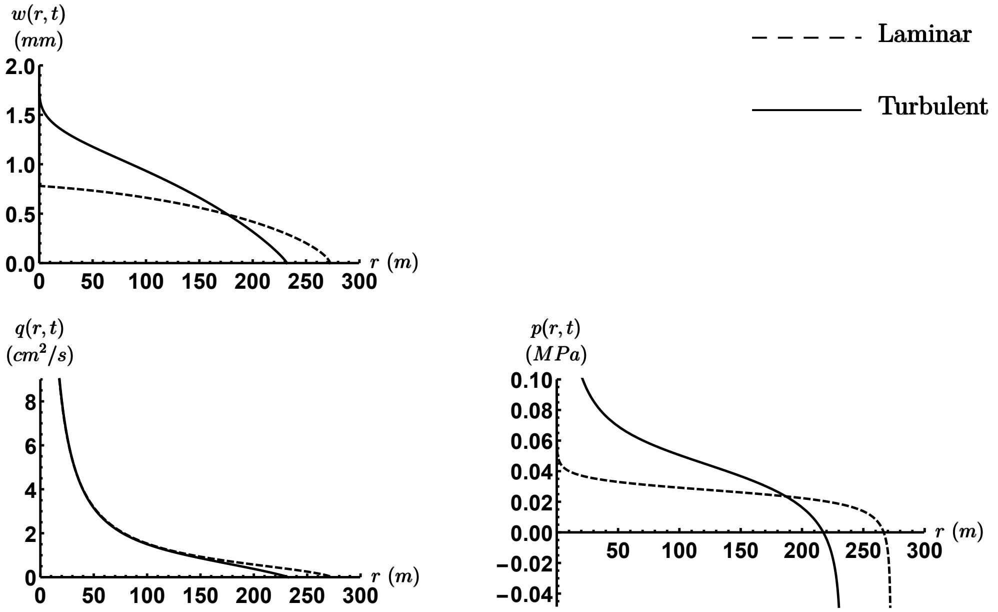

Figure IV.9: Comparison of fracture opening, fluid pressure, and fluid flow along the crack for two different cases of laminar and turbulent regime.

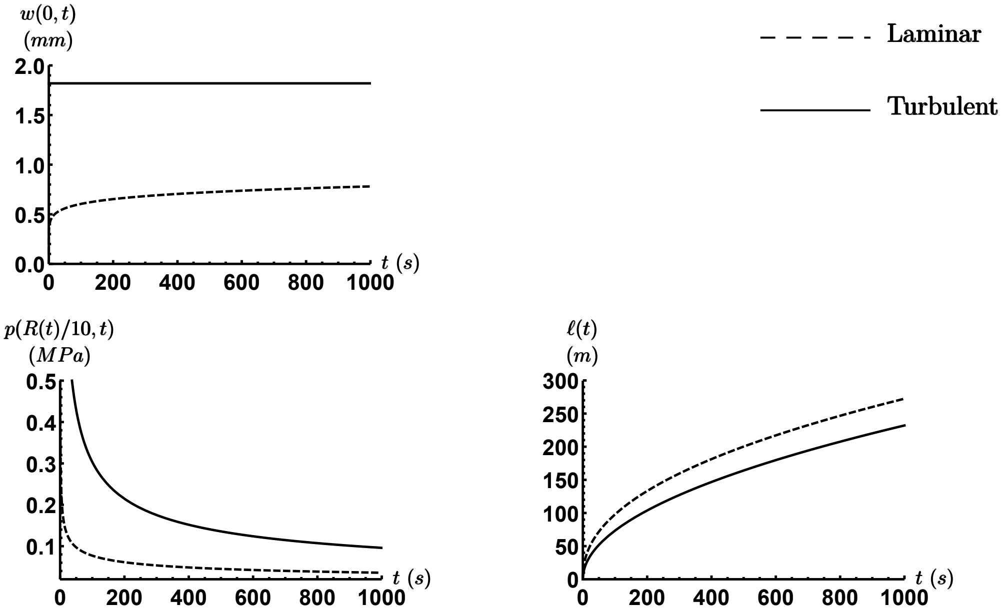

Figure IV.10: Comparison of inlet fracture opening, crack length, and fluid pressure at $1/10$ of the radius versus time for two cases of laminar and fully turbulent assumptions.

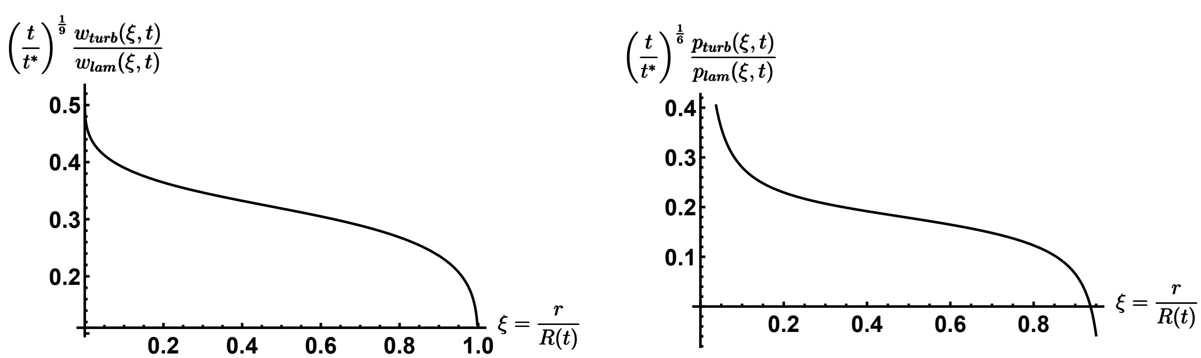

Figure IV.11: Difference of fracture opening and fluid pressure along the crack at any time.

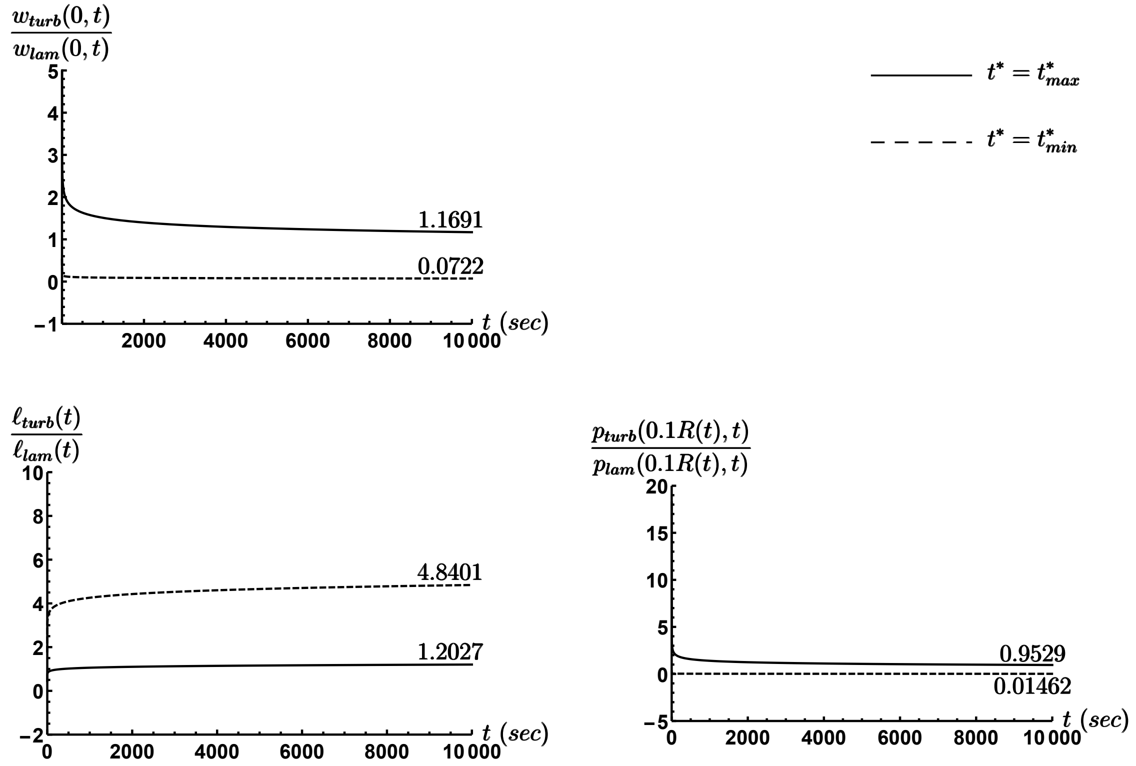

Figure IV.12: Difference of fracture opening, crack length, and fluid pressure versus time for two contrasting limits of $t^*_{min}$ and $t^*_{max}$ (see Table IV.4 ).

Table IV.4: Different limits of parameters used to generate Figure IV.12.

| Parameter | Minimum | Maximum |
|---|---|---|
| $Q_0$ | $2.5\ m^3/s$ | $0.05\ m^3/s$ |
| $k$ | 0.01 mm | 2 mm |
| $\nu$ | 0.15 | 0.35 |
| $E$ | 5 GPa | 100 GPa |

### 4. Laminar to Turbulent Transition Solution

Based on the comparison provided in Figures IV.9 and IV.10, it is clear that selecting a solution corresponding to the correct fluid flow regime is vital for accurate predictions. In this section, we compare: 1) the asymptotic solution provided for GMS, 2) the laminar asymptotic given by Savitski and Detournay (2002), and 3) a numerical solution. The numerical solution is described in detail by Zolfaghari and Bunger (Submitted B). To obtain the friction factor for laminar, turbulent, and transition regimes, we used the formula given by Yang and Dou (2010). Following this model to predict the friction factor, we can recreate the Nikurase's graph, as shown in Figure IV.13. Figure IV.13 clearly indicates how well this model captures the behavior for laminar, turbulent, and transition regimes. It also shows that the GMS approximation for a rough-walled channel is captured by considering this numerical approach.

One of the important parameters in this model is Reynold's number (Re). Here, we define the characteristic Reynold's number ($Re^*$) as

$$Re^* = \frac{\rho Q_0}{\mu R}$$

where $R$ is the crack radius. Figure IV.14 indicates the variation of fracture length, fracture opening, and fluid pressure versus this characteristic Reynolds number. Note that:

- In order to be consistent, we computed the characteristic Reynolds number for laminar, turbulent, and numerical solution with using the laminar crack radius as the length scale in definition of Reynolds number.

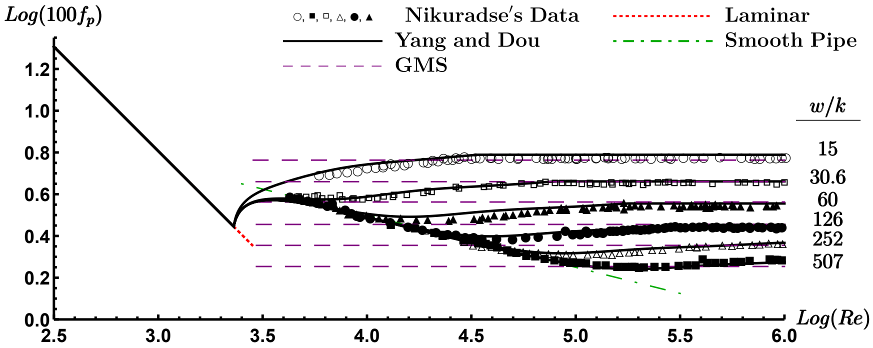

Figure IV.13: Variation of Darcy-Weisbach friction factor versus pipe roughness and Reynolds number. The experimental Nikuradse's data are obtained from Nikuradse (1954) from Table 2-7 of the reference.

- The numerical simulation is based on the data given in Table IV.3.
- In order to capture the changes of Reynolds number, we kept all the parameters constant except the value of the viscosity.
- Figure IV.14 and IV.15 are made after 1000 seconds of injection.
- Because of the strong singularity at inlet, the opening and pressure at wellbore are infinity from Equation IV.1, so the opening and pressure are made for the $r = 50\ m$.

In order to better show the transition from turbulent to laminar flow, we choose three instants that represent the laminar, transition, and turbulent regime as in Figure IV.15. Here it is interesting to note that the applied inlet solution is in a very good agreement with numerical solution, thus confirming the validity of the approach defined in Equations IV.27 and IV.28 to approximate the inlet pressure singularity in the solution method.

We further observe in Figure IV.15 that as the crack develops, the inlet opening in the turbulent regime stays constant while in laminar regime the opening increases. This observation confirms that the opening at inlet is indeed independent of time for the fully turbulent rough-walled regime, as predicted by the scaling.

Observing the comparison in Figure IV.15 also shows that the laminar solution corresponding to each time increases until it surpasses the turbulent solution, with the numerical solution matching

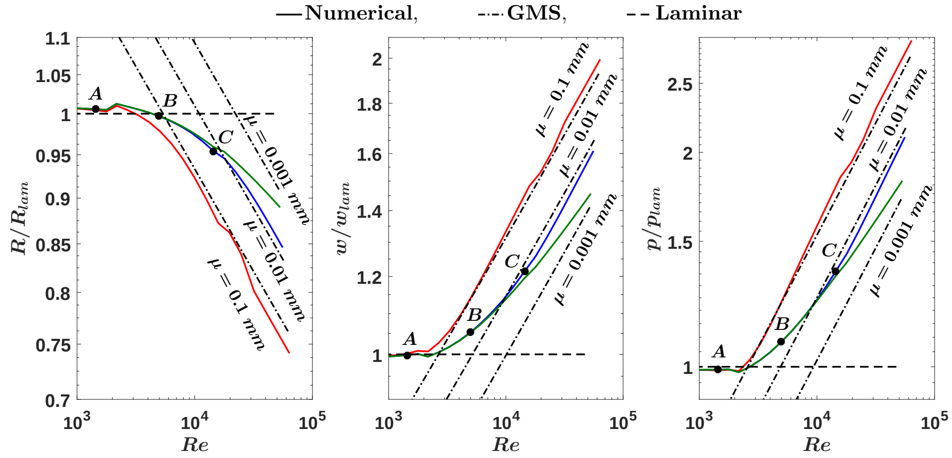

Figure IV.14: Study the change of fracture radius, fracture opening and fluid pressure at $r = 50\ m$.

reasonably well to whichever of the two asymptotic solutions (laminar or turbulent) corresponds to the larger value of the inlet opening. This behavior suggests that we can estimate the fracture parameters with an often acceptable precision by only using the asymptotic solutions. Furthermore, the exceeding of the predicted inlet opening for the turbulent regime by the predicted inlet opening for the laminar regime can be considered as criteria that indicates the convergence of solution to the laminar regime after this point.

## H. CONCLUSIONS

The main outcome of this work is an asymptotic solution to estimate crack length, fracture opening, fluid flux, and fluid pressure for a rough-walled, radial hydraulic fracture driven by a fully turbulent fluid. For the specific case of GMS fluid flow model, the asymptotic solution retaining two terms in the polynomial series is given by Equation IV.1. This solution is indeed shown to be accurate with only two terms of an orthogonal polynomial series, with such rapid convergence enabled by embedding appropriate crack tip and inlet singularities in the structure of the family of Jacobi polynomials used in the solution method. The solution is intended for benchmarking 3D and Planar3D simulators in the limit of the rough-walled fully turbulent regime, as well as

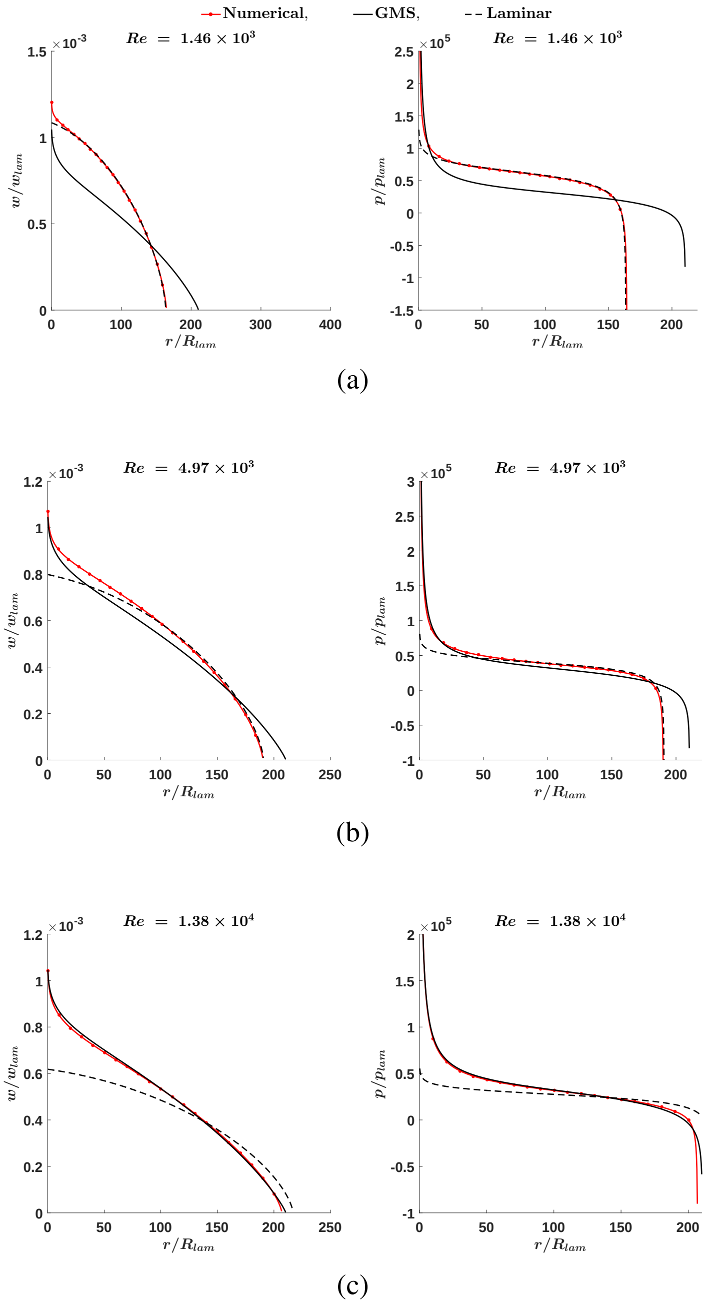

Figure IV.15: Comparison of fracture opening and fluid pressure with numerical model for three different cases of, **a)** laminar fluid flow, **b)** transition, and **c)** turbulent regime corresponding to points $A$, $B$, and $C$ from Figure IV.14, respectively. These plots are for the instance of $1000\ sec$, and the Reynolds number is regularized with the radius of the crack defined with laminar flow.

to provide rapid estimation of fracture dimensions in cases where the turbulent regime provides a more appropriate estimate than the laminar regime. By comparison with numerical simulations that consider the laminar-turbulent transition, we find that such an estimate is expected to be sufficient for practical purposes when the inlet opening predicted by the turbulent solution exceeds the inlet opening predicted by the laminar solution.

# V. NUMERICAL MODEL FOR A PENNY-SHAPED HYDRAULIC FRACTURE DRIVEN BY LAMINAR/TURBULENT FLUID IN AN IMPERMEABLE ROCK

## A. PREAMBLE

This chapter comprises a preprint of Zolfaghari and Bunger (Submitted B). In this chapter a numerical simulator is developed to model HF growth driven by fluid across the laminar-turbulent transition. The numerical results are compared with the laminar asymptotic solution (Savitski and Detournay, 2002) and rough-walled fully turbulent asymptotic solution (Zolfaghari and Bunger, Submitted A). This comparison indicates good agreement with the relevant asymptotic limits and thus confirms the accuracy of the numerical approach proposed here. The evolution of the fluid regime along the crack is also examined.

## B. ABSTRACT

As hydraulic fracturing at high injection rates with low viscosity fluids grows in popularity, so also there is a growing need to include not only the more common laminar fluid flow, but also turbulent and transition flow regimes in numerical simulators. One common scenario is embodied in the behavior of a radial (penny-shaped) hydraulic fracture where flow is turbulent near the inlet, laminar near the tip, and in transition somewhere between. The main goal of this paper is to investigate the impact of this transition on hydraulic fracture growth through development and use of a numerical simulator for penny-shaped hydraulic fractures using the so-called drag reduction method to estimate the friction factor inside the crack for all relevant flow regimes. Upon solving this problem numerically for the case of zero toughness, comparing the results with fully laminar

and fully turbulent asymptotic solutions shows that the early time behavior of radial hydraulic fractures is predominantly turbulent while large time behavior if predominantly laminar. The time scale associated with this transition determines the relevance of either limiting regime to practical cases, i.e. when the transition takes place in a small fraction of the total treatment time it suffices to approximate growth using the laminar asymptotic solution and when the transition requires are large time compared to the treatment time it suffices to approximate growth using the turbulent asymptotic solution.

## C. INTRODUCTION

High injection fluid flow with low viscosity fluids are growing in popularity in hydraulic fracture (HF) stimulation of oil and gas wells. As a result, the fluid regime often deviates from the typically-assumed laminar conditions, and this divergence from the laminar assumption can lead to inaccurate predictions (Ames and Bunger, 2015). Recognition of the turbulent flow in HF backs to seminal works of Perkins and Kern (1961), who modeled the vertically confined HF geometry using both laminar and turbulent assumptions, while also modeling radial HF growth in the laminar fluid flow regime. Thereafter, Nilson (1981, 1988) modeled plane-strain and radial HF growth using a constant inlet fluid pressure condition. On the other hand, Emerman et al. (1986), and Siriwardane and Layne (1991) used inlet fluid influx boundary condition in their model for a plane-strain HF in both the laminar and turbulent regimes. Recently, Anthonyrajah et al. (2013) numerically modeled blade-like (PKN) HF growth using a general inlet boundary condition. Turbulent flow-driven crack propagation also received attention from other fields, for example investigating the influence of turbulent flow in magma transport and natural geothermal injections Lister (1990); Lister and Kerr (1991). Moreover, turbulent flow-driven crack propagation is considered in subglacial drainage Tsai and Rice (2010).

Recently, a growing body of literature aims at investing the influence of turbulent flow in HF growth. Dontsov (2016) provides an asymptotic solution for a laminar-turbulent HF in plane strain geometry using the Churchill approximation for the friction factor. Dontsov (2016) also explores the near-tip transition of fluid flow to laminar regime and compares his results with numerical simulations. Also, Zia and Lecampion (2017) use a drag reduction method to estimate the friction factor by employing the approach proposed by Yang and Dou (2010). Besides that, Zia and Lecampion (2016, 2017) developed a semi-analytical solution to rough-walled and smooth-walled HF including the impact on height growth HF.

To date, several studies have focused on developing semi-analytical solutions for rapid calculations and providing asymptotic benchmarking solution for HF with turbulent flow. These have addressed:

- Blade-shaped (PKN) geometry, large leakoff, and zero toughness with fully turbulent flow in a rough-walled hydraulic fracture (Kano et al., 2015).
- Blade-shaped (PKN) geometry, zero leakoff (impermeable rock), and zero toughness with fully turbulent flow in a rough-walled hydraulic fracture (Zolfaghari et al., 2017).
- Plane strain geometry, zero leakoff, and zero toughness with fully turbulent flow in a rough-walled hydraulic fracture (Zolfaghari et al., 2017).
- Radial geometry, zero leakoff, and zero toughness with fully turbulent flow in a rough-walled hydraulic fracture (Zolfaghari and Bunger, Submitted A).
- Smooth-walled HF, and rough-walled HF with fully turbulent regime (Zia and Lecampion, 2017).

The main goal of this study is to numerically simulate rough-walled HF growth in the radial geometry for fluid flow in the laminar, transition, and/or turbulent regimes. To accomplish this, we use the drag reduction (DR) model from Yang and Dou (2010) to predict the friction factor. We tailored the DR method to the radial HF problem by adding adjusting parameters and using the hydraulic diameter to extend the solution from pipe flow. We then use a moving mesh method to discretize the crack into constant number of elements in each propagation step by stretching the elements. This problem is formulated with fixed-length scale stepping and an implicit solution is used to step through the time domain. Within this scheme, an iterative approach is applied to solve the coupled fluid flow-elasticity equations. At the end, the results are compared with laminar and GMS semi-analytical approximations.

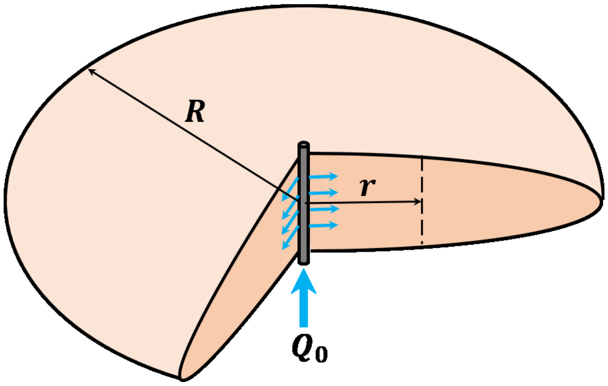

Figure V.1: Radial crack geometry.

## D. GOVERNING EQUATIONS

Radial or penny-shaped hydraulic fracture geometry refers to axis-symmetric growth that is not (yet) bounded with fracture height restricting barriers from top and bottom Perkins and Kern (1961). The quantities corresponding the solution are crack width ($w(r,t)$), fluid pressure ($p(r,t)$), and fluid flux ($q(r,t)$) for any specified time ($t$) and radius ($r$) (see Figure V.1) as well as the crack radius ($R(t)$). The main goal of this paper is to provide a numerical solution for all these quantities in the laminar, turbulent, and/or transition from laminar to turbulent fluid flow regimes. Note that the analytical solution for fully turbulent rough-walled radial HF is developed by Zolfaghari and Bunger (Submitted A). However, in the radial geometry there will often be a turbulent region near the inlet, laminar near the tip, and transition in between. Hence, we will herein seek a solution capturing this transition.

We begin, then, with the Darcy-Weisbach equation, which gives a relation between pressure drop and fluid flux for circular pipes. Using the hydraulic diameter, one can extend Darcy-Weisbach equation so that it becomes suitable for non-circular conduits, that is Streeter (1961b)

$$\frac{\partial p}{\partial r} = -f_p \frac{\rho}{2} \frac{V^2}{D_h}$$

where $\rho$ is the fluid density, $V$ is the average fluid velocity along the width of the crack, $f_p$ is the Darcy-Weisbach friction factor, and $D_h$ is the hydraulic diameter of the cross-section and is

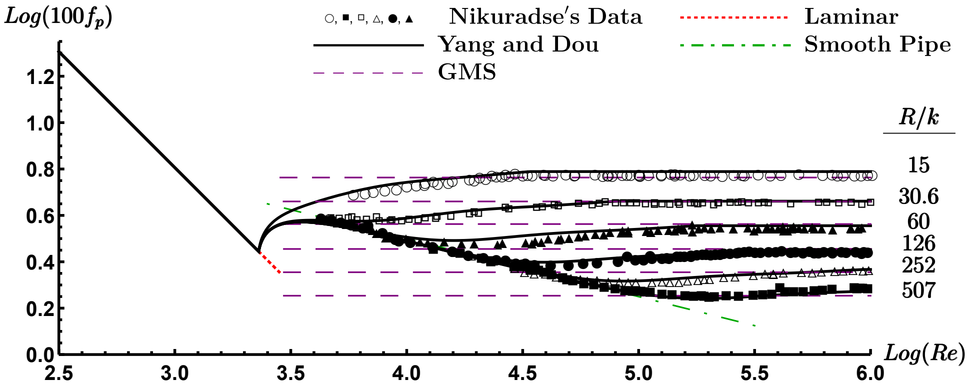

Figure V.2: Effect of Darcy-Weisbach friction factor parameter ($\alpha$) on the obtained solution.

defined as $D_h = 4A/P$ where $A$ is the area of the fluid flow cross-section and $P$ is the perimeter of the wetted area. Later in this section, we will show that in DR model, $f_p \propto u_*/V$, where $u_*$ is the shear velocity (see Equation V.2). After manipulating the Darcy-Weisbach equation for radial flow, we obtain

$$q = \left(-\frac{4w^3}{\rho f_p}\frac{\partial p}{\partial r}\right)^{\frac{1}{2}} \tag{V.1}$$

where $q = Vw$ is the fluid flux classically used in HF modeling. It remains to describe the friction factor $f_p$, typically considered to be a function of Reynold's number and the surface roughness. In this paper, we will use the fluid flow model based on drag reduction (DR) (see Yang and Dou, 2010). The main reason to choose the DR model is that it can predict the friction factor for the laminar, transition, and fully rough turbulent regimes very well. Figure V.2 indicates the accuracy of the DR model and shows the confirmation with Nikuradse's experimental data Nikuradse (1954).

In this section, at first we will explain the DR model, and then we expand that model for HF problem.

### 1. DR Model

Fluid flow in a pipe produces fluid friction. But, by inclusion of additives, the fluid turbulent friction can reduce and the term "drag reduction" refers to this phenomenon. Before going further, it is necessary here to clarify some additional terminology and definitions.

The first term to introduce is the shear velocity, $u_*$, that is, a velocity that defines the shear between layers in the flow stream. In fact, shear velocity is not really a velocity, per se, but rather it is shear stress that has been defined in the units of velocity using a scaling involving the fluid density, $\rho$. Normally, the shear velocity is defined as $\sqrt{\tau_w/\rho}$ where $\tau_w$ is the wall shear stress (Streeter, 1961b). Also, the definition of friction factor (Darcy-Weisbach) is

$$f_p = 8\left(\frac{u_*}{V}\right)^2. \tag{V.2}$$

The other important terminology in this section is the definition of Reynolds number. In this model, Yang and Dou (2010) use various definition of Reynolds number classified into three categories:

I. Shear Reynolds number ($Re^+$), or the Reynolds number for shear velocity, which is defined as

$$Re^+ = \vartheta\frac{\rho u_* R_h}{\mu} \tag{V.3}$$

where $\mu$ is the fluid viscosity, and $\vartheta$ is an adjusting constant that makes Equation V.3 usable for a crack geometry instead of a circular cross section.

II. The roughness Reynolds number, that is defined as

$$Re_* = \frac{\rho u_* \delta}{\mu} \tag{V.4}$$

where $\delta$ is the roughness of the rock.

III. The characteristic Reynolds number which is expressed as

$$Re = \frac{\rho V D_h}{\mu} \tag{V.5}$$

Note, there are relationships between different Reynolds numbers that connect them together. For example, the roughness Reynolds number and shear Reynolds number are related as

$$Re_* = Re^+ \frac{\delta}{\vartheta R_h} \tag{V.6}$$

Also, we can show that

$$\frac{V}{u_*} = \vartheta \frac{Re}{4Re^+} \tag{V.7}$$

The DR model uses these quantities to first define

$$r_l(Re^+) = \begin{cases} 1 & , \quad Re^+ < Re_c^+ \\ \left(\frac{Re_c^+}{Re^+}\right)^2 e^{\left(\frac{Re_c^+}{Re^+}\right)^2 - 1} & , \quad Re^+ \geq Re_c^+ \end{cases} \tag{V.8}$$

where $Re_c^+$ is the critical value of the shear Reynolds number and is the limiting value that after that the turbulent burst starts to appear, $r_l(Re^+)$ is the probability of the laminar occurrence, and $r_t(Re^+)$ is the probability of the turbulent occurrence. Note that $r_l + r_t = 1$. So based on the DR approach, for $Re_* \leq Re_{*c}$ (that is, the fluid flow is not wholly turbulent yet in another words, the surface roughness is not dominant over the laminar sub-layer)

$$\frac{V}{u_*} = \frac{r_l}{m} Re^+ + r_t \left[2.5 \ln Re^+ - 66.69 \left(Re^+\right)^{-0.72} + 1.8 - \mathcal{C}_1(Re_*)\right] \tag{V.9}$$

and

$$\begin{aligned} \mathcal{C}_1(Re_*) =& 2.5 \ln \left(\frac{1 + \frac{\alpha_c Re_*}{5}}{1 + \frac{\alpha_c \beta_c Re_*}{5}}\right) + 0.282 \left[\left(\frac{\alpha_c Re_*}{1 + \frac{\alpha_c Re_*}{5}}\right)^2 \right. \\ & \left. - \left(\frac{\alpha_c \beta_c Re_*}{1 + \frac{\alpha_c \beta_c Re_*}{5}}\right)^2\right] + \frac{0.5 \alpha_c Re_* (1 - \beta_c)}{\left(1 + \frac{\alpha_c Re_*}{5}\right)\left(1 + \frac{\alpha_c \beta_c Re_*}{5}\right)} \\ \theta_c =& \begin{cases} 0 & , \quad Re_* \leq Re_{*l} \\ \pi \left(\frac{\ln\left(\frac{Re_*}{Re_{*l}}\right)}{\ln\left(\frac{Re_{*c}}{Re_{*l}}\right)}\right) & , \quad Re_{*l} < Re_* \leq Re_{*c} \\ \pi & , \quad Re_* > Re_{*c} \end{cases} \\ \alpha_c =& \frac{1 - \cos\theta_c}{2} \\ \beta_c =& 1 - 0.4465 \left(\alpha_c + \frac{\theta_c}{\pi}\right) \end{aligned} \tag{V.10}$$

where $Re_{*l}$ and $Re_{*c}$ are the critical Reynolds numbers that define the angle of separation behind the roughness particles (see Yang and Dou (2010) for more details). Note that when $Re_* \leq Re_{*l}$, $\theta_c$ and $\alpha_c$ are $0$, and $\beta_c = 1$, thus $\mathcal{C}_1(Re_*) = 0$. After comparing the DR approach with Nikuradse's data, the value of $Re_{*l}$ and $Re_{*c}$ are found to be $1.25$ and $100$, respectively Yang and Dou (2010). According to the experimental data, when the Reynolds number increases, for very large values of Re, the friction factor will be independent of Re and will only be function of roughness (the rough-walled pipes, following the Gauckler-Manning-Strickler (GMS) model). Therefore, for $Re_* > Re_{*c}$, in order to capture Nikuradse's plot, we need to consider that the Reynolds number is no longer increasing and remains the constant value of $Re_{*c}$. From Equation V.6, DR model gives the relation between $Re_*$ and $Re^+$. Thus, for the case of $Re_* > Re_{*c}$, the Reynolds number $Re_*$ will not increase anymore and stays constant as $Re_{*c}$, so if we call $Re_T^+ = \frac{\vartheta R_h}{\delta} Re_{*c}$, from Equation V.9, DR model gives

$$\frac{V}{u_*} = \frac{r_l}{m} Re_T^+ + r_t \left[ 2.5 \ln Re_T^+ - 66.69 \left( Re_T^+ \right)^{-0.72} + 1.8 - \mathcal{C}_1(Re_{*c}) \right].$$

Equation V.9 modifies the equation originally provided by Yang and Dou (2010). The biggest difference is the introducing of variable $m$ in order to adjust the DR model to non-circular pipes, i.e. crack-like geometry. A close look at Equation V.9 shows that the first part of the equation handles the laminar regime and the second part is to take care of turbulent flow and the transition from laminar to turbulent. In general the friction factor in laminar regime is defined as $f_p = g/Re$ (see Munson et al. (2002)), where for circular pipes $g = 64$ while for parallel plates $g = 96$. This shows that we cannot use the same laminar equation for both geometries. The other difference between Equation V.9 relative to the original equation from Yang and Dou (2010) is related to the fact that we considered the DR parameters (defined as $D_*$ and $D_{*0}$ in original paper) to be equal to one because we do not consider any polymer in our fluid.

So far, only two parameters remain to set the value of the friction factor: the adjustment parameter $m$ in Equation V.9 and the critical Reynolds number ($Re_c^+$) from Equation V.8. We start with finding the value of $m$. If we consider the case that fluid regime is fully laminar ($Re^+ \leq Re_c^+$, or $r_l = 1$), from Equation V.9, we can obtain that $V/u_* = Re^+/m$. By combining this relation with Equation V.7, we can solve for $Re^+$ as function of $m$

$$Re^+ = \sqrt{\frac{m \vartheta Re}{4}} \tag{V.11}$$

Also from one side, the friction factor for fully laminar flow is defined as $g/Re$, and from the other side it defines as in Equation V.2. Thus, by equating these two definitions of friction factor and replacing the value of $Re^+$ from Equation V.11, we can show that

$$m = \frac{g\vartheta}{32} \tag{V.12}$$

So, for circular conduits (pipes), $m = 4$ (the same value as in original equations of Yang and Dou (2010)) and $\vartheta = 2$ while for two parallel plates the value of $m$ is $3\vartheta$.

Now we can move forward to find the value of $Re_c^+$. Now going back to Equation V.11 for the critical case we can read that (the fully laminar condition is still valid)

$$Re_c^+ = \sqrt{\frac{\vartheta m}{4} Re_c}$$

where $Re_c$ is the critical characteristic Reynolds number that is defined through Equation V.5. Following from pipe flow, the critical characteristic Reynolds number is $Re_c \approx 2300$ after that the fluid is no longer laminar. Therefore for the crack geometry ($m = 3\vartheta$), we argue that

$$Re_c^+ = 5\sqrt{69}\vartheta.$$

Moreover, we modified the equation for calculating $V/u_*$ for non-circular pipes by adding the parameter $m$. This adjustment will only affect the laminar portion of the equation and will not effect the turbulent part. This use of turbulent flow from the pipe model will add some error to this approach. Namely, for the turbulent and transition regimes, it is common to define the Reynolds number (Re) for non-circular conduits through the hydraulic diameter. Nevertheless, there is some evidence to suggest that keeping the friction factor depends on the aspect ratio of the cross-section of the flow. This implies that hydraulic diameter is not the only factor that can effect the value of friction factor. Following Jones (1976), the corrected Reynolds number is $2/3$ of the calculated Re by using hydraulic diameter. In this study we do not attempt a correction because: 1) an appropriate aspect ratio correction is not calculable; all the calculations are based on hydraulic diameter only, and 2) we introduced some other parameters like $\vartheta$ that can at least partially mediate the miscalculation due to only using of hydraulic diameter. Resolution of this issue for the hydraulic fracture geometry remains an issue of open research.

### 2. DR Model for Radial Flow

Now we will specify the DR model to the current boundary value problem. The fluid flux from Darcy-Weisbach friction factor is given by Equation V.1, which we modify to avoid imaginary values when $\partial p/\partial r > 0$.

$$q = -\operatorname{sgn}\left(\frac{\partial p}{\partial r}\right)\left|\frac{4w^3}{\rho f_p}\frac{\partial p}{\partial r}\right|^{1/2}, \tag{V.13}$$

For the radial crack the hydraulic diameter is $D_h = 2w(x,t)$, so

$$\begin{aligned} Re &= 2\frac{\rho V w}{\mu} \\ \frac{\delta}{R_h} &= \frac{2\delta}{w} \end{aligned} \tag{V.14}$$

where $R_h$ is the hydraulic radius ($R_h = D_h/4$), and $\delta$ is the roughness of the crack. Now, if we combine Equation V.13 with V.2 and use Equation V.12 for parallel plates ($g = 96$), and replace the result in Equation V.14 for Reynolds number, and finally using Equation V.7, we can show

$$Re^+ = 3\vartheta\left|\frac{2\rho w^3}{\mu'^2}\frac{\partial p}{\partial r}\right|^{1/2} \tag{V.15}$$

where $\mu' = 12\mu$. Now by knowing the shear Reynolds number $Re^+$, we can find $r_t$ and $r_l$ through Equation V.8, and from there we can find $R_*$ and $C_1$. Then by knowing $V/u_*$ we can finally find $f_p$ (Equation V.2) and calculate fluid flux (Equation V.13).

According to the DR method we can find the friction factor, and after that by using Equation V.13 we can find the proper fluid flow. Therefore, based on the discussion given section V.D.1, the fluid flow will fall into one the following conditions:

I. Laminar: $Re_* \leq Re_{*l}$ and $Re^+ < Re_c^+$. In this case, based on Equation V.10, $\mathcal{C}_1(Re_*) = 0$, and from Equation V.8, $r_l$=1 and $r_t = 0$. Note that $Re_*$ is connected to $Re^+$ through Equation V.6.

II. Smooth-walled: $Re_* \leq Re_{*l}$ but $Re^+ \geq Re_c^+$. In this case, based on Equation V.10, $\mathcal{C}_1(Re_*) = 0$, and from Equation V.8, $r_t \neq 0$ and we have $r_l + r_t = 1$. Also, $Re_*$ is connected to $Re^+$ through Equation V.6.

III. Laminar: $Re_{*l} < Re_* \leq Re_{*c}$ and $Re^+ < Re_c^+$. In this case, based on Equation V.10, $\mathcal{C}_1(Re_*) \neq 0$, and from Equation V.8, $r_l$=1 and $r_t = 0$. Also, $Re_*$ is connected to $Re^+$ through Equation V.6.

IV. Transition-Turbulent: $Re_{*l} < Re_* \leq Re_{*c}$ and $Re^+ \geq Re_c^+$. In this case, based on Equation V.10, $\mathcal{C}_1(Re_*) \neq 0$, and from Equation V.8, $r_t \neq 0$ and we have $r_l + r_t = 1$. Also, $Re_*$ is connected to $Re^+$ through Equation V.6.

V. Laminar: $Re_* > Re_{*c}$ and $Re^+ < Re_c^+$. In this case, based on Equation V.10, $\mathcal{C}_1(Re_*) = \mathcal{C}_1(Re_{*c})$ and will remain constant. It is important to bear in mind that sequence of applying the limits is very important in this case and case VI. Since $Re_*$ will stay constant, from Equation V.6, we should redefine $Re^+$ as $Re_{*c}\vartheta w/2\delta$. It is radially confirmed that because $Re^+ < Re_c^+$, we have $r_l = 1$ and $r_t = 0$, which means that the value of $\mathcal{C}_1(Re_*)$ is irrelevant because it will multiply to zero. This simplification is correct as long as we understand that the value of $Re^+$ is redefined in its use for this.

VI. Rough-walled fully turbulent: $Re_* > Re_{*c}$ and $Re^+ \geq Re_c^+$. In this case, based on Equation V.10, $\mathcal{C}_1(Re_*) = \mathcal{C}_1(Re_{*c})$ and will stay constant. As in case V the value of $Re^+$ will redefined as $Re_{*c}\vartheta w/2\delta$ and remains constant unless $w$ changes.

Note we always have $Re_{*c} \geq Re_c^+ > Re_{*l}$, so basically case I and III can be combined to one case of $Re^+ \frac{2\delta}{\theta w} \leq Re_{*c}$ with $Re^+ < Re_c^+$. Therefore, the fluid flow is categorize into five groups. The summary of the previous discussion is provided in Figure V.3

## 3. Governing Equations for a Radial Hydraulic Fracture

Having established the fluid flow equations, the model is completed using a classical HF formulation, very similar to Savitski and Detournay (2002) in its details. From elasticity for radial cracks, we can relate pressure and the opening as

$$-\frac{R^2}{E'}p(r,t) = \int_0^R G(\frac{r}{R}, \frac{s}{R})w(s,t)ds \tag{V.16}$$

where $R$ is the radius of the crack as shown Figure V.1, and $G(r,s)$ is the kernel of the elasticity integral Sneddon and Lowengrub (1969) where

$$G(\xi,\eta) = \begin{cases} \frac{1}{\xi}\mathcal{F}\left(\arcsin\sqrt{\frac{1-\xi^2}{1-\eta^2}}, \frac{\eta^2}{\xi^2}\right), & \xi > \eta \\ \frac{1}{\eta}\mathcal{F}\left(\arcsin\sqrt{\frac{1-\eta^2}{1-\xi^2}}, \frac{\xi^2}{\eta^2}\right), & \xi < \eta \end{cases} \tag{V.17}$$

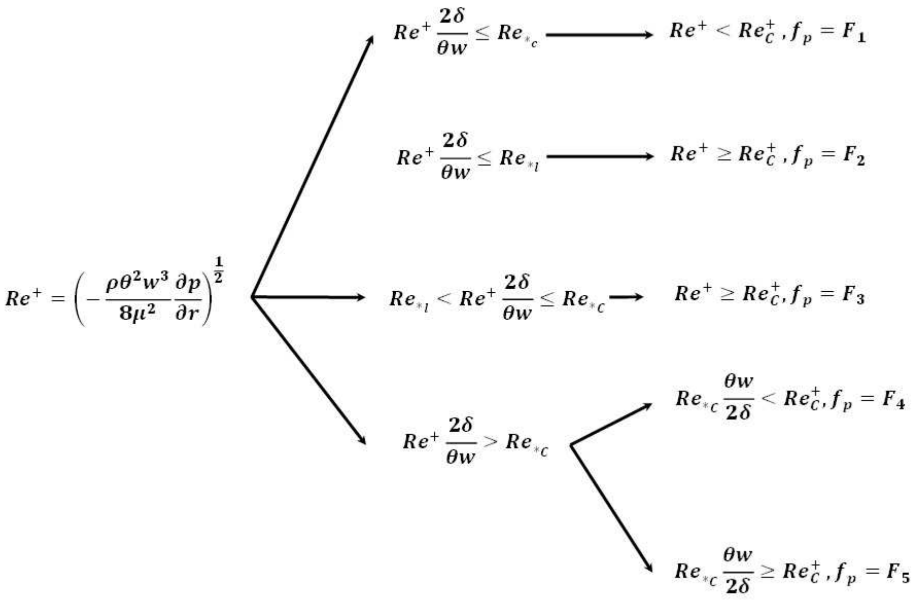

Figure V.3: Flow graph.

There is also different methods to represent the kernel of the elasticity integral. For the purpose of the numerical modeling, we will use the kernel that is developed by displacement discontinuity model Hills et al. (1996); Korsunsky (1994). To make the equations simpler let us define

$$E' = \frac{E}{1-\nu^2} \quad , \qquad K' = \frac{8}{\sqrt{2\pi}} K_{IC} \tag{V.18}$$

From conservation of mass for an in-compressible fluid flowing in a radial crack, we can obtain the fluid continuity equation

$$\frac{\partial w}{\partial t} + \frac{1}{r}\frac{\partial}{\partial r}(rq) = 0 \tag{V.19}$$

For the purpose of crack propagation criteria, based on the LEFM, the crack will propagate if the crack intensity factor ($K_I$) becomes equal or greater than fracture toughness ($K_{IC}$) of the material (or $K_I = K_{IC}$ for stable crack growth). The stress intensity factor for the radial crack geometry is defined as Rice (1968)

$$K_I = \frac{2}{\sqrt{\pi R}} \int_0^R \frac{pr}{\sqrt{R^2 - r^2}} dr \tag{V.20}$$

It has been known that because of multiscale nature of the crack tip in hydraulic fracture, the strain energy release rate in crack tip is either dominated by the singularity induced from fluid continuity,

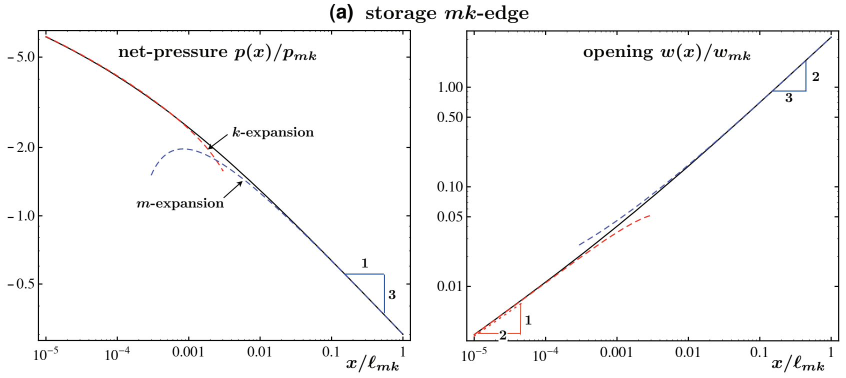

Figure V.4: Universal crack tip solution for no leakoff case Garagash et al. (2011), with permission.

or from the elasticity equation Desroches et al. (1994). Garagash et al. (2011) introduced a universal crack tip solution for hydraulic fracture. Following the solution provided by Garagash et al. (2011) for universal crack tip solution for no-leakoff case (mk-edge), if we have

$$\begin{gathered}\ell_k = \left(\frac{K'}{E'}\right)^2 \quad , \qquad \ell_m = V\frac{\mu'}{E'} \quad , \qquad \ell_{mk} = \frac{\ell_k^3}{\ell_m^2} \\ w_{mk} = \frac{\ell_k^2}{\ell_m} \quad , \qquad p_{mk} = E'\frac{\ell_m}{\ell_k}\end{gathered} \tag{V.21}$$

where $V$ is the crack propagation velocity, and

And finally the initial conditions and boundary conditions are:

$$\begin{aligned}&2\pi \lim_{r\to 0} rq = Q_0 \\ &w(R,t) = 0 \;\; , \;\; q(R,t) = 0 \\ &w(r,0) = 0 \;\; , \;\; q(r,0) = 0\end{aligned} \tag{V.22}$$

It will also be convenient to integrate V.19 subject to V.22 to obtain the global mass balance, expressed as

$$Q_0 t = 2\pi \int_0^R w r dr \tag{V.23}$$

## E. SCALING

In order to non-dimensionalize and eventually simplify the problem, we used the following scaling

$$
\begin{aligned}
&w = \varepsilon L \Omega(\xi, t) \ , \quad p = \varepsilon E' \Pi(\xi, t) \ , \quad R = L\gamma(t) \\
&q = Q_0 \Psi(\xi, t) \ , \qquad \xi = \frac{r}{R} \qquad , \quad t = \tau T
\end{aligned}
\tag{V.24}
$$

where $\varepsilon$, $L$, and $T$ are the scaling parameters that will be chosen later. To make the equations simpler we can consider $\Omega = \gamma^{1/2}\overline{\Omega}$, and $\Pi = \gamma^{-1/2}\overline{\Pi}$. Moreover, if we consider $\tilde{\Psi} = \xi\Psi$, we we can find the scaled governing equations as:

I. Continuity equation:

$$
\dot{\overline{\Omega}} + \frac{\dot{\gamma}}{2\gamma}\overline{\Omega} - \xi\frac{\dot{\gamma}}{\gamma}\frac{\partial\overline{\Omega}}{\partial\xi} = -\frac{TQ_0}{\xi\varepsilon L^2}\frac{1}{\gamma^{3/2}}\frac{\partial}{\partial\xi}(\tilde{\Psi})
\tag{V.25}
$$

where $(\dot{\ })$ is defined as derivative with respect to $\tau$. Also we can define global mass balance as:

$$
\tau = \frac{2\pi\varepsilon L^3}{Q_0 T}\gamma^{5/2}\int_0^1 \overline{\Omega}\zeta d\zeta
\tag{V.26}
$$

II. Elasticity Equation:

$$
\overline{\Pi} = -\int_0^1 G(\xi,\zeta)\overline{\Omega} d\zeta
\tag{V.27}
$$

III. Initial and boundary conditions

$$
\begin{aligned}
&\lim_{\xi\to 0}\tilde{\Psi} = \frac{1}{2\pi L\gamma} \\
&\overline{\Omega}(1,\tau) = 0 \ , \ \ \tilde{\Psi}(1,\tau) = 0
\end{aligned}
\tag{V.28}
$$

From scaled equations we find the following non-dimensional groups:

$$
\mathcal{G}_v = \frac{Q_0 T}{2\pi\varepsilon L^3} \quad , \quad \mathcal{G}_k = \frac{K'}{\varepsilon E'\sqrt{L}} \quad , \quad \mathcal{G}_T = \frac{L}{T\varepsilon}\left(\frac{2\rho}{E'}\right)^{\frac{1}{2}} \quad , \quad \mathcal{G}_m = \frac{\mu'}{TE'\varepsilon^3}.
\tag{V.29}
$$

Since we added three unknowns $(\varepsilon,\ L,\ T)$, we can define three conditions. So, by considering $\mathcal{G}_v = \mathcal{G}_T = \mathcal{G}_m = 1$, we obtain

$$\begin{aligned}
\varepsilon &= \mu' \left( \frac{\pi}{\sqrt{2} Q_0 \rho^{3/2} E'^{1/2}} \right)^{\frac{1}{2}} \\
L &= \frac{Q_0 \rho}{\pi \mu'} \\
T &= 2^{3/4} \frac{Q_0^{3/2} \rho^{9/4}}{\pi^{3/2} \mu'^2 E'^{1/4}} \\
\mathcal{G}_k &= \frac{2^{1/4} \rho^{1/4} K'}{\mu'^{1/2} E'^{3/4}}
\end{aligned} \tag{V.30}$$

Also, by scaling the DR model, we can define

$$\mathcal{R}_t = \frac{\rho^{1/4} Q_0^{1/2}}{2^{5/4} \sqrt{\pi} \delta E'^{1/4}},$$

so that

$$\begin{aligned}
Re^{+} &= 3\vartheta \left| -\overline{\Omega}^3 \frac{\partial \overline{\Pi}}{\partial \xi} \right|^{1/2} \\
Re_{*l} \frac{\vartheta w}{2\delta} &= \vartheta Re_{*l} \mathcal{R}_t \gamma^{1/2} \overline{\Omega} \\
Re_{*c} \frac{\vartheta w}{2\delta} &= \vartheta Re_{*c} \mathcal{R}_t \gamma^{1/2} \overline{\Omega}
\end{aligned} \tag{V.31}$$

Here we can re-write all the governing equations (V.25 - V.28 ) as

I. Continuity equation:

$$\dot{\overline{\Omega}} + \frac{\dot{\gamma}}{2\gamma} \overline{\Omega} - \xi \frac{\dot{\gamma}}{\gamma} \frac{\partial \overline{\Omega}}{\partial \xi} = -\frac{1}{\xi} \frac{1}{\gamma^{3/2}} \frac{\partial}{\partial \xi} \frac{Q_0 T}{\varepsilon L^2} \tilde{\Psi} \tag{V.32}$$

Also we can define global mass balance as:

$$\tau = \gamma^{5/2} \int_0^1 \overline{\Omega} \zeta d\zeta \tag{V.33}$$

II. Elasticity Equation:

$$\overline{\Pi} = - \int_0^1 G(\xi, \zeta) \overline{\Omega} d\zeta \tag{V.34}$$

III. Initial and boundary conditions

$$\begin{aligned}
&\lim_{\xi \to 0} \frac{Q_0 T}{\varepsilon L^2} \tilde{\Psi} = \frac{1}{\gamma} \\
&\overline{\Omega}(1, \tau) = 0 \ , \quad \tilde{\Psi}(1, \tau) = 0
\end{aligned} \tag{V.35}$$

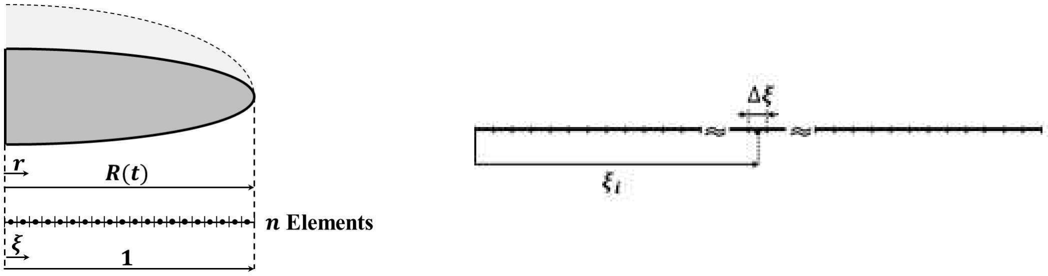

Figure V.5: Discretized crack.

## F. NUMERICAL METHOD

The numerical analysis is based on the conceptual framework proposed by Lecampion and Detournay (2007); Bunger (2005). Wherein: 1) An implicit crack length-stepping approach is adopted and the governing equations are discretized using moving mesh algorithm. 2) Fluid flow equations are solved using a finite difference method, and 3) the elasticity equation is discretized using the displacement discontinuity method (DDM, Crouch et al. (1983)). In the DDM, we consider that the crack is discretized to $n$ equidistant elements. Because we are working on the scaled coordinate, the distribution of elements are from $0 < \xi < 1$, as in Figure V.5. Once the elements are established, the opening and fluid pressure are assumed to be uniform for each element. We represent the $i^{th}$ element's location by its middle point with $\xi_i$.

Hence, $\overline{\Omega}_i^\tau$ and $\overline{\Pi}_i^\tau$ are the opening and pressure of the $i^{th}$ element at time $\tau$, respectively, and $\gamma^\tau$ is the crack length at time $\tau$. Therefore, if we define

$$\mathcal{S} = \frac{2\Delta\tau}{\Delta\gamma\sqrt{\gamma^\tau}(\Delta\xi)^2}$$

the discretized governing equations become (for more detail see Appendix D.A)

I. Continuity equation

for $i = 1$ (first element):

$$\left(1+\frac{\gamma^\tau}{\Delta\gamma}\right)\Delta\overline{\Omega}_1^\tau - \frac{1}{2}\Delta\overline{\Omega}_2^\tau = \frac{1}{2}\overline{\Omega}_2^{\tau-\Delta\tau} - \overline{\Omega}_1^{\tau-\Delta\tau} + \frac{\mathcal{S}}{\gamma^\tau} - \mathcal{S}\frac{Q_0 T}{\varepsilon L^2}\tilde{\Psi}^\tau_{\frac{3}{2}} \tag{V.36}$$

which incorporates inlet boundary condition applied at the first node whereby

$$\frac{Q_0 T}{\varepsilon L^2}\tilde{\Psi}^{\tau}_{\frac{1}{2}} = \frac{1}{\gamma^{\tau}} \tag{V.37}$$

for $i = 2, \cdots, n-1$:

$$\begin{aligned}\left(1+\frac{2\gamma^{\tau}}{\Delta\gamma}\right)\Delta\overline{\Omega}^{\tau}_{i} - \left(i-\frac{1}{2}\right)\Delta\overline{\Omega}^{\tau}_{i+1} + \left(i-\frac{1}{2}\right)\Delta\overline{\Omega}^{\tau}_{i-1} = \\ \left(i-\frac{1}{2}\right)\overline{\Omega}^{\tau-\Delta\tau}_{i+1} - \left(i-\frac{1}{2}\right)\overline{\Omega}^{\tau-\Delta\tau}_{i-1} - \overline{\Omega}^{\tau-\Delta\tau}_{i} \\ + \frac{\mathcal{S}}{i-\frac{1}{2}}\left[\frac{Q_0 T}{\varepsilon L^2}\tilde{\Psi}^{\tau}_{i-\frac{1}{2}} - \frac{Q_0 T}{\varepsilon L^2}\tilde{\Psi}^{\tau}_{i+\frac{1}{2}}\right]\end{aligned} \tag{V.38}$$

and for $i = n$ (tip element):

$$\begin{aligned}\left(\frac{2\gamma^{\tau}}{\Delta\gamma}+n+\frac{1}{2}\right)\Delta\overline{\Omega}^{\tau}_{n} + \left(n-\frac{1}{2}\right)\Delta\overline{\Omega}^{\tau}_{n-1} = -\left(n+\frac{1}{2}\right)\Delta\overline{\Omega}^{\tau-\Delta\tau}_{n} \\ - \left(n-\frac{1}{2}\right)\Delta\overline{\Omega}^{\tau-\Delta\tau}_{n-1} + \frac{\mathcal{S}}{n-\frac{1}{2}}\frac{Q_0 T}{\varepsilon L^2}\tilde{\Psi}^{\tau}_{n-\frac{1}{2}}\end{aligned} \tag{V.39}$$

which incorporates the zero flux condition at the tip whereby

$$\tilde{\Psi}^{\tau}_{n+\frac{1}{2}} = 0 \tag{V.40}$$

Note that the algorithm will also make use of global mass balance

$$\tau = \gamma^{\tau\,5/2}\left(\Delta\xi\right)^2 \sum_{j=1}^{n} \overline{\Omega}^{\tau}_{j}\left(j-\frac{1}{2}\right) \tag{V.41}$$

II. Elasticity Equation: The DDM representation of the elasticity equation is given by

$$\overline{\boldsymbol{\Pi}}^{\boldsymbol{\tau}} = -\boldsymbol{M}\overline{\boldsymbol{\Omega}}^{\boldsymbol{\tau}}, \quad \text{or} \quad \overline{\Pi}^{\tau}_{i} = -\sum_{j=1}^{n} M_{ij}\overline{\Omega}^{\tau}_{j} \tag{V.42}$$

where the influence matrix is defined as

$$M_{ij} = g(\xi_i, \xi_j + \Delta\xi/2) - g(\xi_i, \xi_j - \Delta\xi/2)$$

with

$$g(\xi,\eta) = -1\frac{1}{4\eta}\bar{J}_{101}(\frac{\xi}{\eta}, 0)$$

and wherein $\bar{J}_{mnp}(x,y)$ is the Lifshitz-Hankel integral (for more details see Appendix D.A.1). Hence, In the elasticity equation the $n \times n$ influence matrix $\boldsymbol{M}$ connects the opening at the center of the elements ($\overline{\boldsymbol{\Omega}}^{\tau}$) at time step $\tau$ to the fluid pressure at the center of elements ($\overline{\boldsymbol{\Pi}}^{\tau}$). T

III. Fluid flow:

Based on the scheme illustrated in Figure V.3 and detailed in Equation D.18, the discretized form of the DR fluid flow law is (for more detail see Appendix D.A.5)

- $F_1$ (Laminar): If $\mathcal{E}^{\tau}_{1,i+\frac{1}{2}} \leq \mathcal{E}^{\tau}_{2,i+\frac{1}{2}}$ and $\mathcal{E}^{\tau}_{1,i+\frac{1}{2}} < \mathcal{E}^{\tau}_{3,i+\frac{1}{2}}$

$$\mathcal{S}\frac{Q_0 T}{\varepsilon L^2}\tilde{\Psi}^{\tau}_{i+\frac{1}{2}} = \mathcal{T}^{\tau}_{4,i}\sum_{j=1}^{n}\mathcal{H}_{i,j}\overline{\Omega}^{\tau-\Delta\tau}_{j} + \mathcal{T}^{\tau}_{4,i}\sum_{j=1}^{n}\mathcal{H}_{i,j}\Delta\overline{\Omega}^{\tau}_{j} \tag{V.43a}$$

- $F_2$ (Smooth-walled): If $\mathcal{E}^{\tau}_{3,i+\frac{1}{2}} \leq \mathcal{E}^{\tau}_{1,i+\frac{1}{2}} \leq \mathcal{E}^{\tau}_{4,i+\frac{1}{2}}$

$$\mathcal{S}\frac{Q_0 T}{\varepsilon L^2}\tilde{\Psi}^{\tau}_{i+\frac{1}{2}} = \mathcal{T}^{\tau}_{1,i}\sum_{j=1}^{n}\mathcal{H}_{i,j}\overline{\Omega}^{\tau-\Delta\tau}_{j} + \mathcal{T}^{\tau}_{1,i}\sum_{j=1}^{n}\mathcal{H}_{i,j}\Delta\overline{\Omega}^{\tau}_{j} \tag{V.43b}$$

- $F_3$ (Transition-Turbulent): If $\mathcal{E}^{\tau}_{4,i+\frac{1}{2}} < \mathcal{E}^{\tau}_{1,i+\frac{1}{2}} \leq \mathcal{E}^{\tau}_{2,i+\frac{1}{2}}$ and $\mathcal{E}^{\tau}_{3,i+\frac{1}{2}} \leq \mathcal{E}^{\tau}_{1,i+\frac{1}{2}}$

$$\mathcal{S}\frac{Q_0 T}{\varepsilon L^2}\tilde{\Psi}^{\tau}_{i+\frac{1}{2}} = \mathcal{T}^{\tau}_{5,i}\sum_{j=1}^{n}\mathcal{H}_{i,j}\overline{\Omega}^{\tau-\Delta\tau}_{j} + \mathcal{T}^{\tau}_{5,i}\sum_{j=1}^{n}\mathcal{H}_{i,j}\Delta\overline{\Omega}^{\tau}_{j} \tag{V.43c}$$

- $F_4$ (Laminar): If $\mathcal{E}^{\tau}_{2,i+\frac{1}{2}} < \mathcal{E}^{\tau}_{3,i+\frac{1}{2}}$ and $\mathcal{E}^{\tau}_{2,i+\frac{1}{2}} < \mathcal{E}^{\tau}_{1,i+\frac{1}{2}}$

$$\mathcal{S}\frac{Q_0 T}{\varepsilon L^2}\tilde{\Psi}^{\tau}_{i+\frac{1}{2}} = \mathcal{T}^{\tau}_{3,i}\sum_{j=1}^{n}\mathcal{H}_{i,j}\overline{\Omega}^{\tau-\Delta\tau}_{j} + \mathcal{T}^{\tau}_{3,i}\sum_{j=1}^{n}\mathcal{H}_{i,j}\Delta\overline{\Omega}^{\tau}_{j} \tag{V.43d}$$

- $F_5$ (Rough-walled fully turbulent): If $\mathcal{E}^{\tau}_{3,i+\frac{1}{2}} \leq \mathcal{E}^{\tau}_{2,i+\frac{1}{2}}$ and $\mathcal{E}^{\tau}_{2,i+\frac{1}{2}} < \mathcal{E}^{\tau}_{1,i+\frac{1}{2}}$

$$\mathcal{S}\frac{Q_0 T}{\varepsilon L^2}\tilde{\Psi}^{\tau}_{i+\frac{1}{2}} = \mathcal{T}^{\tau}_{2,i}\sum_{j=1}^{n}\mathcal{H}_{i,j}\overline{\Omega}^{\tau-\Delta\tau}_{j} + \mathcal{T}^{\tau}_{2,i}\sum_{j=1}^{n}\mathcal{H}_{i,j}\Delta\overline{\Omega}^{\tau}_{j} \tag{V.43e}$$

In order to make the fluid flow equation less symbolically intensive here, we defined the quantities ($\mathcal{H}_{i,j}$, $\mathcal{T}^{\tau}_{i,j}$, $\mathcal{E}^{\tau}_{i,j}$) which are long expressions relegated to Appendix D.A.5, Equations D.22, D.21, and D.19, respectively.

IV. Tip criterion:

The accuracy of the numerical solution is strongly dependant on appropriate handling of the near crack tip behavior using a suitable crack tip solution. In order to achieve the solution using LEFM, we would need to use many elements and specially when the fluid regime is more turbulent the laminar region at crack tip will be very small and it will get to the point that the numerical model will not be computationally efficient or even feasible to carry out in a practically relevant time-frame Lecampion et al. (2013). Therefore, we instead achieve the crack tip solution from analytical models. In this paper, recall that, we focused on modeling the zero toughness solution. Therefore, following the m-vertex solution the crack tip Desroches et al. (1994); Garagash et al. (2011)

$$w = 2^{1/3} \times 3^{5/6} \left( \frac{\mu' \dot{R} R^2}{E'} \right)^{1/3} \left(1 - \frac{r}{R}\right)^{2/3} + O\left[ \left(1 - \frac{r}{R}\right)^{5/3} \right]$$

and integrating the volume of the crack tip, we obtain that

$$\mathcal{V} = 2\pi \int_{r_d}^{R} \eta w(\eta, t) d\eta = \frac{3^{11/6}\pi}{2^{5/3} \times 5} \left( \frac{\mu' \dot{R} R^8}{E'} \right)^{1/3} \left(3 + 5\frac{r_d}{R}\right) \left(1 - \frac{r_d}{R}\right)^{5/3}$$

After scaling, the tip volume becomes

$$\int_{\xi_d}^{1} \eta \overline{\Omega}(\eta, \tau) d\eta = \frac{3^{11/6}}{2^{8/3} \times 5} \gamma^{1/6} \dot{\gamma}^{1/3} \left(3 + 5\xi_d\right) \left(1 - \xi_d\right)^{5/3}$$

Anticipating that this equation will be used to govern the advance of the crack tip. For better stability, we use the last $m_l$ number of elements instead of only the last element to find the volume of the crack tip. So if $\xi_d = r_d/R$, the discretized form of the crack tip volume is

$$\Delta\tau = \frac{3^{11/2}}{2^8 \times 5^3} \frac{\gamma^{\tau 1/2} \Delta\gamma \left[(3 + 5(n - m_l)\Delta\xi\right]^3 \left[1 - (n - m_l)\Delta\xi\right]^5}{\Delta\xi^3 \left( \sum_{j=n-m_l+1}^{n} \xi_j \overline{\Omega}_j \right)^3} \qquad \text{(V.44)}$$

Bringing together the elasticity equation to eliminate the pressure in the local continuity equations can be expressed as (see Appendix D.A.6)

$$\boldsymbol{\Xi}(\boldsymbol{\Delta\Omega^{\tau}}) \times \boldsymbol{\Delta\Omega^{\tau}} = \boldsymbol{\mathcal{H}}(\boldsymbol{\Omega^{\tau-\Delta\tau}}) \tag{V.45}$$

where bold notations refer to matrix form and under tilde refers to vector formats. The algorithm to solve the problem consists of an iterative method to solve for change of opening $\Delta\Omega^{\tau}$ according to Equation V.45 corresponding to each fixed length step $\Delta\gamma$ and according time-step given by $\Delta\tau$.

The numerical method that we use to solve the problem is following the bellow steps:

I. Define initial opening from GMS solution, Savitski's solution, or an estimate between these two asymptotic ($\Delta\Omega^{\tau}$).

II. Choose $\Delta\overline{\Omega}^{\tau,1}$ to be zero, and set an initial value for $\Delta\tau^{i}$, i.e. $10^{-6}$.

III. Advanced the scaled crack length by $\Delta\gamma$.

IV. Solve Equation V.44 to find the iterative value of change of opening ($\Delta\Omega^{\tau,\kappa-1}$) for the given values of $\Delta\tau^{i}$, and $\Delta\gamma$. Therefore, we change the local continuity to

$$\boldsymbol{\Xi}(\boldsymbol{\Delta\Omega^{\tau,\kappa-1}}) \times \boldsymbol{\Delta\Omega^{\tau}} = \boldsymbol{\mathcal{H}}(\boldsymbol{\Omega^{\tau-\Delta\tau}}) \tag{V.46}$$

where $\Delta\Omega^{\tau,\kappa-1}$ means the change of opening at time $\tau$ from previous iteration.

V. Compute the residual value from the comparison of the value of the iterative change of opening with the previous iteration as

$$\delta_{\Omega} = \frac{\sum_{j=1}^{n}\left(\Delta\overline{\Omega}_{j}^{\tau,\kappa} - \Delta\overline{\Omega}_{j}^{\tau,\kappa-1}\right)^{2}}{\sum_{j=1}^{n}\left(\Delta\overline{\Omega}_{j}^{\tau,\kappa}\right)^{2}}.$$

If the value of $\delta_{\Omega}$ is less than a tolerance, the solution is converged. If convergence criterion is satisfied, go to next step; otherwise, repeat step V.

VI. Find the time step ($\Delta\tau$) from Equation V.44 and construct a residual value as

$$\delta_{\tau} = \frac{|\Delta\tau - \Delta\tau^{i}|}{\Delta\tau}$$

If the value of $\delta_{\tau}$ is smaller than a provided tolerance, go to next step. If it does not satisfy the convergence criteria for the time step, consider $\Delta\tau^{i} = \Delta\tau$ and go back to step IV.

VII. If the crack length is less than the expected value, go to step II. If the crack length is equal to the expected value, stop the numerical modeling.

## G. RESULTS

Discussion of the results of the numerical simulations will include:

- Checking for the convergence of the numerical solution and its stability,
- Benchmarking of the numerical simulation with laminar/rough-walled asymptotic solutions, and
- Discussion about the effect of the transition/turbulent regime on HF growth.

Unless otherwise stated, parameters used for these benchmarking and parametric study activities are given by Table V.1.

Table V.1: Material properties and physical constants that are used for each run in numerical model.

| **Figures** | **Parameters** | | | | | | | |
|---|---|---|---|---|---|---|---|---|
| | $Q_0$ (m$^3$ s$^{-1}$) | $\nu$ | $\mu$ (cP) | $\rho$ (kg m$^{-3}$) | $k$ (mm) | $m$ | $E$ (GPa) | $\alpha$ |
| V.6 - V.10 | 0.05 | 0.2 | 0.1 | 600 | 0.01 | 0.143 | 25 | 1/3 |
| V.11a | 0.1 | | 10 | 600 | 0.01 | | 25 | |
| V.11b | 0.1 | | 0.1 | 600 | 0.01 | | 25 | |
| V.11c | 0.1 | | 0.001 | 600 | 0.01 | | 25 | |
| V.12,V.13 (Red line) | 2.5 | | 0.1 | 1000 | 0.001 | | 5 | |
| V.12,V.13 (Blue line) | 0.005 | | 0.1 | 600 | 0.01 | | 100 | |
| V.16 | 2.5 | | 0.1 | 1000 | 0.001 | | 5 | |
| V.14, V.15 | 0.005 | | 0.1 | 600 | 0.01 | | 100 | |

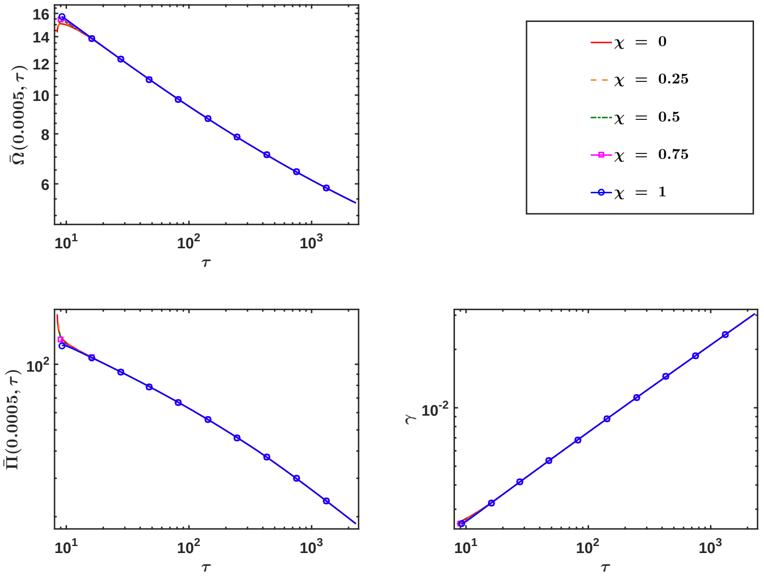

Figure V.6: Study of the effect of various initial conditions, $\chi$, on the numerical code

### 1. Convergence

To verify independence of the solution from the initial conditions, we solved a model with the properties explained in Table V.1 and studied the effect of the initial condition on the convergence of the solution. Figure V.6 indicates that after only few steps the result will converge to a solution that is insensitive to the details of the initial solution of the starting time. In Figure V.6, we vary the imitial condition by linearly interpolating between the laminar and turbulent assymptotic solutions, given in Appendix D.C and D.B, respectively. At first, we vary just the initial condition on the opening using

$$w_{ini} = (1-\chi)w_{laminar} + \chi w_{GMS}. \tag{V.47}$$

Thus, if $\chi = 1$, the initial case is fully turbulent and if $\chi = 0$ the initial case is fully laminar. Figure V.6 demonstrates that there is very little variation in the results of the numerical model due to different value of the interpolating parameter $\chi$.

Next, we studied the sensitivity of the solution to different values of the initial length. Figure V.7 shows that the initial length impacts only the solution over the first few time steps, after which the solution converges to a result that is insensitive to the initial length.

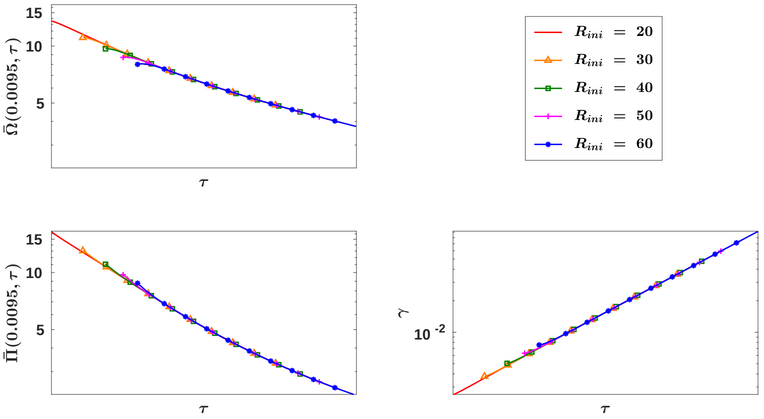

Figure V.7: Study the effect of initial length on the solution

In spite of this apparent insensitivity of the solution to the initial conditions, sometimes it is useful to reduce initial inaccuracy associated with the solution. This is helpful, for example, when multiple runs are used to track growth over a wide range of time. A primary iterative scheme can reduce this inaccuracies using the following steps:

I. Choose a starting opening ($\Omega^{initial}$) for the initiation from Equation V.47 (it is better to guess a proper $\chi$ that is sensibly close).

II. Solve numerically for only one step. Assume that the crack is advanced by $\Delta\gamma$.

III. Find the opening for the next step (call it $\Omega_2^{initial}$) but do not advance the length for the next step. Compare the opening with initial opening and construct a residual value as

$$\delta_{\Omega}^{initial} = \frac{\sum_{j=1}^{n}\left(\overline{\Omega}_j^{initial} - \overline{\Omega}_j^{initial,2}\right)^2}{\sum_{j=1}^{n}\left(\overline{\Omega}_j^{initial}\right)^2}.$$

If the value of $\delta_{\Omega}^{initial}$ is smaller than a provided tolerance, terminate the running and choose the value of opening as more accurate initial guess for the problem. If it does not satisfy the convergence criteria for the opening, consider $\Omega^{initial} = \Omega_2^{initial}$ and repeat step II.

Using the iterative solving approach at the first time step results in more stable numerical convergence at early time. Figure V.8 illustrates the effect of correcting the initial guess and solving the problem for different starting length (compare it with Figure V.7).

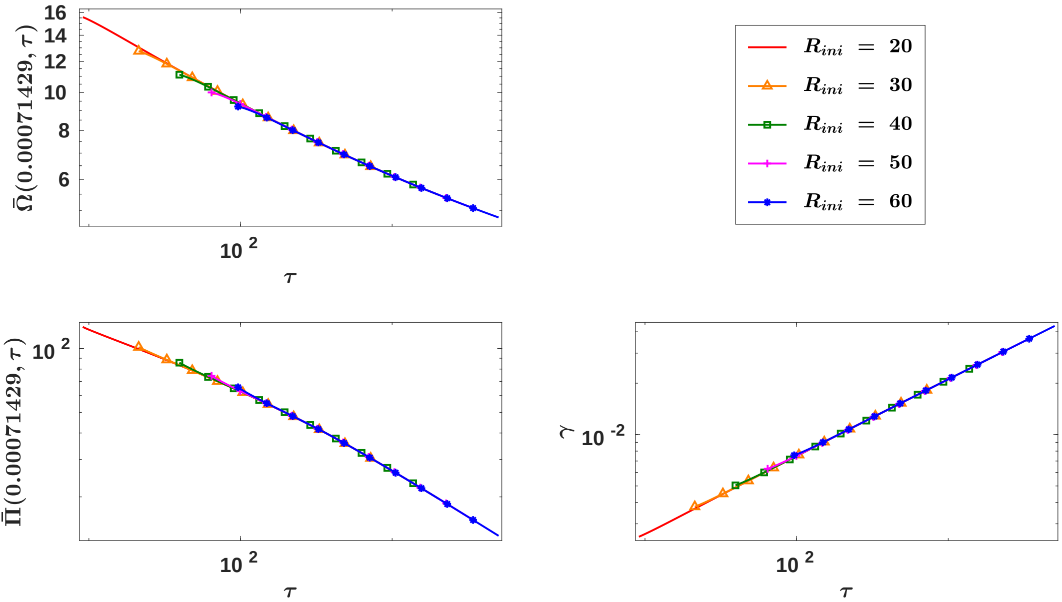

Figure V.8: Study the effect of initial length on the solution with using corrected initial guess.

Having established sufficient insensitivity of the solution to initial conditions, next we investigate the sensitivity of the solution to the number of the elements. This step is important, because it will help us understand if the solution is mesh dependant. Figure V.9 indicates the relative difference of the scaled crack opening, fluid pressure, and crack length for various numbers of elements to the solution obtained with the finest mesh division (800 elements). Also, we examine how well the solution satisfies global volume balance by showing the percentage error of the crack volume relative to the amount of fluid pumped. Based on Figure V.9, when using 400 elements the relative error is less than $10^{-4}$ $(0.01\%)$ for the crack volume, and the relative difference compared to simulations with 800 elements is $0.02$ $(2\%)$ for the inlet crack opening, about $0.01$ $(1\%)$ for pressure (checked here at $54\ m$ after $100\ sec$), and at most $0.01$ $(1\%)$ for the crack length. Hence, the solution can be considered to have converged with 400 elements. Even with only 60 elements, the error on the volume is only about $0.002$ $(0.2\%)$, with relative differences of inlet opening, pressure, and length around $10\ \%$, $1\ \%$, and $0.01 - 1\ \%$, respectively.

It is important to realize that considering the inlet opening comprises a worst case location. Figure V.10 demonstrates the change of crack opening and fluid pressure along the crack by changing

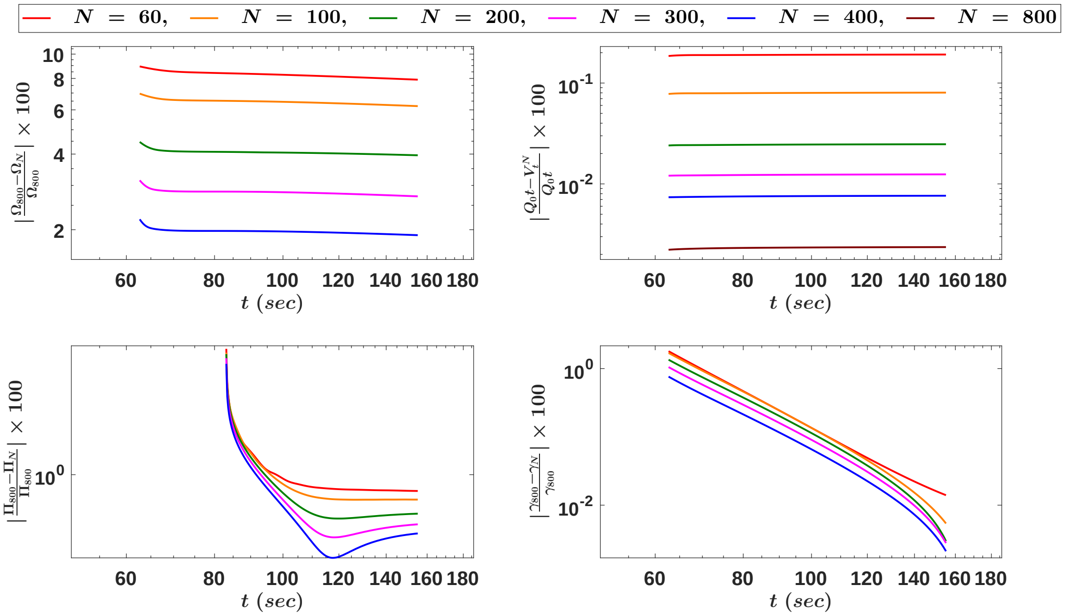

Figure V.9: Percentage error for wellbore scaled opening, fluid pressure at $54\ m$, crack volume, and crack length.

the number of the elements. Here, we can see that away from the inlet, the error on the opening is $\sim 1\%$ for the case with $60$ elements.

### 2. Benchmarking

Having established the convergence of the model, in this part we focus on benchmarking by comparing numerical simulations with relevant semi-analytical solutions. In broad terms, this benchmark entails ensuring that the numerical solution attains the laminar asymptote (Appendix D.C) for small Reynolds number and the turbulent asymptote (Appendix D.B) for large Reynolds number, while smoothly transitioning between these limits for intermediate Reynolds numbers. Pursuant to this goal, Figure V.11 contrast the fracture opening and fluid pressure for three different cases: 1) fully laminar regime, 2) intermediate case with transition from turbulent regime to laminar regime, and 3) fully turbulent regime. From the previous discussion (Section V.D.1), recall that the Reynolds number will change along the HF. Therefore, it is not possible to define a unique

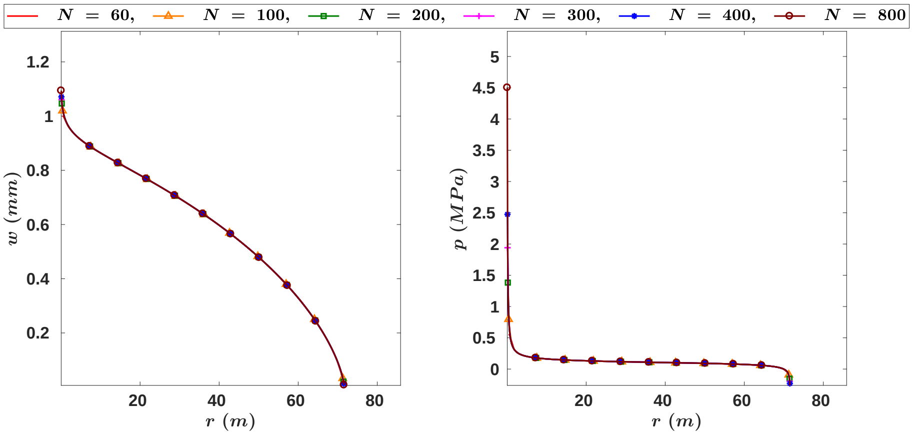

Figure V.10: Study the effect of number of elements on the results for different value of numbers of elements at $t = 150\ sec$.

value for the Reynolds number that characterizes the fluid regime. However, inspired from the global definition of a characteristic Reynolds number in the plane-strain problem Tsai and Rice (2010); Zolfaghari et al. (2017), we can suggest a characteristic Reynolds number for the radial crack given by

$$Re_{oc} = \frac{\rho Q_0}{\mu R}. \tag{V.48}$$

All the Reynolds numbers reported in Figure V.11 are defined using this characteristic Reynolds number ($Re_{oc}$), where $R$ is computed based on the radius from the laminar solution.

Next, we investigate the behavior of the crack at small and large time. Based upon the form of their respective asymptotic solutions (See Appendices D.C and D.B), it will be useful to scale the dimensionless length $\gamma$ by $\tau^{-1/2}$ and $\tau^{-4/9}$. In doing this, we obtain a constant value of this scaled quantity at large and small time, respectively, provided that the numerical solution for $\gamma$ is coming from and approaching the correct asymptotics, namely the turbulent solution at small time and laminar solution at large time (we will discuss this transition in detail in Section V.G.3). These scaled results are shown in Figure V.12, which includes results for two different values of the dimensionless inverse roughness parameter, namely, $\mathcal{R}_t = 14.6$ and $\mathcal{R}_t = 7851.1$, as described as practical limits via Table V.2. As expected, the roughness impacts the solution only at early time, where the solution is predominantly turbulent. From this examination, it is confirmed that the

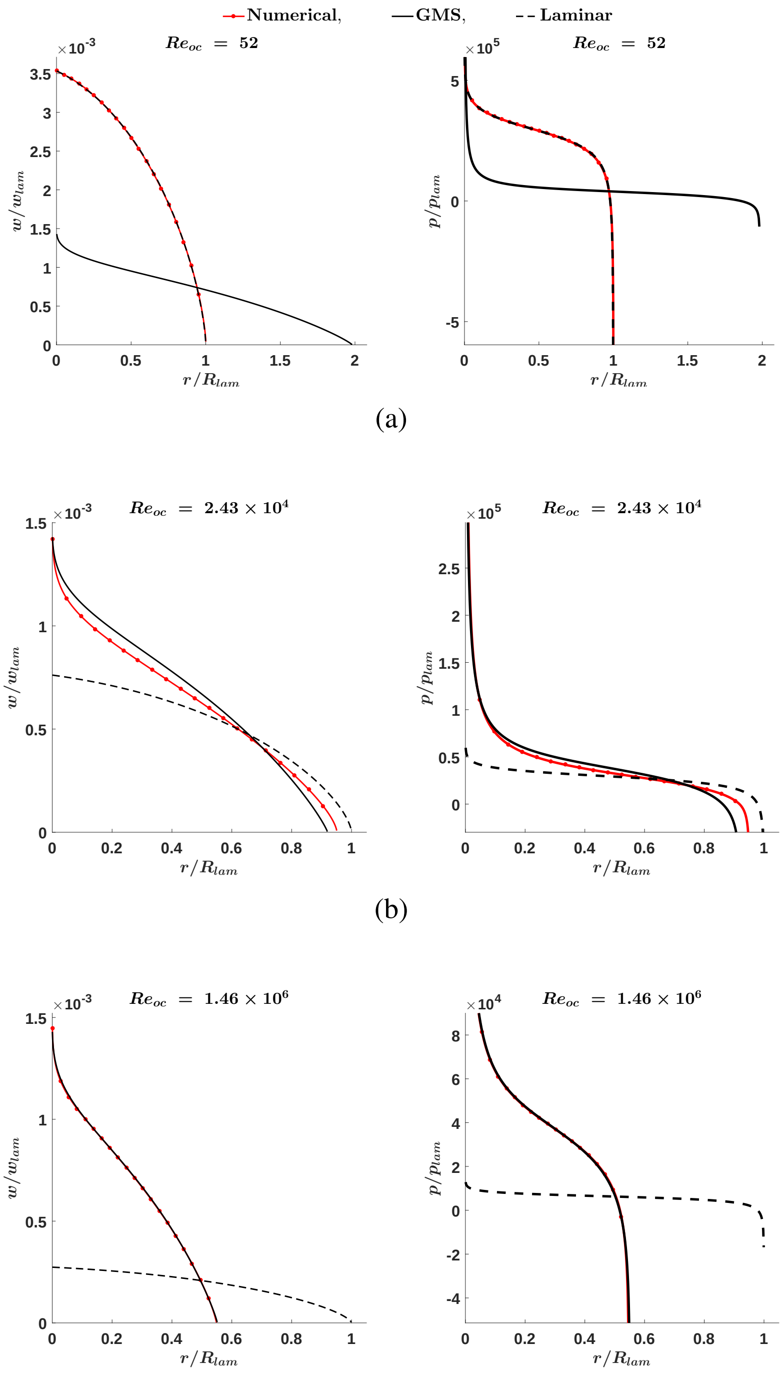

(a)

(b)

(c)

Figure V.11: Comparison of fracture opening and fluid pressure with numerical model for three different cases of laminar, turbulent, and transition.

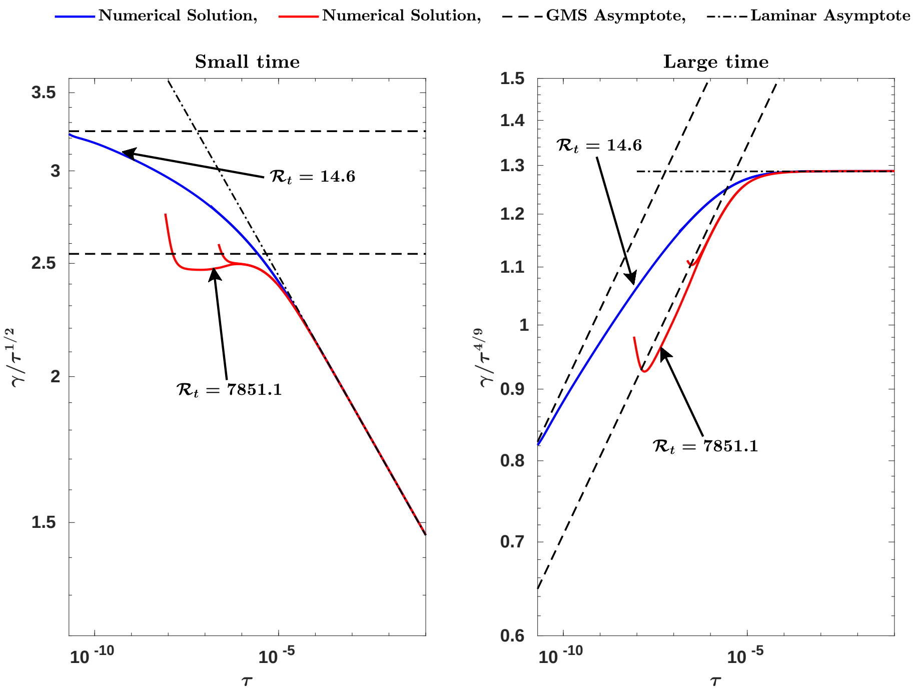

Figure V.12: The fluid flow convergence at short and long time

solution indeed attains the appropriate behavior from the laminar asymptote at large time (Figure V.12) and, after a brief period of adjustment from the initial solution, it behaves at small time in a manner consistent with the turbulent asymptote (Figure V.12).

## 3. Discussion

Having established satisfactory convergence of the solution to appropriate benchmarks, as well as demonstrating suitable insensitivity to the initial solution and the mesh density, we now turn attention to a few characteristics of the solution . Namely we examine:

- Evolution of the HF,
- Parameters defining the HF regime and influencing the solution,
- Crack opening at the inlet as independent of time in the fully turbulent regime.

The first topic that we will study is the evolution of the HF. As previously discussed by Zolfaghari and Bunger (Submitted A), there is a strong pressure singularity at inlet that can impact

Table V.2: Practical limits of parameters involved in scaled inverse roughness parameter $\mathcal{R}_t$.

| Parameter | Minimum | Maximum |
|---|---|---|
| $Q_0$ | $2.5\ m^3/s$ | $0.05\ m^3/s$ |
| $\delta$ | 0.001 mm | 0.1 mm |
| $\rho$ | $600\ kg/m^3$ | $1000\ kg/m^3$ |
| $E'$ | 5 GPa | 100 GPa |
| $\mathcal{R}_t$ | 7850 | 14 |

the solution especially near the inlet and at early time. In the radial geometry, initially the crack radius is small but the fluid pressure gradient and accompanying fluid flux are large. Therefore, the fluid regime is predominately turbulent. Then, by growing of the HF, the flux decreases with the distance from the inlet. As a result, the turbulent regime will be constrained to a region near the inlet. The size of this turbulent region decreases relative to the HF length as time progresses. Meanwhile, the near tip laminar region (discussed by Dontsov (2016)) grows relative to the HF length. This trend will continue until the turbulent regime is negligible and the crack behavior is defined through laminar fluid flow. Figure V.13 shows this evolution of the crack from turbulent asymptote to laminar asymptote via the behavior of the crack length. As explained previously, the effect of the fracture roughness on turbulent regime will appears via $\mathcal{R}_t$. Recall that from Table V.2, we can estimate the maximum and minimum values of $\mathcal{R}_t$ to be 7850 and 14, respectively. Figure V.13 shows two limits of the $\mathcal{R}_t$ and demonstrates that both solutions converge to the laminar asymptote at large time. Recall a similar result in Figure V.12, which also indicates the growth of the crack at small and large time and the fact that at the beginning it scales with turbulent solution and at the large time it scales with laminar solution.

Continuing demonstration of the evolution from the predominantly turbulent to predominantly laminar regime, Figure V.14a portrays the growth of the HF and compares the opening at different instances with a HF of the same length obtained from the laminar and fully turbulent solutions.

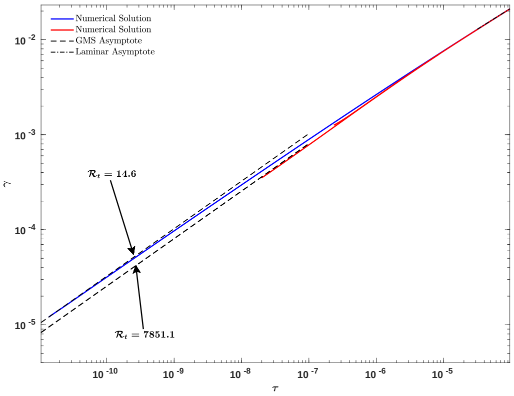

Figure V.13: Scaled length versus scale time

Observe that at early time the numerical solution matches the fully turbulent solution. As the HF grows, the laminar solution increases until eventually the numerical solution merges to the laminar asymptote. Similarly, Figure V.14b shows the pressure profile evolution along the crack. As expected, there is a strong pressure singularity at the inlet and crack tip and a similar evolution from the turbulent to laminar solution.

Furthermore, in Figure V.14a, we confirm the inlet opening of the HF is constant with time during the predominately turbulent period of growth, as predicted by the scaling (see Zolfaghari and Bunger (Submitted A)). This behavior shows itself better when we re-scale the radial coordinate ($r$)) by the radius as in Figure V.15. Here, we can see that all the turbulent solution collapse to one line, thus showing self similarity of the early time solution up to a rescaling of the radial coordinate by the HF radius.

Let us now return to make one more important observation from Figure V.14 regarding the way that the limiting regimes gain dominance. As discussed, the turbulent solution for opening is independent of time. However, the laminar opening is increasing as time increases. At the beginning, the predicted opening of the laminar HF is much smaller than the turbulent solution (see Figure V.14a and V.15). As time progresses and the crack grows, the laminar solution grows and eventually surpasses the turbulent solution. After this change occurs, the numerical solution evolves so as to match the laminar solution. One inference from this observation is that after the opening

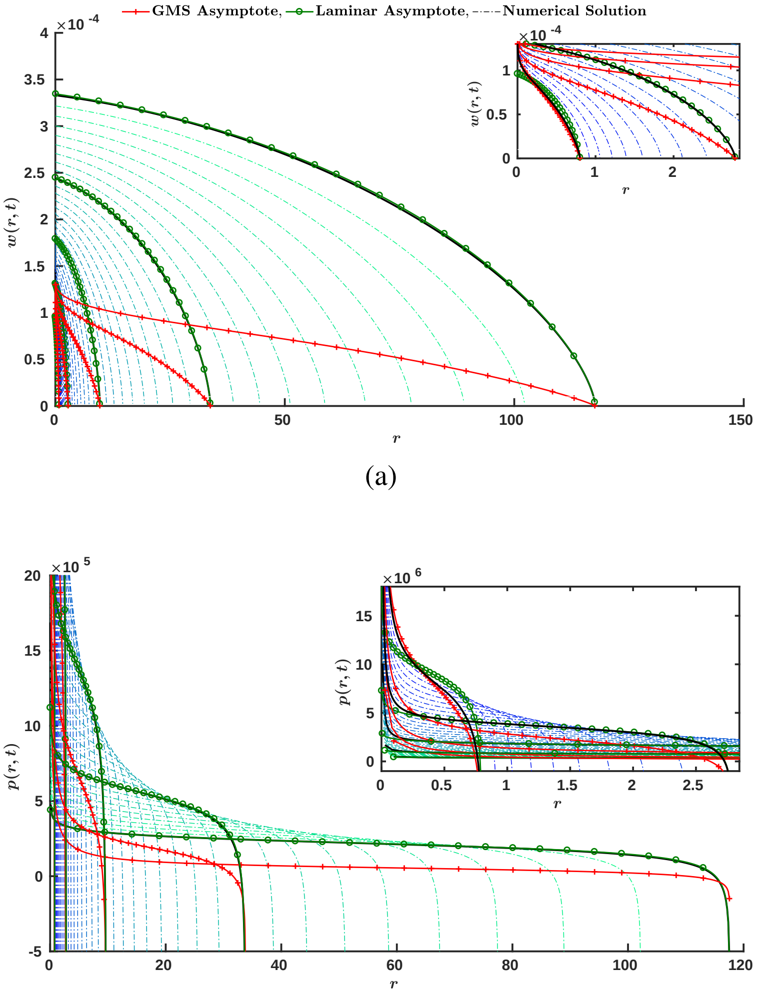

(a)

(b)

Figure V.14: Crack opening evolution and changes of fluid pressure with comparison to laminar and rough-walled turbulent solutions. In this example $\mathcal{R}_t = 14.6$, $t_{min} = 0.04\ sec$ and $t_{max} = 3170\ sec$

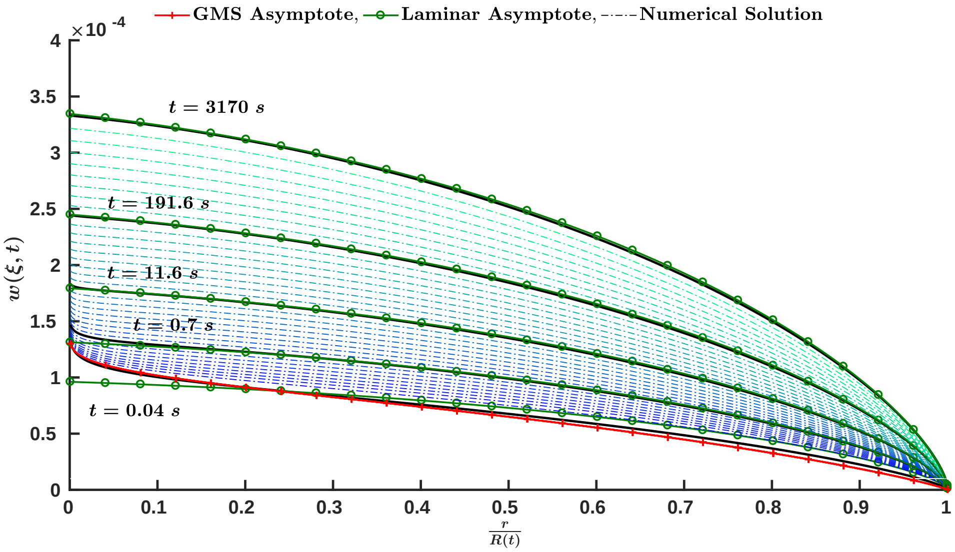

Figure V.15: Crack propagation at different times.

predicted by laminar solution surpasses the turbulent solution, the HF behavior is approximated by the laminar solution. Before this transition, the solution follows the turbulent solution. Therefore, it is useful to clarify a time scale that governs the transition from fully turbulent to fully laminar behavior.

The relevant timescale can be obtained from Zolfaghari and Bunger (Submitted A), who found the ratio of the wellbore crack opening from the fully turbulent solution to laminar solution as

$$\lim_{\xi \to 0} \frac{w_{turb}(\xi, t)}{w_{lam}(\xi, t)} = 0.5168(t^*/t)^{1/9} \tag{V.49}$$

where $t^*$ is the transition timescale given by

$$t^* = \frac{Q_0^{\frac{15}{13}} \rho^{27/13} \delta^{9/13}}{E'^{\frac{1}{13}} \mu'^2}$$

For the case of $w_{turb}(0, t) = w_{lam}(0, t)$, we solve for, the transition time as

$$t_{trans} = 0.0026 \frac{Q_0^{\frac{15}{13}} \rho^{27/13} \delta^{9/13}}{E'^{\frac{1}{13}} \mu'^2}$$

We see, then, that the turbulent dominated period persists for a greater time for larger injection rate, larger density, larger roughness, smaller viscosity, and smaller plane strain elastic modulus.

This final dependence is tied to the relationship between opening and stiffness; for smaller $E'$ the opening is larger and turbulent conditions persist for a longer period of time.

Also, considering the time scaling method given in Equation V.24 and using the scaling parameter derived for the numerical model from Equation V.30, we can obtain that

$$\tau_{trans} = 0.00322\mathcal{R}_t^{-9/13}$$

This definition also adds another meaning to $\mathcal{R}_t$: It is a parameter that determines, in terms of dimensionless time $\tau$, when the inlet opening of the laminar solution and hence the predominant regime transitions from turbulent to laminar.

As a final illustration of the evolving flow regime with times, Figure V.16 shows the HF at different times with color corresponding to the flow regime at each point within the HF. Initially, we can see that almost all of the HF is in the turbulent regime and the inlet is in the fully turbulent rough-walled regime. Then, the smooth-walled turbulent condition grows, close to the crack tip and occupying an increasing portion of the HF. After that, the laminar solution will start to dominate the tip region, from where subsequently expands to eventually comprise the entire HF.

## H. CONCLUSION

The radial (penny-shaped) hydraulic fracture geometry, while relatively simple compared to general planar or fully 3D geometries, provides a useful context for the exploration of the impact of the laminar to turbulent transition on hydraulic fracture growth. The main goal of this article is to explore the impact of this generalized fluid flow consideration using a newly-developed implicit numerical solution to model the turbulent/transition HF in an impermeable, linear-elastic rock with injection from a negligibly-small wellbore. By using the drag reduction model to describe fluid flow, this model gives a tool to capture wide range of the friction factor for various roughness and Reynolds numbers. After scaling, the problem is discretized by using moving mesh algorithm and an iterative approach is employed to solve the sets of coupled non-linear partial differential equations.

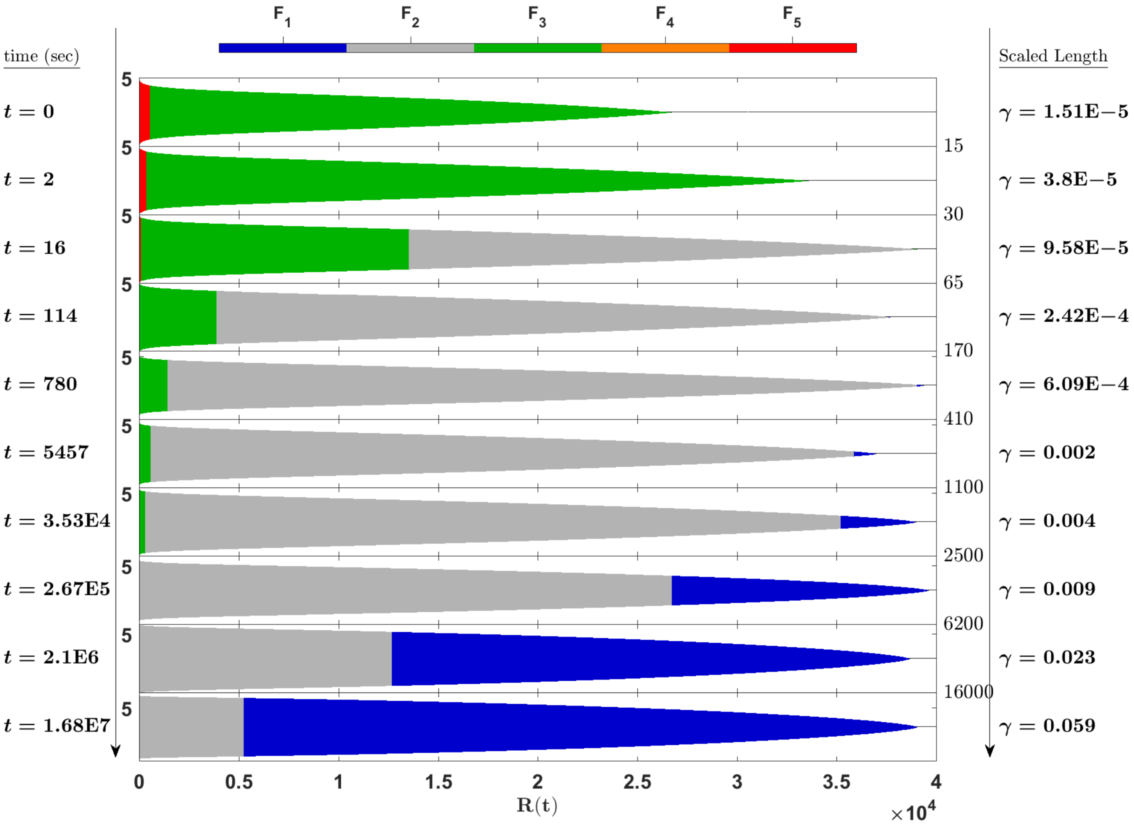

Figure V.16: Evolution of fluid regimes inside the HF, where $Re_{oc}$ is given by Equation V.48.

After confirming independence of the solution from the details of the mesh density and/or the initial (starter) solution, as well as convergence to appropriate benchmark solution, we explore in detail the behavior wherein flow is turbulent near the inlet, laminar near the tip, and in transition somewhere between. These results further show that predominance of the region that is in turbulent flow is a characteristic of the small time behavior. During this period, as predicted by the scaling, the inlet opening is independent of time and the solution is essentially self-similar up to a rescaling of the radial coordinate by the growing HF radius. As time progresses, the average fluid flux reduces driving the system toward predominant laminar flow, with the laminar region beginning at the tip and growing to comprise the majority of the HF at sufficiently large time. The characteristic time scale associated with this turbulent to laminar transition increases, intuitively, with increasing injection rate, increasing fracture roughness, increasing fluid density, decreasing fluid viscosity, and decreasing stiffness of the rock. This time scale is important because it determines the relevance of either limiting regime to practical cases, i.e. when the transition takes place in a small fraction of the total treatment time it suffices to approximate growth using the laminar asymptotic solution and when the transition requires are large time compared to the treatment time it suffices to approximate growth using the turbulent asymptotic solution.

# VI. CONCLUSIONS

This dissertation research was carried out to explain and quantify the effect of turbulent fluid flow on HF growth. The noteworthy contributions of this work begin with providing a complete suite of benchmarks for simplified but practically-relevant geometries that can be used to estimate fracture dimensions and to benchmark more general numerical simulators. This research results in semi-analytical similarity solutions for a fully turbulent rough-walled hydraulic fracture growth in three different classical models: plane strain model, blade-shape model, and radial model. In all three cases solutions are presented in for the limit of zero toughness and an impermeable rock. All the presented solutions come along with an appropriate near tip asymptote for fully turbulent HF growth, and a suitable inlet conditions.

Secondly, this study provides a new numerical approach to HF simulation including laminar, turbulent, and laminar-turbulent transition regimes. An implicit moving mesh algorithm is developed to capture the change of fluid regime in HF via drag reduction method to estimate friction factor.

Thirdly, this investigation demonstrates the evolution of turbulent-laminar regime in a radial HF, which has implications also for the overall behavior and evolution in more general planar fracture growth geometries. Analyzing the results from the numerical model illustrates a striking turbulent-to-laminar transition inside the crack. For an illustration, as a result of the numerical model it has been noticed that at the early time of the crack propagation, the fluid regime is turbulent, and thus the opening of the crack remains constant with time in accordance with the prediction based on the turbulent regime scaling. During this time the solution is nearly self-similar up to a re-scaling of the radial coordinate by the HF radius. This turbulent regime persists for a while, but eventually the region of laminar flow grows from the tip and dominates the majority of the HF. In the end the wellbore opening of the HF obtained from the laminar approximation becomes larger than the solution for the fully turbulent regime. And after that the crack propagation behaves like laminar regime.

Fourthly, this study has identified that the transition range of fluid regime from turbulent-to-laminar fluid flow is relatively small and practically, it will often suffice to approximate the HF growth using the asymptotic solutions obtained from either the laminar or turbulent solution. The choice of which asymptote provides a suitable approximation to the full solution requires simply selecting the solution that gives the largest pressure or opening.

It is interesting to observe that for the radial HF there is an intermediate regime in which most of the fluid inside the HF is in the smooth-walled turbulent condition. Future investigation should firstly be directed at deriving a solution for this intermediate asymptotic and investigating the range of its applicability. Further natural extensions to this work include designing and performing laboratory experiments to study the influence of turbulent flow on HF growth. Besides providing a useful benchmark data, a well designed experiment is needed to assess several aspects of the appropriateness of the model and to characterize quantities that impact the solution. For example, the Reynolds number corresponding to laminar-to-transition and transition-to-turbulent regimes is one of the main parameters that needs to be defined. However, existing experiments are limited to flow in circular channels (pipe flow). Also, finding the values of the constants in the general GMS method, specifically $\alpha$ and $m$ defined in the Darcy-Weisbach equation (III.3). Another possible area of future work is to investigate the singularity in the inlet for radial geometry using detailed 3D numerical simulations or via laboratory experiments is needed to clarify how the mathematical singularity in the opening is mitigated in real systems.

Finally, investigating the effect of proppant on HF growth and the impact of laminar-turbulent transition in prppant transport is important for expanding the use of simulations to engineering practice. One of the benefits of using the drag reduction (DR) model in the numerical model presented here is an ability of it to extend to incorporate proppant by activating terms in DR model that are switched off in the current model.

In summary, the research comprising this dissertation shows both the qualitative and quantitative impacts of turbulent flow on all classical HF growth geometries and provides a useful numerical algorithm to simulate the HF or developing benchmark solutions for laboratory experiments.

# APPENDIX A

# APPENDICES FOR "BLADE-SHAPED HYDRAULIC FRACTURE DRIVEN BY A TURBULENT FLUID IN AN IMPERMEABLE ROCK"

## A. APPENDIX. INTEGRATED FLUID FLOW EQUATION

From elasticity and by assuming that the cross section of the crack is elliptical, it is possible to say that Nordgren (1972)

$$W(x,z,t)=\frac{1-\nu}{G}(H^2-4z^2)^{1/2}(p-\sigma). \tag{A.1}$$

At $z=0$ the maximum opening is given as

$$W(x,0,t)=\omega(x,t)=\frac{1-\nu}{G}H\left(p(x,t)-\sigma\right). \tag{A.2}$$

Thus, the pressure gradient is

$$\frac{\partial p}{\partial x}=\frac{G}{1-\nu}\frac{1}{H}\frac{\partial\omega(x,t)}{\partial x}. \tag{A.3}$$

Inserting the crack opening expression Equation A.1 into the GMS parametrization Equation II.4 gives

$$q_{2D}=\left[\frac{4}{\rho m k^{\alpha}}\omega^{3+\alpha}\left(1-\left(\frac{2z}{H}\right)^2\right)^{\frac{3+\alpha}{2}}\left(-\frac{\partial p}{\partial x}\right)\right]^{1/2}, \tag{A.4}$$

which is the two-dimensional flow at every height $z$, viz. Figure A1. We can find the total flow rate by integrating $q_{2D}$ over the height of the fracture, which gives

$$q=\int_{-H/2}^{H/2}q_{2D}dz=\left(\frac{4}{\rho m k^{\alpha}}\frac{G}{1-\nu}\frac{1}{H}\right)^{1/2}\left(-\omega^{3+\alpha}\frac{\partial\omega}{\partial x}\right)^{1/2}\int_{-H/2}^{H/2}\left[1-\left(\frac{2z}{H}\right)^2\right]^{\frac{(3+\alpha)}{4}}dz. \tag{A.5}$$

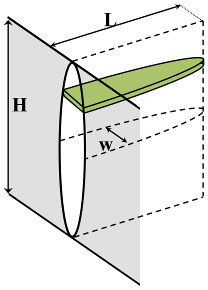

Figure A1: Representation of two dimensional element in three dimensional crack. The integration of infinitesimal elements over the height of the crack will give the flow through a given cross section at location $x$.

Now letting $\varphi = (3+\alpha)/4$ and making the change of variable $\sin\theta = 2z/H$ we have

$$q = \left(\frac{4}{\rho m k^{\alpha}}\frac{G}{1-\nu}\frac{1}{H}\right)^{1/2} \omega^{2\varphi}\left(-\frac{\partial\omega}{\partial x}\right)^{1/2}\frac{H}{2}\int_{-\pi/2}^{\pi/2}(\cos\theta)^{2\varphi+1}d\theta. \tag{A.6}$$

Thus, we can write the total flux $q$ in terms of the Beta function $\beta(x,y)$ as

$$q = \frac{H}{2}\left(\frac{4}{\rho m k^{\alpha}}\frac{G}{1-\nu}\frac{1}{H}\right)^{1/2} \omega^{2\varphi}\left(-\frac{\partial\omega}{\partial x}\right)^{1/2}\beta\left(\frac{1}{2},\varphi+1\right), \tag{A.7}$$

where the Beta function is defined as Abramowitz and Stegun (1972)

$$\beta(x,y) = \int_0^1 t^{x-1}(1-t)^{y-1}dt, \tag{A.8}$$

or

$$\beta(x,y) = \frac{\Gamma(x)\Gamma(y)}{\Gamma(x+y)}, \tag{A.9}$$

for $\mathbb{R}(x) > 0$ and $\mathbb{R}(y) > 0$ and $\Gamma(x)$ is the Gamma function Abramowitz and Stegun (1972).

## B. TURBULENT FLOW

A better understanding of the physics of turbulent flows would allow for the determination of the pressure drop in a turbulent flow through a crack. This section uses dimensional analysis to make an analogy between flow through a crack and flow through a pipe. Most studies of HF with turbulent flow have only been carried out with either pipe flow assumption or channel flow, which fails to resolve the contradiction that crack growth cannot be categorized as either pipe flow, nor channel flow assumptions. This study is unable to encompass the entire discussion about turbulent flow; however, using dimensional analysis to obtain flow equation for turbulent regime can enhance the clarity of this method. The fluid pressure drop inside the pipe depends on different parameters and can be described as $\Delta P = \mathcal{F}(V, D, l, k, \mu, \rho)$ where $V$ is the mean velocity of the fluid, $D$ is the pipe diameter, $l$ is the pipe length, $k$ is the pipe roughness, $\mu$ is the fluid viscosity, and $\rho$ is the fluid density. The Buckingham-$\Pi$ theorem gives that

$$\frac{\partial P}{\partial x} = \rho V^2 \frac{1}{D} \mathcal{F}(Re, \frac{k}{D}), \tag{A.10}$$

by replacing the mean velocity $V$ with $q/D$ and re-arranging the equation, we find that

$$q = \left( -\frac{D^3}{\rho \mathcal{F}} \frac{\partial P}{\partial x} \right)^{1/2}, \tag{A.11}$$

where $\mathcal{F}$ depends on Reynolds number and roughness of the crack. This equation is the same as for GMS (eqn 4 in the paper) where $\mathcal{F}$ is assumed to be independent of Reynolds number and a power law in roughness given by:

$$f_p = m \left( \frac{k}{W} \right)^{\alpha}. \tag{A.12}$$

This is clearly shown in the Moody diagram, Fig. A2. For Reynolds numbers greater than about $10^5$, the friction factor is nearly independent of Reynolds number. Additional roughness, however, affects the friction considerably and the inset to Fig. A2 shows that the friction varies as a power law in roughness.

No-slip condition on the contact boundary of fluid with solid will cause a viscous layer to form. In this viscous layer, the shear force is mainly described based on viscosity of the fluid. On the other hand, the thickness of viscous layer has inverse relation to the value of Reynolds number.

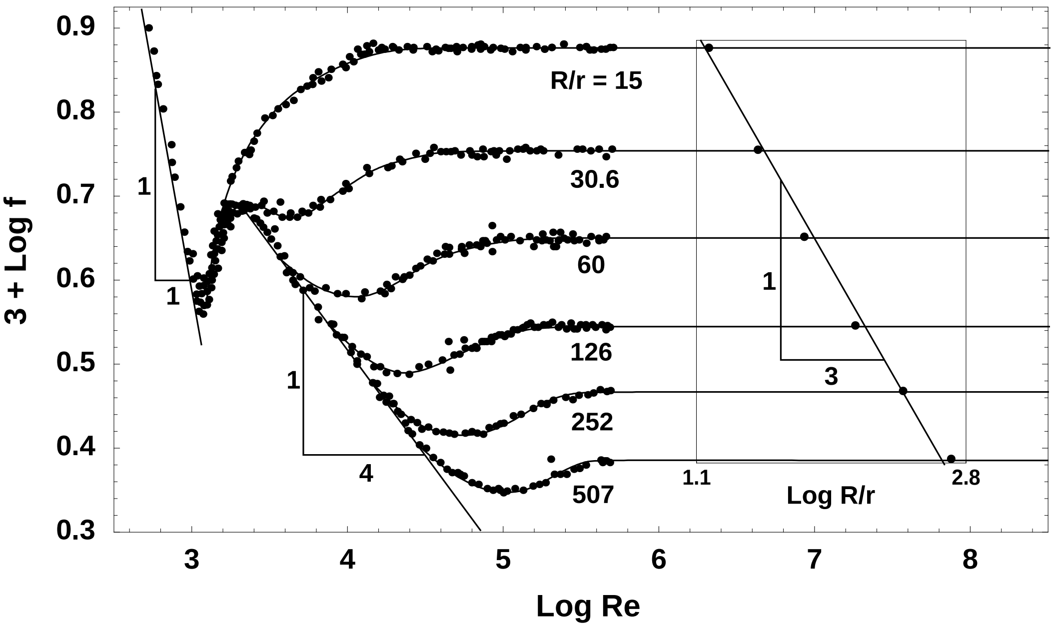

Figure A2: Moody diagram for pipe flow Gioia and Chakraborty (2006), with permission.

When the Reynolds number is very large, the viscous sublayer is very thin and the shear stress is mostly defined by Reynolds stress. In such a cases the shear stress is more in the format of $K\rho V^2/2$ where $K$ is a parameter that depends on roughness of the wall (see Munson et al. (2002) for more detail). Therefor, by increasing the Reynolds number, in contrast to laminar flow, the shear force is more dependent on fluid density and crack roughness rather than fluid viscosity. And that is why in turbulent equations like in Equation A.11 and A.12, the fluid density will appear but in Poiseuille equation, the viscosity will appear instead. This phenomena is also explainable based on the Moody diagram.

In general, the Moody diagram is mainly developed to calculate the friction factor in the circular pipes. However, by introducing hydraulic radius, it is possible to connect non-circular cross sections and channels to the friction factor. For the laminar part of the Moody diagram, there is one unique line that explains the friction factor which confirms the fact that friction factor is only function of Reynolds number. However, by increasing Reynolds number, as was pointed out above, the viscous sublayer will become smaller. As this trend continuous, the height of the viscous sublayer will reduce until the length of the surface roughness is comparable with the height of the sublayer. Therefore, the friction factor will become function of two parameters: surface roughness and Reynolds number. In fact, these two parameters are acting as a counterbalance against each other. As an illustration, if Reynolds increases, the viscous sublayer will become smaller and friction factor reduces. On the other hand, the effect of surface roughness will become more important which will cause the friction factor to increase. Hence, the final value of friction factor is the combination of the effect of this two values. This phenomena is illustrated in the Moody digram very well. After the laminar region, since the friction factor is function of two variables, it will not be possible to explain it with one plot and that is why there is several branches for different values of surface roughness. Besides, in Moody diagram, as Reynolds increase, the friction factor will decrease. And as surface roughness, increase, the friction factor will increase. So the increase of friction factor is due to either decreasing Reynolds number or increasing surface roughness.

For very large Reynolds numbers, the value of laminar sublayer diminishes so much that the fracture toughness will become dominant and the effect of Reynolds number is eliminated. In such a cases, the friction factor will be only a function of the surface roughness $f(\varepsilon/D)$, in contrast to laminar flow which was only function of Reynolds number $f(Re)$. When the flow is just function of surface roughness, the fluid flow is called wholly turbulent flow. Looking at Moody diagram for turbulent flow, you can observe that first of all, as much as the surface roughness increases, the plot will become more flat, which means that for large span of Reynolds numbers and fixed value of surface roughness, the changes of friction factor will become smaller. That is, friction factor will become independent to Reynolds number and become more linked to surface roughness which indicate that wholly turbulent flow is happening. Also, for larger Reynolds numbers, the plot will again become flat, again indicating occurance of a wholly turbulent regime.

In hydraulic fracturing, usually the surface roughness is large when compared to the fracture opening. For example, the ratio of roughness height to fracture opening is in more than 0.1 ($\varepsilon/W > 0.1$). So according to the Moody diagram, the friction factor plot is almost horizontal line and is mostly in wholly turbulent region. And that is why mainly in GMS equation, the friction factor is only function of scaled roughness rather than Reynolds number.

# C. LAMINAR TO TURBULENT TRANSITION MODEL

## 1. Regime Transition for Different Fluids Based on General Open Channel Fluid Mechanics

We define a characteristic Reynolds number that depends on parameters such as the fluid density $\rho$, viscosity $\mu$, pumping rate $q_{in}$, and the layer thickness $H$, which combine into

$$Re = \frac{\rho q_{in}}{H\mu}.$$

The fluid flow is assumed to be laminar for Reynolds number less than 500 and fully-developed turbulence for Reynolds numbers greater than 12500. From 500 to 12500 is the transition between laminar to turbulent flow. Typical heights of HFs fall in the range 20 m $< H <$ 200 m Fisher and Warpinski (2012) and $\rho$, $\mu$ are material properties of the fluid. We will consider injection rates between 0.01 m$^3$ s$^{-1}$ $< q_{in} <$ 0.2 m$^3$ s$^{-1}$. Thus, the ratio of injection rate to layer thickness falls in the range $5 \times 10^{-5}$ m$^3$ s$^{-1}$ $< q_{in}/H <$ 0.01 m$^3$ s$^{-1}$.

The summary of the change of Reynolds number for different fluids is shown in Fig. A3. For example, we can compute the Reynolds number for water pumped at $q_{in} = 0.2$ m$^3$ s$^{-1}$ into a layer with height $H = 50$ m. First, we mark point A at $H = 50$, then we draw a horizontal line from point A until it hits the curve for $q_{in} = 0.2$ m$^3$ s$^{-1}$, which we call point B. We then draw a vertical line from point B until it hits the line for water and we call it point C. Finally, we can draw a horizontal line from point C to the left y-axis to read the value of $\log(Re)$ (point D). The background color at point C indicates the regime and practical fluxes fall in the range $q_{in} = 0.05$ m$^3$ s$^{-1}$ to $q_{in} = 0.2$ m$^3$ s$^{-1}$. Thus, for all practical applications the flow regime for cross-linked and linear gel is laminar. Water, however, falls in the transition zone and CO$_2$ is transitional or fully-developed turbulence depending on $q_{in}/H$.

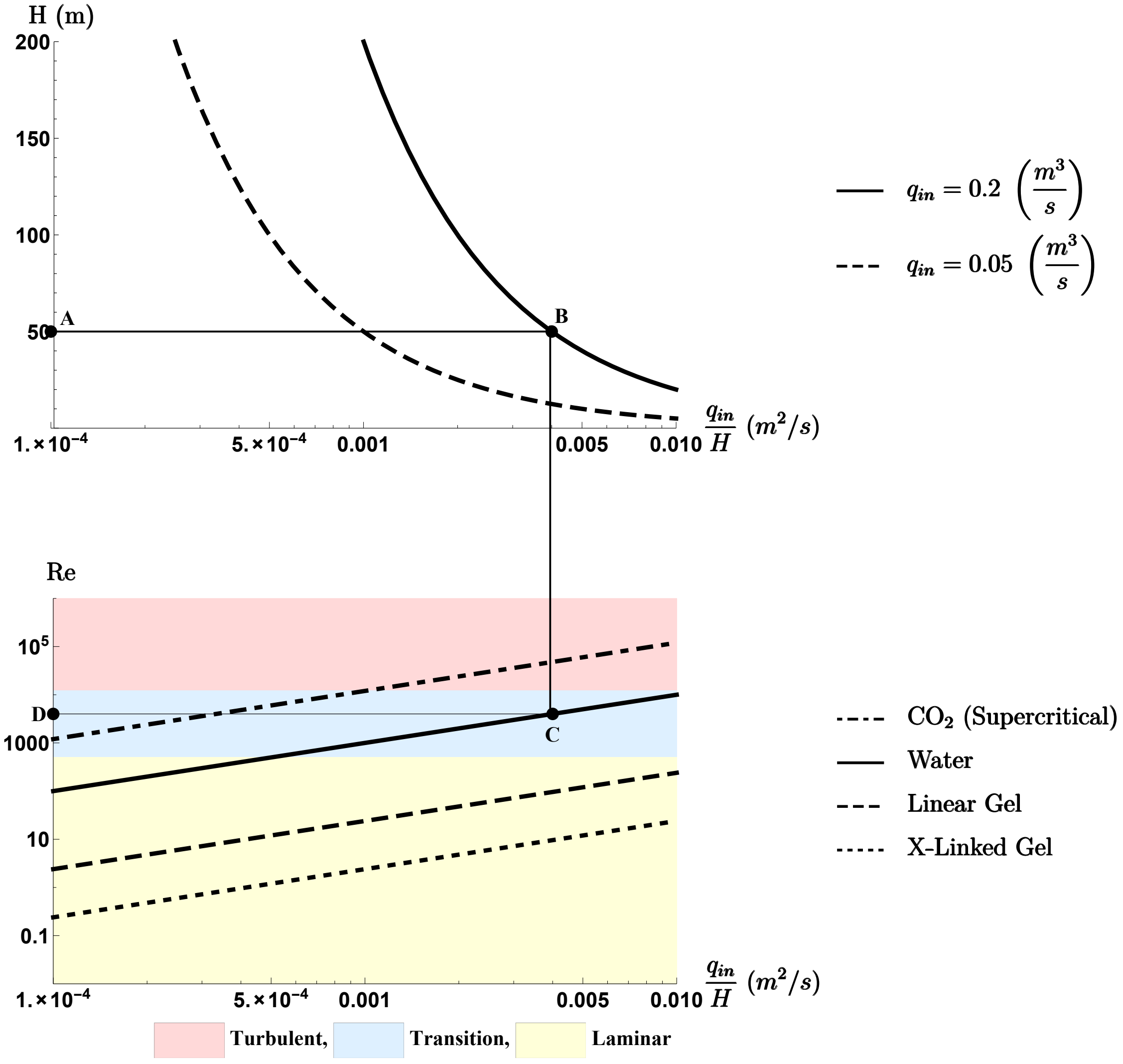

Figure A3: Variation of fluid flow regime by changing the fluid properties.

## 2. Regime Transition for Different Fluids Based on General Open Channel Fluid Mechanics, Pressure Approach

By increasing the Reynolds number above 500, turbulent bursts begin to occur inside the flow Emmons (1951). When the Reynolds number increases beyond a critical value, the whole flow is fully-developed turbulence. The transition to turbulent flow is depending on parameters like roughness and channel geometry. As a general case, some texts offer 12500 as the limit for Reynolds number. However, they also note that this number is an estimation and is not well defined number for all cases (e.g. Munson et al. (2002)). Moreover, Reynolds numbers above 500 have turbulent behavior but the frequency of this turbulent behavior will increase as Reynolds number increase. Hence, the transition remains imprecisely defined. Recalling the Nordgren and turbulent flow solution for pressure:

$$p^N_{net}(0,t) = 2.5\left[\frac{\mu q_{in}^2}{H^6}\frac{G^4}{(1-\nu)^4}\right]^{\frac{1}{5}} t^{\frac{1}{5}} \tag{A.13a}$$

$$p^T_{net}(x,t) = 0.8122\left(\frac{k q_{in}^9 \rho^3}{H^{22}}\left(\frac{G}{1-\nu}\right)^{13}\right)^{\frac{1}{16}} t^{\frac{3}{16}}\left(1-\frac{x}{\ell(t)}\right)^{\frac{3}{7}}\left(1+0.05497\,\frac{x}{\ell(t)}\right) \tag{A.13b}$$

An alternative method for defining transition is by looking at the condition that fluid pressure from the laminar solution equates with the pressure found from our turbulent solution. Specifically, letting $P_{laminar} = P^N_{net}(0,t)$ (Equation A.13a) and letting $P_{turb} = P^T_{net}(0,t)$ (Equation A.13b), we define $P_{laminar} > P_{turb}$ as the laminar regime and $P_{laminar} < P_{turb}$ as the turbulent regime. Finding the transition point entails solution to

$$P_{net_N}(0,t)\Big|_{\text{Equation A.13a}} = P_{net}(0,t)\Big|_{\text{Equation A.13b}},$$

which simplifies to

$$\log\left(\frac{q_{in}}{H}\right) = 3.005 + \frac{1}{13}\log\left[\frac{\mu^{16}Ht}{\rho^{15}k^5}\left(\frac{1-\nu}{G}\right)\right] \tag{A.14}$$

Here we can see the transition point depends not only on $q_{in}/H$ but also on $\mu, H, t, \rho, k, \nu$, and $G$. Thus, we cannot define the transition based exclusively on $Re^*$. Still, for ranges of these parameters we can define transitions specifically for each of the 4 fluids. The result is shown in Fig. A4 (for range of different parameters see Table A1). Again the relevant range is between the

$q_{in} = 0.05$ m$^3$ s$^{-1}$ and $q_{in} = 0.2$ m$^3$ s$^{-1}$ curves and note that the transition region is here defined as the range in which different choices from the typical ranges of parameters can result in either $P_{laminar} > P_{turb}$ or vice versa. Within this range, by the definition of Equation A.14, CO$_2$ is always turbulent and water is turbulent for nearly all relevant cases.

## D. NEAR-TIP ASYMPTOTICS

Here we start with the equation

$$-\Omega + \frac{4\varphi + 1}{4\varphi + 2}(\xi\Omega)' = \left[\Omega^{2\varphi}\left(-\Omega'\right)^{1/2}\right]'. \tag{A.15}$$

We know that $\Omega$ will be small so we scale it with power series solution as

$$\Omega = \epsilon^a f + \epsilon^{a+\gamma} g + \dots \quad \text{and} \quad a,\ \gamma > 0.$$

The distance to the fracture tip is scaled as

$$\xi = 1 - \epsilon^b \zeta + \dots \quad \text{and} \quad b > 0,$$

Derivatives with respect to $\xi$ become derivatives with respect to $\zeta$ through

$$\frac{d}{d\xi} = -\epsilon^{-b}\frac{d}{d\zeta},$$

which says that the derivative is large near the fracture tip, as expected.

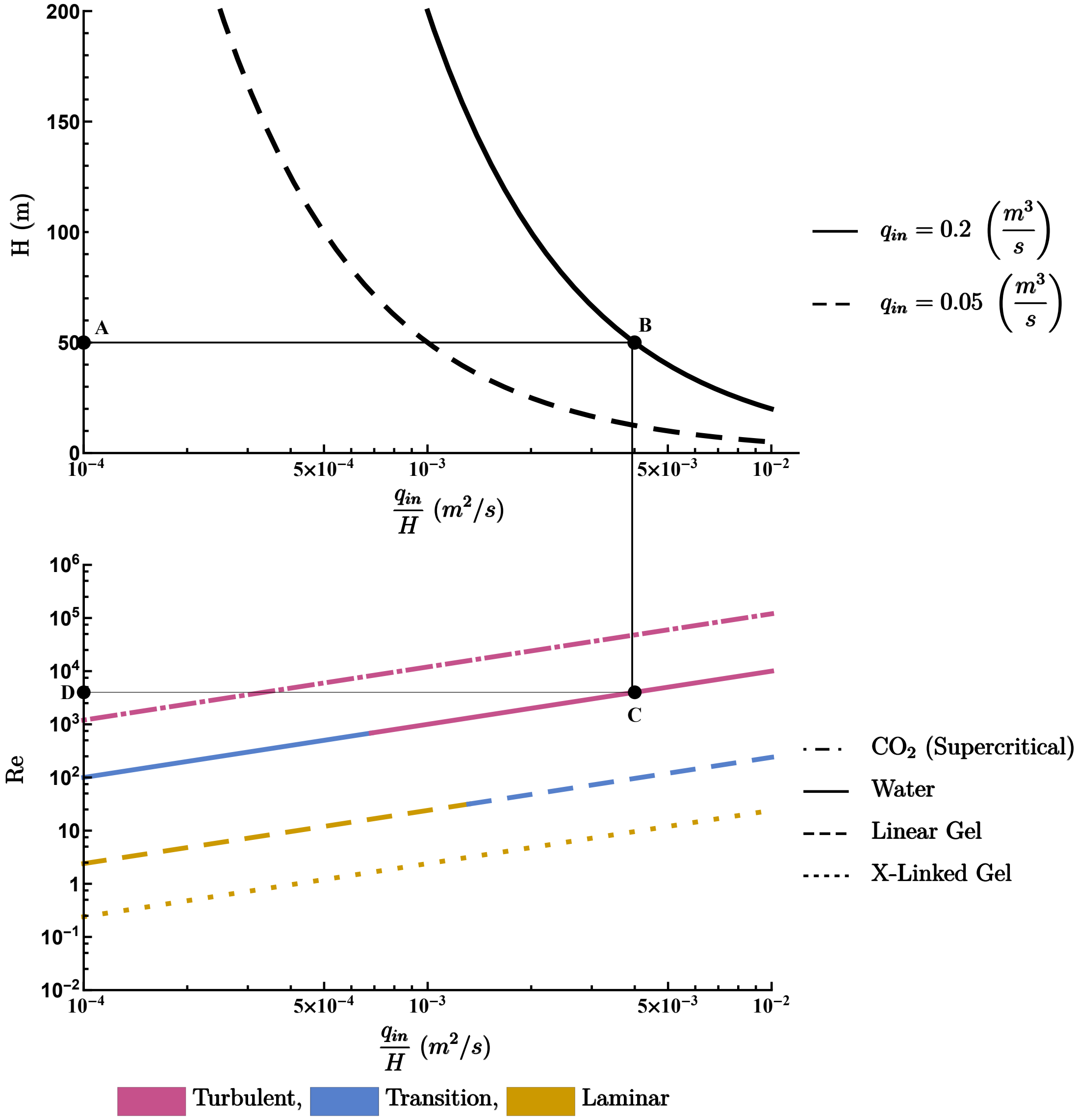

Figure A4: Flow regime variation with regimes determined by comparison of characteristic pressures.

### 1. First Order Analysis

We start by examining the leading order equations. Thus, we can rewrite Equation (A.15) as

$$-\epsilon^a f - \frac{4\varphi+1}{4\varphi+2}\epsilon^{-b}\left[(1-\epsilon^b\zeta)\epsilon^a f\right]' = -\epsilon^{-b}\left[(\epsilon^a f)^{2\varphi}\left(\epsilon^{a-b}f'\right)^{1/2}\right]', \tag{A.16}$$

where the primes now indicate derivatives with respect to $\zeta$. Combining terms we find

$$-\epsilon^a f - \frac{4\varphi+1}{4\varphi+2}\epsilon^{a-b}f' + \frac{4\varphi+1}{4\varphi+2}\epsilon^a\left[\zeta f\right]' = -\epsilon^{\left(2\varphi+\frac{1}{2}\right)a-\frac{3}{2}b}\left[f^{2\varphi}\left(f'\right)^{1/2}\right]', \tag{A.17}$$

We can see that the first and third terms scale as $\epsilon^a$ and are smaller than the second and fourth terms. Therefore, we equate the powers of the second and fourth terms and find

$$b = (4\varphi - 1)\,a,$$

which is true for any positive $a$ so long as $\varphi > 1/4$. In general GMS equation, $\varphi = (3+\alpha)/4$, and considering $\varphi > 1/4$ will lead to $\alpha > -2$ which is always true; for example, in Manning equation $\alpha = 1/3 > -2$ which satisfy $\varphi > 1/4$. Now we need to choose a positive value for $a$. Thus, if we choose $a = 1$, our dominant balance will become

$$\frac{4\varphi+1}{4\varphi+2}f' = \left[f^{2\varphi}\left(f'\right)^{1/2}\right]'. \tag{A.18}$$

This is the same equation as derived heuristically before, but the dependent variable $u = (1-\xi)/\epsilon^b$. The boundary conditions are flipped and therefore,

$$f(\zeta=0) = 0, \quad \left[f^{2\varphi}(f')^{1/2}\right]_{\zeta=0} = 0.$$

Integrating Equation (A.18) and solving for it will direct us to

$$f = \left[\sqrt{4\varphi-1}\left(\frac{4\varphi+1}{4\varphi+2}\right)\right]^{2/(4\varphi-1)}\zeta^{1/(4\varphi-1)}.$$

We can reinsert $\zeta = (1-\xi)/\epsilon^b$ and find

$$\Omega = \epsilon^a f = \epsilon^{b/(4\varphi-1)}f = \left[\sqrt{4\varphi-1}\left(\frac{4\varphi+1}{4\varphi+2}\right)\right]^{2/(4\varphi-1)}(1-\xi)^{1/(4\varphi-1)},$$

which is the result we derived previously.

## 2. Second Order Analysis

Now that we have found $f$ as a function of $\zeta$, we look to the next order in $\epsilon$ to find the function $g(\zeta)$ i.e.

$$\Omega = \epsilon f + \epsilon^{1+\gamma} g + \dots \quad \text{and} \quad \gamma > 0.$$

where $\gamma$ is an unknown exponent. The coordinate $\zeta$ is still scaled as

$$\xi = 1 - \epsilon^b \zeta,$$

where $b = 4\varphi - 1$ and $\varphi > 1/4$.

We can insert these scalings into the full ode for $\Omega$, Equation (A.15), to find

$$\begin{aligned} -\epsilon f - \epsilon^{1+\gamma} g - \frac{4\varphi+1}{4\varphi+2}\epsilon^{-b}\left[\left(1-\epsilon^b\zeta\right)\left(\epsilon f + \epsilon^{1+\gamma} g\right)\right]' \\ = -\epsilon^{-b}\left[\left(\epsilon f + \epsilon^{1+\gamma} g\right)^{2\varphi}\left(\epsilon^{1-b} f' + \epsilon^{1+\gamma-b} g'\right)^{1/2}\right]'. \end{aligned} \tag{A.19}$$

Expanding out the left side we find that

$$\begin{aligned} -\epsilon^{b+1} f - \epsilon^{1+\gamma+b} g - \frac{4\varphi+1}{4\varphi+2}\left(\epsilon f' + \epsilon^{1+\gamma} g'\right) + \frac{4\varphi+1}{4\varphi+2}\epsilon^{b+1}\left[\zeta\left(f + \epsilon^{\gamma} g\right)\right]' \\ = -\left[\left(\epsilon f + \epsilon^{1+\gamma} g\right)^{2\varphi}\left(\epsilon^{1-b} f' + \epsilon^{1+\gamma-b} g'\right)^{1/2}\right]'. \end{aligned} \tag{A.20}$$

We now expand the right side as

$$\begin{aligned} -\epsilon^{b+1} f - \epsilon^{1+\gamma+b} g - \frac{4\varphi+1}{4\varphi+2}\left(\epsilon f' + \epsilon^{1+\gamma} g'\right) + \frac{4\varphi+1}{4\varphi+2}\epsilon^{b+1}\left[\zeta\left(f + \epsilon^{\gamma} g\right)\right]' \\ = -\left[\epsilon f^{2\varphi}\left(f'\right)^{1/2}\left(1 + 2\varphi\epsilon^{\gamma}\frac{g}{f}\right)\left(1 + \frac{\epsilon^{\gamma}}{2}\frac{g'}{f'}\right)\right]', \end{aligned} \tag{A.21}$$

Now the terms that are linear in $\epsilon$ group as

$$-\frac{4\varphi+1}{4\varphi+2} f' = -\left[f^{2\varphi}\left(f'\right)^{1/2}\right]',$$

which is the same equation that we solved in the earlier section. The terms that are a slight departure from linear in $\epsilon$

$$-\epsilon^{b+1} f - \frac{4\varphi+1}{4\varphi+2}\epsilon^{1+\gamma} g' + \frac{4\varphi+1}{4\varphi+2}\epsilon^{b+1}\left[\zeta f\right]' = -\epsilon^{1+\gamma}\left[f^{2\varphi}\left(f'\right)^{1/2}\left(2\varphi\frac{g}{f} + \frac{1}{2}\frac{g'}{f'}\right)\right]'.$$

Thus, we set $\gamma = b$ and cross out the term $\epsilon^{b+1}$ from both side of equation. For simplicity, we also do the following change of variables

$$\kappa = \left[\sqrt{4\varphi - 1}\left(\frac{4\varphi+1}{4\varphi+2}\right)\right]^{2/(4\varphi-1)} \quad \text{and} \quad c = \frac{4\varphi+1}{4\varphi+2},$$

which help us to define $f(\zeta) = \kappa\zeta^{1/b}$. This gives the equation

$$-\kappa\zeta^{1/b} - cg' + c\left[\zeta f\right]' = -\left[f^{2\varphi}\left(f'\right)^{1/2}\left(2\varphi\frac{g}{f} + \frac{1}{2}\frac{g'}{f'}\right)\right]'.$$

After calculating derivations for $f$ and replacing them back into the equation, our equation reduces to

$$-\kappa\zeta^{1/b} - cg' + \frac{c\kappa}{b}(1+b)\zeta^{1/b} = -\frac{\kappa^{b/2}}{2b^{1/2}}\left(g' + b[\zeta g]''\right).$$

Parameter $\kappa$, that has been defined earlier, can also be explained as

$$\kappa^{b/2} = b^{1/2}c,$$

thus, we can divide by $c$ and find

$$\frac{\kappa}{c}\zeta^{1/b} + \frac{1}{2}g' - \frac{b}{2}[\zeta g]'' = \frac{\kappa}{b}(1+b)\zeta^{1/b}.$$

This is an equidimensional equation, thus, we try for a solution of the form

$$g = A\zeta^{\lambda},$$

which gives

$$\frac{\kappa}{c}\zeta^{1/b} + \frac{\lambda}{2}A\zeta^{\lambda-1} - \frac{b}{2}A\lambda(\lambda+1)\zeta^{\lambda-1} = \frac{\kappa}{b}(1+b)\zeta^{1/b}.$$

To match powers on each side, we must have that $\lambda = (b+1)/b$. Thus, we can solve for $A$ from

$$\frac{b+1}{b}A - \frac{b+1}{b}A\left(2b+1\right) = \frac{2\kappa}{b}(1+b) - \frac{2\kappa}{c},$$

which gives

$$A = \frac{\kappa}{c(1+b)} - \frac{\kappa}{b},$$

This solution satisfies the boundary conditions

$$g(0) = 0 \quad \text{and} \quad g^{2\varphi}g'(0) = 0,$$

and, therefore, we have

$$g(\zeta) = \kappa \left( \frac{1}{c(1+b)} - \frac{1}{b} \right) \zeta^{(b+1)/b}.$$

From $g(\zeta)$ we can determine $\Omega$ as

$$\Omega = \epsilon\kappa\zeta^{1/b} + \epsilon^{1+b} A \zeta^{(b+1)/b}.$$

Using the similarity variable $\xi = 1 - \epsilon^b \zeta$, we find that

$$\Omega = \kappa \left(1 - \xi\right)^{1/b} + \epsilon^{1+b} A \left( \frac{1-\xi}{\epsilon^b} \right)^{(b+1)/b}.$$

Thus, the powers of epsilon cancel in all terms and we find

$$\Omega = \frac{\kappa}{b} \left(1 - \xi\right)^{1/b} \left[ b - 1 + \frac{b}{c(b+1)} + \left( 1 - \frac{b}{c(b+1)} \right) \xi \right].$$

We now convert back to $\alpha$. We know that $\varphi = (3+\alpha)/4$ and $b = 4\varphi - 1 = \alpha + 2$. The pre-factor $\kappa$ is calculated as

$$\kappa = \left[ \sqrt{4\varphi - 1} \left( \frac{4\varphi + 1}{4\varphi + 2} \right) \right]^{2/(4\varphi - 1)} = \left[ \sqrt{\alpha + 2} \left( \frac{\alpha + 4}{\alpha + 5} \right) \right]^{2/(2+\alpha)}$$

Thus,

$$\begin{aligned} \Omega = (\alpha + 2)^{-\frac{\alpha+1}{\alpha+2}} \left[ \frac{\alpha + 4}{\alpha + 5} \right]^{2/(\alpha+2)} (1 - \xi)^{1/(\alpha+2)} \Bigg( 1 + \alpha + \frac{(\alpha+2)(\alpha+5)}{(\alpha+3)(\alpha+4)} \\ + \left( 1 - \frac{(\alpha+2)(\alpha+5)}{(\alpha+3)(\alpha+4)} \right) \xi \Bigg]. \end{aligned}$$

A typical value for $\alpha$ is $\alpha = 1/3$. This gives that

$$\Omega = (1 - \xi)^{3/7} \left( 1.132 + 0.0714\, \xi \right).$$

## E. ALTERNATIVE SCALING APPROACH

In this section an alternative approach to scale the problem is presented. This method is following in the spirit of previous scaling approach done by prior authors including (Adachi and Detournay, 2002; Savitski and Detournay, 2002; Bunger and Detournay, 2007). As was pointed out in the paper, non-linear partial differential equation governing the maximum opening $\omega(x,t)$ and boundary conditions, which are given by

$$\begin{aligned} \frac{\partial \omega}{\partial t} &= -\Xi \frac{\partial}{\partial x}\left[\omega^{2\varphi}\left(-\frac{\partial \omega}{\partial x}\right)^{\frac{1}{2}}\right] \\ x = \ell \quad &\Rightarrow \quad \omega(\ell,t) = 0 \\ x = \ell \quad &\Rightarrow \quad q(\ell,t) = 0 \\ x = 0 \quad &\Rightarrow \quad q(0,t) = q_{in} \end{aligned} \tag{A.22}$$

The scaling begins with introduction of dimensionless opening $\tilde{\Omega}(\xi,t)$ and length $\gamma(t)$, as well as a scaled coordinate $\xi$, according to

$$\begin{aligned} \omega(x,t) &= \mathcal{W}(t)\tilde{\Omega}(\xi,t) \\ \ell(t) &= \mathcal{L}(t)\gamma(t) \\ \xi &= \frac{x}{\ell(t)} \end{aligned} \tag{A.23}$$

where $\mathcal{W}$ and $\mathcal{L}$ represent characteristic HF width and length, to be specified later. Substituting Equation A.23 into Equation A.22 and the accompanying boundary conditions leads to (see Section A.E.1 for details)

$$\begin{aligned} -\frac{\xi t}{\mathcal{L}}\frac{\partial \mathcal{L}}{\partial t}\frac{\partial \tilde{\Omega}}{\partial \xi} + \frac{t}{\mathcal{W}}\frac{\partial \mathcal{W}}{\partial t}\tilde{\Omega} &= -\Xi \frac{\mathcal{W}^{2\varphi-\frac{1}{2}}t}{\mathcal{L}^{\frac{3}{2}}}\frac{1}{\gamma^{\frac{3}{2}}}\frac{\partial}{\partial \xi}\left[\tilde{\Omega}^{2\varphi}\left(-\frac{\partial \tilde{\Omega}}{\partial \xi}\right)^{\frac{1}{2}}\right] \\ \frac{\pi H \Xi \mathcal{W}^{2\varphi}}{4q_{in}}\left(\frac{\mathcal{W}}{\mathcal{L}}\right)^{\frac{1}{2}}\frac{\tilde{\Omega}^{2\varphi}}{\gamma^{\frac{1}{2}}}\left(-\frac{\partial \tilde{\Omega}}{\partial \xi}\right)^{\frac{1}{2}}\Bigg|_{\xi=0} &= 1 \\ \mathcal{W}^{2\varphi}\left(\frac{\mathcal{W}}{\mathcal{L}}\right)^{\frac{1}{2}}\frac{\tilde{\Omega}^{2\varphi}}{\gamma^{\frac{1}{2}}}\left(-\frac{\partial \tilde{\Omega}}{\partial \xi}\right)^{\frac{1}{2}}\Bigg|_{\xi=1} &= 0 \\ \tilde{\Omega}(1,t) &= 0 \end{aligned} \tag{A.24}$$

Observing Equation A.24, three dimensionless groups can be defined:

$$\begin{aligned} \mathcal{G}_1 &= \Xi \frac{\mathcal{W}^{2\varphi-\frac{1}{2}} t}{\mathcal{L}^{\frac{3}{2}}} \\ \mathcal{G}_2 &= \mathcal{W}^{2\varphi} \left( \frac{\mathcal{W}}{\mathcal{L}} \right)^{\frac{1}{2}} \\ \mathcal{G}_3 &= \frac{\pi H \Xi}{4 q_{in}} \end{aligned} \tag{A.25}$$

Choosing the characteristic scales $\mathcal{L}$ and $\mathcal{W}$ so that $\mathcal{G}_1 = 1$ and $\mathcal{G}_2 = 1$ leads to

$$\begin{aligned} \mathcal{W}(t) &= (\Xi t)^{\frac{1}{4\varphi+2}} \\ \mathcal{L}(t) &= (\Xi t)^{\frac{4\varphi+1}{4\varphi+2}} \end{aligned} \tag{A.26}$$

Now by replacing the result from Equation A.26 into Equation A.24 and considering the changes of variables $\gamma^{\frac{3}{4\varphi-1}} \Omega = \tilde{\Omega}$ and $\gamma(t) = \lambda(t)/\varrho$, where $\varrho = \left( \frac{\pi H \Xi}{4 q_{in}} \right)^{\frac{4\varphi-1}{4\varphi+2}}$, leads to the final form of the scaled governing equations (compare with Equation 15 in the paper)

$$-\xi \frac{4\varphi+1}{4\varphi+2} \frac{d\Omega}{d\xi} + \frac{\Omega}{4\varphi+2} = -\frac{d}{d\xi} \left[ \Omega^{2\varphi} \left( -\frac{d\Omega}{d\xi} \right)^{\frac{1}{2}} \right] \tag{A.27a}$$

$$\Omega^{2\varphi} \left( -\frac{d\Omega}{d\xi} \right)^{\frac{1}{2}} \Bigg|_{\xi=1} = 0 \tag{A.27b}$$

$$\Omega(1) = 0 \tag{A.27c}$$

$$\lambda^{\frac{4\varphi+2}{4\varphi-1}} \Omega^{2\varphi} \left( -\frac{d\Omega}{d\xi} \right)^{\frac{1}{2}} \Bigg|_{\xi=0} = 1 \tag{A.27d}$$

The scaling has therefore resulted in an ordinary differential equation (ODE) for $\Omega$, Equation A.27a. There are two homogeneous boundary conditions (flux at tip, Equation A.27c, and crack width at tip, Equation A.27c), and one inhomogeneous boundary condition (flux at source, Equation A.27d). Importantly, this ODE depends on only the scaled coordinate $\xi$ and the parameter $\varphi$. It does not depend upon the scaled length, $\lambda$, which only enters via the now-decoupled inlet condition (Equation A.27d). Hence, a solution can be obtained firstly for $\Omega$ and then can be substituted into Equation A.27d to obtain $\lambda$. Furthermore, the parameter $\varphi$ is determined based on an *a priori* choice of fluid flow law, for example upon specification to GMS, $\varphi = 5/6$. In other words, the dependence upon input parameters such as reservoir height, rock/fluid properties, and injection rate is all accounted for by the scaling.

Finally, by taking the integral from both sides of the equation from $\xi$ to 1 and imposing the boundary conditions, a convenient form of the ODE for $\Omega$ (Equation A.27) is given by

$$
\begin{aligned}
\int_{\xi}^{1} \Omega d\eta = -\xi \frac{4\varphi+1}{4\varphi+2}\Omega + \Omega^{2\varphi}\left(-\frac{d\Omega}{d\xi}\right)^{\frac{1}{2}} \\
\Omega(1) = 0 \ , \ \ \Omega^{2\varphi}\left(-\frac{d\Omega}{d\xi}\right)^{\frac{1}{2}}\Bigg|_{\xi=1} = 0 \\
\lambda^{\frac{4\varphi+2}{4\varphi-1}}\Omega^{2\varphi}\left(-\frac{d\Omega}{d\xi}\right)^{\frac{1}{2}}\Bigg|_{\xi=0} = 1
\end{aligned}
\tag{A.28}
$$

### 1. Deriving Dimensionless Form of the Equations

After introducing the scaling in Equation A.23, from application of the chain rule

$$
\frac{\partial}{\partial x} = \frac{1}{l}\frac{\partial}{\partial \xi} = \frac{1}{\mathcal{L}\gamma}\frac{\partial}{\partial \xi}
\tag{A.29}
$$

These two variables, $\xi$ and $t$, represent location and time, respectively. Furthermore, while $t$ is an independent variable, $\xi$ depends implicitly on time because of the time-dependence of $\ell(t)$. Hence the complete time derivative is expressed by

$$
\frac{d}{dt} = \frac{\partial}{\partial t} + \frac{\partial \xi}{\partial t}\frac{\partial}{\partial \xi}.
\tag{A.30}
$$

Applying to Equation A.23, Equation A.22, and the boundary conditions gives

$$
\begin{aligned}
\frac{t}{\mathcal{W}}\frac{d(\mathcal{W}\tilde{\Omega})}{dt} = -\Xi\frac{\mathcal{W}^{2\mu-\frac{1}{2}}t}{\mathcal{L}^{\frac{3}{2}}}\frac{1}{\gamma^{\frac{3}{2}}}\frac{\partial}{\partial \xi}\left[\tilde{\Omega}^{2\mu}\left(-\frac{\partial\tilde{\Omega}}{\partial\xi}\right)^{\frac{1}{2}}\right] \\
\frac{\pi H \Xi \mathcal{W}^{2\varphi}}{4q_{in}}\left(\frac{\mathcal{W}}{\mathcal{L}}\right)^{\frac{1}{2}}\frac{\tilde{\Omega}^{2\varphi}}{\gamma^{\frac{1}{2}}}\left(-\frac{\partial\tilde{\Omega}}{\partial\xi}\right)^{\frac{1}{2}}\Bigg|_{\xi=0} = 1 \\
\mathcal{W}^{2\varphi}\left(\frac{\mathcal{W}}{\mathcal{L}}\right)^{\frac{1}{2}}\frac{\tilde{\Omega}^{2\varphi}}{\gamma^{\frac{1}{2}}}\left(-\frac{\partial\tilde{\Omega}}{\partial\xi}\right)^{\frac{1}{2}}\Bigg|_{\xi=1} = 0 \\
\tilde{\Omega}(1,t) = 0
\end{aligned}
\tag{A.31}
$$

Note we multiplied both sides by $t/\mathcal{W}$ to non-dimensionalize the equations. From the product rule and the definition of the complete time derivative

$$\frac{d(\mathcal{W}\tilde{\Omega})}{dt} = \left(\tilde{\Omega}\frac{d\mathcal{W}}{dt}\right) + \left(\mathcal{W}\frac{d\tilde{\Omega}}{dt}\right) = \left(\tilde{\Omega}\frac{d\mathcal{W}}{dt}\right) + \left(\mathcal{W}\left[\frac{\partial\tilde{\Omega}}{\partial t} + \frac{\partial\tilde{\Omega}}{\partial\xi}\frac{\partial\xi}{\partial t}\right]\right) \tag{A.32}$$

Then using $\frac{\partial\xi}{\partial t} = -\frac{\xi}{\mathcal{L}}\frac{\partial\mathcal{L}}{\partial t} - \frac{\xi}{\gamma}\frac{\partial\gamma}{\partial t}$ leads to

$$\frac{t}{\mathcal{W}}\frac{d(\mathcal{W}\tilde{\Omega})}{dt} = t\frac{\partial\tilde{\Omega}}{\partial t} - \frac{\xi t}{\mathcal{L}}\frac{\partial\mathcal{L}}{\partial t}\frac{\partial\tilde{\Omega}}{\partial\xi} - \frac{\xi t}{\gamma}\frac{\partial\gamma}{\partial t}\frac{\partial\tilde{\Omega}}{\partial\xi} + \frac{t}{\mathcal{W}}\tilde{\Omega}\frac{d\mathcal{W}}{dt} \tag{A.33}$$

It is now important to realize there are no evolution parameters appearing explicitly in the problem. This would be different if, for example, we were to consider fluid leakoff; an additional term would appear in Equation A.31 containing both a leak-off coefficient and time. However, in this limit of an impermeable rock, $\partial\tilde{\Omega}/\partial t = 0$ and $d\gamma/dt = 0$. Hence

$$\frac{t}{\mathcal{W}}\frac{d(\mathcal{W}\tilde{\Omega})}{dt} = -\frac{\xi t}{\mathcal{L}}\frac{\partial\mathcal{L}}{\partial t}\frac{\partial\tilde{\Omega}}{\partial\xi} + \frac{t}{\mathcal{W}}\tilde{\Omega}\frac{d\mathcal{W}}{dt} \tag{A.34}$$

Combining Equation A.34 and Equation A.31 we arrive to Equation A.24.

Table A1: Limit of variables in Equation A.14

| Parameter | Minimum | Maximum |
|---|---|---|
| $H$ | 20 m | 200 m |
| $t$ | 0.001 s | 1000 s |
| $k$ | 0.5 mm | 50 mm |
| $\nu$ | 0 | 0.5 |
| $G$ | 1 GPa | 100 GPa |

# APPENDIX B

# APPENDICES FOR “SOLUTION FOR A PLANE STRAIN ROUGH-WALLED HYDRAULIC FRACTURE DRIVEN BY TURBULENT FLUID THROUGH IMPERMEABLE ROCK”

## A. SOLUTION FOR LAMINAR FLOW

For the laminar solution, we will use the equations provided by Adachi (2001b), that is

$$\begin{aligned}
w(x,t) &= 0.6162\left(\frac{\mu' Q_0^3}{E'}\right)^{1/6} t^{1/3}\left[\sqrt{3}(1-\frac{x^2}{\ell^2})^{2/3} + \mathcal{M}(1-\frac{x^2}{\ell^2})^{5/3}\right.\\
&\quad \left. + \mathcal{N}\left(4\sqrt{1-\frac{x^2}{\ell^2}} + 2\frac{x^2}{\ell^2} ln\left|\frac{1-\sqrt{1-\frac{x^2}{\ell^2}}}{1+\sqrt{1-\frac{x^2}{\ell^2}}}\right|\right)\right]\\
p(x,t) &= \left(\frac{\mu' E'^2}{t}\right)^{1/3}\left[\frac{1}{3\pi}\beta(\frac{1}{2},\frac{2}{3})\left(\sqrt{3}\ {}_2F_1\left(\frac{-1}{6},1;\frac{1}{2};\frac{x^2}{\ell^2}\right)\right.\right.\\
&\quad \left.\left. + \frac{10}{7}\mathcal{M}\ {}_2F_1\left(\frac{-7}{6},1;\frac{1}{2};\frac{x^2}{\ell^2}\right)\right) + \mathcal{N}\left(2-\pi\left|\frac{x}{\ell}\right|\right)\right]\\
q(x,t) &= 0.3797 Q_0\left[\frac{2}{7}\left(\sqrt{3}+\frac{10\mathcal{M}}{13}\right)\beta(\frac{1}{2},\frac{2}{3}) - \sqrt{3}\left(\frac{x}{\ell}\right)\ {}_2F_1\left(\frac{1}{2},-\frac{2}{3};\frac{3}{2};\frac{x^2}{\ell^2}\right)\right.\\
&\quad + \frac{2}{\sqrt{3}}\left(\frac{x}{\ell}\right)(1-\frac{x^2}{\ell^2})^{2/3} - \mathcal{M}\left(\frac{x}{\ell}\right)\ {}_2F_1\left(\frac{1}{2},-\frac{5}{3};\frac{3}{2};\frac{x^2}{\ell^2}\right)\\
&\quad \left. + \frac{2\mathcal{M}}{3}\left(\frac{x}{\ell}\right)(1-\frac{x^2}{\ell^2})^{5/3} + \frac{4\mathcal{N}}{3}\left(\arccos\left(\frac{x}{\ell}\right) + \frac{x^3}{2\ell^3}\ln\left|\frac{1-\sqrt{1-\frac{x^2}{\ell^2}}}{1+\sqrt{1-\frac{x^2}{\ell^2}}}\right|\right)\right]\\
\ell(t) &= 0.6162\left(\frac{E' Q_0^3}{\mu'}\right)^{1/6} t^{2/3}
\end{aligned} \tag{B.1}$$

where $\mathcal{M} = -0.15601, \mathcal{N} = 0.066322$, ${}_2F_1(a, b; c; d)$ is Gauss' hypergeometric function, and $\beta$ is the beta function Abramowitz and Stegun (1972).

## B. CRACK-TIP SOLUTION

Initially, Tsai and Rice (2010) derived the tip asymptotic solution for GMS approach. Tsai and Rice demonstrated that the pressure gradient and crack tip velocity relation is analogous to the problem of power-law viscous fluid. Hence, they adapted the zero toughness solution of Desroches et al. (1994) for the crack tip. In this manuscript, we are following the solution developed by Adachi (2001b) for laminar fluid flow.

Obtaining the correct relationship between pressure and opening requires the elasticity equation and continuity to be solved simultaneously. We expect that due to the singularity, close to crack tip the opening of the crack be small but the crack opening changes rapidly and the pressure becomes very large. Therefore, we anticipate to capture the singularity in our solution by solving for it. The coupling between the elasticity equation and continuity that we talked about should be also hold at crack tip. It is possible to say that the singularity at crack tip for elasticity should match with the singularity of the continuity equation at crack tip (after Desroches et al. (1994); Detournay (2004)). So we propose the Ansatz solution for the pressure

$$p = \delta \cos(b\pi)(\ell - x)^{b-1} \tag{B.2}$$

where $\delta$ and $b$ are constants that need to be calculated. From Equation B.2, the width Ansatz should be of the form

$$w = \frac{4\delta}{E'b} \sin(b\pi)(\ell - x)^{b} \tag{B.3}$$

Therefore, defining the scaling

$$w = \varepsilon L \Omega(\xi, t), \quad p = \varepsilon E' \Pi(\xi, t), \quad \ell = L\gamma(t), \quad q = Q_0 \Psi(\xi, t), \quad \xi = \frac{x}{\ell},$$

and also the change of variables

$$\gamma^{4/(2+\alpha)} \bar{\Omega} = \Omega \ , \ \gamma^{(2-\alpha)/(2+\alpha)} \bar{\Pi} = \Pi$$

we obtain

$$\begin{aligned}\bar{\Omega} &= \frac{4\delta}{E'b\varepsilon} L^{b-1}\gamma^{b-4/(2+\alpha)}\sin(b\pi)(1-\xi)^b = A_\Omega(1-\xi)^b \\ \bar{\Pi} &= \frac{\delta}{\varepsilon E'} L^{b-1}\gamma^{b-4/(2+\alpha)}\cos(b\pi)(1-\xi)^{b-1} = B_\Pi(1-\xi)^{b-1}\end{aligned} \tag{B.4}$$

Here, the constants $A_\Omega$ and $B_\Pi$ are related through the following equation

$$B_\Pi = \frac{bA_\Omega}{4} cot(\pi b) \tag{B.5}$$

Now we can substitute Equation B.4 into the scaled continuity Equation III.17a.

$$\frac{-A_\Omega}{b+1}(1-\xi)^{b+1} = -\frac{\alpha+4}{\alpha+6}\xi A_\Omega(1-\xi)^b + A_\Omega^{\frac{3+\alpha}{2}} B_\Pi^{1/2}(1-\xi)^{2b+\frac{\alpha b}{2}-1}(b-1)^{1/2} \tag{B.6}$$

We know that when we approach the crack tip, the value of opening will rapidly decrease. Also, by approaching the crack tip, a variable we will call $\varepsilon$, where $\varepsilon = \lim_{\xi\to 1}(1-\xi)$, becomes very small. Therefore, since on the left hand side of the Equation B.6, we have $\varepsilon^{b+1}$, we can neglect it compared with terms having a smaller exponent. To avoid a trivial solution the two terms on the left hand side should be of the same order of magnitude, so

$$b = 2b + \frac{\alpha b}{2} - 1 \quad \Rightarrow \quad b = \frac{2}{2+\alpha} \tag{B.7}$$

From the rest of the equation we can then say that

$$\frac{\alpha+4}{\alpha+6} = A_\Omega^{\frac{1+\alpha}{2}} B_\Pi^{1/2}(b-1)^{1/2} \quad , \qquad \xi \to 1 \tag{B.8}$$

Also, using Equation B.5 combined with Equations B.8 and B.7

$$\begin{aligned}A_\Omega &= \left[(2+\alpha)\left(\frac{\alpha+4}{\alpha+6}\right)\sqrt{\frac{2}{\alpha}\tan(\frac{\alpha\pi}{2+\alpha})}\right]^{\frac{2}{2+\alpha}} \\ B_\Pi &= \frac{cot(\frac{2\pi}{2+\alpha})}{4+2\alpha}\left[(2+\alpha)\left(\frac{\alpha+4}{\alpha+6}\right)\sqrt{\frac{2}{\alpha}\tan(\frac{\alpha\pi}{2+\alpha})}\right]^{\frac{2}{2+\alpha}}\end{aligned} \tag{B.9}$$

Because of the symmetry of the plane strain problem about the y axis, we should have the same solution when we get closer to the other tip of the crack. So if $\xi \to -1$, the solution should be

$$\bar{\Omega} = A_\Omega(1+\xi)^b$$

$$\bar{\Pi} = B_\Pi(1+\xi)^{b-1}.$$

Hence, near the crack tip, the behavior of the solution is

$$\bar{\Omega} = A'_{\Omega}(1-\xi^2)^b$$

$$\bar{\Pi} = B'_{\Pi}(1-\xi^2)^{b-1}.$$

We should find the value of $A'_{\Omega}$ and $B'_{\Pi}$ in a way that guarantees the same behavior near the ends of the crack, so

$$\lim_{\xi\to\pm1} A'_{\Omega}(1-\xi^2)^b = \lim_{\xi\to\pm1} A_{\Omega}(1-\xi)^b$$

$$\lim_{\xi\to\pm1} B'_{\Pi}(1-\xi^2)^{b-1} = \lim_{\xi\to\pm1} B_{\Pi}(1-\xi)^{b-1}.$$

These considerations lead to

$$\begin{aligned} A'_{\Omega} &= \left[\left(\frac{2+\alpha}{2}\right)\left(\frac{\alpha+4}{\alpha+6}\right)\sqrt{\frac{2}{\alpha}\tan\left(\frac{\alpha\pi}{2+\alpha}\right)}\right]^{\frac{2}{2+\alpha}} \\ B'_{\Pi} &= \frac{cot(\frac{2\pi}{2+\alpha})}{4+2\alpha}\left[\left(\frac{2+\alpha}{2}\right)\left(\frac{\alpha+4}{\alpha+6}\right)\sqrt{\frac{2}{\alpha}\tan\left(\frac{\alpha\pi}{2+\alpha}\right)}\right]^{\frac{2}{2+\alpha}} \end{aligned} \tag{B.10}$$

which in turn gives the solution presented in Equations III.18.

## C. PARTICULAR SOLUTION

The general solution for opening and pressure satisfies the tip solution. But we should check it for the injection point, too. From fluid flow (Equation III.2), we know that the crack opening is always positive ($W > 0$). Thus, if the flow is to be defined at the inlet, the gradient of the pressure should be negative, viz.

$$\frac{d\bar{\Pi}}{d\xi} < 0.$$

However at $\xi = 0$, the derivative of the general solution is zero. So we should construct a particular solution that satisfies the continuity and elasticity equations at the inlet. The simplest solution is to consider that the pressure gradient at the inlet is a constant negative number (if $a > 0$)

$$\frac{d\bar{\Pi}}{d\xi} = -a \quad , \qquad \xi \to 0.$$

So after taking the integral of both sides we obtain

$$\bar{\Pi} = -a|\xi| + \varrho,$$

where $\varrho$ is also a constant. From LEFM (Equation III.17c)

$$\int_0^1 \frac{-a|\zeta| + \varrho}{\sqrt{1-\zeta^2}} d\zeta = -a + \frac{\pi}{2}\varrho.$$

Thus if the LEFM is to hold, we should have $a = \pi/2\varrho$. So without loss of any generality, we can assign $\varrho = 2$, and so

$$\bar{\Pi} = 2 - \pi|\xi| \tag{B.11}$$

Next, we should find an appropriate solution for the opening that satisfies the elasticity equation based on the calculated pressure. The inverse of the elasticity Equation III.6 is Sneddon and Lowengrub (1969)

$$w(x,t) = -\frac{4}{\pi E'} \int_0^l p(s,t) ln \left| \frac{\sqrt{l^2 - x^2} + \sqrt{l^2 - s^2}}{\sqrt{l^2 - x^2} - \sqrt{l^2 - s^2}} \right| ds \tag{B.12}$$

After the scaling given in Equations III.9 and III.15, and the change of variables $\gamma^{4/(2+\alpha)}\bar{\Omega} = \Omega$ and $\gamma^{(2-\alpha)/(2+\alpha)}\bar{\Pi} = \Pi$ (Equation III.16), this becomes

$$\bar{\Omega} = -\frac{4}{\pi} \int_0^1 \bar{\Pi} ln \left| \frac{\sqrt{1-\xi^2} + \sqrt{1-\eta^2}}{\sqrt{1-\xi^2} - \sqrt{1-\eta^2}} \right| d\eta \tag{B.13}$$

So after substitution of Equation B.11 into Equation B.13

$$\bar{\Omega} = -\frac{4}{\pi} \int_0^1 (2 - \pi|\xi|) ln \left| \frac{\sqrt{1-\xi^2} + \sqrt{1-\eta^2}}{\sqrt{1-\xi^2} - \sqrt{1-\eta^2}} \right| d\eta.$$

Taking the integral we arrive to

$$\bar{\Omega} = 4\sqrt{1-\xi^2} + 2\xi^2 ln \left| \frac{1 - \sqrt{1-\xi^2}}{1 + \sqrt{1-\xi^2}} \right| \tag{B.14}$$

Taken together, Equations B.11 and B.14 give the particular solutions used in Equations III.26 and III.27

## D. INTEGRAL OF THE OPENING

The opening is given as (Equation III.28)

$$\begin{aligned}\bar{\Omega} &= \mathcal{A}_0 \Xi (1-\xi^2)^{\varphi} + \sum_{j=1}^{\infty} \mathcal{A}_j (1-\xi^2)^{\varphi+1} C_{2j-2}^{(\varphi+\frac{1}{2})}(\xi) \\ &+ \mathcal{B}\left[4\sqrt{1-\xi^2} + 2\xi^2 ln\left|\frac{1-\sqrt{1-\xi^2}}{1+\sqrt{1-\xi^2}}\right|\right]\end{aligned}$$

In this section we want to calculate $\int_{\xi}^{1} \bar{\Omega} d\zeta$. But before going further we need to develop an equation that helps on finding the integral.

**Lemma 1.** *If $C_n^m$ is a Gegenbauer funtion, then*

$$\frac{d}{dx}\left[\left(1-x^2\right)^{a+2} C_n^m(x)\right] = \left(1-x^2\right)^{a+1}\left[-(n+2a+4)xC_n^m(x) + (n+2m-1)C_{n-1}^m(x)\right]$$

*Proof.* Expanding, the left hand side derivation, gives (using Equation B.41 in Appendix B.E)

$$\frac{d}{dx}\left[\left(1-x^2\right)^{a+2} C_n^m(x)\right] = -2(a+2)x\left(1-x^2\right)^{a+1} C_n^m + 2m\left(1-x^2\right)^{a+2} C_{n-1}^{m+1} \tag{B.15}$$

Also, for the Gegenbauer function

$$C_n^m(x) = \frac{m}{n+m}\left(C_n^{m+1}(x) - C_{n-2}^{m+1}(x)\right) \tag{B.16a}$$

$$C_n^{m+1}(x) = \frac{(n+2m)(n+2m+1)C_n^m(x) - (n+1)(n+2)C_{n+2}^m(x)}{4m(n+m+1)(1-x^2)} \tag{B.16b}$$

so by replacing n with $n-1$ in Equation B.16b and replacing back into Equation B.15

$$\begin{aligned}\frac{d}{dx}\left[\left(1-x^2\right)^{a+2} C_n^m(x)\right] &= \left(1-x^2\right)^{a+1} \times \left[-(2a+4)xC_n^m(x)\right. \\ &\left.+\frac{(n+2m-1)(n+2m)C_{n-1}^m(x) - n(n+1)C_{n+1}^m(x)}{2(n+m)}\right]\end{aligned} \tag{B.17}$$

Also from Equation B.42 in Appendix B.E

$$(n+1)C_{n+1}^m(x) = 2x(n+m)C_n^m(x) - (n+2m-1)C_{n-1}^m(x) \tag{B.18}$$

Thus combining Equations B.18 and B.17 and after simplification,

$$\begin{aligned}\frac{d}{dx}\left[\left(1-x^2\right)^{a+2} C_n^m(x)\right] &= \left(1-x^2\right)^{a+1} \times \left[-(n+2a+4)xC_n^m(x)\right. \\ &\left.+(n+2m-1)C_{n-1}^m(x)\right]\end{aligned} \tag{B.19}$$

□

Now in Lemma 1, if we substitute $m$ with $\lambda+1$, $a$ with $\lambda-3/2$, and $n$ with $k-1$, then

$$\frac{d}{dx}\left[\left(1-x^2\right)^{\lambda+1/2}C_{k-1}^{\lambda+1}(x)\right]=(k+2\lambda)\left(1-x^2\right)^{\lambda-1/2}\left[-xC_{k-1}^{\lambda+1}(x)+C_{k-2}^{\lambda+1}(x)\right] \tag{B.20}$$

Also by using Equation B.42 in Appendix B.E with some simplification,

$$xC_{k-1}^{\lambda+1}(x)=\frac{k}{2(k+\lambda)}C_k^{\lambda+1}(x)+\frac{k+2\lambda}{2(k+\lambda)}C_{k-2}^{\lambda+1}(x).$$

Combining this result with Equation B.20 leads to

$$\frac{d}{dx}\left[\left(1-x^2\right)^{\lambda+1/2}C_{k-1}^{\lambda+1}(x)\right]=\frac{k(k+2\lambda)}{2(k+\lambda)}\left(1-x^2\right)^{\lambda-1/2}\left[-C_k^{\lambda+1}(x)+C_{k-2}^{\lambda+1}\right] \tag{B.21}$$

Now by using Equation B.16

$$C_k^{\lambda}(x)=\frac{\lambda}{k+\lambda}\left(C_k^{\lambda+1}(x)-C_{k-2}^{\lambda+1}(x)\right),$$

so that

$$\frac{d}{dx}\left[\left(1-x^2\right)^{\lambda+1/2}C_{k-1}^{\lambda+1}(x)\right]=\frac{-k(k+2\lambda)}{2\lambda}\left(1-x^2\right)^{\lambda-1/2}C_k^{\lambda} \tag{B.22}$$

We can then take the integral on both sides of Equation B.22 from $0$ to $\xi$, knowing: 1) that if $k$ is an even number, $k-1$ is always an odd number, and 2) the value of $C_m^n(0)$ is zero when $m$ is an odd number. Thus, if $k$ is an even number, $C_{k-1}^n(0)=0$. So

$$\int_0^{\xi}\left(1-\eta^2\right)^{\lambda-1/2}C_k^{\lambda}d\eta=\frac{-2\lambda}{k(k+2\lambda)}\left(1-\xi^2\right)^{\lambda+1/2}C_{k-1}^{\lambda+1}(\xi) \tag{B.23}$$

Now imagine that we want to find the integral of the form

$$\int_0^{\xi}\left(1-\eta^2\right)^{\lambda}C_k^{\lambda-\frac{1}{2}}d\eta$$

So again by using Equation B.16,

$$C_k^{\lambda-\frac{1}{2}}(x)=\frac{\lambda-\frac{1}{2}}{k+\lambda-\frac{1}{2}}\left(C_k^{\lambda+\frac{1}{2}}(x)-C_{k-2}^{\lambda+\frac{1}{2}}(x)\right),$$

so that

$$\begin{aligned}\int_0^\xi \left(1-\eta^2\right)^\lambda C_k^{\lambda-\frac{1}{2}} d\eta = &\frac{\lambda-\frac{1}{2}}{k+\lambda-\frac{1}{2}}\int_0^\xi \left(1-\eta^2\right)^\lambda C_k^{\lambda+\frac{1}{2}}(x) d\eta - \\ &\frac{\lambda-\frac{1}{2}}{k+\lambda-\frac{1}{2}}\int_0^\xi \left(1-\eta^2\right)^\lambda C_{k-2}^{\lambda+\frac{1}{2}}(x) d\eta\end{aligned}$$

Now using Equation B.23

$$\begin{aligned}\int_0^\xi \left(1-\eta^2\right)^\lambda C_k^{\lambda+\frac{1}{2}} d\eta &= \frac{-2\lambda-1}{k(k+2\lambda+1)}\left(1-\xi^2\right)^{\lambda+1} C_{k-1}^{\lambda+\frac{3}{2}}(\xi) \\ \int_0^\xi \left(1-\eta^2\right)^\lambda C_{k-2}^{\lambda+\frac{1}{2}} d\eta &= \frac{-2\lambda-1}{(k-2)(k+2\lambda-1)}\left(1-\xi^2\right)^{\lambda+1} C_{k-3}^{\lambda+\frac{3}{2}}(\xi)\end{aligned}$$

and so

$$\begin{aligned}\int_0^\xi \left(1-\eta^2\right)^\lambda C_k^{\lambda-\frac{1}{2}}(\eta) d\eta = -&\frac{4\lambda^2-1}{2k+2\lambda-1}\left(1-\xi^2\right)^{\lambda+1}\times \\ &\left[\frac{C_{k-1}^{\lambda+\frac{3}{2}}(\xi)}{k(k+2\lambda+1)}-\frac{C_{k-3}^{\lambda+\frac{3}{2}}(\xi)}{(k-2)(k+2\lambda-1)}\right]\end{aligned} \tag{B.24}$$

We are now ready to calculate $\int_\xi^1 \bar{\Omega} d\zeta$. Firstly we split the integral as

$$\int_\xi^1 \bar{\Omega} d\zeta = \int_0^1 \bar{\Omega} d\zeta - \int_0^\xi \bar{\Omega} d\zeta$$

Looking at Equation III.28, in the interval 0 and 1, $\widehat{\Omega}$ is only singular at $\xi = 1$. Using Equation III.28

$$\begin{aligned}\int_0^\xi \bar{\Omega} d\eta = &\int_0^\xi \mathcal{A}_0 \Xi (1-\eta^2)^\varphi d\eta + \sum_{j=1}^{\infty} \mathcal{A}_j \int_0^\xi (1-\eta^2)^{\varphi+1} C_{2j-2}^{(\varphi+\frac{1}{2})}(\eta) d\eta \\ &+ \mathcal{B}\left[4\int_0^\xi \sqrt{1-\eta^2} d\eta + 2\int_0^\xi \eta^2 ln\left|\frac{1-\sqrt{1-\eta^2}}{1+\sqrt{1-\eta^2}}\right| d\eta\right]\end{aligned} \tag{B.25}$$

From Equation B.24, by considering $\lambda = \varphi + 1$, and $k = 2j - 2$,

$$\begin{aligned}\int_0^\xi \left(1-\eta^2\right)^{\varphi+1} C_{2j-2}^{\varphi+\frac{1}{2}}(\eta) d\eta = -&\frac{4(\varphi+1)^2-1}{4j+2\varphi-3}\left(1-\xi^2\right)^{\varphi+2}\times \\ &\left[\frac{C_{2j-3}^{\varphi+\frac{5}{2}}(\xi)}{(2j-2)(2j+2\varphi+1)}-\frac{C_{2j-5}^{\varphi+\frac{5}{2}}(\xi)}{(2j-4)(2j+2\varphi-1)}\right]\end{aligned} \tag{B.26}$$

for $j > 2$, because we want to be able to define $C_{2j-5}^{\varphi+5/2}$. We know that $C_2^{\lambda}(\xi) = -\lambda + 2\lambda(1+\lambda)\xi^2$. So for $j = 2$

$$\begin{aligned}&\int_0^{\xi}\left(1-\eta^2\right)^{\varphi+1} C_2^{\varphi+\frac{1}{2}}(\eta)d\eta = \\ &(\varphi+\frac{1}{2})\int_0^{\xi}\left(1-\eta^2\right)^{\varphi+1}\left((2\varphi+3)\eta^2-1\right)d\eta = \frac{2\varphi+1}{(2\varphi+3)(2\varphi+5)\xi} \\ &\times\left[\frac{(1-\xi^2)^{2+\varphi}}{2}(2-(3+2\varphi)^2\xi^2) - {}_2F_1\left(-\frac{1}{2},-1-\varphi;\frac{1}{2};\xi^2\right)\right]\end{aligned} \tag{B.27}$$

and for $j = 1$, since $C_0^m(\xi) = 1$,

$$\int_0^{\xi}\left(1-\eta^2\right)^{\varphi+1}d\eta = \xi\ {}_2F_1\left(\frac{1}{2},-1-\varphi;\frac{3}{2};\xi^2\right) \tag{B.28}$$

By knowing that $C_m^n(0) = 0$ for all odd value of m,

$$\int_0^1\left(1-\eta^2\right)^{\varphi+1}d\eta = \frac{\sqrt{\pi}\Gamma(2+\varphi)}{2\Gamma(\frac{5}{2}+\varphi)},$$

$$\int_0^1\left(1-\eta^2\right)^{\varphi+1}C_2^{\varphi+\frac{1}{2}}(\eta)d\eta = -\frac{\sqrt{\pi}(1+2\varphi)\Gamma(2+\varphi)}{4\Gamma(\frac{7}{2}+\varphi)},$$

and

$$\int_0^1\left(1-\eta^2\right)^{\varphi+1}C_{2j}^{\varphi+\frac{1}{2}}(\eta)d\eta = 0\ \ ,\qquad j > 2$$

so

$$\sum_{i=1}^{\infty}\mathcal{A}_i\int_0^1(1-\eta^2)^{\varphi+1}C_{2j-2}^{(\varphi+\frac{1}{2})}(\eta)d\eta = \frac{\sqrt{\pi}\Gamma(2+\varphi)}{2\Gamma(\frac{5}{2}+\varphi)}\left[\mathcal{A}_1-\mathcal{A}_2\left(\frac{1+2\varphi}{5+2\varphi}\right)\right] \tag{B.29}$$

Or, based on the beta function Abramowitz and Stegun (1972)

$$\sum_{i=1}^{\infty}\mathcal{A}_i\int_0^1(1-\eta^2)^{\varphi+1}C_{2j-2}^{(\varphi+\frac{1}{2})}(\eta)d\eta = \frac{1}{2}\beta(\frac{1}{2},2+\varphi)\left[\mathcal{A}_1-\mathcal{A}_2\left(\frac{1+2\varphi}{5+2\varphi}\right)\right] \tag{B.30}$$

Also

$$\int_{\xi}^1\mathcal{A}_0\Xi(1-\eta^2)^{\varphi}d\eta = \mathcal{A}_0\Xi\frac{\sqrt{\pi}\Gamma(1+\varphi)}{2\Gamma(\frac{3}{2}+\varphi)} - \mathcal{A}_0\Xi\xi\ \ {}_2F_1\left(\frac{1}{2},-\varphi;\frac{3}{2};\xi^2\right) \tag{B.31}$$

and

$$\int_{\xi}^1\sqrt{1-\eta^2}d\eta = \frac{1}{2}\left(-\xi\sqrt{1-\xi^2}+\arccos(\xi)\right) \tag{B.32}$$

The last integral is then given by

$$\int_0^{\xi} \eta^2 ln \left| \frac{1-\sqrt{1-\eta^2}}{1+\sqrt{1-\eta^2}} \right| d\eta.$$

This integral has singularity at its boundary. So we need to find the Cauchy principal value of this integral:

$$\int_0^{1} \eta^2 ln \left| \frac{1-\sqrt{1-\eta^2}}{1+\sqrt{1-\eta^2}} \right| d\eta = -\frac{\pi}{6} \tag{B.33}$$

For the regular part we can use integration by parts $\int udv = uv - \int vdu$, where

$$u = ln \left| \frac{1-\sqrt{1-\eta^2}}{1+\sqrt{1-\eta^2}} \right| \quad , \quad dv = \eta^2 d\eta \tag{B.34}$$

and

$$du = \frac{2}{\eta\sqrt{1-\eta^2}} d\eta \ , \quad v = \frac{\eta^3}{3} \tag{B.35}$$

The singularity of the integral is at $\xi = 0$, and using a series expansion

$$\lim_{\xi \to 0^+} uv = \lim_{\xi \to 0^+} \frac{\xi^3}{3} ln \left| \frac{1-\sqrt{1-\xi^2}}{1+\sqrt{1-\xi^2}} \right| = 0 \ , \quad \lim_{\xi \to 1} uv = 0 \tag{B.36}$$

Thus

$$\begin{aligned} \int_0^{\xi} \eta^2 ln \left| \frac{1-\sqrt{1-\eta^2}}{1+\sqrt{1-\eta^2}} \right| d\eta = -\frac{2}{3} \int_0^{\xi} \frac{\eta^2}{\sqrt{1-\eta^2}} d\eta = \\ \frac{\xi^3}{3} ln \left| \frac{1-\sqrt{1-\xi^2}}{1+\sqrt{1-\xi^2}} \right| - \frac{1}{3} \left[ -\xi\sqrt{1-\xi^2} + \arcsin(\xi) \right] \end{aligned} \tag{B.37}$$

and

$$\begin{aligned} \int_{\xi}^{1} \eta^2 ln \left| \frac{1-\sqrt{1-\eta^2}}{1+\sqrt{1-\eta^2}} \right| d\eta = -\frac{\pi}{6} - \frac{\xi^3}{3} ln \left| \frac{1-\sqrt{1-\xi^2}}{1+\sqrt{1-\xi^2}} \right| \\ + \frac{1}{3} \left[ -\xi\sqrt{1-\xi^2} + \arcsin(\xi) \right] \end{aligned} \tag{B.38}$$

Then, by knowing that

$${}_2F_1\left(-\frac{1}{2}, -1-\varphi; \frac{1}{2}; \xi^2\right) - (1-\xi^2)^{2+\varphi} = (3+2\varphi)\xi^2 \ {}_2F_1\left(\frac{1}{2}, -1-\varphi; \frac{3}{2}; \xi^2\right)$$

$$\begin{aligned}\int_{\xi}^{1}\bar{\Omega}d\eta = {} & \mathcal{A}_0\Xi\left[\frac{\beta(1+\varphi,\frac{1}{2})}{2} - \xi\ {}_2F_1\left(\frac{1}{2},-\varphi;\frac{3}{2};\xi^2\right)\right] \\ & + \mathcal{A}_1\left[\frac{\beta(2+\varphi,\frac{1}{2})}{2} - \xi\ {}_2F_1\left(\frac{1}{2},-1-\varphi;\frac{3}{2};\xi^2\right)\right] \\ & + \mathcal{A}_2\left(\frac{1+2\varphi}{4}\right)\left[-2\beta(2+\varphi,\frac{3}{2}) + \frac{2(3+2\varphi)}{(5+2\varphi)}\xi(1-\xi^2)^{2+\varphi}\right. \\ & \qquad \left. + \frac{4}{5+2\varphi}\xi\ {}_2F_1\left(\frac{1}{2},-1-\varphi;\frac{3}{2};\xi^2\right)\right] \\ & + \frac{(2\varphi+1)(2\varphi+3)}{2}\left(1-\xi^2\right)^{\varphi+2}\sum_{j=3}^{\infty}\frac{\mathcal{A}_j}{(4j+2\varphi-3)}\times \\ & \qquad \left[\frac{C_{2j-3}^{\varphi+\frac{5}{2}}(\xi)}{(j-1)(2j+2\varphi+1)} - \frac{C_{2j-5}^{\varphi+\frac{5}{2}}(\xi)}{(j-2)(2j+2\varphi-1)}\right] \\ & + \frac{2\mathcal{B}}{3}\left[-\xi^3 ln\left|\frac{1-\sqrt{1-\xi^2}}{1+\sqrt{1-\xi^2}}\right| + 2\left[\arccos(\xi) - 2\xi\sqrt{1-\xi^2}\right]\right]\end{aligned} \tag{B.39}$$

Finally, since there is no time dependent parameter:

$$\int_{\xi}^{1}\dot{\bar{\Omega}}d\eta = 0 \tag{B.40}$$

Which leaves Equation III.32.

### E. DERIVING DIMENSIONLESS EQUATIONS

Prior to undertaking the derivations, some necessary definitions are:

I. The derivating of the in Gegenbauer is defined as Szeg (1975)

$$\frac{d}{d\xi}C_n^{\lambda}(\xi) = 2\lambda C_{n-1}^{\lambda+1}(\xi) \tag{B.41}$$

II. The recurrence relation of the Gegenbauer function over its subscript is defined as Abramowitz and Stegun (1972)

$$nC_n^{\lambda}(\xi) = 2\xi(n+\lambda-1)C_{n-1}^{\lambda}(\xi) - (n+2\lambda-2)C_{n-2}^{\lambda}(\xi) \tag{B.42}$$

III. The recurrence relation over the superscript is

$$\begin{aligned}\frac{(2\lambda+n)(2\lambda+n+1)}{2\lambda}C_n^{\lambda}(\xi) = \left[2\lambda - 2(\xi^2-1)(\lambda+n+1)+1\right]C_n^{\lambda+1}(\xi) - \\ 2(\lambda+1)(\xi^2-1)C_n^{\lambda+2}(\xi)\end{aligned} \tag{B.43}$$

IV. From the recurrence relation for Gegenbauer polynomials Abramowitz and Stegun (1972), we have

$$C_1^{\lambda}(\xi) = 2\lambda\xi \tag{B.44}$$

V. From complex variables we have the following identities:

$$\begin{aligned} &e^{\mp\frac{i\pi}{2}} = \mp i \ , \quad e^{\mp i\pi} = -1 \ , \quad e^{\pm\frac{i}{2}\pi(-2r)} = (-1)^r \\ &e^{\pm\frac{i}{2}\pi(1-2r)} = \pm(-1)^r i \ , \quad e^{\mp\frac{i}{2}\pi(2r+1)} = \mp(-1)^r i \ , \quad e^{\mp ir\pi} = (-1)^r \end{aligned} \tag{B.45}$$

VI. For the Gamma function Abramowitz and Stegun (1972)

$$\Gamma(x+1) = x\Gamma(x) \tag{B.46}$$

VII. The beta function is defined as Abramowitz and Stegun (1972)

$$\beta(m,n) = \frac{\Gamma(m)\Gamma(n)}{\Gamma(m+n)} \tag{B.47}$$

We also require some theorems:

**Theorem 1.** *If $\beta \leq k$ and for $Real(\lambda) > -1/2$ (look at Gradshteyn and Ryzhik Gradshteyn and Ryzhik (2014)):*

$$\int_{-1}^{1}\frac{\zeta^{\beta}(1-\zeta^2)^{\lambda-1/2}C_k^{\lambda}(\zeta)}{\zeta-\xi}d\zeta = -\frac{2^{3/2-\lambda}\sqrt{\pi}}{\Gamma(\lambda)}\xi^{\beta}(\xi^2-1)^{\lambda/2-1/4}e^{-(\lambda-1/2)\pi i}Q_{k+\lambda-1/2}^{\lambda-1/2}(\xi)$$

*where $Q_m^{\lambda}(\xi)$ is the Legendre function Abramowitz and Stegun (1972).*

Also the following identity is valid for Legendre functions when $(|\xi|^2 < 1)$ Abramowitz and Stegun (1972)

$$\begin{aligned} &e^{-\mu\pi i}Q_{\nu}^{\mu}(\xi) = \sqrt{\pi}2^{\mu}(\xi^2-1)^{-\frac{\mu}{2}}\times \\ &\left[\frac{\Gamma(\frac{1}{2}+\frac{\nu}{2}+\frac{\mu}{2})}{2\Gamma(1+\frac{\nu}{2}-\frac{\mu}{2})}e^{\pm\frac{i}{2}\pi(\mu-\nu-1)}{}_2F_1\left(-\frac{\nu}{2}-\frac{\mu}{2},\frac{\nu}{2}+\frac{1}{2}-\frac{\mu}{2};\frac{1}{2};\xi^2\right)+\right. \\ &\left.\frac{\xi\Gamma(1+\frac{\nu}{2}+\frac{\mu}{2})}{\Gamma(\frac{1}{2}+\frac{\nu}{2}-\frac{\mu}{2})}e^{\pm\frac{i}{2}\pi(\mu-\nu)}{}_2F_1\left(\frac{1}{2}-\frac{\nu}{2}-\frac{\mu}{2},1+\frac{\nu}{2}-\frac{\mu}{2};\frac{3}{2};\xi^2\right)\right] \end{aligned} \tag{B.48}$$

**Theorem 2.** *A Cauchy-type integral is defined as*

$$\Phi(z) = \int_{\mathcal{C}} \frac{\varphi(x)}{x-z} dx,$$

*where $\mathcal{C}$ is a simple closed curve in the complex plane and function $\varphi(x)$ is analytic on and inside the region surounded by curve $\mathcal{C}$ (see Arfken and Weber (2005)). The Sokhotski-Plemelj Plemelj (1908); Sokhotskii (1873) theorem for the real line states that the principle value of the Cauchy integral over an interval $\mathcal{C}$ on the real line is Muskhelishvili (1953)*

$$P.V. \int_{\mathcal{C}} \frac{\varphi(x)}{x-z} dx = \frac{1}{2}(\mathcal{L}^{+} + \mathcal{L}^{-}),$$

*where*

$$\mathcal{L}^{\pm}(z) = \lim_{\varepsilon \to 0^{+}} \int_{\mathcal{C}} \frac{\varphi(x)}{x-(z \pm i\varepsilon)} dx, \quad \textit{and} \quad i = \sqrt{(-1)}.$$

## 1. Solution

We mentioned that the solution for the opening is in the form of polynomial series with base function $\hat{\Omega}$ as

$$\bar{\Omega}^{*} = \sum_{i=0}^{\infty} \mathcal{A}_i \hat{\Omega}_i$$

Our goal is to construct the pressure, also in the form of the polynomial series, that satisfies the elasticity equation as well and be in the form of

$$\bar{\Pi}^{*} = \sum_{i=0}^{\infty} \mathcal{A}_i \hat{\Pi}_i$$

So at first we propose the solution for the opening to be in the form of Gegenbauer polynomial because the given tip asymptotic is in the form of $(1-\xi^2)^{\varphi}$. So the proposed solution will be

$$\begin{aligned} \hat{\Omega}_0 &= (1-\xi^2)^{\varphi} \\ \hat{\Omega}_j &= (1-\xi^2)^{\varphi+1} C_m^n(\xi) \quad , \quad j > 0 \end{aligned} \tag{B.49}$$

The Gegenbauer function ($C_m^n(\xi)$) is an odd function when m is odd and it is an even function when m is even. Also, because of symmetry of the crack growth around the well bore, which implies that $\hat{\Omega}_j$ is an even function, the $C^n_m(\xi)$ should be an even function. Thus $m$ should an even number like $m = 2r$ so

$$\hat{\Omega}_j = (1-\xi^2)^{\varphi+1} C^n_{2r}(\xi).$$

then, from elasticity

$$\hat{\Pi}_j = -\frac{1}{4\pi}\int_{-1}^{1} \frac{d\hat{\Omega}_j}{d\eta}\frac{d\eta}{\eta-\xi} \tag{B.50}$$

By considering Equation B.50, we can find the appropriate solution for the pressure along the crack. Using also Equations B.41 and B.49, we obtain

$$\frac{d\hat{\Omega}_0}{d\eta} = -2\varphi\eta(1-\eta^2)^{\varphi-1}$$

$$\frac{d\hat{\Omega}_j}{d\eta} = -2\eta(\varphi+1)(1-\eta^2)^{\varphi} C^n_{2r}(\eta) + 2n(1-\eta^2)^{\varphi+1} C^{n+1}_{2r-1}(\eta).$$

So the elasticity equation will become

$$\begin{aligned} \hat{\Pi}_0 &= \frac{\varphi}{2\pi}\int_{-1}^{1} \eta(1-\eta^2)^{\varphi-1}\frac{d\eta}{\eta-\xi} \\ \hat{\Pi}_j &= \frac{(\varphi+1)}{2\pi}\int_{-1}^{1} \frac{\eta(1-\eta^2)^{\varphi}C^n_{2r}(\eta)d\eta}{\eta-\xi} - \frac{n}{2\pi}\int_{-1}^{1}\frac{(1-\eta^2)^{\varphi+1}C^{n+1}_{2r-1}(\eta)d\eta}{\eta-\xi} \quad , \qquad j>0 \end{aligned} \tag{B.51}$$

In order to solve for the pressure, we need to find three integrals:

$$\begin{aligned} \mathcal{L}_1 &= \frac{\varphi}{2\pi}\int_{-1}^{1} \frac{\eta(1-\eta^2)^{\varphi-1}}{\eta-\xi}d\eta \\ \mathcal{L}_2 &= -\frac{n}{2\pi}\int_{-1}^{1} \frac{(1-\eta^2)^{\varphi+1}C^{n+1}_{2r-1}(\eta)}{\eta-\xi}d\eta \\ \mathcal{L}_3 &= \frac{(\varphi+1)}{2\pi}\int_{-1}^{1} \frac{\eta(1-\eta^2)^{\varphi}C^n_{2r}(\eta)}{\eta-\xi}d\eta \end{aligned} \tag{B.52}$$

For the first integral, using Equation B.44,

$$\mathcal{L}_1 = \frac{\varphi}{2\pi}\int_{-1}^{1} \frac{\eta(1-\eta^2)^{\varphi-1}}{\eta-\xi}d\eta = \frac{\varphi}{2(2\varphi-1)\pi}\int_{-1}^{1} \frac{(1-\eta^2)^{\varphi-1}C^{\varphi-1/2}_{1}(\eta)}{\eta-\xi}d\eta \tag{B.53}$$

Now from theorem 1, choosing $\beta = 0$, $\lambda = \varphi - 1/2$, and $k = 1$:

$$\int_{-1}^{1} \frac{(1-\eta^2)^{\varphi-1}C^{\varphi-1/2}_{1}(\eta)}{\eta-\xi}d\eta = -\frac{2^{2-\varphi}\sqrt{\pi}}{\Gamma(\varphi-1/2)}(\xi^2-1)^{\frac{\varphi-1}{2}} e^{-(\varphi-1)\pi i} Q^{\varphi-1}_{\varphi}(\xi) \tag{B.54}$$

So by comparing Equations B.53 and B.54

$$\mathcal{L}_1 = -\frac{\varphi}{2(2\varphi-1)\pi}\frac{2^{2-\varphi}\sqrt{\pi}}{\Gamma(\varphi-1/2)}(\xi^2-1)^{\varphi/2-1/2}e^{-(\varphi-1)\pi i}Q_{\varphi}^{\varphi-1}(\xi) \tag{B.55}$$

Also from Equation B.48, and knowing that

$${}_2F_1\left(1-\varphi,\frac{3}{2};\frac{3}{2};\xi^2\right) = (1-\xi^2)^{\varphi-1},$$

we obtain

$$\begin{gathered} e^{-(\varphi-1)\pi i}Q_{\varphi}^{\varphi-1}(\xi) = \sqrt{\pi}2^{\varphi-1}(\xi^2-1)^{-\frac{\varphi-1}{2}}\times \\ \left[-\frac{\Gamma(\varphi)}{\sqrt{\pi}}{}_2F_1\left(\frac{1}{2}-\varphi,1;\frac{1}{2};\xi^2\right) \mp i\frac{\xi\Gamma(\frac{1}{2}+\varphi)}{(1-\xi^2)^{1-\varphi}}\right] \end{gathered} \tag{B.56}$$

Now by replacing the Equation B.56 into Equation B.55 (for Gamma and Beta function see Equations B.46 and B.47)

$$\mathcal{L}_1 = \frac{\varphi}{2}\left[\frac{\beta(\frac{1}{2},\varphi)}{\pi}{}_2F_1\left(\frac{1}{2}-\varphi,1;\frac{1}{2};\xi^2\right) \pm \frac{i\xi}{(1-\xi^2)^{1-\varphi}}\right] \tag{B.57}$$

In order to find the principal value of this integral on the real line, theorem 2 leads to

$$\hat{\Pi}_0 = \frac{1}{2}(\mathcal{L}_1^+ + \mathcal{L}_1^-) = \frac{\varphi}{2\pi}\beta(\frac{1}{2},\varphi){}_2F_1\left(\frac{1}{2}-\varphi,1;\frac{1}{2};\xi^2\right) \tag{B.58}$$

with the condition that $Real(\varphi) \geq 0$.

Now we want to solve for $\mathcal{L}_2$. Since we are constructing a solution that solves our coupling problem, we have freedom to choose parameters as long as they support all the boundary conditions and governing equations. Until now there is no limitation on the value of $n$. But, if we choose $n = \varphi + 1/2$, we can take the integral easily. Also in order to use theorem 1, we choose $\beta = 0$, $\lambda = \varphi + 3/2$, and $k = 2r - 1$. So from theorem 1 we have:

$$\int_{-1}^{1}\frac{(1-\zeta^2)^{\varphi+1}C_{2r-1}^{\varphi+3/2}(\zeta)}{\zeta-\xi}d\zeta = -\frac{2^{-\varphi}\sqrt{\pi}}{\Gamma(\varphi+3/2)}(\xi^2-1)^{\frac{\varphi+1}{2}}e^{-(\varphi+1)\pi i}Q_{2r+\varphi}^{\varphi+1}(\xi) \tag{B.59}$$

And also from Equation B.48, (see also Equation B.45):

$$\begin{gathered} e^{-(\varphi+1)\pi i}Q_{2r+\varphi}^{\varphi+1}(\xi) = \sqrt{\pi}2^{\varphi+1}(\xi^2-1)^{-\frac{\varphi+1}{2}}(-1)^r\times \\ \left[\frac{\Gamma(1+r+\varphi)}{2\Gamma(r+\frac{1}{2})}{}_2F_1\left(-r-\varphi-\frac{1}{2},r;\frac{1}{2};\xi^2\right) \pm i \right. \\ \left. \frac{\xi\Gamma(r+\varphi+\frac{3}{2})}{\Gamma(r)}{}_2F_1\left(-r-\varphi,r+\frac{1}{2};\frac{3}{2};\xi^2\right)\right] \end{gathered} \tag{B.60}$$

thus by combining Equation B.60, B.59, and B.52

$$\begin{aligned}\mathcal{L}_2 = (-1)^r \Bigg[&\frac{1}{2\beta(\varphi+1/2, r+\frac{1}{2})} {}_2F_1\left(-r-\varphi-\frac{1}{2}, r; \frac{1}{2}; \xi^2\right) \\ &\pm i\frac{\xi(r+\varphi+\frac{1}{2})}{\beta(\varphi+1/2, r)} {}_2F_1\left(-r-\varphi, r+\frac{1}{2}; \frac{3}{2}; \xi^2\right)\Bigg]\end{aligned} \tag{B.61}$$

Again by using theorem 2, the principal value of $\mathcal{L}_2$ is called $\mathcal{J}_2$ and is equal to

$$\mathcal{J}_2 = \frac{1}{2}(\mathcal{L}_2^+ + \mathcal{L}_2^-) = \frac{(-1)^r}{2\beta(\varphi+1/2, r+\frac{1}{2})} {}_2F_1\left(-r-\varphi-\frac{1}{2}, r; \frac{1}{2}; \xi^2\right) \tag{B.62}$$

With the conditions $r \geq 0.5$ and $\varphi > -2$.

And finally, for the third integral, we can consider that $\beta = 1$, $\lambda = \varphi + 1/2$, $k = 2r$, so from theorem 1, we have:

$$\int_{-1}^{1} \frac{\zeta(1-\zeta^2)^{\varphi} C_{2r}^{\varphi+1/2}(\zeta)}{\zeta-\xi} d\zeta = -\frac{2^{1-\varphi}\sqrt{\pi}}{\Gamma(\varphi+\frac{1}{2})} \xi(\xi^2-1)^{\varphi/2} e^{-(\varphi)\pi i} Q_{2r+\varphi}^{\varphi}(\xi) \tag{B.63}$$

and from Equation B.48 (see also Equation B.45):

$$\begin{aligned}&e^{-\varphi\pi i} Q_{2r+\varphi}^{\varphi}(\xi) = \sqrt{\pi}2^{\varphi}(\xi^2-1)^{-\frac{\varphi}{2}}(-1)^r \times \\ &\left[\mp i\frac{\Gamma(\frac{1}{2}+r+\varphi)}{2\Gamma(1+r)} {}_2F_1\left(-r-\varphi, r+\frac{1}{2}; \frac{1}{2}; \xi^2\right) + \frac{\xi\Gamma(1+r+\varphi)}{\Gamma(\frac{1}{2}+r)} {}_2F_1\left(\frac{1}{2}-r-\varphi, 1+r; \frac{3}{2}; \xi^2\right)\right]\end{aligned} \tag{B.64}$$

So, by replacing Equation B.64 into Equation B.63 and then following Equation B.52

$$\begin{aligned}\mathcal{L}_3 = &-(\varphi+1)\xi(-1)^r \times \\ &\Bigg[\mp i\frac{1}{2r\beta(\varphi+\frac{1}{2}, r)} {}_2F_1\left(-r-\varphi, r+\frac{1}{2}; \frac{1}{2}; \xi^2\right) \\ &+\frac{\xi}{\beta(\varphi+\frac{1}{2}, \frac{1}{2}+r)} {}_2F_1\left(\frac{1}{2}-r-\varphi, 1+r; \frac{3}{2}; \xi^2\right)\Bigg]\end{aligned} \tag{B.65}$$

The principal value of integral $\mathcal{L}_3$ is thus called $\mathcal{J}_3$ and is equal to

$$\mathcal{J}_3 = \frac{1}{2}(\mathcal{L}_3^+ + \mathcal{L}_3^-) = \frac{-(-1)^r\xi^2(\varphi+1)}{\beta(\varphi+\frac{1}{2}, \frac{1}{2}+r)} {}_2F_1\left(\frac{1}{2}-r-\varphi, 1+r; \frac{3}{2}; \xi^2\right) \tag{B.66}$$

with the condition that $r \geq 0.5$ and $\varphi > -1$. Thus the pressure integral Equation B.51 for $j > 0$ is

$$\hat{\Pi}_j = \frac{(-1)^r}{\beta(\varphi + 1/2, r + \frac{1}{2})} \left[ \frac{1}{2} {}_2F_1 \left( -r - \varphi - \frac{1}{2}, r; \frac{1}{2}; \xi^2 \right) \right. \\ \left. -\xi^2 (\varphi + 1) {}_2F_1 \left( \frac{1}{2} - r - \varphi, 1 + r; \frac{3}{2}; \xi^2 \right) \right] \tag{B.67}$$

Since $r \geq 0.5$ and it is an integer, and also $j$ is an integer such that $j > 0$, so we can say that $r = j$. Thus

$$\begin{aligned} \hat{\Omega}_0 &= (1 - \xi^2)^{\varphi} \\ \hat{\Omega}_j &= (1 - \xi^2)^{\varphi + 1} C_{2j}^{\varphi + \frac{1}{2}}(\xi) \ , \quad j > 0 \end{aligned} \tag{B.68}$$

and

$$\begin{aligned} \hat{\Pi}_0 &= \frac{\varphi}{2\pi} \beta(\frac{1}{2}, \varphi) {}_2F_1 \left( \frac{1}{2} - \varphi, 1; \frac{1}{2}; \xi^2 \right) \\ \hat{\Pi}_j &= \frac{(-1)^j}{\beta(\varphi + 1/2, j + \frac{1}{2})} \left[ \frac{1}{2} {}_2F_1 \left( -j - \varphi - \frac{1}{2}, j; \frac{1}{2}; \xi^2 \right) \right. \\ &\qquad \left. -\xi^2 (\varphi + 1) {}_2F_1 \left( \frac{1}{2} - j - \varphi, 1 + j; \frac{3}{2}; \xi^2 \right) \right] \end{aligned} \tag{B.69}$$

On the other hand, letting $r = j - 1$, which will help with accuracy of the results, because $\hat{\Omega}_1 = (1 - \xi^2)^{\varphi + 1}$ is the second order solution for the crack tip. In the case of r=j-1,

$$\begin{aligned} \hat{\Omega}_0 &= (1 - \xi^2)^{\varphi} \\ \hat{\Omega}_j &= (1 - \xi^2)^{\varphi + 1} C_{2j-2}^{\varphi + \frac{1}{2}}(\xi) \ , \quad j > 0 \end{aligned} \tag{B.70}$$

and

$$\begin{aligned} \hat{\Pi}_0 &= \frac{\varphi}{2\pi} \beta(\frac{1}{2}, \varphi) {}_2F_1 \left( \frac{1}{2} - \varphi, 1; \frac{1}{2}; \xi^2 \right) \\ \hat{\Pi}_1 &= \frac{\varphi(\varphi + 1)}{(2\varphi + 1)\pi} \beta(\frac{1}{2}, \varphi) {}_2F_1 \left( -\frac{1}{2} - \varphi, 1; \frac{1}{2}; \xi^2 \right) \\ \hat{\Pi}_j &= \frac{2j - 1}{2\pi} \beta(\varphi + j, \frac{1}{2} - j) \left[ \xi^2 (\varphi + 1) {}_2F_1 \left( \frac{3}{2} - j - \varphi, j; \frac{3}{2}; \xi^2 \right) \right. \\ &\qquad \left. -\frac{1}{2} {}_2F_1 \left( \frac{1}{2} - j - \varphi, j - 1; \frac{1}{2}; \xi^2 \right) \right] \end{aligned} \tag{B.71}$$

Using identities for Hypergeometric functions

$$\begin{aligned} {}_2F_1\left(\frac{1}{2}-\varphi,1;\frac{1}{2};\xi^2\right) &= \frac{\Gamma(\frac{1}{2})\Gamma(\varphi-1)}{\Gamma(\varphi)\Gamma(-\frac{1}{2})}{}_2F_1\left(\frac{1}{2}-\varphi,1;2-\varphi;1-\xi^2\right) \\ &+(1-\xi^2)^{\varphi-1}\frac{\Gamma(\frac{1}{2})\Gamma(1-\varphi)}{\Gamma(\frac{1}{2}-\varphi)}{}_2F_1\left(\varphi,-\frac{1}{2};\varphi;1-\xi^2\right) \end{aligned} \tag{B.72}$$

$${}_2F_1\left(\varphi,-\frac{1}{2};\varphi;1-\xi^2\right) = |\xi| \tag{B.73}$$

Then, knowing that

$$\frac{\Gamma(\frac{1}{2})}{-\Gamma(\frac{1}{2})} = -\frac{1}{2}, \qquad \Gamma(z)\Gamma(1-z) = \frac{\pi}{\sin(\pi z)},$$

we can say

$$\begin{aligned} &\frac{1}{2\sqrt{\pi}}\frac{\Gamma(\varphi+1)}{\Gamma(\varphi+\frac{1}{2})}\,{}_2F_1\left(\frac{1}{2}-\varphi,1;\frac{1}{2};\xi^2\right) = \\ &\frac{\varphi\cot(\pi\varphi)}{2}|\xi|(1-\xi^2)^{\varphi-1} - \frac{\varphi}{4\sqrt{\pi}}\frac{\Gamma(\varphi-1)}{\Gamma(\varphi+\frac{1}{2})}{}_2F_1\left(\frac{1}{2}-\varphi,1;2-\varphi;1-\xi^2\right) \end{aligned} \tag{B.74}$$

Thus, $\hat{\Pi}_0$ from Equation B.69 (or B.71) is expressed as

$$\begin{aligned} &\hat{\Pi}_0 = \frac{1}{2\sqrt{\pi}}\frac{\Gamma(\varphi+1)}{\Gamma(\frac{1}{2}+\varphi)}{}_2F_1\left(\frac{1}{2}-\varphi,1;\frac{1}{2};\xi^2\right) = \\ &\frac{\varphi\cot(\pi\varphi)}{2}|\xi|(1-\xi^2)^{\varphi-1} - \frac{\varphi}{4\sqrt{\pi}}\frac{\Gamma(\varphi-1)}{\Gamma(\varphi+\frac{1}{2})}{}_2F_1\left(\frac{1}{2}-\varphi,1;2-\varphi;1-\xi^2\right) \end{aligned} \tag{B.75}$$

Now to find the value of the opening at crack tip, let $\xi \to \pm 1$ so that

$$\hat{\Pi}_{tip} = \mathcal{A}_0\Xi\lim_{\xi\to\pm 1}\hat{\Pi}_0 = \mathcal{A}_0\Xi\frac{\varphi\cot(\pi\varphi)}{2}(1-\xi^2)^{\varphi-1} - \mathcal{A}_0\Xi\frac{\varphi}{4\sqrt{\pi}}\frac{\Gamma(\varphi-1)}{\Gamma(\varphi+\frac{1}{2})} \tag{B.76}$$

Also,

$$\bar{\Pi}_{tip} \sim \mathcal{A}_0\frac{\varphi\cot(\varphi\pi)}{2}\Xi(1-\xi^2)^{\varphi-1}$$

So we can see that the solution embeds the tip solution for the pressure.

# APPENDIX C

# APPENDICES FOR "SEMI-ANALYTICAL SOLUTION FOR A PENNY-SHAPED ROUGH-WALLED HYDRAULIC FRACTURE DRIVEN BY TURBULENT FLUID IN AN IMPERMEABLE ROCK"

## A. CRACK-TIP SOLUTION

Close to the tip the crack opening is decreasing to zero and the pressure is singular. We can define the $\delta$ as distance from crack tip ($\delta = 1 - \xi$). Therefore, using a perturbation approach, we seek a power series as

$$\begin{aligned} \bar{\Omega}_{\text{tip}} &= \sum_{i=0}^{\infty} a_i \delta^{m_i} \\ \bar{\Pi}_{\text{tip}} &= \sum_{i=0}^{\infty} b_i \delta^{r_i} \end{aligned} \tag{C.1}$$

where $a_i$, $b_i$, $m_i$, and $r_i$ are unknowns that need to be found and we know that for $0 < i$, we have $0 \leq m_i < m_{i+1}$ and $r_i < r_{i+1}$. Also, following the solution provided by Garagash and Detournay (2000), the fluid pressure and crack opening are connected through the following equations:

$$\begin{aligned} r_0 &= m_0 - 1 \\ b_0 &= \frac{m_0 a_0}{4} \cot\left(\pi m_0\right) \end{aligned} \tag{C.2}$$

Close to the crack tip, the continuity equation (IV.18a) can be simplified to

$$\frac{d\bar{\Omega}}{d\xi} = 2\frac{d}{d\xi}\left(\bar{\Omega}^{\frac{3+\alpha}{2}}\left(-\frac{d\bar{\Pi}}{d\xi}\right)^{\frac{1}{2}}\right)$$

Substituting Equation C.1 into the continuity equation, and knowing the fact that in the limiting case

$$(1+\delta)^m \cong 1 + m\delta + ...$$

we find that

$$\begin{aligned}
-\sum_{i=0}^{\infty} m_i a_i \delta^{m_i-1} = -2a_0^{\frac{3+\alpha}{2}}\sqrt{r_0 b_0}\Bigg[&\frac{3m_0+\alpha m_0+r_0-1}{2}\delta^{\frac{3m_0+\alpha m_0+r_0-3}{2}} \\
&+\frac{3+\alpha}{2}\sum_{i=1}^{\infty}\frac{a_i}{a_0}\left(\frac{m_0+\alpha m_0+r_0-1}{2}+m_i\right)\delta^{\frac{3m_0+\alpha m_0+r_0-3}{2}+m_i-m_0} \\
&+\sum_{i=1}^{\infty}\frac{r_i b_i}{2r_0 b_0}\left(\frac{3m_0+\alpha m_0+r_0-1}{2}+r_i-r_0\right)\delta^{\frac{3m_0+\alpha m_0+r_0-3}{2}+r_i-r_0} \\
&+\frac{3+\alpha}{2}\frac{d}{d\delta}\sum_{i=1}^{\infty}\sum_{j=1}^{\infty}\frac{r_i b_i}{2r_0 b_0}\delta^{\frac{3m_0+\alpha m_0+r_0-1}{2}+r_i-r_0}\frac{a_j}{a_0}\delta^{m_j-m_0}\Bigg]
\end{aligned} \tag{C.3}$$

Also, we know that a power series solution will become satisfied if the coefficient of both sides of the equation becomes equal term by term. The smallest power of the $\delta$ on the left side of the equation is $m_0 - 1$, and for the right hand side since $m_i - m_0$ and $r_i - r_0$ are always positive, the smallest power of $\delta$ therefore is $(3m_0 + \alpha m_0 + r_0 - 3)/2$. Hence, by forcing the power and coefficient be equal in both side of the equation for the first term (first order calculation), we can obtain

$$\begin{aligned}
m_0 - 1 &= \frac{3m_0+\alpha m_0+r_0-3}{2} \\
-m_0 a_0 &= -2a_0^{\frac{3+\alpha}{2}}\sqrt{r_0 b_0}\times\frac{3m_0+\alpha m_0+r_0-1}{2}
\end{aligned} \tag{C.4}$$

Using Equation C.2, we solve the system of unknown equations to find $a_0$, $b_0$, $m_0$, and $r_0$ where the first order solution for the crack tip is

$$\begin{aligned}
\bar{\Omega}_{\text{tip}} &= a_0(1-\xi)^{m_0} \\
\bar{\Pi}_{\text{tip}} &= b_0(1-\xi)^{r_0}
\end{aligned} \tag{C.5}$$

which yields

$$
\begin{aligned}
m_0 &= \frac{2}{2+\alpha} \\
r_0 &= \frac{-\alpha}{2+\alpha} \\
a_0 &= \left[\left(\frac{\alpha+2}{2}\right)\sqrt{\frac{2}{\alpha}\tan\frac{\alpha\pi}{\alpha+2}}\right]^{\frac{2}{2+\alpha}} \\
b_0 &= \frac{\cot\frac{2\pi}{\alpha+2}}{2\alpha+4}\left[\left(\frac{\alpha+2}{2}\right)\sqrt{\frac{2}{\alpha}\tan\frac{\alpha\pi}{\alpha+2}}\right]^{\frac{2}{2+\alpha}}
\end{aligned}
\tag{C.6}
$$

## B. RELATION BETWEEN PRESSURE AND OPENING CONSTANTS

In this section, we are following the method of Savitski and Detournay (2002) to find the relation between constants of the crack opening and fluid pressure. From Equation IV.22, and IV.18b, we have

$$\sum_{i=1}^{\infty}\mathcal{A}_i\widehat{\Omega}_i(\xi) = \frac{8}{\pi}\sum_{i=1}^{\infty}\mathcal{C}_i\int_0^1 G(\xi,\eta)\widehat{\Pi}_i(\eta)\eta d\eta.$$

Note that $\bar{\Omega}^*$ and $\bar{\Pi}^*$ are already related through the elasticity equation and can be simplified on both sides of the equation. To do this, we multiply both sides of the equation by $\xi\widehat{\Omega}_k(\xi)$ and take the integral over $\xi$ from 0 to 1, thus

$$\sum_{i=1}^{\infty}\mathcal{A}_i\int_0^1\widehat{\Omega}_i(\xi)\widehat{\Omega}_k(\xi)\xi d\xi = \frac{8}{\pi}\sum_{i=1}^{\infty}\mathcal{C}_i\int_0^1\widehat{\Omega}_k(\xi)\xi\int_0^1 G(\xi,\eta)\widehat{\Pi}_i(\eta)\eta d\eta d\xi.$$

From the orthogonality condition that we defined for $\widehat{\Omega}_i(\xi)$ and $\widehat{\Pi}_i(\xi)$ (Equation IV.23) we can obtain that

$$\mathcal{A}_k = \frac{8}{\pi}\sum_{i=1}^{\infty}\mathcal{C}_i\int_0^1\widehat{\Omega}_k(\xi)\xi\int_0^1 G(\xi,\eta)\widehat{\Pi}_i(\eta)\eta d\eta d\xi.$$

or (compare with Equation IV.29)

$$\mathcal{A}_k = \sum_{i=1}^{\infty}\mathcal{C}_iL_{ki} = \sum_{i=1}^{\infty}\mathcal{C}_i\left[\frac{8}{\pi}\int_0^1\widehat{\Omega}_k(\xi)\xi\int_0^1 G(\xi,\eta)\widehat{\Pi}_i(\eta)\eta d\eta d\xi\right]$$

In another words

$$L_{ki} = \frac{8}{\pi}\int_0^1\widehat{\Omega}_k(\xi)I_i(\xi)\xi d\xi \tag{C.7}$$

where

$$I_i(\xi) = \int_0^1 G(\xi,\eta)\widehat{\Pi}_i(\eta)\eta d\eta \tag{C.8}$$

After using Equation IV.8 to expand Equation C.8

$$I_i(\xi) = \int_0^{\xi} \frac{\eta}{\xi}\mathcal{F}\left(\arcsin\sqrt{\frac{1-\xi^2}{1-\eta^2}}, \frac{\eta^2}{\xi^2}\right)\widehat{\Pi}_i(\eta)d\eta + \int_{\xi}^1 \mathcal{F}\left(\arcsin\sqrt{\frac{1-\eta^2}{1-\xi^2}}, \frac{\xi^2}{\eta^2}\right)\widehat{\Pi}_i(\eta)d\eta \tag{C.9}$$

The integrals in Equation C.9 are singular and require regularization. To do this, we separate the singular parts from the integrals and treat them separately. Before continuing, we need to mention that the expansion of the incomplete elliptical integral F when both defining parameters of it goes to 1 can be defined as (see Savitski and Detournay (2002))

$$\begin{cases} \mathcal{F}\left(\arcsin\sqrt{\frac{1-\xi^2}{1-\eta^2}}, \frac{\eta^2}{\xi^2}\right) \cong \frac{1}{2}\ln\left(\frac{1-\xi}{1+\xi}\frac{16\xi^2}{\xi^2-\eta^2}\right), & \xi \to \eta \\ \mathcal{F}\left(\arcsin\sqrt{\frac{1-\eta^2}{1-\xi^2}}, \frac{\xi^2}{\eta^2}\right) \cong \frac{1}{2}\ln\left(\frac{1-\eta}{1+\eta}\frac{16\xi^2}{\eta^2-\xi^2}\right), & \eta \to \xi \end{cases} \tag{C.10}$$

Also we know that

$$\int_{\xi}^1 \mathcal{F}\left(\arcsin\sqrt{\frac{1-\xi^2}{1-\eta^2}}, \frac{\eta^2}{\xi^2}\right) = 1-\xi$$

and

$$\int_0^{\xi} \ln\left(\frac{1-\xi}{1+\xi}\frac{16\xi^2}{\xi^2-\eta^2}\right)d\eta = \xi\left[2+\ln\frac{4(1-\xi)}{1+\xi}\right]$$

Thus by adding and subtracting the singular parts in the integral, using the above relations, and re-ordering the equations, we will have $\left(\widehat{\Pi}_i(\xi) = \omega_i - \widetilde{\Pi}_i(\xi)\right)$

$$\begin{aligned} I_i(\xi) =& \frac{\omega_i}{\xi}\int_0^{\xi}\left[\eta\mathcal{F}\left(\arcsin\sqrt{\frac{1-\xi^2}{1-\eta^2}}, \frac{\eta^2}{\xi^2}\right) - \frac{\xi}{2}\ln\left(\frac{1-\xi}{1+\xi}\frac{16\xi^2}{\xi^2-\eta^2}\right)\right]d\eta \\ &+ \frac{1}{h_{i-1}^{1/2}(2\varphi,2)}\int_0^{\xi}\left[\frac{(1-\xi)^{\varphi-1}G_{i-1}(2\varphi,2,\xi)}{2}\ln\left(\frac{1-\xi}{1+\xi}\frac{16\xi^2}{\xi^2-\eta^2}\right)\right. \\ &\left.-\frac{\eta(1-\eta)^{\varphi-1}}{\xi}G_{i-1}(2\varphi,2,\eta)\mathcal{F}\left(\arcsin\sqrt{\frac{1-\xi^2}{1-\eta^2}}, \frac{\eta^2}{\xi^2}\right)\right]d\eta \\ &+ \frac{1}{h_{i-1}^{1/2}(2\varphi,2)}\int_{\xi}^1 \mathcal{F}\left(\arcsin\sqrt{\frac{1-\eta^2}{1-\xi^2}}, \frac{\xi^2}{\eta^2}\right)\times \\ &\left[(1-\xi)^{\varphi-1}G_{i-1}(2\varphi,2,\xi) - (1-\eta)^{\varphi-1}G_{i-1}(2\varphi,2,\eta)\right]d\eta \\ &\left(\omega_i - \frac{(1-\xi)^{\varphi-1}}{h_{i-1}^{1/2}(2\varphi,2)}G_{i-1}(2\varphi,2,\xi)\right)\left(1+\frac{\xi}{2}\ln\left(\frac{4(1-\xi)}{1+\xi}\right)\right) \end{aligned} \tag{C.11}$$

So if we define

$$\begin{aligned}
\mathcal{H}(\xi) &= \int_0^{\xi} \left[ \frac{\eta}{\xi}\mathcal{F}\left(\arcsin\sqrt{\frac{1-\xi^2}{1-\eta^2}}, \frac{\eta^2}{\xi^2}\right) - \frac{1}{2}\ln\left(\frac{1-\xi}{1+\xi}\frac{16\xi^2}{\xi^2-\eta^2}\right)\right] d\eta \\
\mathcal{M}_i(\xi) &= \int_{\xi}^{1} \left(\frac{(1-\xi)^{\varphi-1}G_{i-1}(2\varphi,2,\xi) - (1-\eta)^{\varphi-1}G_{i-1}(2\varphi,2,\eta)}{h_{i-1}^{\frac{1}{2}}(2\varphi,2)}\right) \times \\
&\quad \mathcal{F}\left(\arcsin\sqrt{\frac{1-\eta^2}{1-\xi^2}}, \frac{\xi^2}{\eta^2}\right) d\eta - \frac{1}{h_{i-1}^{\frac{1}{2}}(2\varphi,2)} \times \\
&\quad \int_0^{\xi} \left[\frac{\eta(1-\eta)^{\varphi-1}G_{i-1}(2\varphi,2,\eta)}{\xi}\mathcal{F}\left(\arcsin\sqrt{\frac{1-\xi^2}{1-\eta^2}}, \frac{\eta^2}{\xi^2}\right)\right. \\
&\quad \left. -\frac{(1-\xi)^{\varphi-1}G_{i-1}(2\varphi,2,\xi)}{2}\ln\left(\frac{1-\xi}{1+\xi}\frac{16\xi^2}{\xi^2-\eta^2}\right)\right] d\eta
\end{aligned} \tag{C.12}$$

we can re-write Equation C.11 as

$$\begin{aligned}
I_i(\xi) = \omega_i\mathcal{H}(\xi) + \mathcal{M}_i(\xi) + &\left(\omega_i - \frac{(1-\xi)^{\varphi-1}}{h_{i-1}^{1/2}(2\varphi,2)}G_{i-1}(2\varphi,2,\xi)\right) \times \\
&\left(1 + \frac{\xi}{2}\ln\left(\frac{4(1-\xi)}{1+\xi}\right)\right)
\end{aligned} \tag{C.13}$$

Therefore, Equation C.7 will change to

$$\begin{aligned}
L_{ki} =& \frac{8}{\pi}\frac{1}{h_{k-1}^{\frac{1}{2}}(2\varphi+2,2)}\int_0^1 \xi(1-\xi)^{\varphi}G_{k-1}(2\varphi+2,2,\xi)\left[\omega_i\mathcal{H}(\xi) + \mathcal{M}_i(\xi)\right. \\
&\left. + \left(\omega_i - \frac{(1-\xi)^{\varphi-1}}{h_{i-1}^{1/2}(2\varphi,2)}G_{i-1}(2\varphi,2,\xi)\right)\left(1 + \frac{\xi}{2}\ln\left(\frac{4(1-\xi)}{1+\xi}\right)\right)\right] d\xi
\end{aligned} \tag{C.14}$$

and if we define

$$\begin{aligned}
\mathcal{N}_k &= \int_0^1 \xi(1-\xi)^{\varphi}G_{k-1}(2\varphi+2,2,\xi)\left(1 + \frac{\xi}{2}\ln\left(\frac{4(1-\xi)}{1+\xi}\right)\right) d\eta \\
&\quad + \int_0^1 \mathcal{H}(\xi)\xi(1-\xi)^{\varphi}G_{k-1}(2\varphi+2,2,\xi) d\eta \\
\mathcal{P}_{k,i} &= \int_0^1 \mathcal{M}_i(\xi)\xi(1-\xi)^{\varphi}G_{k-1}(2\varphi+2,2,\xi) d\xi \\
&\quad - \frac{1}{h_{i-1}^{\frac{1}{2}}(2\varphi,2)}\int_0^1 \xi(1-\xi)^{2\varphi-1}G_{k-1}(2\varphi+2,2,\xi) \times \\
&\quad G_{i-1}(2\varphi,2,\xi)\left(1 + \frac{\xi}{2}\ln\left(\frac{4(1-\xi)}{1+\xi}\right)\right) d\xi
\end{aligned} \tag{C.15}$$

we can find that

$$L_{ki} = \frac{8}{\pi} \frac{\omega_i \mathcal{N}_k + \mathcal{P}_{k,i}}{h_{k-1}^{\frac{1}{2}}(2\varphi + 2, 2)} \tag{C.16}$$

Since calculating the integrals are cumbersome and time consuming, we visualize the answer of the integrals in Figure C1.

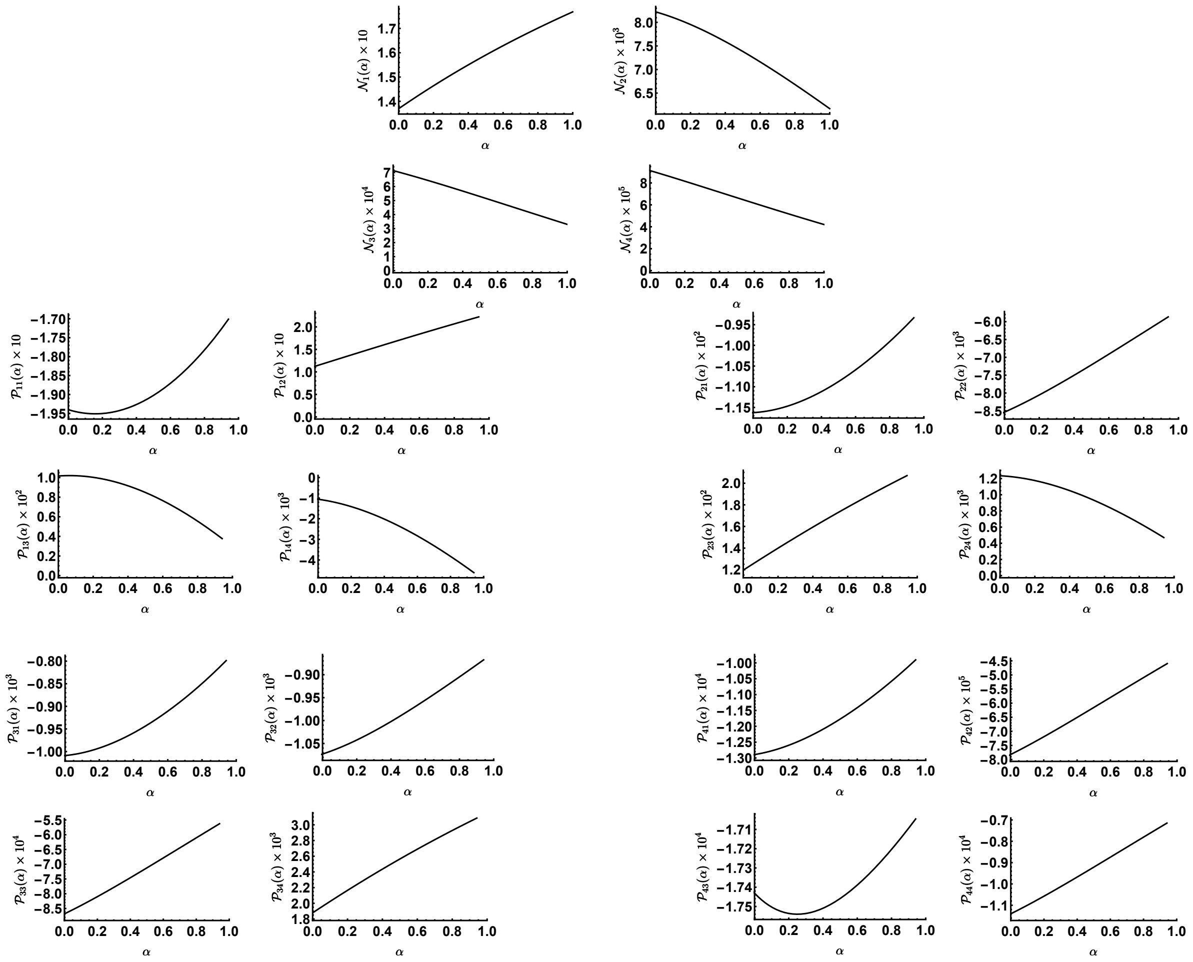

Figure C1: Behavior of the integrals that have been introduced in Equation IV.30.

# APPENDIX D

# APPENDICES FOR “NUMERICAL MODEL FOR A PENNY-SHAPED HYDRAULIC FRACTURE DRIVEN BY LAMINAR/TURBULENT FLUID IN AN IMPERMEABLE ROCK”

## A. NUMERICAL METHOD

Before deriving the equations, we need to explain notation as indicated in Figure V.5, whereby

$$\begin{aligned}
\xi_i &= (i-\frac{1}{2})\Delta\xi \\
\Delta\overline{\Omega}_i^{\tau} &= \overline{\Omega}_i^{\tau} - \overline{\Omega}_i^{\tau-\Delta\tau} \\
\Delta\overline{\Pi}_i^{\tau} &= \overline{\Pi}_i^{\tau} - \overline{\Pi}_i^{\tau-\Delta\tau} \\
\Delta\gamma^{\tau} &= \gamma^{\tau} - \gamma^{\tau-\Delta\tau}
\end{aligned} \tag{D.1}$$

with $\Delta\overline{\Omega}_i^{\tau}$, $\Delta\overline{\Pi}_i^{\tau}$, and $\Delta\gamma^{\tau}$ giving the change of opening, pressure, and length respectively at element $i^{th}$ and at time $\tau$. We know that all the parameters are defined at the middle of the element. However, we also know that the boundary conditions, like the fluid injection and the opening at the tip of the crack, are not defined at the middle of the elements. These values are defined at one edge of certain elements. On the other hand, the fluid flux has the derivative of the pressure inside it and we can use a central difference method to define the derivative at the center of elements. Thus, in order to collaborate the effect of boundary conditions at nodes, we define the fluid flux at the edges rather than at the center of the elements (see Figure D1)

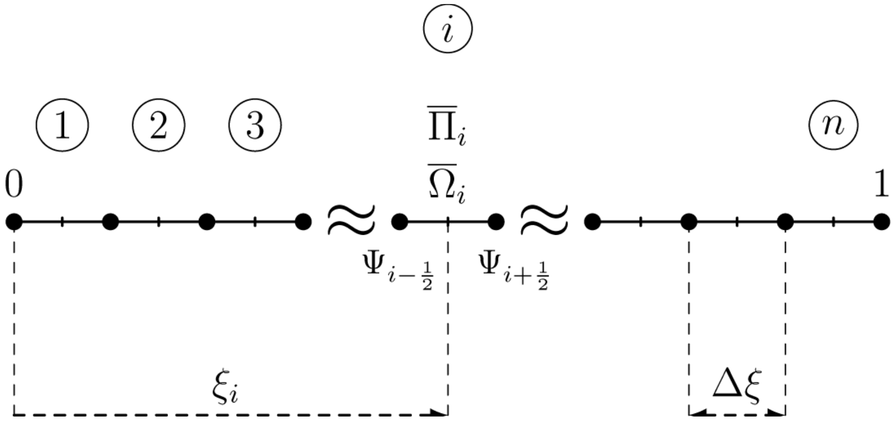

Figure D1: Discretization scheme for half radial hydraulic fracture.

Since, all the equations are presented at the center of the elements, we can transfer the flow from the nodes to the center using linear interpolation, thus

$$\frac{\partial}{\partial \xi}\frac{Q_0 T}{\varepsilon L^2}\tilde{\Psi} = \frac{\frac{Q_0 T}{\varepsilon L^2}\tilde{\Psi}_{i+\frac{1}{2}} - \frac{Q_0 T}{\varepsilon L^2}\tilde{\Psi}_{i-\frac{1}{2}}}{\Delta \xi} \tag{D.2}$$

## 1. Elasticity Equation

In order to discretize the elasticity equation, we follow the approach taken by Zhang et al. (2002); Bunger (2005). The elasticity equation is given in Equation V.34. We can break the integral over each elements as

$$\overline{\Pi}_i = -\int_0^1 G(\xi_i, \zeta)\overline{\Omega} d\zeta = -\sum_{j=1}^{n} \int_{\xi_j-\Delta\xi/2}^{\xi_j+\Delta\xi/2} G(\xi_i, \zeta)\overline{\Omega} d\zeta \tag{D.3}$$

Since for each element the value of the opening and pressure are uniform, so

$$\overline{\Pi}_i = -\sum_{j=1}^{n} \overline{\Omega}_j \int_{\xi_j-\Delta\xi/2}^{\xi_j+\Delta\xi/2} G(\xi_i, \zeta) d\zeta \tag{D.4}$$

where the kernel is given by Zhang et al. (2002)

$$G(\rho, \xi) = \frac{\partial}{\partial \xi} g(\rho, \xi) \tag{D.5}$$

where

$$g(\xi,\eta) = -\frac{1}{4\eta}\overline{J}_{101}(\frac{\xi}{\eta},0) \tag{D.6}$$

and $\overline{J}_{mnp}(x,y)$ is the Lifshitz-Hankel (also known as Lipshitz-Hankel) integral Eason et al. (1955). Using the complete elliptical integrals to express Lifshitz-Hankel integral, one can find that Eason et al. (1955)

$$\overline{J}_{101}(\xi,\eta) = \frac{k^3(1-\xi^2-\eta^2)}{8\pi k'^2\xi^{3/2}}\boldsymbol{E}(k) + \frac{k}{2\pi\rho^{1/2}}\boldsymbol{K}(k) \tag{D.7}$$

where $\boldsymbol{E}(k)$ and **K**(k) are the complete elliptical integrals Abramowitz and Stegun (1972)

$$\begin{aligned}
\boldsymbol{E}(k) &= \int_0^{\pi/2}\sqrt{1-k^2\sin^2\zeta}d\zeta \\
\boldsymbol{K}(k) &= \int_0^{\pi/2}\frac{1}{\sqrt{1-k^2\sin^2\zeta}}d\zeta
\end{aligned} \tag{D.8}$$

Here, $k$ and $k'$ are

$$\begin{aligned}
k(\xi,\eta) &= \sqrt{\frac{4\xi}{(1+\xi)^2+\eta^2}} \\
k'(\xi,\eta) &= \sqrt{\frac{(1-\xi)^2+\eta^2}{(1+\xi)^2+\eta^2}}
\end{aligned} \tag{D.9}$$

If we consider $M_{ij} = g(\xi_i,\xi_j+\Delta\xi/2) - g(\xi_i,\xi_j-\Delta\xi/2)$, we can simplify Equation D.4 to

$$\overline{\Pi}_i = -\sum_{j=1}^{n} M_{ij}\overline{\Omega}_j \tag{D.10}$$

or in tensor notation as

$$\overline{\boldsymbol{\Pi}} = -\boldsymbol{M}\overline{\boldsymbol{\Omega}} \tag{D.11}$$

Therefore, the influence matrix ($\boldsymbol{M}_{n\times n}$) relates the opening of the crack to the fluid pressure and being used in the elasticity equations (see Equation V.42),

## 2. Global Continuity

The global continuity equation is given from Equation V.33 by expanding over the elements and considering that the opening is uniform over each elements. In this way we can show

$$\tau = \gamma^{\tau 5/2} \sum_{j=1}^{n} \overline{\Omega}_j \int_{\xi_j - \Delta\xi/2}^{\xi_j + \Delta\xi/2} \zeta d\zeta \tag{D.12}$$

then combining Equation D.12 with Equation D.1,

$$\tau = \gamma^{\tau 5/2} \left(\Delta\xi\right)^2 \sum_{j=1}^{n} \overline{\Omega}_j \left(j - \frac{1}{2}\right) \tag{D.13}$$

## 3. Continuity Equation

The continuity equation is given from Equation V.32 by taking the derivative over time for $\gamma$ and $\overline{\Omega}_i^\tau$ using Equation D.1, leading to

$$\dot{\gamma} = \frac{\gamma^\tau - \gamma^{\tau-\Delta\tau}}{\Delta\tau} = \frac{\Delta\gamma}{\Delta\tau} \quad , \quad \dot{\overline{\Omega}}_i^\tau = \frac{\overline{\Omega}_i^\tau - \overline{\Omega}_i^{\tau-\Delta\tau}}{\Delta\tau} = \frac{\Delta\overline{\Omega}_i^\tau}{\Delta\tau} \tag{D.14}$$

Also in order to obtain the derivative at the center of the element, we have

$$\begin{aligned}
\left.\frac{\partial\overline{\Omega}}{\partial\xi}\right|_{1<i<n} &= \frac{\overline{\Omega}_{i+\frac{1}{2}}^\tau - \overline{\Omega}_{i-\frac{1}{2}}^\tau}{\Delta\xi} = \frac{\overline{\Omega}_{i+1}^{\tau-\Delta\tau} + \Delta\overline{\Omega}_{i+1}^\tau - \overline{\Omega}_{i-1}^{\tau-\Delta\tau} - \Delta\overline{\Omega}_{i-1}^\tau}{2\Delta\xi} \\
\left.\frac{\partial\overline{\Omega}}{\partial\xi}\right|_{i=1} &= \frac{\overline{\Omega}_{\frac{3}{2}}^\tau - \overline{\Omega}_{\frac{1}{2}}^\tau}{\Delta\xi} = \frac{\overline{\Omega}_2^{\tau-\Delta\tau} + \Delta\overline{\Omega}_2^\tau - \overline{\Omega}_1^{\tau-\Delta\tau} - \Delta\overline{\Omega}_1^\tau}{\Delta\xi} \\
\left.\frac{\partial\overline{\Omega}}{\partial\xi}\right|_{i=n} &= \frac{\overline{\Omega}_{n+\frac{1}{2}}^\tau - \overline{\Omega}_{n-\frac{1}{2}}^\tau}{\Delta\xi} = \frac{-\overline{\Omega}_n^{\tau-\Delta\tau} - \Delta\overline{\Omega}_n^\tau - \overline{\Omega}_{n-1}^{\tau-\Delta\tau} - \Delta\overline{\Omega}_{n-1}^\tau}{2\Delta\xi}
\end{aligned} \tag{D.15}$$

In Equation D.15, index $i \pm 1/2$ refers to the value at the node. Combining Equations D.14 and D.15 with D.1 and the discretized form of Equation V.32 over element $i$ yields

$$1 < i < n :$$

$$\begin{aligned}\left(1+\frac{2\gamma^{\tau}}{\Delta\gamma}\right)\Delta\overline{\Omega}_{i}^{\tau} - \left(i-\frac{1}{2}\right)\Delta\overline{\Omega}_{i+1}^{\tau} + \left(i-\frac{1}{2}\right)\Delta\overline{\Omega}_{i-1}^{\tau} = \\ \left(i-\frac{1}{2}\right)\overline{\Omega}_{i+1}^{\tau-\Delta\tau} - \overline{\Omega}_{i}^{\tau-\Delta\tau} - \left(i-\frac{1}{2}\right)\overline{\Omega}_{i-1}^{\tau-\Delta\tau} \\ - \frac{2\Delta\tau}{\Delta\gamma\sqrt{\gamma^{\tau}}(i-\frac{1}{2})(\Delta\xi)^{2}}\left(\frac{Q_0T}{\varepsilon L^2}\tilde{\Psi}_{i+\frac{1}{2}}^{\tau} - \frac{Q_0T}{\varepsilon L^2}\tilde{\Psi}_{i-\frac{1}{2}}^{\tau}\right)\end{aligned} \tag{D.16a}$$

$$i = 1 :$$

$$\begin{aligned}\left(1+\frac{\gamma^{\tau}}{\Delta\gamma}\right)\Delta\overline{\Omega}_{1}^{\tau} - \frac{1}{2}\Delta\overline{\Omega}_{2}^{\tau} = \frac{1}{2}\overline{\Omega}_{2}^{\tau-\Delta\tau} - \overline{\Omega}_{1}^{\tau-\Delta\tau} \\ - \frac{2\Delta\tau}{\Delta\gamma\sqrt{\gamma^{\tau}}(\Delta\xi)^{2}}\left(\frac{Q_0T}{\varepsilon L^2}\tilde{\Psi}_{\frac{3}{2}}^{\tau} - \frac{Q_0T}{\varepsilon L^2}\tilde{\Psi}_{\frac{1}{2}}^{\tau}\right)\end{aligned} \tag{D.16b}$$

$$i = n :$$

$$\begin{aligned}\left(\frac{2\gamma^{\tau}}{\Delta\gamma}+n+\frac{1}{2}\right)\Delta\overline{\Omega}_{n}^{\tau} + \left(n-\frac{1}{2}\right)\Delta\overline{\Omega}_{n-1}^{\tau} = -\left(n+\frac{1}{2}\right)\overline{\Omega}_{n}^{\tau-\Delta\tau} \\ - \left(n-\frac{1}{2}\right)\overline{\Omega}_{n-1}^{\tau-\Delta\tau} + \frac{2\Delta\tau}{\Delta\gamma}\frac{\frac{Q_0T}{\varepsilon L^2}\tilde{\Psi}_{n-\frac{1}{2}}^{\tau}}{\sqrt{\gamma^{\tau}}(n-\frac{1}{2})(\Delta\xi)^{2}}\end{aligned} \tag{D.16c}$$

where $\overline{\Omega}_{i}^{\tau} = \Delta\overline{\Omega}_{i}^{\tau} + \overline{\Omega}_{i}^{\tau-\Delta\tau}$ and $\overline{\Pi}_{i}^{\tau} = \overline{\Pi}_{i}^{\tau-\Delta\tau} + \Delta\overline{\Pi}_{i}^{\tau}$

### 4. Initial and Boundary Conditions

One of the crucial steps in any numerical modeling is the correct definition of initial and boundary conditions. From this case, we go back to Equation V.35 to define these conditions in discretized form as

$$\begin{aligned}\frac{Q_0T}{\varepsilon L^2}\tilde{\Psi}_{\frac{1}{2}}^{\tau} = \frac{1}{\gamma^{\tau}} \\ \frac{Q_0T}{\varepsilon L^2}\tilde{\Psi}_{n+\frac{1}{2}}^{\tau} = 0\end{aligned} \tag{D.17}$$

These conditions are incorporated via Equation D.16a.

## 5. Fluid Flow

Based on Equations V.13 and V.2, the fluid flux is

$$q = -\operatorname{sgn}\left(\frac{\partial p}{\partial r}\right)\left|\frac{V}{u^*}\right|\left|\frac{w^3}{2\rho}\frac{\partial p}{\partial r}\right|^{\frac{1}{2}}$$

Therefore, following Figure V.3, we obtain that

- $F_1$ (Laminar): $Re^+ \leq \frac{\vartheta w}{2\delta} Re_{*c}$ and $Re^+ < Re_c^+$

$$q = -\operatorname{sgn}\left(\frac{\partial p}{\partial r}\right)\left|\frac{w^3}{\mu'}\frac{\partial p}{\partial r}\right| \tag{D.18a}$$

  This is also known as Poiseuille equation.

- $F_2$ (Smooth-walled): $Re_c^+ \leq Re^+ \leq \frac{\vartheta w}{2\delta} Re_{*l}$

$$\begin{aligned} q = -\operatorname{sgn}\left(\frac{\partial p}{\partial r}\right)&\left|\left(\frac{Re_c^{+2}}{9\vartheta^2\left|\frac{2\rho w^3}{\mu'^2}\frac{\partial p}{\partial r}\right|^{\frac{1}{2}}}\right) e^{\frac{Re_c^{+2}}{9\vartheta^2\left|\frac{2\rho w^3}{\mu'^2}\frac{\partial p}{\partial r}\right|^{\frac{1}{2}}}-1}\right. \\ &+\left(1-\left(\frac{Re_c^{+2}}{9\vartheta^2\left|\frac{2\rho w^3}{\mu'^2}\frac{\partial p}{\partial r}\right|^{\frac{1}{2}}}\right) e^{\frac{Re_c^{+2}}{9\vartheta^2\left|\frac{2\rho w^3}{\mu'^2}\frac{\partial p}{\partial r}\right|^{\frac{1}{2}}}-1}\right)\times \\ &\left.\left[2.5\ln\left|\frac{18\vartheta^2\rho w^3}{\mu'^2}\frac{\partial p}{\partial r}\right|^{\frac{1}{2}}-\frac{66.69}{(Re^+)^{0.72}}+1.8\right]\right|\left|\frac{w^3}{2\rho}\frac{\partial p}{\partial r}\right|^{\frac{1}{2}} \end{aligned} \tag{D.18b}$$

- $F_3$ (Transition-Turbulent): $\frac{\vartheta w}{2\delta} Re_{*l} < Re^+ \leq \frac{\vartheta w}{2\delta} Re_{*c}$ and $Re_c^+ \leq Re^+$

$$\begin{aligned} q = -\operatorname{sgn}\left(\frac{\partial p}{\partial r}\right)&\left|\left(\frac{Re_c^{+2}}{9\vartheta^2\left|\frac{2\rho w^3}{\mu'^2}\frac{\partial p}{\partial r}\right|^{\frac{1}{2}}}\right) e^{\frac{Re_c^{+2}}{9\vartheta^2\left|\frac{2\rho w^3}{\mu'^2}\frac{\partial p}{\partial r}\right|^{\frac{1}{2}}}-1}\right. \\ &+\left(1-\left(\frac{Re_c^{+2}}{9\vartheta^2\left|\frac{2\rho w^3}{\mu'^2}\frac{\partial p}{\partial r}\right|^{\frac{1}{2}}}\right) e^{\frac{Re_c^{+2}}{9\vartheta^2\left|\frac{2\rho w^3}{\mu'^2}\frac{\partial p}{\partial r}\right|^{\frac{1}{2}}}-1}\right)\left[2.5\ln\left|\frac{18\vartheta^2\rho w^3}{\mu'^2}\frac{\partial p}{\partial r}\right|^{\frac{1}{2}}\right. \\ &\left.\left.-\frac{66.69}{(Re^+)^{0.72}}+1.8-\mathcal{C}_1\left(\frac{2\delta}{w}\left|\frac{18\vartheta^2\rho w^3}{\mu'^2}\frac{\partial p}{\partial r}\right|^{\frac{1}{2}}\right)\right]\right|\left|\frac{w^3}{2\rho}\frac{\partial p}{\partial r}\right|^{\frac{1}{2}} \end{aligned} \tag{D.18c}$$

- $F_4$ (Laminar): $Re_T^+ = \frac{\vartheta w}{2\delta} Re_{*c} < Re_c^+$ and $\frac{\vartheta w}{2\delta} Re_{*c} < Re^+$

$$q = -\operatorname{sgn}\left(\frac{\partial p}{\partial r}\right) \left| \frac{Re_{*c} w}{3 \times 2^{\frac{3}{2}\delta\rho^{\frac{1}{2}}}} \right| \left| w^3 \frac{\partial p}{\partial r} \right|^{\frac{1}{2}} \tag{D.18d}$$

- $F_5$ (Rough-walled fully turbulent): $Re_T^+ = \frac{\vartheta w}{2\delta} Re_{*c} \geq Re_c^+$ and $\frac{\vartheta w}{2\delta} Re_{*c} < Re^+$

$$\begin{aligned} q = -\operatorname{sgn}\left(\frac{\partial p}{\partial r}\right) \Bigg| &\left(\frac{2\delta Re_c^{+2}}{3\vartheta^2 w Re_{*c}}\right) e^{\left(\frac{Re_c^+}{\frac{\vartheta w}{2\delta} Re_{*c}}\right)^2 - 1} \\ &+ \left(1 - \left(\frac{Re_c^+}{\frac{\vartheta w}{2\delta} Re_{*c}}\right)^2 e^{\left(\frac{Re_c^+}{\frac{\vartheta w}{2\delta} Re_{*c}}\right)^2 - 1}\right) \Bigg[2.5 \ln \frac{\vartheta w}{2\delta} Re_{*c} \\ &- \frac{66.69}{\left(\frac{\vartheta w}{2\delta} Re_{*c}\right)^{0.72}} + 1.8 - \mathcal{C}_1(Re_{*c})\Bigg]\Bigg| \left| \frac{w^3}{2\rho} \frac{\partial p}{\partial r} \right|^{\frac{1}{2}} \end{aligned} \tag{D.18e}$$

Now if we use the scaling parameters from Equations V.24 and V.30, we find the scaled form of the fluid flow. But before going forward, we can re-define the scaled form of the conditions determining regimes of fluid flow as:

$$\begin{aligned} \mathcal{E}_1 &= \frac{Re^+}{\vartheta} = 3\left|\overline{\Omega}^3 \frac{\partial \overline{\Pi}}{\partial \xi}\right|^{\frac{1}{2}} \\ \mathcal{E}_2 &= \frac{w}{2\delta} Re_{*c} = \mathcal{R}_t Re_{*c} \sqrt{\gamma} \overline{\Omega} \\ \mathcal{E}_3 &= \frac{Re_c^+}{\vartheta} \\ \mathcal{E}_4 &= \frac{w}{2\delta} Re_{*l} = \mathcal{R}_t Re_{*l} \sqrt{\gamma} \overline{\Omega} \end{aligned} \tag{D.19}$$

Thus if we want to continue the scaling for the rest of the fluid flow equations, we can obtain

- $F_1$ (Laminar): $\mathcal{E}_1 \leq \mathcal{E}_2$ and $\mathcal{E}_1 < \mathcal{E}_3$

$$\frac{TQ_0}{\varepsilon L^2} \tilde{\Psi} = -\operatorname{sgn}\left(\frac{\partial \overline{\Pi}}{\partial \xi}\right) \xi \left|\overline{\Omega}^3 \frac{\partial \overline{\Pi}}{\partial \xi}\right|$$

- $F_2$ (Smooth-walled): $\mathcal{E}_3 \leq \mathcal{E}_1 \leq \mathcal{E}_4$

$$\frac{TQ_0}{\varepsilon L^2}\tilde{\Psi} = -\operatorname{sgn}\left(\frac{\partial\overline{\Pi}}{\partial\xi}\right)\xi\left|\left(\frac{Re_c^{+2}}{9\vartheta^2\left|\overline{\Omega}^3\frac{\partial\overline{\Pi}}{\partial\xi}\right|^{\frac{1}{2}}}\right)e^{\left(\frac{Re_c^{+2}}{9\vartheta^2\left|\overline{\Omega}^3\frac{\partial\overline{\Pi}}{\partial\xi}\right|^{\frac{1}{2}}}\right)-1}\right.$$
$$+\left(1-\left(\frac{Re_c^{+2}}{9\vartheta^2\left|\overline{\Omega}^3\frac{\partial\overline{\Pi}}{\partial\xi}\right|^{\frac{1}{2}}}\right)e^{\left(\frac{Re_c^{+2}}{9\vartheta^2\left|\overline{\Omega}^3\frac{\partial\overline{\Pi}}{\partial\xi}\right|^{\frac{1}{2}}}\right)-1}\right)\left[2.5\ln\left|9\vartheta^2\overline{\Omega}^3\frac{\partial\overline{\Pi}}{\partial\xi}\right|^{\frac{1}{2}}\right.$$
$$\left.\left.-\frac{66.69}{\left|9\vartheta^2\overline{\Omega}^3\frac{\partial\overline{\Pi}}{\partial\xi}\right|^{0.36}}+1.8\right]\right|\left|\overline{\Omega}^3\frac{\partial\overline{\Pi}}{\partial\xi}\right|^{\frac{1}{2}}$$

- $F_3$ (Transition-Turbulent): $\mathcal{E}_4 < \mathcal{E}_1 \leq \mathcal{E}_2$ and $\mathcal{E}_3 \leq \mathcal{E}_1$

$$\frac{TQ_0}{\varepsilon L^2}\tilde{\Psi} = -\operatorname{sgn}\left(\frac{\partial\overline{\Pi}}{\partial\xi}\right)\xi\left|\left(\frac{Re_c^{+2}}{9\vartheta^2\left|\overline{\Omega}^3\frac{\partial\overline{\Pi}}{\partial\xi}\right|^{\frac{1}{2}}}\right)e^{\left(\frac{Re_c^{+2}}{9\vartheta^2\left|\overline{\Omega}^3\frac{\partial\overline{\Pi}}{\partial\xi}\right|^{\frac{1}{2}}}\right)-1}\right.$$
$$+\left(1-\left(\frac{Re_c^{+2}}{9\vartheta^2\left|\overline{\Omega}^3\frac{\partial\overline{\Pi}}{\partial\xi}\right|^{\frac{1}{2}}}\right)e^{\left(\frac{Re_c^{+2}}{9\vartheta^2\left|\overline{\Omega}^3\frac{\partial\overline{\Pi}}{\partial\xi}\right|^{\frac{1}{2}}}\right)-1}\right)\left[2.5\ln\left|9\vartheta^2\overline{\Omega}^3\frac{\partial\overline{\Pi}}{\partial\xi}\right|^{\frac{1}{2}}\right.$$
$$\left.\left.-\frac{66.69}{\left|9\vartheta^2\overline{\Omega}^3\frac{\partial\overline{\Pi}}{\partial\xi}\right|^{0.36}}+1.8-\mathcal{C}_1\left(\frac{3}{\sqrt{\gamma}\mathcal{R}_t}\left|\overline{\Omega}\frac{\partial\overline{\Pi}}{\partial\xi}\right|^{\frac{1}{2}}\right)\right]\right|\left|\overline{\Omega}^3\frac{\partial\overline{\Pi}}{\partial\xi}\right|^{\frac{1}{2}}$$

- $F_4$: (Laminar) $\mathcal{E}_2 < \mathcal{E}_3$ and $\mathcal{E}_2 < \mathcal{E}_1$

$$\frac{TQ_0}{\varepsilon L^2}\tilde{\Psi} = -sign\left(\frac{\partial\overline{\Pi}}{\partial\xi}\right)\frac{\mathcal{R}_t Re_{*c}\sqrt{\gamma}}{3}\xi\left|\overline{\Omega}^5\frac{\partial\overline{\Pi}}{\partial\xi}\right|^{\frac{1}{2}}$$

- $F_5$: (Rough-walled Fully turbulent) $\mathcal{E}_2 \geq \mathcal{E}_3$ and $\mathcal{E}_2 < \mathcal{E}_1$

$$\frac{TQ_0}{\varepsilon L^2}\tilde{\Psi} = -\operatorname{sgn}\left(\frac{\partial\overline{\Pi}}{\partial\xi}\right)\xi\left|\overline{\Omega}^3\frac{\partial\overline{\Pi}}{\partial\xi}\right|^{\frac{1}{2}}\left|\left(\frac{Re_c^{+2}}{3\vartheta^2\mathcal{R}_t\sqrt{\gamma}\overline{\Omega}Re_{*c}}\right)e^{\left(\frac{Re_c^{+}}{\vartheta\mathcal{R}_t\sqrt{\gamma}\overline{\Omega}Re_{*c}}\right)^2-1}\right.$$
$$+\left(1-\left(\frac{Re_c^{+}}{\vartheta\mathcal{R}_t\sqrt{\gamma}\overline{\Omega}Re_{*c}}\right)^2e^{\left(\frac{Re_c^{+}}{\vartheta\mathcal{R}_t\sqrt{\gamma}\overline{\Omega}Re_{*c}}\right)^2-1}\right)\left[2.5\ln\left(\vartheta\mathcal{R}_t\sqrt{\gamma}\overline{\Omega}Re_{*c}\right)\right.$$
$$\left.\left.-\frac{66.69}{\left(\vartheta\mathcal{R}_t\sqrt{\gamma}\overline{\Omega}Re_{*c}\right)^{0.72}}+1.8-\mathcal{C}_1(Re_{*c})\right]\right|$$

After scaling we discretize the equations that represent the fluid flow. We emphasize that the flow is written on the nodes rather than middle points of the elements. So, we need to make sure that, using Equation D.1 for the coordinate,

$$\begin{aligned}
\overline{\Omega}_{i+\frac{1}{2}} &= \frac{\overline{\Omega}_{i+1}+\overline{\Omega}_i}{2} \\
\xi_{i+\frac{1}{2}} &= \xi_i + \frac{\Delta\xi}{2} = i\Delta\xi \\
\left(\frac{\partial\overline{\Pi}}{\partial\xi}\right)_{i+\frac{1}{2}} &= \frac{\overline{\Pi}_{i+1}-\overline{\Pi}_i}{\Delta\xi} = \frac{1}{\Delta\xi}\sum_{j=1}^{n}\left(M_{ij}-M_{(i+1)j}\right)\overline{\Omega}_j
\end{aligned}$$

Before moving forward we can define:

$$I_{1,i} = \left|\overline{\Omega}^3\frac{\partial\overline{\Pi}}{\partial\xi}\right| = \overline{\Omega}^3\left|\frac{\partial\overline{\Pi}}{\partial\xi}\right| \Rightarrow -\operatorname{sgn}\left(\frac{\partial\overline{\Pi}}{\partial\xi}\right)I_{1,i} = \overline{\Omega}^3\frac{\partial\overline{\Pi}}{\partial\xi}$$

So after discretizing

$$\begin{aligned}
-\operatorname{sgn}\left(\frac{\partial\overline{\Pi}}{\partial\xi}\right)I_{1,i} =& \frac{1}{\Delta\xi}\left(\frac{\overline{\Omega}_{i+1}^{\tau-\Delta\tau}+\Delta\overline{\Omega}_{i+1}^{\tau}+\overline{\Omega}_{i}^{\tau-\Delta\tau}+\Delta\overline{\Omega}_{i}^{\tau}}{2}\right)^3\times \\
&\sum_{j=1}^{n}\left(M_{(i+1)j}-M_{ij}\right)(\overline{\Omega}_{j}^{\tau-\Delta\tau}+\Delta\overline{\Omega}_{j}^{\tau})
\end{aligned} \tag{D.20a}$$

$$I_{2,i} = \sqrt{\gamma}\overline{\Omega} = \sqrt{\gamma}\left(\frac{\overline{\Omega}_{i+1}^{\tau-\Delta\tau}+\Delta\overline{\Omega}_{i+1}^{\tau}+\overline{\Omega}_{i}^{\tau-\Delta\tau}+\Delta\overline{\Omega}_{i}^{\tau}}{2}\right) \tag{D.20b}$$

Also,

$$\begin{aligned}
\sqrt{I_{1,i}} = \left|\overline{\Omega}^3\frac{\partial\overline{\Pi}}{\partial\xi}\right|^{\frac{1}{2}} = & \frac{1}{\sqrt{\Delta\xi}}\left(\frac{\overline{\Omega}_{i+1}^{\tau-\Delta\tau}+\Delta\overline{\Omega}_{i+1}^{\tau}+\overline{\Omega}_{i}^{\tau-\Delta\tau}+\Delta\overline{\Omega}_{i}^{\tau}}{2}\right)^{3/2}\times \\
&\left|\sum_{j=1}^{n}\left(M_{(i+1)j}-M_{ij}\right)(\overline{\Omega}_{j}^{\tau-\Delta\tau}+\Delta\overline{\Omega}_{j}^{\tau})\right|^{\frac{1}{2}}
\end{aligned}$$

and therefore

$$\begin{aligned}
-\operatorname{sgn}\left(\frac{\partial\overline{\Pi}}{\partial\xi}\right)\sqrt{I_{1,i}} =& \frac{\frac{1}{\sqrt{\Delta\xi}}\left(\frac{\overline{\Omega}_{i+1}^{\tau-\Delta\tau}+\Delta\overline{\Omega}_{i+1}^{\tau}+\overline{\Omega}_{i}^{\tau-\Delta\tau}+\Delta\overline{\Omega}_{i}^{\tau}}{2}\right)^{3/2}}{\sqrt{\sum_{j=1}^{n}\left(M_{(i+1)j}-M_{ij}\right)(\overline{\Omega}_{j}^{\tau-\Delta\tau}+\Delta\overline{\Omega}_{j}^{\tau})}}\times \\
&\sum_{j=1}^{n}\left(M_{(i+1)j}-M_{ij}\right)(\overline{\Omega}_{j}^{\tau-\Delta\tau}+\Delta\overline{\Omega}_{j}^{\tau})
\end{aligned}$$

Now, in order to simplify the representation of the equations, we will use the following change of variables

$$
\begin{aligned}
\mathcal{W}_i^\tau &= \left(\frac{\overline{\Omega}_{i+1}^{\tau-\Delta\tau}\Delta\overline{\Omega}_{i+1}^{\tau} + \overline{\Omega}_i^{\tau-\Delta\tau} + \Delta\overline{\Omega}_i^{\tau}}{2}\right)^3 \\
\mathcal{J}_i^\tau &= \sqrt{\frac{\mathcal{W}_i^\tau}{\Delta\xi\sum_{j=1}^{n}\mathcal{H}_{i,j}\left(\overline{\Omega}_j^{\tau-\Delta\tau} + \Delta\overline{\Omega}_j^{\tau}\right)}}\ ,\ \mathcal{H}_{i,j} = M_{(i+1),j} - M_{i,j} \\
\mathcal{I}_{1,i}^\tau &= \left|\frac{\mathcal{W}_i^\tau}{\Delta\xi}\sum_{j=1}^{n}\mathcal{H}_{i,j}\left(\overline{\Omega}_i^{\tau-\Delta\tau} + \Delta\overline{\Omega}_i^{\tau}\right)\right|\ ,\ \mathcal{I}_{2,i}^\tau = (\gamma^\tau)^{1/2}|\mathcal{W}_i^\tau|^{1/3} \\
\mathcal{M}_i^\tau &= \left(\frac{Re_c^{+2}}{9\vartheta^2(\mathcal{I}_{1,i}^\tau)^{1/2}}\right)e^{\frac{Re_c^{+2}}{9\vartheta^2\mathcal{I}_{1,i}^\tau}-1} \\
\mathcal{N}_{1,i}^\tau &= \left(\frac{Re_c^{+2}}{3\vartheta^2\mathcal{R}_t\mathcal{I}_{2,i}^\tau Re_{*c}}\right)e^{\left(\frac{Re_c^{+}}{\vartheta\mathcal{R}_t\mathcal{I}_{2,i}^\tau Re_{*c}}\right)^2-1} \\
\mathcal{N}_{2,i}^\tau &= \left(\frac{Re_c^{+}}{\vartheta\mathcal{R}_t\mathcal{I}_{2,i}^\tau Re_{*c}}\right)^2 e^{\left(\frac{Re_c^{+}}{\vartheta\mathcal{R}_t\mathcal{I}_{2,i}^\tau Re_{*c}}\right)^2-1} \\
\mathcal{L}_{1,i}^\tau &= 2.5\ln\left(3\vartheta(\mathcal{I}_{1,i}^\tau)^{1/2}\right) - \frac{66.69}{\left(3\vartheta(\mathcal{I}_{1,i}^\tau)^{1/2}\right)^{0.72}} + 1.8 \\
\mathcal{L}_{2,i}^\tau &= 2.5\ln\left(\vartheta\mathcal{R}_t\mathcal{I}_{2,i}^\tau Re_{*c}\right) - \frac{66.69}{\left(\vartheta\mathcal{R}_t\mathcal{I}_{2,i}^\tau Re_{*c}\right)^{0.72}} + 1.8
\end{aligned}
\tag{D.21}
$$

so that

$$
-\operatorname{sgn}\left(\frac{\partial\overline{\Pi}}{\partial\xi}\right)\sqrt{I_{1,i}^\tau} = \mathcal{J}_i^\tau\sum_{j=1}^{n}\mathcal{H}_{i,j}\overline{\Omega}_j^{\tau-\Delta\tau} + \mathcal{J}_i^\tau\sum_{j=1}^{n}\mathcal{H}_{i,j}\Delta\overline{\Omega}_j^{\tau},
$$

$$
-\Delta\xi\operatorname{sgn}\left(\frac{\partial\overline{\Pi}}{\partial\xi}\right)I_{1,i}^\tau = \mathcal{W}_i^\tau\sum_{j=1}^{n}\mathcal{H}_{i,j}\overline{\Omega}_j^{\tau-\Delta\tau} + \mathcal{W}_i^\tau\sum_{j=1}^{n}\mathcal{H}_{i,j}\Delta\overline{\Omega}_j^{\tau},
$$

and

$$
I_{2,i}^\tau = \sqrt{\gamma}|\mathcal{W}_i^\tau|^{\frac{1}{3}}
$$

Introducing

$$
\mathcal{S} = \frac{2\Delta\tau}{\Delta\gamma\sqrt{\gamma}(\Delta\xi)^2}
$$

and also choosing

$$\begin{aligned}
\mathcal{T}_{1,i}^{\tau} &= \mathcal{S} i\Delta\xi \mathcal{J}_i^{\tau}\left|\mathcal{M}_i^{\tau} + \left(1 - \frac{\mathcal{M}_i^{\tau}}{(\mathcal{I}_{1,i}^{\tau})^{1/2}}\right)\mathcal{L}_{1,i}^{\tau}\right| \\
\mathcal{T}_{2,i}^{\tau} &= \mathcal{S} i\Delta\xi \mathcal{J}_i^{\tau}\left|\mathcal{N}_{1,i}^{\tau} + (1 - \mathcal{N}_{2,i}^{\tau})(\mathcal{L}_{2,i}^{\tau} - \mathcal{C}_1(Re_{*c}))\right| \\
\mathcal{T}_{3,i}^{\tau} &= \mathcal{S}\frac{i\Delta\xi Re_{*c}\mathcal{R}_t}{3}\mathcal{I}_{2,i}^{\tau}\mathcal{J}_i^{\tau} \qquad , \qquad \mathcal{T}_{4,i}^{\tau} = \mathcal{S} i \mathcal{W}_i^{\tau} \\
\mathcal{T}_{5,i}^{\tau} &= \mathcal{S} i\Delta\xi \mathcal{J}_i^{\tau}\left|\mathcal{M}_i^{\tau} + \left(1 - \frac{\mathcal{M}_i^{\tau}}{\sqrt{\mathcal{I}_{1,i}^{\tau}}}\right)\left[\mathcal{L}_{1,i}^{\tau} - \mathcal{C}_1\left(\frac{3}{\mathcal{R}_t}\frac{(\mathcal{I}_{1,i}^{\tau})^{1/2}}{\mathcal{I}_{2,i}^{\tau}}\right)\right]\right|
\end{aligned} \tag{D.22}$$

For the limits, by assigning that

$$\begin{aligned}
\mathcal{E}_{1,i+\frac{1}{2}}^{\tau} &= 3\sqrt{\mathcal{W}_i^{\tau}\mathcal{I}_{1,i}^{\tau}} \qquad , \qquad \mathcal{E}_{3,i+\frac{1}{2}}^{\tau} = \frac{Re_c^{+}}{\vartheta} \\
\mathcal{E}_{2,i+\frac{1}{2}}^{\tau} &= \mathcal{R}_t Re_{*c}\sqrt{\gamma^{\tau}}\left(\frac{\overline{\Omega}_{i+1}^{\tau-\Delta\tau}\Delta\overline{\Omega}_{i+1}^{\tau} + \overline{\Omega}_{i}^{\tau-\Delta\tau} + \Delta\overline{\Omega}_{i}^{\tau}}{2}\right) \\
\mathcal{E}_{4,i+\frac{1}{2}}^{\tau} &= \mathcal{R}_t Re_{*l}\sqrt{\gamma^{\tau}}\left(\frac{\overline{\Omega}_{i+1}^{\tau-\Delta\tau}\Delta\overline{\Omega}_{i+1}^{\tau} + \overline{\Omega}_{i}^{\tau-\Delta\tau} + \Delta\overline{\Omega}_{i}^{\tau}}{2}\right)
\end{aligned} \tag{D.23}$$

we can find:

- $F_1$: (Laminar) If $\mathcal{E}_{1,i+\frac{1}{2}}^{\tau} \leq \mathcal{E}_{2,i+\frac{1}{2}}^{\tau}$ and $\mathcal{E}_{1,i+\frac{1}{2}}^{\tau} < \mathcal{E}_{3,i+\frac{1}{2}}^{\tau}$

$$\mathcal{S}\frac{Q_0 T}{\varepsilon L^2}\tilde{\Psi}_{i+\frac{1}{2}}^{\tau} = \mathcal{T}_{4,i}^{\tau}\sum_{j=1}^{n}\mathcal{H}_{i,j}\overline{\Omega}_j^{\tau-\Delta\tau} + \mathcal{T}_{4,i}^{\tau}\sum_{j=1}^{n}\mathcal{H}_{i,j}\Delta\overline{\Omega}_j^{\tau} \tag{D.24a}$$

- $F_2$: (Smooth-Walled) If $\mathcal{E}_{3,i+\frac{1}{2}}^{\tau} \leq \mathcal{E}_{1,i+\frac{1}{2}}^{\tau} \leq \mathcal{E}_{4,i+\frac{1}{2}}^{\tau}$

$$\mathcal{S}\frac{Q_0 T}{\varepsilon L^2}\tilde{\Psi}_{i+\frac{1}{2}}^{\tau} = \mathcal{T}_{1,i}^{\tau}\sum_{j=1}^{n}\mathcal{H}_{i,j}\overline{\Omega}_j^{\tau-\Delta\tau} + \mathcal{T}_{1,i}^{\tau}\sum_{j=1}^{n}\mathcal{H}_{i,j}\Delta\overline{\Omega}_j^{\tau} \tag{D.24b}$$

- $F_3$: (Transition-Turbulent) If $\mathcal{E}_{4,i+\frac{1}{2}}^{\tau} < \mathcal{E}_{1,i+\frac{1}{2}}^{\tau} \leq \mathcal{E}_{2,i+\frac{1}{2}}^{\tau}$ and $\mathcal{E}_{3,i+\frac{1}{2}}^{\tau} \leq \mathcal{E}_{1,i+\frac{1}{2}}^{\tau}$

$$\mathcal{S}\frac{Q_0 T}{\varepsilon L^2}\tilde{\Psi}_{i+\frac{1}{2}}^{\tau} = \mathcal{T}_{5,i}^{\tau}\sum_{j=1}^{n}\mathcal{H}_{i,j}\overline{\Omega}_j^{\tau-\Delta\tau} + \mathcal{T}_{5,i}^{\tau}\sum_{j=1}^{n}\mathcal{H}_{i,j}\Delta\overline{\Omega}_j^{\tau} \tag{D.24c}$$

- $F_4$: (Laminar) If $\mathcal{E}_{2,i+\frac{1}{2}}^{\tau} < \mathcal{E}_{3,i+\frac{1}{2}}^{\tau}$ and $\mathcal{E}_{2,i+\frac{1}{2}}^{\tau} < \mathcal{E}_{1,i+\frac{1}{2}}^{\tau}$

$$\mathcal{S}\frac{Q_0 T}{\varepsilon L^2}\tilde{\Psi}_{i+\frac{1}{2}}^{\tau} = \mathcal{T}_{3,i}^{\tau}\sum_{j=1}^{n}\mathcal{H}_{i,j}\overline{\Omega}_j^{\tau-\Delta\tau} + \mathcal{T}_{3,i}^{\tau}\sum_{j=1}^{n}\mathcal{H}_{i,j}\Delta\overline{\Omega}_j^{\tau} \tag{D.24d}$$

- $F_5$: (Rough-walled fuly turbulent) If $\mathcal{E}_{3,i+\frac{1}{2}}^{\tau} \leq \mathcal{E}_{2,i+\frac{1}{2}}^{\tau}$ and $\mathcal{E}_{2,i+\frac{1}{2}}^{\tau} < \mathcal{E}_{1,i+\frac{1}{2}}^{\tau}$

$$\mathcal{S}\frac{Q_0 T}{\varepsilon L^2}\tilde{\Psi}_{i+\frac{1}{2}}^{\tau} = \mathcal{T}_{2,i}^{\tau}\sum_{j=1}^{n}\mathcal{H}_{i,j}\overline{\Omega}_j^{\tau-\Delta\tau} + \mathcal{T}_{2,i}^{\tau}\sum_{j=1}^{n}\mathcal{H}_{i,j}\Delta\overline{\Omega}_j^{\tau} \tag{D.24e}$$

which are the conditions given in Equation V.43.

## 6. Local Continuity

Now we can re-order the equation of local continuity as (combining Equations V.36-V.39 and fluid flow from Appendix D.A.5):

$$\begin{aligned}\left(1+\frac{\gamma^\tau}{\Delta\gamma}\right)\Delta\overline{\Omega}_1^\tau-\frac{1}{2}\Delta\overline{\Omega}_2^\tau+\mathcal{T}_{\lambda,1}^\tau\sum_{j=1}^{n}\mathcal{H}_{1,j}\Delta\overline{\Omega}_j^\tau&\\=\frac{1}{2}\overline{\Omega}_2^{\tau-\Delta\tau}-\overline{\Omega}_1^{\tau-\Delta\tau}+\frac{\mathcal{S}}{\gamma^\tau}-\mathcal{T}_{\lambda,1}^\tau\sum_{j=1}^{n}\mathcal{H}_{1,j}\overline{\Omega}_j^{\tau-\Delta\tau}&\end{aligned}\tag{D.25}$$

for $i=2,\cdots,n-1$:

$$\begin{aligned}\left(1+\frac{2\gamma^\tau}{\Delta\gamma}\right)\Delta\overline{\Omega}_i^\tau-\left(i-\frac{1}{2}\right)\Delta\overline{\Omega}_{i+1}^\tau+\left(i-\frac{1}{2}\right)\Delta\overline{\Omega}_{i-1}^\tau&\\-\frac{1}{i-\frac{1}{2}}\left[\mathcal{T}_{\lambda,i-1}^\tau\sum_{j=1}^{n}\mathcal{H}_{i-1,j}\Delta\overline{\Omega}_j^\tau-\mathcal{T}_{\lambda',i}^\tau\sum_{j=1}^{n}\mathcal{H}_{i,j}\Delta\overline{\Omega}_j^\tau\right]&\\=\left(i-\frac{1}{2}\right)\overline{\Omega}_{i+1}^{\tau-\Delta\tau}-\left(i-\frac{1}{2}\right)\overline{\Omega}_{i-1}^{\tau-\Delta\tau}-\overline{\Omega}_i^{\tau-\Delta\tau}&\\+\frac{1}{i-\frac{1}{2}}\left[\mathcal{T}_{\lambda,i-1}^\tau\sum_{j=1}^{n}\mathcal{H}_{i-1,j}\overline{\Omega}_j^{\tau-\Delta\tau}-\mathcal{T}_{\lambda',i}^\tau\sum_{j=1}^{n}\mathcal{H}_{i,j}\overline{\Omega}_j^{\tau-\Delta\tau}\right]&\end{aligned}\tag{D.26}$$

and for $i=n$:

$$\begin{aligned}\left(\frac{2\gamma^\tau}{\Delta\gamma}+n+\frac{1}{2}\right)\Delta\overline{\Omega}_n^\tau+\left(n-\frac{1}{2}\right)\Delta\overline{\Omega}_{n-1}^\tau-\frac{\mathcal{T}_{\lambda,n-1}^\tau}{n-\frac{1}{2}}\sum_{j=1}^{n}\mathcal{H}_{1,j}\Delta\overline{\Omega}_j^\tau&\\=-\left(n+\frac{1}{2}\right)\Delta\overline{\Omega}_n^{\tau-\Delta\tau}-\left(n-\frac{1}{2}\right)\Delta\overline{\Omega}_{n-1}^{\tau-\Delta\tau}&\\+\frac{\mathcal{T}_{\lambda,n-1}^\tau}{n-\frac{1}{2}}\sum_{j=1}^{n}\mathcal{H}_{1,j}\overline{\Omega}_j^{\tau-\Delta\tau}&\end{aligned}\tag{D.27}$$

where $\lambda$, and $\lambda'$ are the index of $\mathcal{T}$ that depends on the flow regime according to:

- If $\mathcal{E}_{1,i+\frac{1}{2}}^\tau\leq\mathcal{E}_{2,i+\frac{1}{2}}^\tau$ and $\mathcal{E}_{1,i+\frac{1}{2}}^\tau<\mathcal{E}_{3,i+\frac{1}{2}}^\tau$

$$\lambda=4\tag{D.28a}$$

- If $\mathcal{E}_{3,i+\frac{1}{2}}^\tau\leq\mathcal{E}_{1,i+\frac{1}{2}}^\tau\leq\mathcal{E}_{4,i+\frac{1}{2}}^\tau$

$$\lambda=1\tag{D.28b}$$

- If $\mathcal{E}^{\tau}_{4,i+\frac{1}{2}} < \mathcal{E}^{\tau}_{1,i+\frac{1}{2}} \leq \mathcal{E}^{\tau}_{2,i+\frac{1}{2}}$ and $\mathcal{E}^{\tau}_{3,i+\frac{1}{2}} \leq \mathcal{E}^{\tau}_{1,i+\frac{1}{2}}$
$$\lambda = 5 \tag{D.28c}$$
- If $\mathcal{E}^{\tau}_{2,i+\frac{1}{2}} < \mathcal{E}^{\tau}_{3,i+\frac{1}{2}}$ and $\mathcal{E}^{\tau}_{2,i+\frac{1}{2}} < \mathcal{E}^{\tau}_{1,i+\frac{1}{2}}$
$$\lambda = 3 \tag{D.28d}$$
- If $\mathcal{E}^{\tau}_{3,i+\frac{1}{2}} \leq \mathcal{E}^{\tau}_{2,i+\frac{1}{2}}$ and $\mathcal{E}^{\tau}_{2,i+\frac{1}{2}} < \mathcal{E}^{\tau}_{1,i+\frac{1}{2}}$
$$\lambda = 2 \tag{D.28e}$$

Hence, if we are dealing with the first element, $i = 1$, and we will find $\lambda$ for first node. If $i = n$, the value of $\lambda$ is according to node $n - 1/2$. And if $1 < i < n$, $\lambda$ is based on node $i - 1/2$ and $\lambda'$ is based on node $i + 1/2$.

Using this discretization, we can finally linearize the continuity equation and construct a matrix equation in the form of

$$\boldsymbol{\Xi}(\boldsymbol{\Delta\Omega^{\tau}}) \times \boldsymbol{\Delta\Omega^{\tau}} = \boldsymbol{\mathcal{H}}(\boldsymbol{\Omega^{\tau-\Delta\tau}})$$

which is the relationship presented in Equation V.45 in the main body of the paper.

## B. GMS APPROACH

According to the solution provided by Zolfaghari and Bunger (Submitted A), the solution for fully turbulent rough-wall HF for GMS condition, zero toughness hydraulic fracture in an impermeable rock is given by

$$\begin{aligned}
w &= \Bigg[\left(0.694 + 0.6148\frac{r}{R}\right)\left(1 - \frac{r}{R}\right)^{\frac{6}{7}} - 0.275\sqrt{1 - \left(\frac{r}{R}\right)^{2}} \\
&\quad -0.6798\left(\frac{r}{R}\right)^{0.31} + 0.8873\,{}_2F_1\left(\frac{1}{2}, -0.155; 0.845; \left(\frac{r}{R}\right)^{2}\right)\Bigg]\left(\frac{Q_0}{\beta'\sqrt{E'}}\right)^{\frac{6}{13}} \\
p &= \left[1.0452 - \frac{0.7683}{(1 - r/R)^{\frac{1}{7}}} + 0.0967\left(\frac{r}{R}\right)^{-0.69}\right]\left(\frac{E'^{17}Q_0^{5}}{\beta'^{18}}\right)^{\frac{1}{26}} t^{\frac{-1}{2}} \\
R &= 0.854\left(\beta' E'^{\frac{1}{2}} Q_0^{\frac{7}{6}}\right)^{\frac{3}{13}} t^{\frac{1}{2}} \\
q &= \beta' w^{\frac{5}{3}}\left(-\frac{\partial p}{\partial r}\right)^{\frac{1}{2}}
\end{aligned} \tag{D.29}$$

## C. LAMINAR SOLUTION

According to the solution given by Savitski and Detournay (2002), the asymptotic solution for a zero toughness, penny-shaped hydraulic fracture with zero leakoff is

$$
\begin{aligned}
w &= 0.6955 \left[ 1.9093 \left(1 - \frac{r}{R}\right)^{\frac{2}{3}} + 0.0705 \left(13 \left(\frac{r}{R}\right) - 6\right) \left(1 - \frac{r}{R}\right)^{\frac{2}{3}} \right. \\
&\qquad \left. +0.236 \left(1 - \left(\frac{r}{R}\right)^2\right)^{\frac{1}{2}} - \frac{r}{R} \arccos\left(\frac{r}{R}\right) \right] \left(\frac{Q_0^3 \mu'^2}{E'^2}\right)^{\frac{1}{9}} t^{\frac{1}{9}} \\
p &= \left(0.8593 - \frac{0.2387}{\left(1 - \frac{r}{R}\right)^{\frac{1}{3}}} - 0.09269 \ln\left(\frac{r}{R}\right)\right) \left(\mu' E'^2\right)^{\frac{1}{3}} t^{\frac{-1}{3}} \\
R &= 0.6955 \left(\frac{Q_0^3 E'}{\mu'}\right)^{\frac{1}{9}} t^{\frac{4}{9}} \\
q &= -\frac{w^3}{\mu'} \frac{\partial p}{\partial r}
\end{aligned}
\tag{D.30}
$$

# BIBLIOGRAPHY

Abramowitz, M. and Stegun, I. A. (1972). *Handbook of Mathematical Functions: with Formulas, Graphs, and Mathematical Tables*, volume 10. Dover, New York.

Adachi, J., Siebrits, E., Peirce, A., and Desroches, J. (2007). Computer simulation of hydraulic fractures. *International Journal of Rock Mechanics and Mining Sciences*, 44:739–757.

Adachi, J. I. (2001a). *Fluid-Driven Fracture in Permeable Rock*. PhD thesis, University of Minnesota.

Adachi, J. I. (2001b). *Fluid-driven fracture in permeable rock*. PhD thesis, University of Minnesota.

Adachi, J. I. and Detournay, E. (2002). Self-similar solution of a plane-strain fracture driven by a power-law fluid. *International Journal for Numerical and Analytical Methods in Geomechanics*, 26(6):579–604.

Adachi, J. I. and Peirce, A. P. (2008). Asymptotic analysis of an elasticity equation for a finger-like hydraulic fracture. *Journal of Elasticity*, 90(1):43–69.

Adams, J. and Rowe, C. (2013). Differentiating applications of hydraulic fracturing. In *Effective and Sustainable Hydraulic Fracturing*. InTech.

Ames, B. C. and Bunger, A. P. (2015). Role of turbulent flow in generating short hydraulic fractures with high net pressure in slickwater treatments. In *SPE Hydraulic Fracturing Technology Conference*, The Woodlands, Texas, USA. Society of Petroleum Engineers. SPE 173373.

Anthonyrajah, M., Mason, D. P., and Fareo, A. G. (2013). Propagation of a pre-existing turbulent fluid fracture. *International Journal of Non-Linear Mechanics*, 54:105–114.

Arfken, G. B. and Weber, H. J. (2005). *Mathematical methods for physicists international student edition*. Academic press.

Barenblatt, G. I. (1996). *Scaling, self-similarity, and intermediate asymptotics: dimensional analysis and intermediate asymptotics*, volume 14. New York, Cambridge University Press.

Blasius, V. H. (1913). *Das Ähnlichkeitsgesetz bei Reibungsvorgängen in Flüssigkeiten*, pages 1–41. Springer Berlin Heidelberg, Berlin, Heidelberg.

Bunger, A. P. (2005). *Near-surface hydraulic fracture*. PhD thesis, University of Minnesota.

Bunger, A. P. and Detournay, E. (2007). Early-time solution for a radial hydraulic fracture. *Journal of engineering mechanics*, 133(5):534–540.

Bunger, A. P. and Detournay, E. (2008). Experimental validation of the tip asymptotics for a fluid-driven crack. *Journal of the Mechanics and Physics of Solids*, 56(11):3101–3115.

Carbonell, R. S. (1996). *Self-similar solution of a fluid-driven fracture.* PhD thesis, University of Minnesota, Minneapolis.

Churchill, S. W. (1977). Friction-factor equation spans all fluid-flow regimes. *Chemical engineering*, 84(24):91–92.

Cornet, F. and Valette, B. (1984). In situ stress determination from hydraulic injection test data. *Journal of Geophysical Research: Solid Earth*, 89(B13):11527–11537.

Crouch, S. L., Starfield, A. M., and Rizzo, F. (1983). Boundary element methods in solid mechanics. *Journal of Applied Mechanics*, 50:704.

Darcy, H. (1857). *Recherches expérimentales relatives au mouvement de l'eau dans les tuyaux*, volume 1. Mallet-Bachelier.

De Pater, H. J. (2015). Hydraulic fracture containment: New insights into mapped geometry. In *SPE Hydraulic Fracturing Technology Conference*. Society of Petroleum Engineers.

Desroches, J., Detournay, E., Lenoach, B., Papanastasiou, P., Pearson, J., Thiercelin, M., and Cheng, A. (1994). The crack tip region in hydraulic fracturing. In *Proceedings of the Royal Society of London A: Mathematical, Physical and Engineering Sciences*, volume 447, pages 39–48. The Royal Society.

Detournay, E. (2004). Propagation regimes of fluid-driven fractures in impermeable rocks. *International Journal of Geomechanics*, 4(1):35–45.

Detournay, E. and Peirce, A. (2014). On the moving boundary conditions for a hydraulic fracture. *International Journal of Engineering Science*, 84:147–155.

Dontsov, E. and Peirce, A. (2016). Comparison of toughness propagation criteria for blade-like and pseudo-3d hydraulic fractures. *Engineering Fracture Mechanics*, 160:238–247.

Dontsov, E. V. (2016). Tip region of a hydraulic fracture driven by a laminar-to-turbulent fluid flow. *Journal of Fluid Mechanics*, 797:R2 (12 pages).

Dontsov, E. V. (2017). An approximate solution for a plane strain hydraulic fracture that accounts for fracture toughness, fluid viscosity, and leak-off. *International Journal of Fracture*, 205(2):221–237.

Eason, G., Noble, B., and Sneddon, I. (1955). On certain integrals of lipschitz-hankel type involving products of bessel functions. *Philosophical Transactions of the Royal Society of London A: Mathematical, Physical and Engineering Sciences*, 247(935):529–551.

Economides, M. J. and Nolte, K. G. (2000). *Reservoir stimulation*, volume 18. Wiley New York.

Emanuele, M., Minner, W., Weijers, L., Broussard, E., Blevens, D., Taylor, B., et al. (1998). A case history: completion and stimulation of horizontal wells with multiple transverse hydraulic fractures in the lost hills diatomite. In *SPE Rocky Mountain Regional/Low-Permeability Reservoirs Symposium*. Society of Petroleum Engineers.

Emerman, S. H., Turcotte, D., and Spence, D. (1986). Transport of magma and hydrothermal solutions by laminar and turbulent fluid fracture. *Physics of the earth and planetary interiors*, 41(4):249–259.

Emmons, H. W. (1951). The laminar-turbulent transition in a boundary layer-part I. *Journal of the Aeronautical Sciences*, 18(7):490–498.

Erdogan, F., Gupta, G. D., and Cook, T. (1973). Numerical solution of singular integral equations. In *Methods of analysis and solutions of crack problems*, pages 368–425. Dordrecht, Springer.

Fischer, T., Hainzl, S., Eisner, L., Shapiro, S., and Le Calvez, J. (2008). Microseismic signatures of hydraulic fracture growth in sediment formations: Observations and modeling. *Journal of Geophysical Research: Solid Earth*, 113(B2).

Fisher, M. K. and Warpinski, N. R. (2012). Hydraulic-fracture-height growth: Real data. *SPE Production & Operations*, 27(1):8–19.

Garagash, D. and Detournay, E. (2000). The tip region of a fluid-driven fracture in an elastic medium. *Journal of applied mechanics*, 67(1):183–192.

Garagash, D. I. (2006). Propagation of a plane-strain hydraulic fracture with a fluid lag: Early-time solution. *International journal of solids and structures*, 43(18):5811–5835.

Garagash, D. I., Detournay, E., and Adachi, J. I. (2011). Multiscale tip asymptotics in hydraulic fracture with leak-off. *Journal of Fluid Mechanics*, 669:260–297.

Gauckler, P. (1867). Etudes théoriques et pratiques sur l'ecoulement et le mouvement des eaux. *Comptes rendus de l'Acadéemie des Sciences, Gauthier-Villars 1867*; T. 64:818–822.

Geertsma, J. and De Klerk, F. (1969). A rapid method of predicting width and extent of hydraulically induced fractures. *Journal of Petroleum Technology*, 21(12):1–571.

Gérard, A., Genter, A., Kohl, T., Lutz, P., Rose, P., and Rummel, F. (2006). The deep egs (enhanced geothermal system) project at soultz-sous-forêts (alsace, france). *Geothermics*, 35(5):473–483.

Gioia, G. and Chakraborty, P. (2006). Turbulent friction in rough pipes and the energy spectrum of the phenomenological theory. *Physical review letters*, 96(4):044502.

Gradshteyn, I. S. and Ryzhik, I. M. (2014). *Table of Integrals, Series, and Products*. Academic press, eighth edition.

Hayashi, K. and Taniguchi, A. (1999). Response of a geothermal reservoir consisting of multiple cracks to hydraulic stimulation. *Geothermal science and technology*, 6(1-4):163–179.

Henderson, F. M. (1966). *Open channel flow*. Macmillan series in civil engineering. Macmillan.

Hills, D., Kelly, P., Dai, D., and Korsunsky, A. (1996). Solution of crack problems; the distributed dislocation technique. *Springer, Netherlands, 1996.*

Huang, N. C., Szewczyk, A. A., and Li, Y. C. (1990). Self-similar solution in problems of hydraulic fracturing. *Journal of Applied Mechanics*, 57(4):877–881.

Huppert, H. E. (1982). The propagation of two-dimensional and axisymmetric viscous gravity currents over a rigid horizontal surface. *Journal of Fluid Mechanics*, 121:43–58.

Irwin, G. R. (1957). Analysis of stress and strain near the end of a crack traversing a plate. *Journal of Applied Mechanics*, 24:361–364.

Jones, O. (1976). An improvement in the calculation of turbulent friction in rectangular ducts. *Journal of Fluids Engineering*, 98(2):173–180.

Kano, M., Zolfaghari, N., Ames, B. C., and Bunger, A. P. (2015). Solution for a pkn hydraulic fracture driven by turbulent fluid with large leakoff. *Hydraulic Fracturing Journal*, 2(1):34–38.

Khristianovic, S. and Zheltov, Y. (1955). Formation of vertical fractures by means of highly viscous fluids. In *Proc. 4th world petroleum congress, Rome*, volume 2, pages 579–586.

King, G. E. (2010). Thirty years of gas shale fracturing: what have we learned? In *SPE Annual Technical Conference and Exhibition, 19-22 September, Florence, Italy*. Society of Petroleum Engineers. SPE-133456-MS.

Korsunsky, A. M. (1994). *The solution of axisymmetric crack problems in inhomogenous media.* PhD thesis, University of Oxford.

Kovalyshen, Y. and Detournay, E. (2010). A reexamination of the classical pkn model of hydraulic fracture. *Transport in porous media*, 81(2):317–339.

Lecampion, B., Desroches, J., Jeffrey, R. G., Bunger, A., Burghardt, J., and Stanchits, S. (2017). Laboratory experiments versus theory for the initiation of radial hydraulic fracture transverse to a wellbore. In *EGU General Assembly, EGU2017, proceedings from the conference held 23-28 April, 2017 in Vienna, Austria., 2017*, volume 19, page 6577.

Lecampion, B. and Detournay, E. (2007). An implicit algorithm for the propagation of a hydraulic fracture with a fluid lag. *Computer Methods in Applied Mechanics and Engineering*, 196(49):4863–4880.

Lecampion, B., Peirce, A., Detournay, E., Zhang, X., Chen, Z., Bunger, A., Detournay, C., Napier, J., Abbas, S., Garagash, D., et al. (2013). The impact of the near-tip logic on the accuracy and convergence rate of hydraulic fracture simulators compared to reference solutions. In *Effective and sustainable hydraulic fracturing*. InTech.

Li, Y., Wei, C., Qi, G., Li, M., and Luo, K. (2013). Numerical simulation of hydraulically induced fracture network propagation in shale formation. In *IPTC 2013: International Petroleum Technology Conference*, Beijing, China. International Petroleum Technology Conference. IPTC-16981-MS.

Li, Y., Wei, C., Qin, G., Lu, Y., and Luo, K. (2012). Optimizing hydraulic fracturing design for shale gas production through numerical simulations. In *SPE International Production and Operations Conference & Exhibition*, Doha, Qatar. Society of Petroleum Engineers. SPE-157411-MS.

Lister, J. R. (1990). Buoyancy-driven fluid fracture: similarity solutions for the horizontal and vertical propagation of fluid-filled cracks. *Journal of Fluid Mechanics*, 217:213–239.

Lister, J. R. and Kerr, R. C. (1991). Fluid-mechanical models of crack propagation and their application to magma transport in dykes. *Journal of Geophysical Research: Solid Earth*, 96(B6):10049–10077.

Manning, R. (1891). On the flow of water in open channels and pipes. *Transactions of the Institution of Civil Engineers of Ireland*, 20:161–207.

Martin, A. N. and Economides, M. (2010). Best practices for candidate selection, design and evaluation of hydraulic fracture treatments. In *SPE Production and Operations Conference and Exhibition*, Tunis, Tunisia. Society of Petroleum Engineers. SPE-135669-MS.

Matsunaga, I. and Yamaguchi, T. (1992). A three-month circulation test at the hot dry test site in hijiori, japan. *Geothermal Resources Council BULLETIN*, 21(5):162–166.

Maxwell, S. C., Urbancic, T., Steinsberger, N., Zinno, R., et al. (2002). Microseismic imaging of hydraulic fracture complexity in the barnett shale. In *SPE annual technical conference and exhibition*. Society of Petroleum Engineers.

Mayerhofer, M. J., Walker Jr, R. N., Urbancic, T., Rutledge, J. T., et al. (2000). East texas hydraulic fracture imaging project: Measuring hydraulic fracture growth of conventional sandfracs and waterfracs. In *SPE Annual Technical Conference and Exhibition, 1-4 October, Dallas, Texa*. Society of Petroleum Engineers. SPE-63034-MS.

Meyer, B. R. (1989). Three-dimensional hydraulic fracturing simulation on personal computers: theory and comparison studies. In *SPE Eastern Regional Meeting*. Society of Petroleum Engineers. doi:10.2118/19329-MS, 213–230.

Montgomery, C. T. and Smith, M. B. (2010). Hydraulic fracturing: history of an enduring technology. *Journal of Petroleum Technology*, 62(12):26–40.

Moody, L. F. (1944). Friction factors for pipe flow. *Trans. ASME*, 66(8):671–684.

Munson, B. R., Young, B. F., and Okiishi, T. H. (2002). *Fundamentals of Fluid Mechanics*. John Wiley and Sons, United States of America, 4 edition.

Murdoch, L. C. and Slack, W. W. (2002). Forms of hydraulic fractures in shallow fine-grained formations. *Journal of Geotechnical and Geoenvironmental Engineering*, 128(6):479–487.

Muskhelishvili, N. I. (1953). *Singular Integral Equations: Boundary Problems of Functions Theory and Their Application to Mathematical Physics*. P. Noordhoff.

Newman, D. (2016). *Turbulent hydraulic fracturing described by Prandtl's mixing length*. PhD thesis.

Nikuradse, J. (1954). *Laws of flow in rough pipes*. *Technical Report*, National Advisory Committee for Aeronautics (NACA); Washington, DC, United States.

Nilson, R. (1981). Gas-driven fracture propagation. *Journal of Applied Mechanics*, 48(4):757–762.

Nilson, R. (1986). An integral method for predicting hydraulic fracture propagation driven by gases or liquids. *International Journal for Numerical and Analytical Methods in Geomechanics*, 10(2):191–211.

Nilson, R. (1988). Similarity solutions for wedge-shaped hydraulic fractures driven into a permeable medium by a constant inlet pressure. *International Journal for Numerical and Analytical Methods in Geomechanics*, 12(5):477–495.

Nilson, R. H. and Griffiths, S. K. (1983). Numerical analysis of hydraulically-driven fractures. *Computer Methods in Applied Mechanics and Engineering*, 36(3):359–370.

Nordgren, R. (1972). Propagation of a vertical hydraulic fracture. *Society of Petroleum Engineers Journal*, 12(4):306–314.

Perkins, T. K. and Kern, L. R. (1961). Widths of hydraulic fractures. *Journal of Petroleum Technology*, 13(9):937–949.

Plemelj, J. (1908). Ein ergänzungssatz zur cauchyschen integraldarstellung analytischer funktionen, randwerte betreffend. *Monatshefte für Mathematik*, 19(1):205–210.

Reynolds, O. (1883). An experimental investigation of the circumstances which determine whether the motion of water shall be direct or sinuous, and of the law of resistance in parallel channels. *Philosophical Transactions of the Royal Society of London*, 174:935–982.

Rice, J. R. (1968). Mathematical analysis in the mechanics of fracture. *Fracture: an advanced treatise*, 2:191–311.

Rice, J. R., Tsai, V. C., Fernandes, M. C., and Platt, J. D. (2015). Time scale for rapid draining of a surficial lake into the greenland ice sheet. *Journal of Applied Mechanics*, 82(7):071001.

Rivalta, E., Taisne, B., Bunger, A., and Katz, R. (2015). A review of mechanical models of dike propagation: Schools of thought, results and future directions. *Tectonophysics*, 638:1–42.

Rutledge, J. T. and Phillips, W. S. (2003). Hydraulic stimulation of natural fractures as revealed by induced microearthquakes, carthage cotton valley gas field, east texas. *Geophysics*, 68(2):441–452.

Savitski, A. A. and Detournay, E. (2002). Propagation of a penny-shaped fluid-driven fracture in an impermeable rock: asymptotic solutions. *International Journal of Solids and Structures*, 39(26):6311–6337.

Settari, A., Bale, A., Bachman, R., and Floisand, V. (2002). General correlation for the effect of non-darcy flow on productivity of fractured wells. In *SPE Gas Technology Symposium*, Calgary, Alberta, Canada. Society of Petroleum Engineers. SPE-75715-MS.

Siriwardane, H. and Layne, A. (1991). Improved model for predicting multiple hydraulic fracture propagation from a horizontal well. In *SPE Eastern Regional Meeting*, Lexington, Kentucky. Society of Petroleum Engineers. SPE-23448-MS.

Sneddon, I. and Lowengrub, M. (1969). Crack problems in the classical theory of elasticity, john willey & sons. *New York*, page 29.

Sokhotskii, Y. V. (1873). On definite integrals and functions employed in expansions into series.

Streeter, V. L. (1961a). Handbook of fluid dynamics. In *Handbook of fluid dynamics*. New York, McGraw-Hill.

Streeter, V. L. (1961b). *Handbook of fluid dynamics*. McGraw-Hill Book Company, INC., 1 edition.

Strickler, A. (1923). *Beiträge zur Frage der Geschwindigkeitsformel und der Rauhigkeitszahlen für Ströme, Kanäle und geschlossene Leitungen*. Technical Report Tech. Rep. 16, Mitteilungen des Eidgenossischen Amtes für Wasserwirtschaft, Bern.

Strickler, A. (1981). Contributions to the question of a velocity formula and roughness data for streams, channels and closed pipelines. Technical Report 16, Technical Report Rep. translation T-10, Lab. of Hydraulic and Water Resource, California Institute of Technology, Pasadena. Translated from German by T. Roesgen et al.

Szeg, G. (1975). *Orthogonal polynomials*, volume 23. American Mathematical Society, Providence, Rhode Island, USA, 4 edition.

Tada, H., Paris, P. C., and Irwin, G. R. (2000). *The stress analysis of cracks handbook*. 3 edition.

Te Chow, V. (1959). *Open channel hydraulics*. McGraw-Hill Book Company, Inc; New York.

Tsai, V. C. and Rice, J. R. (2010). A model for turbulent hydraulic fracture and application to crack propagation at glacier beds. *Journal of Geophysical Research: Earth Surface*, 115(F3).

Tsai, V. C. and Rice, J. R. (2012). Modeling turbulent hydraulic fracture near a free surface. *Journal of Applied Mechanics*, 79(3):031003.

Van As, A. and Jeffrey, R. G. (2000). Caving induced by hydraulic fracturing at northparkes mines. In *4th North American Rock Mechanics Symposium*. American Rock Mechanics Association.

Wang, Z. and Sun, B. and Wang, J. and Hou L. (2014). Experimental study on the friction coefficient of supercritical carbon dioxide in pipes. *International Journal of Greenhouse Gas Control*, 25:151–161.

Warpinski, N., Branagan, P., Mahrer, K., Wolhart, S., and Moschovidis, Z. (1999). Microseismic monitoring of the mounds drill cuttings injection tests. In *The 37th U.S. Symposium on Rock Mechanics (USRMS), 7-9 June, Vail, Colorado*, pages 1025–1032. ARMA-99-1025.

Wei, Y. and Economides, M. J. (2005). Transverse hydraulic fractures from a horizontal well. In *SPE Annual Technical Conference and Exhibition*, Dallas, Texas. Society of Petroleum Engineers. SPE-94671-MS.

Weisbach, J. L. (1855). *Die Experimental Hydraulik*. Engelhardt.

Whitaker, S. (1968). *Introduction to fluid mechanics*. Prentice-Hall.

Wright, C., Weijers, L., Davis, E., and Mayerhofer, M. (1999). Understanding hydraulic fracture growth: tricky but not hopeless. In *SPE annual technical conference*, pages 661–670.

Xing, P., Yoshioka, K., Adachi, J., El-Fayoumi, A., and Bunger, A. P. (2017). Laboratory measurement of tip and global behavior for zero-toughness hydraulic fractures with circular and blade-shaped (pkn) geometry. *Journal of the Mechanics and Physics of Solids*, 104:172–186.

Yang, Bobby H. and Joseph, Daniel D. (2009). Virtual Nikuradse. *Journal of Turbulence*, (10):N11.

Yang, S.-Q. and Dou, G. (2010). Turbulent drag reduction with polymer additive in rough pipes. *Journal of Fluid Mechanics*, 642:279–294.

Zhang, X., Detournay, E., and Jeffrey, R. (2002). Propagation of a penny-shaped hydraulic fracture parallel to the free-surface of an elastic half-space. *International Journal of Fracture*, 115(2):125–158.

Zia, H. and Lecampion, B. (2016). Laminar-turbulent transition in the propagation of height-contained hydraulic fracture. American Rock Mechanics Association (ARMA), Houston, Texas. ARMA-2016-786.

Zia, H. and Lecampion, B. (2017). Propagation of a height contained hydraulic fracture in turbulent flow regimes. *International Journal of Solids and Structures*, 110:265–278.

Zoback, M. D., Haimson, B. C., et al. (1982). Status of the hydraulic fracturing method for in-situ stress measurements. In *The 23rd US Symposium on Rock Mechanics (USRMS)*. American Rock Mechanics Association.

Zolfaghari, N. and Bunger, A. P. (Submitted A). Semi-analytical solution for a penny-shaped rough-walled hydraulic fracture driven by turbulent fluid in an impermeable rock. *International Journal of Solids and Structures*.

Zolfaghari, N. and Bunger, A. P. (Submitted B). Numerical model for a penny-shaped hydraulic fracture driven by laminar/turbulent fluid in an impermeable rock. *International Journal of Solids and Structures*.

Zolfaghari, N., Dontsov, E., and Bunger, A. (2017). Solution for a plane strain rough-walled hydraulic fracture driven by turbulent fluid through impermeable rock. *International Journal for Numerical and Analytical Methods in Geomechanics*, 1–31.

Zolfaghari, N., Meyer, C. R., and Bunger, A. P. (2017). Blade-shaped hydraulic fracture driven by a turbulent fluid in an impermeable rock. *Journal of Engineering Mechanics*, 143(11):04017130.